# STRUCTURAL AND ELECTRONIC PROPERTIES OF

# $BaV_{10}O_{15}$, $BaV_{10-x}Ti_xO_{15}$, and $BaVO_{3-x}$

By

CRAIG ALLAN BRIDGES, B.Sc.

A Thesis

Submitted to the School of Graduate Studies

in Partial Fulfillment of the Requirements

for the Degree

Doctor of Philosophy

McMaster University

# STRUCTURAL AND ELECTRONIC PROPERTIES OF

# $BaV_{10}O_{15}$, $BaV_{10-x}Ti_xO_{15}$, and $BaVO_{3-x}$

DOCTOR OF PHILOSOPHY (2002)
(Chemistry)

McMaster University
Hamilton, Ontario

TITLE: Structural and Electronic Properties of $BaV_{10}O_{15}$, $BaV_{10-x}Ti_xO_{15}$, and $BaVO_{3-x}$

AUTHOR: Craig Allan Bridges, B.Sc.
(University of Alberta)

SUPERVISOR: Professor John E. Greedan

NUMBER OF PAGES: xviii, 290

# Abstract

The compound $BaV_{10}O_{15}$ exhibits a first-order structural phase transition in the temperature range 105K-135K, depending upon the sample. The variation in transition temperature has been correlated with a variation in the lattice parameters and degree of sample oxidation. Crystal symmetry decreases from Cmca in the high temperature phase, to Pbca in the low temperature phase. Single crystal work has shown a decrease in certain V-V distances, which has been attributed to metal-metal bond formation. A cooperative magnetic transition occurs near 42K that contains features of both spin glass behavior and long range magnetic order. Powder neutron diffraction has shown that the moment is much lower than the expected value of $2.2\mu_B$. Furthermore, the magnetic entropy released below 70K is less than 15% of the entropy release expected for this moment value.

The series $BaV_{10-x}Ti_xO_{15}$ ($x$ = 0-8) is isostructural with the high temperature phase of $BaV_{10}O_{15}$. Spin glass-like behavior is observed up to a doping level of ~50% titanium, above which there is no apparent collective magnetic transition. Two models have been proposed to explain the thermopower and resistivity data for this series. The first model is based upon small polaron hopping of localized carriers. The second involves hole doping of an intrinsic band semiconductor.

A new preparation route has been developed for 5H $BaVO_{2.8}$ using the induction furnace. It was determined that addition of 4% to 8% molar excess of vanadium in the reaction produced a pure material. In a study of $BaVO_{2.8}$ using powder neutron diffraction, peaks due to long-range magnetic order were not detected. The possibilities of either a spin-glass or superparamagnetic ground state remain. Transport property measurements on $BaVO_{2.8}$ suggest that two-dimensional variable range hopping is occurring at low temperatures. With oxidation, the dominant carrier type changes from holes ($BaVO_{2.8}$) to electrons ($BaVO_{3.0}$).

## Acknowledgements

Dr. John E. Greedan deserves a great deal of credit for directing me towards this challenging project, and for encouraging me every step of the way. Thank you for sharing your knowledge and experience with me. I would also like to thank the other members of my committee, Dr. Jacques Barbier and Dr. Graeme Luke for all of their support. Special thanks to the members of the research group over the years, including Mario Bieringer, Chris Wiebe, Gisele Amow, Raju Nandyala, Robert Lam, Athena Sefa-Sefat, and Lisheng Chi. Thank you to Hanna Dabkowska, Anton Dabkowski, Jim Garrett, Bruce Collier, Frank Gibbs, David Levy and Jim Britten for their friendship and insights on research. I would like to thank Dr. Ian Swainson, Dr. Jason Gardner, Dr. Robert Hammond and Ron Donnaberger at NRC in Chalk River, Simine Short at IPNS in Argonne, and Dr. Thomas Hansen at ILL in Grenoble.

The faculty, staff and graduate students of the chemistry department provided an excellent environment for research and learning. I would like to thank you for leaving me with many fond memories. In particular, those summers of fun with the IR Sox.

To my parents, in more than a simply biological way, I would not be here without you. You have always supported me in any endeavor, not the least of which includes this thesis. It is truly wonderful to know that I will always have that. To Leigh, and the rest of my family, thank you for your loving support.

Thank you Tiger and Kyoko, Naoe, Naomi, Hiromi, Tamotsu, Sae, Koji, Nozomi and Chris for making me a part of your family. おとうさん と おかあさん, ほんとうにおせわになりました.

To my true love, Ayumi, thank you for sharing all of the love and generosity in your spirit with me. I am so blessed to have you in my life, Jinkomei.

A final thanks goes to the friends I have had the privilege of knowing during my time here, including Rob, Andrew, Rodica, Klaus, Heidi, Mario, Sudarshi, Sabine, Jamal, Kiersten and Brian.

I would like to dedicate this thesis to Gramie Mowat and Grandpa Bridges, two of the most wonderful role models a person could ever hope for.

# Table of Contents

# List of Tables

# List of Figures

# Introduction

## 1.1 Objective

Much of modern solid state chemistry is devoted to examining the relationship between crystal structure, electronic structure, and physical properties. In recent years, complex oxide systems such as high temperature superconductors based on copper oxides, and magnetoresistive or battery materials based upon manganese oxides, have received a great deal of attention.(Weller and Knee 2001) These fascinating systems have been driven to the forefront of research by the combined interest of industry and academia. Beyond these specific examples, transition metal oxides have attracted a wide range of experimental and theoretical work, due to the occurrence of highly correlated electron phenomena and complicated magnetic behavior. The properties of these materials are determined by the presence of *d* electrons and the chemical environment in which the cations reside. The solid state chemist is interested in modifying the structural and electronic environment, and thereby the resulting properties.

The crystal structure has a significant impact upon the magnetic behavior of a material. This is clearly demonstrated by the influence of competing magnetic interactions to produce magnetic frustration in triangular based lattices. In addition, magnetic frustration can occur as a result of chemical disorder. The exotic magnetic ground states associated with magnetic frustration are of particular interest to this thesis.

In the arena of highly correlated electron phenomena, vanadium oxides have played an important role in the development of theories on metal-insulator transitions (MIT). Metal-insulator transitions which are electronic in nature are subdivided into two classes: the Mott transition and the Anderson transition. These transitions deal with the ability of electron-electron correlations and disorder to stabilize an insulating phase. Two common examples of these transitions are $V_2O_3$, widely cited in the literature as the 'canonical' Mott insulator, and $La_{1-x}Sr_xVO_3$, well known to exhibit a transition versus doping level.(Imada, Fujimori et al. 1998)

The vanadates which are the focus of this thesis, illustrate how the interplay between crystal structure and chemical disorder can produce a high degree of electron correlation and magnetic frustration. The focus of chapter 3 is the material $BaV_{10}O_{15}$, which exhibits a structural phase transition, metal-metal bond formation, unusual transport properties, and a mixed magnetic ground state with features of spin-glass behavior and long range magnetic order. In chapter 4, the series $BaV_{10-x}Ti_xO_{15}$ will be used to illustrate the effects of disorder and hole-doping on the properties of $BaV_{10}O_{15}$. The series of compounds $BaVO_{3-x}$ are presented in chapter 5 to illustrate a transition from $BaVO_{2.8}$, a semiconductor which exhibits spin glass behavior, to $BaVO_{3.0}$, a compound on the edge of a metal-insulator transition. These systems will be summarized in chapter 6, along with potential avenues in which to expand upon this work.

Before presenting the results on these materials, background to the necessary concepts will be presented in the remainder of this chapter, and to experimental methods in chapter 2.

## 1.2 Magnetism

In its most basic form, magnetism may be divided into diamagnetism and paramagnetism. For paramagnetic samples, interactions between magnetic ions can lead to complicated cooperative phenomena that will be discussed further below. It will be more instructive initially to survey the core concepts of magnetochemistry.

When a material is exposed to a magnetic field ($H_o$), a field results inside the sample (B) that differs from the applied field according to:

$$B = H_o + 4\pi I \qquad (1.2.1)$$

where $I$ is the induced magnetic moment per unit volume, known as the induced magnetization. If equation 1.2.1 is divided through by the applied field, the quantity $I$ is replaced by the volume susceptibility ($\kappa$). The susceptibility is commonly used to describe magnetic behavior, and is often converted using the density and molar mass of a substance into the molar susceptibility ($\chi$). This quantity will be referred to not only below, but also extensively throughout the thesis.

### 1.2.1 Diamagnetism

In the absence of an applied field, the net flow of electrons in an atom is zero. In classical terms, application of a magnetic field induces a non-zero current; the direction of this current is such that a magnetic field is produced in opposition to the applied field. If all of the electrons are paired, this induced field is the dominant magnetic response, and the atom is termed a diamagnet. A diamagnetic sample is readily identified

experimentally by a negative susceptibility. This effect is considered for the purposes of this thesis only as a correction to the measured susceptibility.

### 1.2.2 Paramagnetism

In the presence of an applied field, materials that contain unpaired electrons exhibit a magnetic moment, due to orbital and/or spin angular momentum contributions. The susceptibility for materials containing unpaired electrons is positive, and the effect is called paramagnetism.

A general expression for paramagnetic behavior is Van Vleck's susceptibility equation:

$$\chi = \frac{N_A \sum_n [(E_n^{(1)^2} / kT) - 2E_n^{(2)}] e^{(-E_n^{(0)} / kT)}}{\sum_n e^{(-E_n^{(0)} / kT)}}, \quad (1.2.2)$$

where $N_A$ is Avogadro's number, $E_n^{(0)}$ is the energy of the nth level for an atom in the absence of a field, $E_n^{(1)}$ is the first-order Zeeman coefficient, and $E_n^{(2)}$ is the second-order Zeeman coefficient. The first-order Zeeman effect involves the change in energy of the nth level due to the application of a magnetic field. The second-order Zeeman effect arises from the change in energy of the nth level due to mixing in of higher energy levels, via the magnetic field. For the second-order Zeeman effect, application of a field changes the energy of higher levels to the point that they become degenerate with the lower levels. These degenerate levels can now mix to form new states.

Therefore, paramagnetism relies upon the change in energy levels of an atom upon application of a magnetic field, and the temperature dependent occupation of the new states that are created. These states are occupied according to a Boltzmann distribution.(O'Connor 1982)

Application of a magnetic field is not the only manner in which free ion energy levels are perturbed. Before we expand upon the implications of equation 1.2.2, it is useful to consider the perturbation which results from coupling between the spin and orbital angular momenta of an atom. There are two different mechanisms by which a spin-orbit coupling interaction can occur. In the first scheme (Russell-Saunders), individual spin components ($s$) couple to produce the total spin angular momentum quantum number $S$, and orbital components ($l$) will couple to form the total orbital angular momentum quantum number $L$. These will then couple according to:

$$J = L+S, L+S-1 \ldots |L-S|, \quad (1.2.3)$$

where $J$ is the total angular momentum quantum number. In the second coupling scheme($j$-$j$), the $l$ and $s$ for a single electron couple first to form $j$, and then individual $j$ couple to form $J$. The first scheme holds well for the first-row transition metals and the lanthanides. An intermediate coupling scheme between the first and second type is appropriate for the 4d and 5d transition metals, as well as for the actinides. As the effect of spin-orbit coupling on energy levels is much stronger than that of the magnetic field, a treatment of the two effects would consider spin-orbit coupling before Zeeman splitting.

The first-order Zeeman effect splits degenerate free atom states resulting from the spin-orbit coupling into $(2J + 1)$ components. The new states are separated by an energy $g\mu_B H$, where $\mu_B$ is the Bohr magneton. The spectroscopic (or Landé) splitting factor, $g$, is given by:

$$g = 1 + \frac{[S(S+1) + J(J+1) - L(L+1)]}{2J(J+1)}, \qquad (1.2.4)$$

and the effective magnetic moment ($\mu_{eff}$) is:

$$\mu_{eff} = g[J(J+1)]^{1/2}. \qquad (1.2.5)$$

With a negligible second-order Zeeman coefficient, equation 1.2.2 can be reduced to the Curie Law, with an additional temperature independent term:

$$\chi = \frac{C}{T} + \alpha, \qquad (1.2.6)$$

where C is the Curie constant, and $\alpha$ represents the temperature independent paramagnetism (TIP). The TIP term is usually quite small, and only becomes significant at higher temperatures. The Curie constant may be related to the effective magnetic moment as (Mabbs and Machin 1973):

$$C = \frac{N\mu_B{}^2 \mu_{eff}{}^2}{3k_B} \approx \frac{\mu_{eff}{}^2}{8}. \qquad (1.2.7)$$

The constant $k_B$ is the Boltzmann constant. When a number of magnetic atoms are present, the Curie constant may be approximated as the sum of the individual contributions.

For 3d transition metal compounds, the orbital angular momentum is effectively quenched by the crystal field. As a result, equation 1.2.5 reduces to the spin-only formula, where $J$ is replaced by $S$ and $g \approx 2$:

$$\mu_{eff} = g[S(S+1)]^{1/2}. \qquad (1.2.8)$$

### 1.2.3 Cooperative Magnetism

With decreasing temperature, coupling between magnetic spins often results in a transition to an ordered state. There is a competition between the thermal energy, which randomizes the spins, and the exchange energy, which promotes ordering. There are three basic forms of long-range magnetic order: ferromagnetic, antiferromagnetic, and ferrimagnetic. A parallel alignment of spins is energetically favored for ferromagnetic interactions, whereas antiferromagnetic interactions result in an antiparallel arrangement of spins. Ferrimagnetic compounds contain magnetic atoms of different spin values. When atoms of a given type order antiparallel to the other type, a net moment remains from the vector sum of all contributing spins.

When interactions between magnetic atoms are considered, equation 1.2.6 is usually written as:

$$\chi = \frac{C}{T-\theta} + \alpha. \qquad (1.2.9)$$

This is called the Curie-Weiss law, to which a TIP term has been added. The name is derived from the Curie law, plus the addition of the Weiss constant (θ). This constant may be related to the strength of magnetic interactions – a negative value is taken to indicate antiferromagnetic coupling, while a positive value indicates ferromagnetic coupling.[1] Analysis of magnetic susceptibility data typically involves examining a plot of $\chi^{-1}$ versus temperature, in order to extract values of C, θ, and α. If a region is found, typically at higher temperatures, in which C is close to the expected value, the fit is considered successful. This behavior is illustrated in figure 1.1.(Carlin and Duyneveldt 1977)

## Exchange

For paramagnetic centers in magnetic insulators, the most significant coupling interactions are based upon the concept of exchange. Three different types of exchange interactions are briefly presented: direct (cation-cation), superexchange (cation-anion-cation)[2], and double exchange (cation-anion-cation). The direct exchange mechanism requires orbital overlap of neighboring magnetic centers. In oxide materials, as the magnetic ions are typically separated by a shell of anions, the dominant magnetic

---

[1] If the ground state contains degenerate terms, and there are thermally accessible excited terms, the Weiss constant may be added without requiring coupling between magnetic spins.

[2] The rules for this type of coupling do not explicitly deal with more than one intervening diamagnetic atom.

interactions involve coupling through intervening diamagnetic species. The general Hamiltonian for exchange coupling of spins is:

$$H_{ex} = -2JS_1 \cdot S_2, \qquad (1.2.10)$$

where $J$ is a scalar quantity called the exchange constant, and $S_1/S_2$ are spin operators on different atoms. The sign of the scalar indicates whether the triplet (positive $J$) or singlet (negative $J$) state is favored, and the energy of the system is minimized for a colinear spin arrangement.

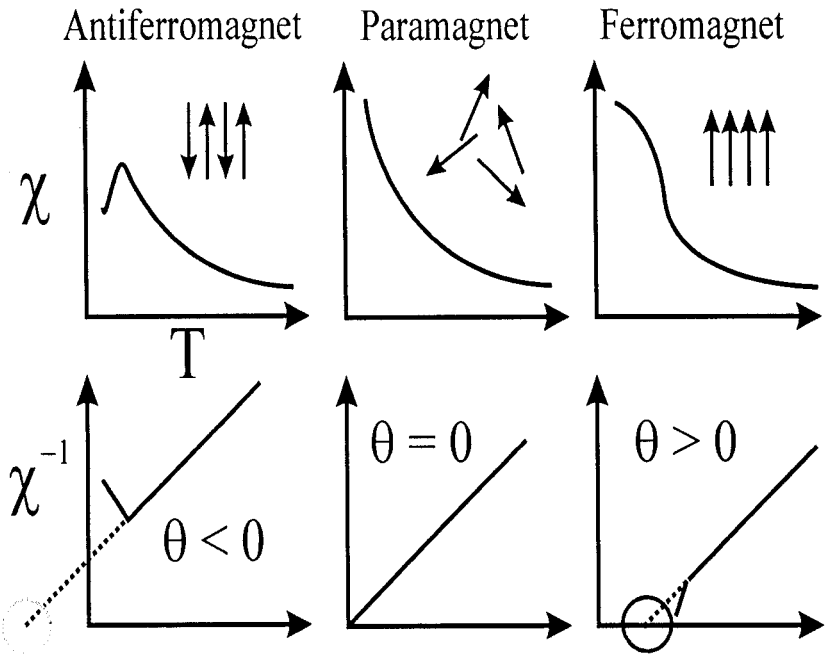


Figure 1.1: Analysis of DC magnetic susceptibility data using the Curie-Weiss law.

Two examples of superexchange interactions for a 180° $M^{n+}$-O-$M^{n+}$ bond angle, and octahedrally coordinated $M^{n+}$ cations with a $d^3$ electronic configuration , are given in figure 1.2. In the upper example, overlap occurs between a $d$ ($t_{2g}$) orbital from each cation and an oxygen $p$ orbital in a π-bonding configuration. The ($t_{2g}$) level is shown at a

higher energy than the ($t_{2g}^{+}$) level as a result of Hund's rule intraatomic exchange. If an electron is allowed to transfer, without change of spin, from the $p_\pi$ orbital to the ($t_{2g}^{-}$) orbital, then this electron must be antiparallel to the electron in the ($t_{2g}^{+}$) state.[3] The spin of the electron in the ($t_{2g}^{-}$) orbital is constrained by the Pauli principle, as are the electrons in the filled $p_\pi$ orbital. As a result, the $d$ electrons experience a net antiferromagnetic interaction.

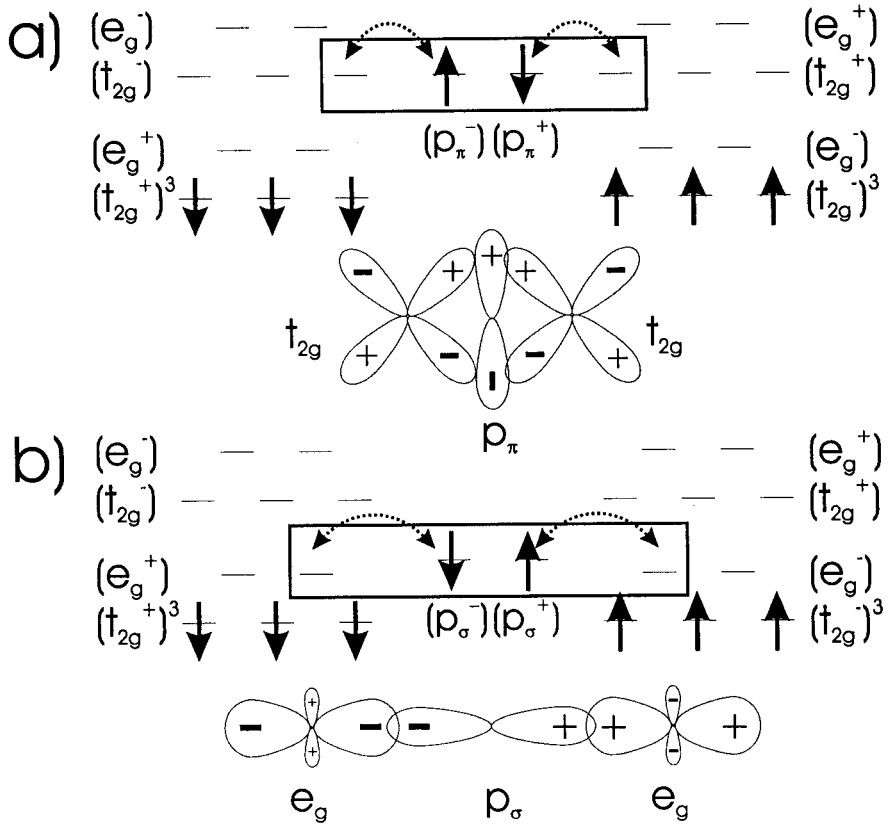


Figure 1.2: Orbital correlation diagrams for two 180° $d^3/d^3$ superexchange interactions in an octahedral crystal field: a) $t_2^3$-$p_\pi^2$-$t_2^3$ and b) $e_g$-$p_\sigma^2$-$e_g$. Both cases result in a net antiferromagnetic interaction. The orbital overlap is illustrated below each correlation diagram.

---

[3] The ground state is obtained again by returning the electron to the $p_\pi$ orbital.

The second example in figure 1.2 illustrates a superexchange interaction involving electron transfer between $e_g$ and $p_\sigma$ orbitals. As a result of Hund's rule and spin correlation, an electron in the $e_g$ orbital must be parallel to electrons in the $t_{2g}$ orbitals. As discussed above, the Pauli principle causes spins on the filled $p$ orbital to be antiparallel. Overall, this results in a net antiferromagnetic interaction between neighboring cations.

The exchange constant between two magnetic centers reflects the sum of various exchange interactions. While the above examples illustrate antiferromagnetic coupling, net ferromagnetic coupling between cations is also possible. The ferromagnetic interactions are generally weaker than antiferromagnetic, and are less commonly observed. The limiting cases in which the set of superexchange interactions are well understood involve 180° and 90° $M^{n+}$-O-$M^{n+}$ angles, and have been described by Goodenough and Kanamori for various electronic configurations involving octahedral coordination. Intermediate angles are more difficult to predict: slight changes in bond angle resulting from chemical substitution can cause a shift from net antiferromagnetic to ferromagnetic interactions (or the reverse). In summary, the exchange interaction is determined by factors including: the Pauli principle, Hund's rule, orbital filling, and the geometry of the M-O-M cluster.(Goodenough 1963)

The double exchange mechanism is important when cations with different oxidation states are present. This involves a net electron transfer from the reduced cation

to the oxidized cation. The same contributing factors are present as in the superexchange case, but the coupling is usually ferromagnetic.(Greedan 1994)

## Dimensionality

The Hamiltonian for coupling of spins in the general case may be rewritten from equation 1.2.10 as (O'Connor 1982):

$$H_{ex} = -2J[a(S_{1x}S_{2x} + S_{1y}S_{2y}) + b(S_{1z}S_{2z})]. \quad (1.2.11)$$

This emphasizes that the components along each axis are not necessarily equivalent. The Ising model results when $a$ is zero, and the spins are all aligned along one axis. The two dimensional case is called the XY model ($b$ = 0), and the three-dimensional case, the Heisenberg model ($a$ = 1, $b$ = 1). The dimensionality of the spin and lattice significantly influences the possibility of long-range magnetic order, as shown in table 1.1.

Table 1.1: Effect of Spin and Lattice Dimensionality on Magnetic Ordering

| Dimensionality | 1d | 2d | 3d |
|---|---|---|---|
| 1D | X | ✓ | ✓ |
| 2D | X | * | ✓ |
| 3D | X | X | ✓ |

Columns = dimensionality of the lattice; rows = dimensionality of the magnetic spins; 1D = one dimensional; 2D = two dimensional; 3D = three dimensional; ✓ = long-range magnetic order; X = only short-range order; * = borderline case

In low dimensional structures, significant exchange cannot occur in all three dimensions. For such materials, only short-range order is observed. Note that the situation for a two-

dimensional lattice with two-dimensional spin correlations is special, as it exists on the borderline between long- and short-range order.(Greedan 1994)

### 1.2.4 Magnetic Frustration

#### Spin Glass

Atomic disorder on the magnetic sublattice can produce a random distribution of ferromagnetic and antiferromagnetic exchange interactions, thereby inhibiting long-range magnetic order. In this situation, the spins are said to be *frustrated.* At a sufficiently low temperature the exchange energy dominates the thermal energy and a transition occurs to a frozen, random spin state. A large number of such random spin configurations are accessible, which leads to a high ground state degeneracy. This form of ordering, known as the spin-glass state, is illustrated in figure 1.3(a).[4] There are a number of characteristic experimental signatures of this state (Binder and Young 1986; Mydosh 1993; Weissman 1993):

(1) divergence at a temperature ($T_D$)[5] between the zero-field cooled (ZFC) and field-cooled (FC) DC magnetic susceptibilities[6],

---

[4] The term spin-glass originally referred to dilute magnetic systems. In more concentrated systems, interactions may result in short-range order above the freezing temperature. These materials were referred to as mictomagnets or cluster-glasses. More recently, the term spin-glass is applied commonly to both types of materials.

[5] The divergence temperature is also referred to as the freezing temperature ($T_F$), though the two temperatures may not exactly coincide. In addition, the term glass temperature ($T_G$) is equivalent to $T_F$.

[6] Field-cooling refers to a DC magnetic susceptibility experiment in which the sample is cooled in the presence of a field to the base temperature, at which point the measurement with increasing temperature is initiated. The zero-field case simply refers to cooling the sample in the absence of an applied field.

(2) time dependent variation of the DC magnetic susceptibility occurs after cooling in zero-field,

(3) a peak occurs for the in-phase ($\chi'$) and out-of-phase components ($\chi''$) of the AC magnetic susceptibility near $T_D$; both $\chi''$ and $\chi'$ exhibit a frequency dependency, such that the maximum near $T_D$ shifts to higher temperature with increasing frequency,

(4) a broad maximum, or a lack of any feature, at $T_D$ in the heat capacity,

(5) the magnetic contribution to the heat capacity produces a linear temperature dependence at low temperatures.

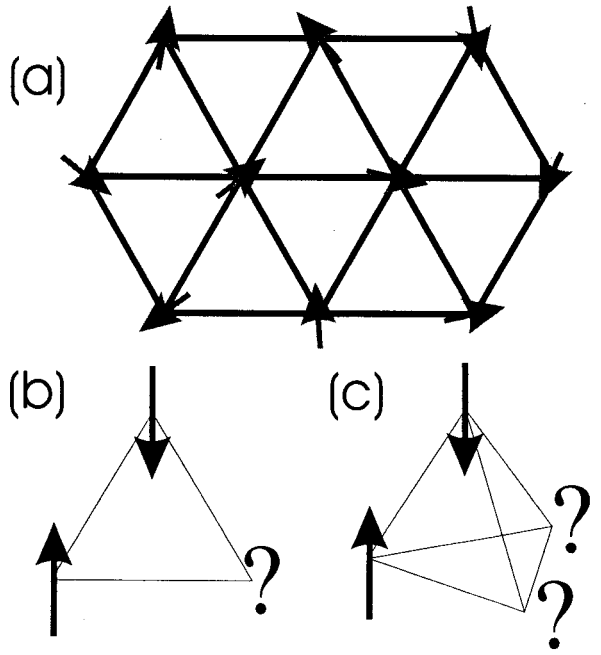


Figure 1.3: Examples of frustrated spin systems. (a) random, frozen spin orientations present in the spin glass state below the freezing temperature; (b) geometric antiferromagnetic frustration for a triangular motif; (c) geometric antiferromagnetic frustration for a tetrahedron.

## Geometric Antiferromagnetic Frustration

Nature has also made it possible to find frustration in the absence of disorder. The basic model for geometric frustration involves a triangular lattice of spins, coupled antiferromagnetically. All three of the nearest-neighbor antiferromagnetic constraints cannot be simultaneously satisfied, leading to geometric antiferromagnetic frustration (figure 1.3(b,c)). In this situation, the ground state is highly degenerate, which leads to similar experimental phenomena as found in spin-glasses. A number of structure types are known to possess the necessary geometric requirements for this type of frustration. These include the magnetic atom *sublattice* of pyrochlores, jarosites, and $SrCr_9Ga_3O_{19}$ (SCGO), as shown in figure 1.4.

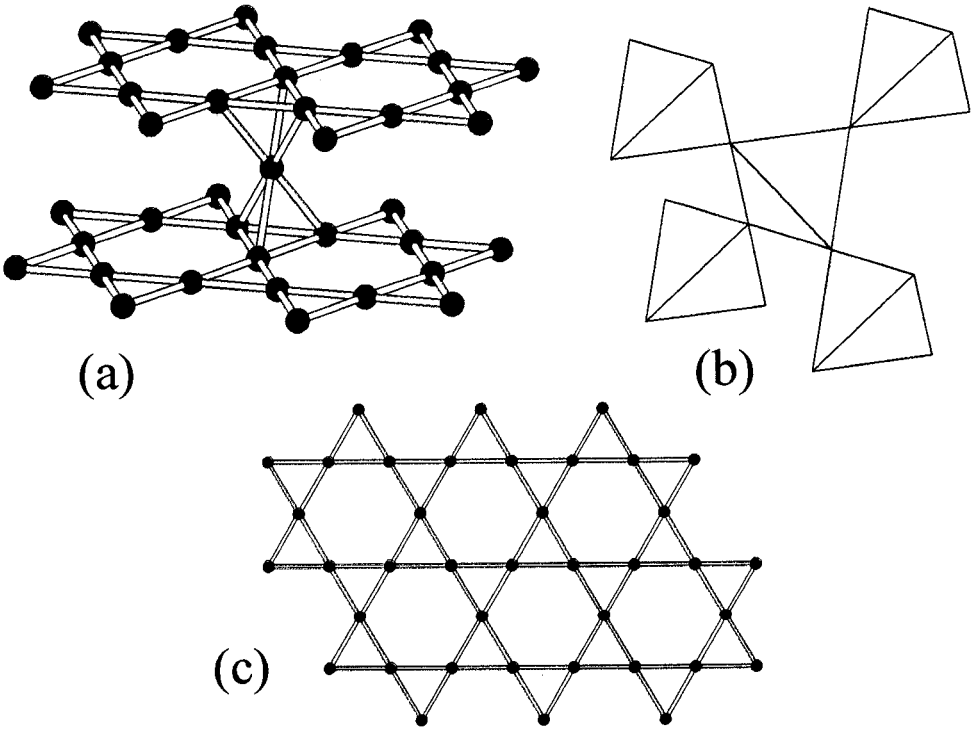


Figure 1.4: Magnetic sublattice of (a) $SrCr_9Ga_3O_{19}$, (b) pyrochlores (vertices of tetrahedra correspond to magnetic ions), and (c) Jarosites.

In some cases, a 120° long-range ordered spin structure is accessible at low temperatures for triangular magnetic ion sublattices, such that the total spin within each triangle is zero. Two possible 120° spin structures for the Kagome sublattice are shown in figure 1.5: the (c) $q = 0$ and (d) $q = \sqrt{3}\times\sqrt{3}$ structures. Equivalent structures are obtained in each case when the spins are simultaneously rotated by an arbitrary angle. Moreover, the chirality of all triangles in a given structure can be simultaneously reversed, which introduces degeneracy into the ground state. For tetrahedral sublattices, such as found in the pyrochlore structure, a 109° long-range ordered spin structure is possible.(Greedan 2001)

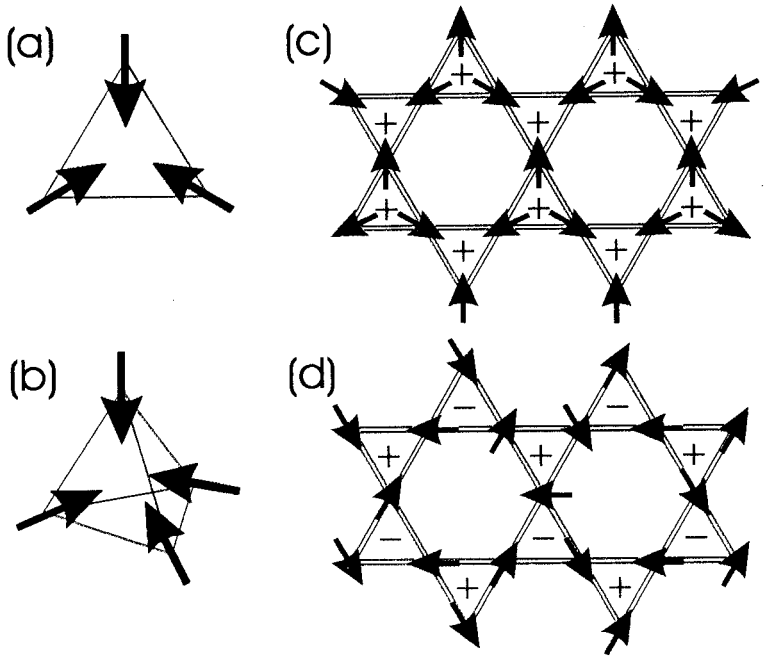


Figure 1.5: Long-range ordered ground states for (a) 120° spin arrangement for a simple triangle, (b) 109° spin structure for a tetrahedral geometry, and (c)/(d) 120° spin structure on the Kagome lattice. The chirality (indicated by '+' and '-' signs) alternates between triangles in (d), but is the same for all triangles in (c).

## Spin Liquid and Spin Ice

A state has been proposed, in particular for frustrated S = ½ systems, in which the spins do not exhibit long-range order or spin freezing at low temperatures. In this model the spins remain dynamic, though strong correlations produce a singlet state for pairs of spins. These pairs remain dynamic by flipping 180°, while remaining in the singlet state. This situation has been described by Anderson as the Resonating Valence Bond (RVB) state, and is alternately referred to as spin liquid behavior, or collective paramagnetism.(Gingras, Hertog et al. 2000; Greedan 2001)

It has been recently suggested that some materials with the pyrochlore structure, namely $Ho_2Ti_2O_7$ and $Dy_2Ti_2O_7$, can exhibit geometric frustration in the presence of ferromagnetic coupling. The necessary condition is a strong single-site anisotropy along the {111} axes. In this case, ground state degeneracy prevents long-range order; instead resulting in a static disordered state with the spins aligned along the {111} axes. This differs from the antiferromagnetic case, in which long-range order is expected.(Bramwell and Gingras 2001; Gingras and Hertog 2001; Matsuhira, Hinatsu et al. 2001)

## Mixed Long-Range Order and Spin Glass Behavior

Due to the difficulties in satisfying the pairwise exchange interactions for all spins in a frustrated compound, a mixture of long-range order and spin glass behavior has been observed for a range of materials. In a model proposed by Villain (Villain 1979) to account for this behavior, a magnetic transition occurs from a ferrimagnetic state, to a

semi-spin glass state. The semi-spin glass state is predicted to display a ferrimagnetic longitudinal component, in conjunction with a spin glass state for the transverse components.(Hubsch and Gavoille 1982) This model has been extended to account for canted random ferromagnetic (CRF) and uniaxial random ferromagnetic (URF) phases.(Chakravarthy, Rao et al. 1991) The CRF model is essentially identical to the Villain semi-spin glass, but is rather applied to a ferromagnet. The URF phase differentiates between long-range ordered spins that lie in the direction of broken symmetry (z-axis), and disordered spins in the x-y plane.

A more general term used to describe this behavior is re-entrant spin glass (RSG).(Nath, Sudhakar et al. 1997) These materials may exist near the percolation threshold, which separates pure spin glass and long-range order.(Srinath and Kaul 2000) It has been proposed that in some materials there are actually two phases present in a given sample, but this cannot account for all instances of RSG behavior.(Coldea, Spring et al. 1999) Regardless of whether antiferromagnetic or ferromagnetic exchange is dominant, a number of compounds have been found to exhibit a transition from an apparently long-range ordered phase to a mixed long-range ordered and spin glass-like phase, or simply back to a fully disordered spin glass phase. A general framework for understanding all such materials is not currently available.

## 1.3 Diffraction Theory

Diffraction methods are used to examine the periodic structure of matter. The requirement for periodicity is met in crystals, which are composed of the type of building blocks shown in figure 1.6. The various methods commonly employed to study crystal structures include electromagnetic radiation (specifically X-rays), electrons, and neutrons. X-ray diffraction is used in the laboratory for qualitative phase identification, quantitative analysis of a mixture of phases, and crystal structure determination. Due to the extremely strong interaction between electrons and the sample, electron diffraction is used to examine individual microcrystals; this technique is particularly well suited to the study of defect structures, and minor contributors to a multiphasic sample. Various applications for neutron diffraction include the study of compounds containing light elements, elements of a similar atomic number, and magnetic ions.

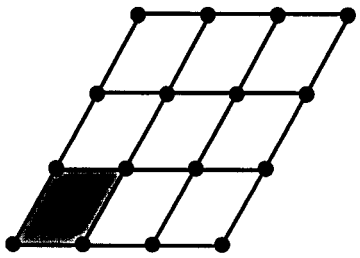

Figure 1.6: Basic schematic of a two-dimensional lattice. The shaded area represents the unit cell.

### 1.3.1 Bragg's Law

A fundamental relation for X-ray, electron and neutron diffraction is Bragg's Law:

$$n\lambda = 2d\sin\theta \qquad (1.3.1)$$

For the case of X-ray diffraction, the incident beam interacts with electrons in the plane and scatters in all directions. Only the part of the beam that is scattered in phase will undergo constructive interference, and produce a peak at the detector. As the equation informs us, the spacing of these planes $(d)$[7], the wavelength of the radiation ($\lambda$), and the angle of interest relative to the incident beam ($\theta$) are each important in determining whether constructive interference occurs.(Stout and Jensen 1989)

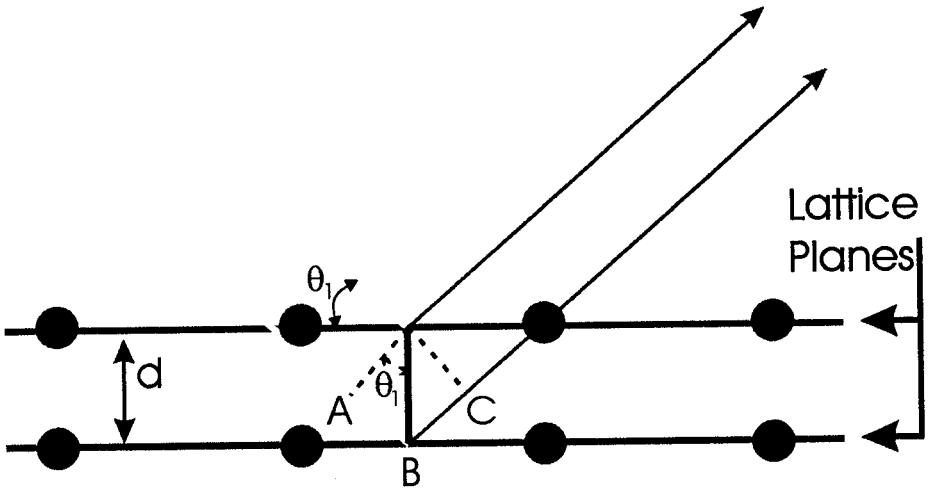


Figure 1.7: Constructive interference of diffracted waves according to Bragg's Law.

The derivation of this law is illustrated in figure 1.7. The lower beam must travel farther than the upper beam, as the lower beam penetrates more deeply into the solid. For the lower beam to exit the solid in phase with the upper beam, the extra distance (AB+BC) traveled must be an integral number of wavelengths. The relationship between the extra distance and the wavelength can be expressed as:

$$AB + BC = d\sin\theta + d\sin\theta \quad (1.3.2)$$

and

$$AB + BC = n\lambda. \quad (1.3.3)$$

A combination of equations 1.3.2 and 1.3.3 yields Bragg's Law. This relationship holds for elastic scattering, in which the incoming beam has the same energy as the diffracted beam.

The set of lattice planes is related only to the size and shape of the unit cell, and is essentially infinite. However, there are a finite number of diffraction planes that are experimentally accessible. A basic estimate of the minimum d-spacing ($d_{MIN}$) is derived by setting $\sin\theta$ to 1, its maximum possible value. The magnitude of $d_{MIN}$ is therefore $\lambda/2$. Using the complete set of experimentally accessible d-spacings, derived from the peak positions in a powder diffraction pattern (figure 1.8), the unit cell can be determined.

### 1.3.2 X-ray Diffraction

A number of different sources can be used to produce X-ray radiation. These include sealed tubes (brilliance of ~$10^7$)[8], rotating anodes (~$10^9$), and synchrotron sources ($10^{10}$-$10^{19}$).(Bassett and Brown 1990) An increase in brilliance is associated with an increase in cost, and a corresponding decrease in availability - sealed tubes are the least expensive, and by far the most commonly used source of X-rays.

---

[7] Note that the planes indicated in the figure are purely imaginary.

[8] Brilliance is defined as the photon flux per second per square millimeter per square milliradian per 0.1% bandwidth.

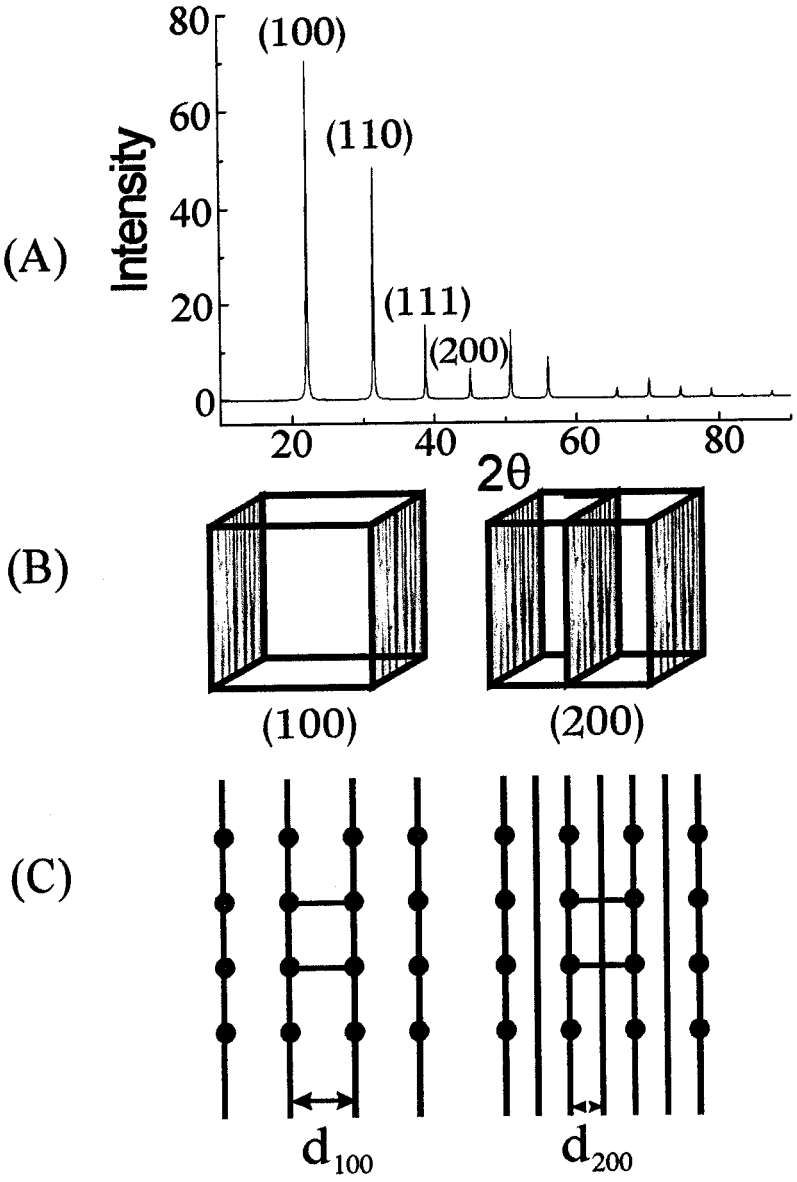


Figure 1.8: Relationship between a powder diffraction pattern and lattice planes. (a) X-ray powder diffraction pattern of a cubic lattice with atoms at the corners. A number of the reflection planes are indicated; (b) the (100) and (200) planes are shown; (c) a view of the (100) and (200) planes from above. The unit cell is outlined at the center of the lattices at the bottom.

In X-ray diffraction, the intensity with which the radiation is scattered is expressed by the scattering factor ($f_o$), which:

(1) increases with increasing atomic number (Z), and

(2) decreases rapidly with increasing $\sin\theta/\lambda$.

The first point is related to the increase in the number of electrons with Z. The probability of a scattering event increases with the number of electrons around an atom. The second point arises from the diffuse nature of the electron cloud from which the X-rays scatter. With increasing $\sin\theta/\lambda$, X-rays scattered from electrons in one part of an atom or ion will be out of phase with X-rays scattered from another part. The size of the electron cloud is a function of the level of atomic displacement caused by thermally accessible vibrational modes, and is therefore a sensitive function of temperature. The effect of this displacement on the scattering factor is expressed by the atomic displacement parameter ($B$), which is related to the mean-square amplitude ($\overline{u^2}$) of atomic vibration by (Stout and Jensen 1989):

$$B = 8\pi^2 \overline{u^2} . \qquad (1.3.4)$$

In consideration of the above discussion, the final expression for the scattering factor is[9]:

$$f = f_o e^{(-B\sin^2\theta/\lambda^2)} . \qquad (1.3.5)$$

With knowledge of the crystal structure, the structure factor ($F_{hkl}$) for each reflection can be calculated according to:

---

[9] The exponential part is referred to as the Debye-Waller factor.

$$F_{hkl} = \sum_j f_j e^{(2\pi i(hx+ky+lz))}, \qquad (1.3.6)$$

where the phase (relative to the origin of the unit cell) of the radiation scattered from atom *j* by the *hkl* plane is given by the exponential. This equation demonstrates that the crystal structure of a material affects the intensity of the measured reflections.

The structure factor is the reciprocal space representation of the direct space electron density. Similarly, through Fourier synthesis the electron density ($\rho_{(x,y,z)}$) can be represented in terms of the structure factor:

$$\rho_{(x,y,z)} = \frac{1}{V}\sum_h\sum_k\sum_l F_{hkl} e^{(-2\pi i(hx+ky+lz))}, \quad (1.3.7)$$

where V is the unit cell volume. This calculation is particularly useful for finding atoms in an incomplete structure solution via a difference synthesis ($\Delta\rho$). This involves replacing $F_{hkl}$ with $\Delta F$ in equation 1.3.7, where $\Delta F$ is the difference between the modulus of the observed structure factor ($|F_o|$) and the modulus of the calculated structure factor ($|F_c|$). To a first approximation, peaks will correspond to missing atoms, and holes to incorrectly placed atoms.(Stout and Jensen 1989)

It is the square of the structure factor that is measured experimentally

$$|F_{hkl}|^2 = I_{obs}, \qquad (1.3.8)$$

where $I_{obs}$ is the measured intensity for the *hkl* reflection.[10] As a result, the information

[10] In practice, the observed intensities must be corrected for Lorentz, polarization, and absorption effects.

about the phase of the scattered wave is lost, a situation which is commonly called the phase problem. Methods exist to determine a trial set of phases, such as direct methods or Patterson methods. From these trial phases, and a significant amount of chemical intuition, the structure can be determined from a set of reflection intensities.

Refinement of single crystal X-ray diffraction data is based on a comparison between $F_o$ and $F_c$. As trial solutions approach the correct crystal structure, the function:

$$D = \sum_{hkl} w_{hkl} \left( |F_o|^2 - k|F_c|^2 \right)^2 \qquad (1.3.9)$$

is minimized. In 1.3.9, $w_{hkl}$ is the weight given to the *hkl* reflection, and $k$ is a scale factor.

Various statistical measures are used to indicate the quality of the fit. These are:

$$wR2 = \left\{ \frac{\sum_{hkl} w_{hkl} \left( |F_o|^2 - |F_c|^2 \right)^2}{\sum_{hkl} w_{hkl} \left( |F_o|^2 \right)^2} \right\}^{1/2}, \qquad (1.3.10)$$

$$R1 = \frac{\sum_{hkl} \left( |F_o| - |F_c| \right)}{\sum_{hkl} \left( |F_o| \right)}, \qquad (1.3.11)$$

$$Goof = S = \frac{\sum_{hkl} w_{hkl} \left( |F_o|^2 - |F_c|^2 \right)^2}{n - p}. \qquad (1.3.12)$$

Here $S$ is the *Goodness of Fit (Goof)*, and *wR2* and *R1* are *R*-indices based upon $F^2$ and $F$, respectively. The variable $n$ is the number of reflections, and $p$ is the total number of parameters refined. As discussed for equation 1.3.9, refinement is performed against $F^2$,

and so 1.3.10 is used in most applications. This will reduce the chances of finding a false minimum in the structure solution, as all data may be used. For refinement against $F$, a threshold value would have to be used to remove weak reflections, as it is difficult to estimate the error from values of $F^2$ which are negative, or near zero. The magnitude of *wR2* is typically approximately double that of *R1*.

### 1.3.3 Neutron Diffraction

Neutrons are a versatile tool for investigating the structure of materials. The neutron is a neutral particle and can therefore penetrate deeply into samples. In addition, as the neutron possesses a magnetic moment, it can be used to study magnetic short or long-range order.

There are two different sources of neutrons in use: spallation and reactor sources. For spallation sources, a pulse of neutrons is created by the impact of high energy particles into a heavy element target. The target is first excited, and then decays to produce neutrons. The pulse contains neutrons with a range of energies, which are separated by their time-of-flight down a long, evacuated tube, before interacting with the sample. According to the De Broglie equation,

$$\lambda = \frac{h}{mv}, \qquad (1.3.13)$$

a change in neutron energy corresponds to a change in wavelength. Therefore, a range of wavelengths are scanned at a constant $2\theta$ to measure all of the reflections. The high

energy, low wavelength tail of the neutron pulse provides extremely good resolution (reflections at low d-spacings) for studies of crystal structure.

The neutrons initially produced from the decay of $U^{235}$ at a reactor have an extremely high energy. To bring the energy into a useful range for diffraction, the neutrons are moderated by collisions with protons or deuterons in the bath that surrounds the core. After a number of collisions, thermal equilibrium is reached and the neutrons acquire an energy distribution with its maximum at the temperature of the moderator. The resulting distribution of neutron wavelengths is known as a Maxwellian; both the position and width of this peak can be changed by passing the neutrons through a moderator at a different temperature. The temperature may vary from 25K ($D_{2(l)}$) to 2400K (block of graphite). A single wavelength is selected by passing the beam through a monochromator, and potentially a filter of higher order wavelengths, before it interacts with the sample.

Neutrons scatter from the nucleus of an atom by a process that involves the formation of an intermediate compound nucleus, which then decays to eject a neutron. In an elastic scattering event, the ejected neutron has the same energy as the incident neutron, and will diffract according to Bragg's law. In neutron diffraction, scattering is described using the scattering vector $\vec{Q}$, as in figure 1.9.

$$\vec{Q} = \vec{k}' - \vec{k}, \qquad (1.3.14)$$

This is related to Bragg's Law according to:

$$\bar{Q} = \frac{4\pi \sin\theta}{\lambda} = \frac{2\pi}{d_{hkl}}. \qquad (1.3.15)$$

The intensity of the scattering does not vary in a continuous fashion with increasing atomic number, as in the case of X-ray diffraction. An extensive list of scattering lengths (*b*) are compared in figure 1.10, and are average values for the given isotope distribution.[11] The scattering length is related to the scattering factor for X-ray diffraction, but differs in its angular dependence; the scattering length is essentially constant up to high angle, due to the fact that the nucleus approximates a point source.

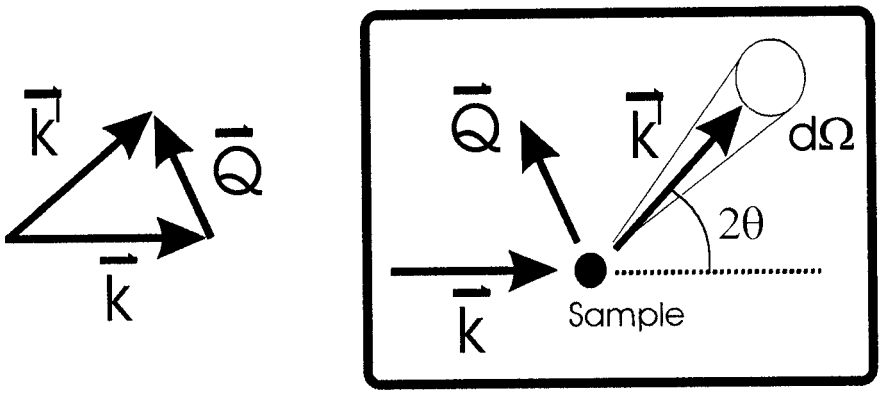


Figure 1.9: Derivation of the **Q** vector from the incident (**k**) and scattered (**k'**) neutron beams.

The probability (σ), referred to as a cross section, for scattering a neutron is composed of three different contributions: the coherent cross section ($\sigma_{coh}$), the incoherent cross section ($\sigma_{incoh}$), and the absorption cross section ($\sigma_{abs}$). The cross section

and scattering length are related by:

$$\sigma = 4\pi b^2 . \quad (1.3.16)$$

The structure factor for neutrons is dependent upon the scattering length, and the phase of the diffracted beam, according to:

$$F_{hkl} = \sum_j b_j e^{(2\pi i(hx+ky+lz))} . \quad (1.3.17)$$

This is similar to equation 1.3.6, but with $f$ replaced by $b$. (Squires 1996)

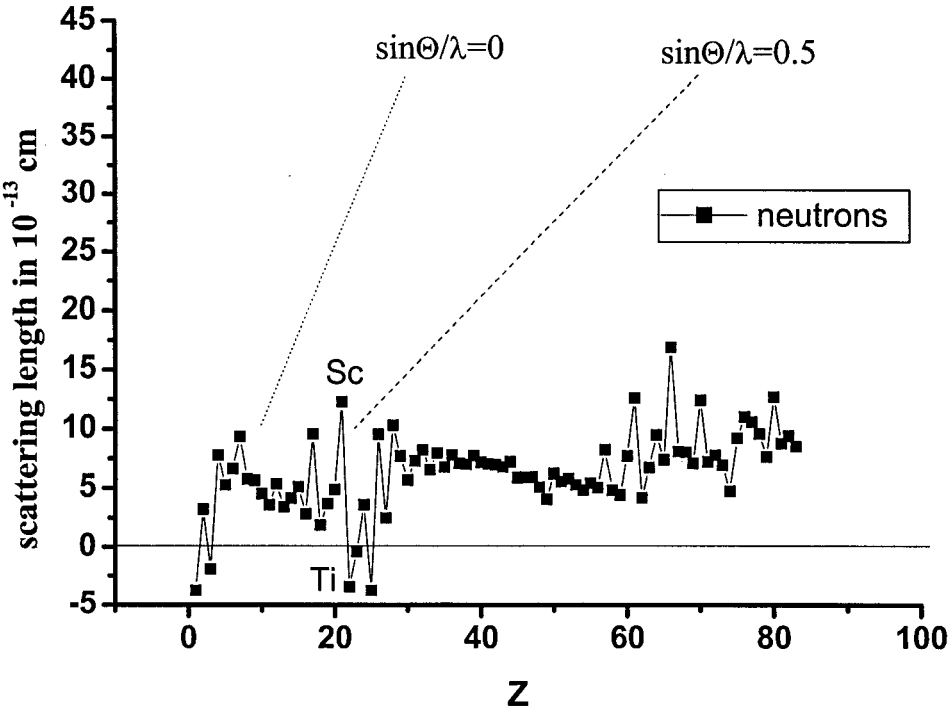


Figure 1.10: List of neutron scattering lengths. A comparison with the X-ray scattering factor (which varies as sinθ/λ) is provided.

[11] The coherent scattering length for vanadium is extremely small. As a result, it is necessary to perform X-ray diffraction measurements to determine the positions of vanadium, which is of great significance to this thesis.

### 1.3.4 Magnetic Neutron Scattering

With the exception of very specialized experiments on synchrotron sources, the coupling of X-rays to the magnetic moment of a sample is orders of magnitude smaller than the interaction with electrons. Moreover, it is difficult to scale the intensity of magnetic X-ray diffraction peaks in order to extract a magnetic moment.(Greedan 1994) As shown below, this difficulty does not arise for neutron diffraction.

Besides the nuclear interaction, the scattering due to the magnetic interaction between unpaired electrons and the moment of the neutron is extremely useful. This can be used to probe various magnetic phenomena, such as magnetic excitations, short-range and long-range magnetic order. Magnetic excitations involve inelastic scattering, while short- and long-range order are both examples of elastic scattering. Long-range magnetic order will appear in a powder diffraction pattern as relatively sharp peaks, which may be on a similar order of magnitude as the nuclear peaks for large moment values. A broad peak in the background can be an indication of short-range order. Peaks can be identified as magnetic in origin by following their temperature dependence; below the ordering temperature these peaks will appear, and then continue to increase in intensity as the temperature is decreased. An alternative, and more conclusive, method is the comparison between neutron and X-ray diffraction patterns at low temperature, due to the generally weak magnetic scattering of X-rays.

Above the transition to magnetic order, the neutrons will respond to the paramagnetic state of the magnetic ions. As there is no periodicity of the spins in the

paramagnetic state, only a contribution to the background, which increases with decreasing angle, will be observed. In this case the paramagnetic differential scattering cross section ($d\sigma_{pm}/d\Omega$) is given by:

$$\frac{d\sigma_{pm}}{d\Omega} = \frac{2}{3}\left(\frac{e^2\gamma}{mc^2}\right)^2 S(S+1)f^2,^{12} \qquad (1.3.18)$$

where $e$ is the electron charge, $\gamma$ is the magnetic moment of the neutron in nuclear magnetons, $m$ is the mass of the electron, $c$ is the speed of light, and $S$ is the spin quantum number. The expression contains the magnetic form factor ($f$), which decreases rapidly with increasing $\sin\theta/\lambda$, as in the case of X-ray scattering. However, only the outer electrons are involved in magnetic scattering, so the drop-off is even faster than in the X-ray case.

The magnetic scattering length ($p$) for a single magnetic moment of $1\mu_B$ at $\vec{Q} = 0$ is $0.2696\times10^{-12}$ cm. When the spin quantum number ($S$) and the magnetic form factor ($f$) are considered, the expression for $p$ is:

$$p = \left(\frac{e^2\gamma}{mc^2}\right)Sf, \qquad (1.3.19)$$

The magnetic scattering length is equivalent to $b$ in the case of nuclear scattering.

Below the onset of magnetic long-range order, equation 1.3.17 becomes:

---

[12] Note that the spin quantum number $S$ would be replaced by the total quantum number $J$ for $f$ electrons.

$$\frac{d\sigma_{mo}}{d\Omega} = q^2 (\frac{e^2\gamma}{mc^2})^2 S^2 f^2 = q^2 p^2 , \quad (1.3.20)$$

where $d\sigma_{mo}/d\Omega$ is now proportional to $S^2$, and the factor $q^2$ is introduced. The magnetic interaction vector ($q$) is defined as:

$$\vec{q} = \vec{\varepsilon}(\vec{\varepsilon} \cdot \vec{K}) - \vec{K} , \quad (1.3.21)$$

where $\vec{\varepsilon}$ is the scattering vector and $\vec{K}$ is the magnetic moment vector. This is illustrated in figure 1.11. The magnitude of $q$ is given by:

$$\vec{q} = \sin\alpha . \quad (1.3.22)$$

The angle between $\vec{\varepsilon}$ and $\vec{K}$ is given by $\alpha$. As a result of the $q$ dependence, the orientation of the moments can be determined. Scattering is proportional to the component of the magnetization ($q$) that is in the reflection plane.

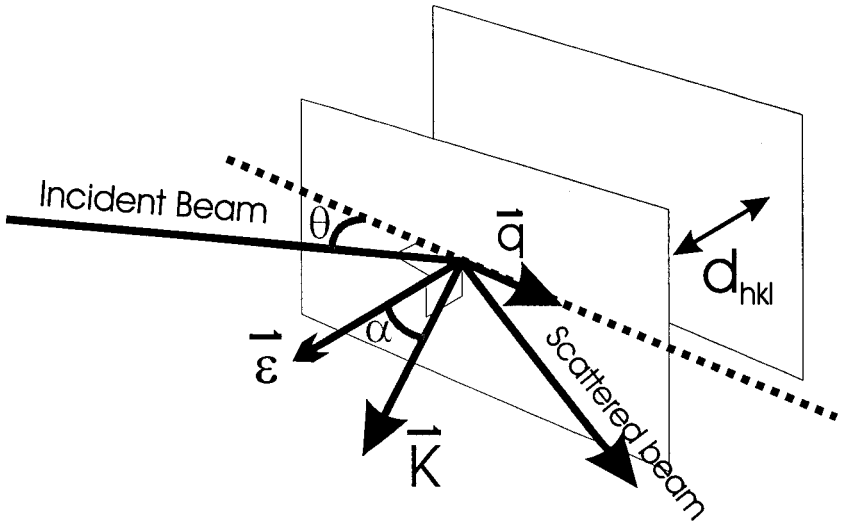


Figure 1.11: Illustration of the contributing vectors to a magnetic neutron scattering event. The vectors are described in the text.

This leads to the magnetic structure factor (Rossat-Mignod 1987):

$$F_{mag} = \sum_{j} qpe^{(2\pi i(hx+ky+lz))} \quad . \quad (1.3.23)$$

For standard powder neutron diffraction experiments the nuclear and magnetic components of the scattering are additive, which results in equation 1.3.24.

$$\left|F_{hkl}\right|^2 = \left|F_{mag}\right|^2 + \left|F_{nucl}\right|^2 \quad . \quad (1.3.24)$$

### 1.3.5 Magnetic Structure Solution

The first step in any structure solution is to determine the unit cell. For magnetic unit cells, this corresponds to determining the ordering wavevector ($k$). The chemical cell is identical to the magnetic cell for ferromagnets. However, for antiferromagnetic ordering, the magnetic cell is often larger than the chemical cell. This situation is illustrated in figure 1.12 for a variety of ordering patterns, along with the corresponding wavevector. The wavevector is determined experimentally by indexing the observed magnetic reflections on the smallest possible unit cell.

The next stage is to determine the modulus of the structure factors by measuring the integrated intensities of the magnetic reflections. These can be used to calculate the directions and magnitudes of the moments, according to equation 1.3.23. The same phase problem exists in magnetic structure solution as exists in crystal structure solution. Therefore, it is worthwhile to use group theoretical arguments to limit the number of

possible structures. If the magnetic ordering transition is second order, a combination of the $k$ vector and the symmetry of the chemical cell can be used to create a set of possible basis vectors.(Wills 2001) Using a trial and error procedure, a set of basis vectors can be found which reproduces the observed magnetic intensities. As there are often many more magnetic spins than observed reflections, the problem is underdetermined, and more than one solution can reproduce the observed pattern. Experiments on single crystals can aid in a unique identification, if a perturbation (such as an applied field) gives an indication of how the symmetry is lowered.(Rossat-Mignod 1987)

### 1.3.6 Analysis of Powder Diffraction Data

The difficulty in using powder diffraction data for crystal structure analysis is greatly enhanced by the overlapping of peaks with similar reflection positions. A highly successful method for dealing with overlapping reflections was devised by Hugo Rietveld in 1967-1969 (Rietveld 1967; Rietveld 1969), and is known as the Rietveld method. The crucial improvement of this method was to carry out a least-squares refinement between the entire observed pattern and entire calculated pattern at once. As a result, allocation of intensity to overlapping reflections can be improved during the refinement. Earlier methods had relied on pattern decomposition (discussed below) as an initial step, which meant that the refinement depended heavily upon the initial attempt at intensity allocation.

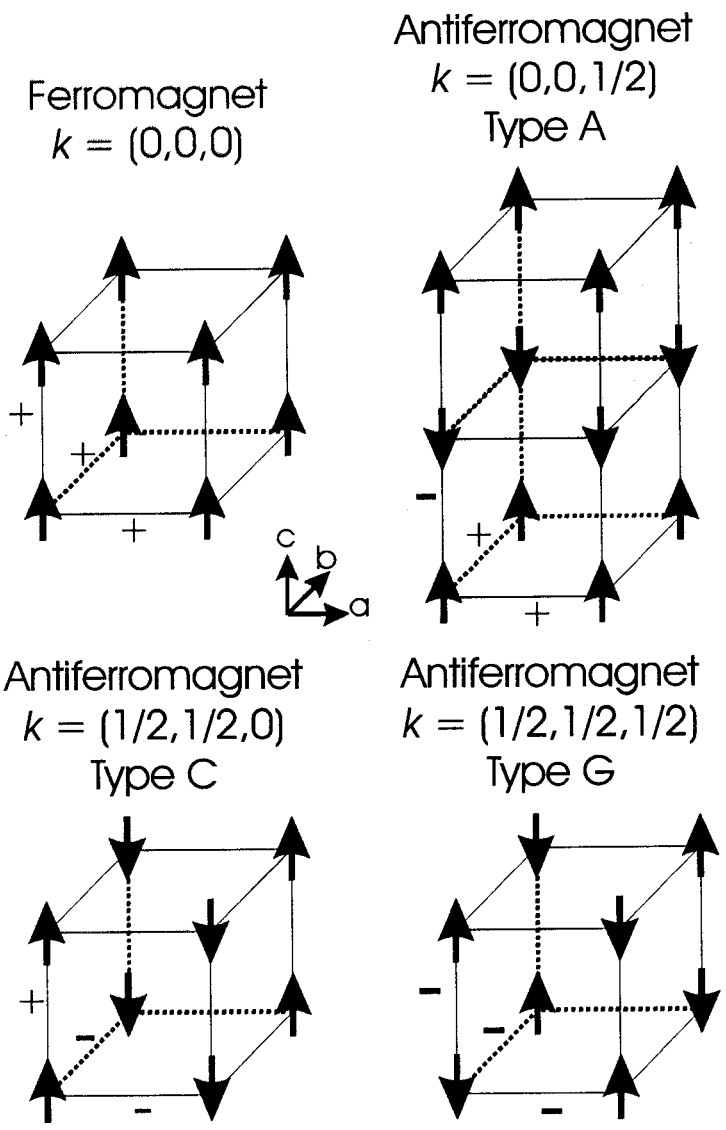


Figure 1.12: Conventional examples of magnetic long-range ordering. The plus (+) and minus (-) signs refer to the sign of the $J$ coupling: positive for ferromagnetic, and negative for antiferromagnetic coupling of spins. The entire magnetic unit cell, which is double the chemical cell, is shown for type A ordering. Though it is not shown, the magnetic unit cell for type C ordering is doubled along the $a$ and $b$ axes, and along the $a$, $b$, and $c$ axes for type G ordering.

A Rietveld refinement involves calculating the profile of a powder pattern using the formula:

$$y_{ci} = s\sum_K L_K \left|F_K^{\,2}\right| \phi(2\theta_i - 2\theta_K) P_K A + y_{bi}, \quad (1.3.25)$$

in order to minimize the residual $S_y$ in a least-squares refinement:

$$S_y = \sum_i w_i (y_i(obs) - y_i(calc))^2 . \quad (1.3.26)$$

where $w_I = 1/y_I$, $y_I(obs)$ is the intensity at the $i$th step, and $y_I(calc)$ is the calculated intensity at the $i$th step. The parameters in equation 1.3.25 include the background ($y_{bi}$), absorption factor ($A$), scale factor ($s$), preferred orientation function ($P_K$), and structure factor for the $K$th Bragg reflection ($F_K$). $L_K$ represents the Lorentz, polarization, and multiplicity factors. The summation is present to include the contribution from all reflections ($K$) on the $i$th point in the pattern.

The reflection profile ($\phi$) is a convolution of instrumental and sample contributions. At low diffraction angles, instrument effects commonly result in peak asymmetry. Sample related profile contributions include peak shifts (caused by sample displacement) and peak broadening (crystallite size and strain effects). To model the angle dependence of the full-width-at-half-maximum (FWHM), and therefore the peak breadth ($H$), a function due to Caglioti et al. is commonly used:

$$H^2 = U\tan^2\theta + V\tan\theta + W . \quad (1.3.26)$$

In this expression, $U$, V, and W are refinable parameters. Though developed for powder neutron diffraction, it is commonly used in a modified form for powder X-ray diffraction.

Refined parameters are either global (such as the background and absorption factor), or phase specific (preferred orientation and scale factor). For large cells and low symmetry structures, due to the large number of parameters, it is quite simple to fall into a false minimum. By turning on these parameters in the appropriate sequence, the correct solution may be found, though it is often useful to try different starting points to confirm that a global, rather than local, minimum has been achieved.(Young 1993)

The Rietveld method is applied to refinement of a structural model, rather than to structure solution, as it usually relies upon an initial model that is close to the correct structure. If an initial model is not known, another approach must be used. After determining the unit cell, the integrated intensities of each reflection may be extracted by a procedure known as pattern decomposition. The most common method for pattern decomposition is currently the Le Bail method, which is based on Rietveld refinement. However, as no structural model is available, only the profile and cell parameters are refinement variables. Another method is the Pawley method, which refines intensities rather than the profile; this method is based on those used for structure solution/refinement before the Rietveld method was developed. The extracted intensities are then analyzed according to the methods commonly used in single crystal structure solution. After a suitable model is found, Rietveld refinement of the original powder data is used to complete the analysis.(Langford and Louer 1996)

A number of agreement factors were used to judge the quality of the fit, as were used in the single crystal case. These are:

$$R_B = \frac{\sum \left| I_K(obs) - I_K(calc) \right|}{\sum I_K(obs)} \quad (1.3.27)$$

$$R_P = \frac{\sum \left| y_i(obs) - y_i(calc) \right|}{\sum y_i(obs)} \quad (1.3.28)$$

$$R_{wp} = \left[ \frac{\sum \left| w_i \left( y_i(obs) - y_i(calc) \right)^2 \right|}{\sum w_i \left( y_i(obs) \right)^2} \right]^{1/2} \quad (1.3.29)$$

$$S = \left[ \frac{\sum \left| w_i \left( y_i(obs) - y_i(calc) \right)^2 \right|}{N - P} \right]^{1/2} = \frac{R_{wp}}{R_e} \quad [13] \quad (1.3.30)$$

$$R_e = \left[ \frac{(N - P)}{\sum w_i y_i(obs)} \right]^{1/2} \quad (1.3.31)$$

As both $R_{wp}$ and $S$ contain the residual being minimized (equation 1.3.26), these are the most meaningful indicators of the fit quality. As a result, most programs refine against one of these agreement factors. The intensities ($I_K(obs)$) used to calculate $R_B$ (R-Bragg) are not actually observed, but are rather the intensities allocated for overlapping reflections based upon the current state of the structure refinement. The parameter $R_e$ is the expected value of $R_{wp}$ based upon the number of points ($N$), the number of parameters ($P$), and the observed intensities.

---

[13] The *Goodness-of-fit* ($S$) is often reported as $\chi^2$, which is fact equivalent to $S^2$.

## 1.4 Transport Properties

### 1.4.1 Charge Transport in Transition Metal Oxides

A current is formed when a net flow of electrical charge in a given direction differs from zero. In transition metal oxides these charges may be ionic, electronic, or a mixture of both. Ionic conduction occurs by the hopping of ions to vacant sites. Therefore, solid state ionic conductors generally require the presence of energetically equivalent defect sites to create a substantial conductivity. In oxide-ion conductors, relatively high temperatures (~500-1000°C) are needed to achieve low resistance.(Goodenough 2000) Electronic conductors may have a low resistance down to liquid helium temperatures. Such materials can be divided on the basis of whether they exhibit localized or delocalized (band) behavior. As ionic conductivity is not significant for the materials considered in this thesis over the temperature range considered, there will be a focus on electronic conduction for the remainder of this section; delocalized behavior will be considered initially, followed by localized models (variable range hopping and polaron hopping).

### 1.4.2 Band Conduction

At an elementary level, the band model arises simply from the overlap of atomic orbitals in a solid. This is represented pictorially in figure 1.13. From the isolated atomic level in (a), overlap of atomic orbitals on two atoms gives an antibonding (upper) level

and bonding (lower) level in (b). With the addition of more atoms, and thus more orbitals, the number of molecular orbitals increases to form (c) and then (d). In (d), the molecular orbitals have broadened into bands. Isolated energy levels are still present, but these levels are separated by a negligible amount of energy. In a solid, these energy levels are referred to as crystal orbitals. This is referred to as the linear combination of atomic orbital (LCAO)[14] method for producing crystal orbitals.(Cox 1987)

Due to the periodic nature of crystals, we can treat this problem by introducing a periodic potential. For example, in a linear, periodic chain of atoms, the crystal orbitals are then given by the expression

$$\Psi_k = \sum_n \exp(ikna)\phi_n \,. \quad (1.4.1)$$

The spacing between unit cells is given by $a$, and $\phi_n$ represents an atomic orbital in unit cell $n$ in the lattice. The quantum number $k$ is known as the wavevector.(Cox 1992) Where three-dimensional interactions are important, $k$ is three-dimensional.

The result of the band model for transition metal oxides is the formation of a conduction band and valence band, as illustrated in figure 1.14. The valence band is composed primarily of oxygen 2p character, and the conduction band of d-like orbitals. As these are typically formed through covalent M-O-M interactions, each band contains contributions from the other. In general, O-O and M-M are sufficiently well separated that they can be neglected; in the 4d and 5d metals, as well as the 3d metals on the left

---

[14] This is also known as the tight binding method, due to the fact that the atomic orbitals used for basis sets represent tightly bound states of atoms, as opposed to the plane waves that describe free electrons.

side of the period, these interactions can become large enough to form bands exclusively of d orbit character. The transport properties are governed by the level of filling of conduction and valence bands by electrons.

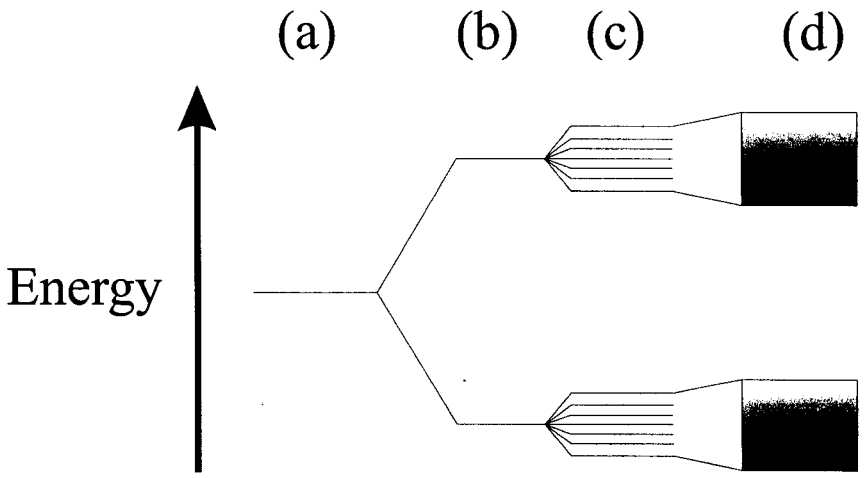


Figure 1.13: Construction of a band based upon the LCAO method. Areas of this figure correspond to (a) atomic energy level, (b) bonding and antibonding levels in a diatomic molecule, (c) molecular orbitals in a larger molecule, (d) band of states present in a crystal.

Metallic conduction occurs when these bands are partially filled. The highest occupied energy level, referred to as the Fermi level ($E_F$), is situated at an intermediate position in the band. In such a case, there are many unoccupied energy levels with a similar energy. Charge transport occurs when carriers are excited to unoccupied energy levels, in which they travel through the solid. Metals are characterized experimentally by a high conductivity, and a positive temperature coefficient of resistance.

When the valence band is full, there are no unoccupied levels of a similar energy available for carrier transport at absolute zero temperature. With increasing temperature, a number of electrons will gain sufficient energy to be promoted to the conduction band.

Both electrons (in the conduction band) and holes (in the valence band) are produced in this manner, so that the conductivity is given by

$$\sigma = ne\mu_e + pe\mu_h \quad (1.4.2)$$

where $n$ and $p$ are the concentration of electrons and holes, respectively. The mobility ($\mu$) of the electrons and holes are defined as the average drift velocity in an electric field of unit strength. Equation 1.4.2 shows that the conductivity represents a sum of the contributions from different carriers[15].

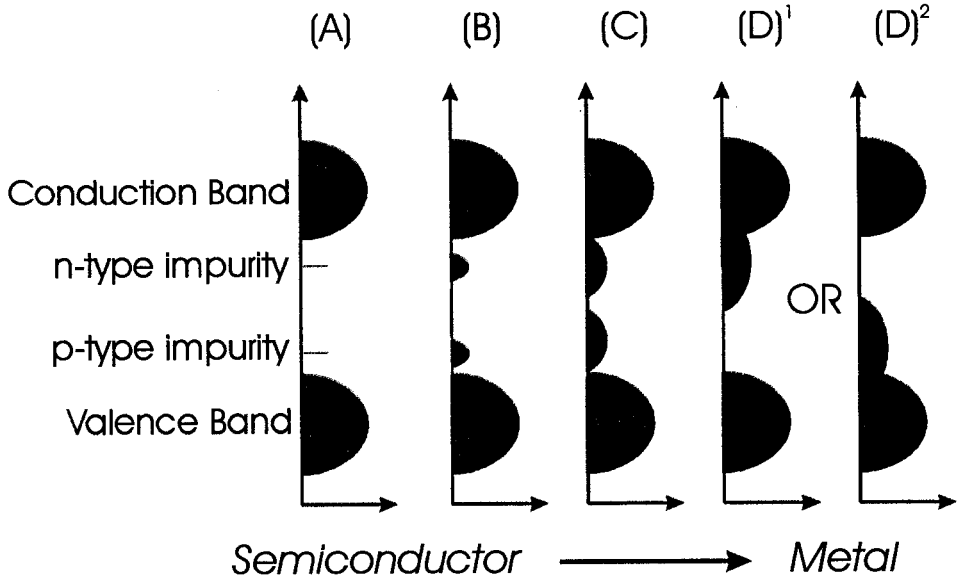


Figure 1.14: Transition from a semiconductor to a metal through doping. Areas of this figure correspond to (a) small impurity level, (b) impurity band is formed, (c) impurity band approaches the edge of the conduction/valence band, $(d)^1/(d)^2$ edge of the impurity band crosses over into the conduction/valence band, forming a metal.

When the band gap is greater than ~3.0eV, the compound is referred to as an insulator; a semiconductor has a band gap between 0.0 to ~3.0eV.(Cardarelli 2000) As

[15] For the remainder of the thesis, carrier will refer to an electron and/or hole, whether delocalized or localized.

the density of charge carriers in these materials increases exponentially with increasing temperature, the Arrhenius equation is often used to interpret the variation in conductivity with temperature.

$$\sigma = \sigma_0 \exp(-E_\sigma / kT). \qquad (1.4.3)$$

In the most basic interpretation, the exponential factor is proportional to the probability of a carrier being promoted to the conduction or valence band, $E_\sigma$ is the activation energy to excite a carrier, and $\sigma_0$ is a constant. This applies for delocalized carriers travelling in a broad band. However, under some conditions there may an additional energy associated with movement of the carriers within the band, and this mobility activation energy will contribute to $E_\sigma$ (see sections 1.4.5.1 and 1.4.6.3).(Cox 1992)

Doping of semiconductors with transition metal ions can substantially increase the conductivity. The carriers excited from the donor levels require a lower activation energy, as they are closer in energy to the conduction or valence band. Figure 1.14 illustrates the manner in which impurity bands form with increased doping levels; with sufficient doping, the impurity band crosses over into the conduction or valence band - forming a metal.[16] A semiconductor in which carriers are excited from energy levels (or an impurity band) near the conduction band is referred to a n-type extrinsic semiconductor; if the dopant energy levels are near the valence band it is called a p-type extrinsic semiconductor.

---

16 In this model the interactions between electrons are not considered.

### 1.4.3 Hubbard Band Model

The above argument did not consider the effect of Coulomb correlations between the charge carriers. For semiconductors in which the conduction band is formed from 3d-like orbitals, the band is sufficiently narrow that the carriers experience significant correlation effects. Electrons on the same site in 3d transition metal oxides experience three different repulsive Coulomb interactions, including: the energy between electrons with opposite spin on the same *d* orbital ($U_0$), electrons of opposite spin on different spatial orbitals ($U_1$), and electrons of the same spin on different orbitals ($U_2$).(Marsh and Parris 1996) The first term is known as the Hubbard U; this energy may result in insulator where arguments of the previous section would suggest a metal. There are two important parameters which characterize the Hubbard model: the Hubbard U, and the *d* orbitals bandwidth (W) created by direct metal-metal overlap. When W<U, the compound is insulating due to a band gap of $E_g \approx$ U-W. Excitations of carriers in the lower band correspond to the transfer of an electron from one transition metal site to another; the result is similar to disproportionation in that reduced and oxidized states are created.(Cox 1992) A classic example of this behavior is given by $V_2O_3$, where excitations correspond to equation 1.4.4.

$$V^{3+} + V^{3+} \rightarrow V^{2+} + V^{4+}. \quad (1.4.4)$$

This compound undergoes a metal-insulator transition[17] (MIT) with temperature, due to a discontinuous change in the vanadium-vanadium separation at a structural phase transition.(Bao, Broholm et al. 1998) The metal-insulator transition of the Hubbard model is classified as a bandwidth controlled transition (BC-MIT).(Imada, Fujimori et al. 1998) While in $V_2O_3$ the bandwidth is controlled by the separation of vanadium ions, the bandwidth can also be controlled by the level of doping in semiconductors. When electron-electron correlations affect the impurity band, it may split into a lower and an upper band. With increased doping, the width of the impurity bands increases until the BC-MIT described by the Hubbard model occurs. Though successfully applied to some 3d transition metal phases, the Hubbard model does not consider covalent mixing of the 3*d* orbitals with the oxygen 2p orbitals, or inter-atomic Coulomb interaction effects.

When a fractional *d* electron concentration is present, such as might occur through doping, the intra-atomic Coulomb repulsion no longer dominates the conduction. The carrier can now transfer without creating additional doubly occupied sites, as in

$$V^{2+} + V^{3+} \rightarrow V^{3+} + V^{2+}. \quad (1.4.5)$$

Partial occupancy of the upper band in figure 1.15 is implied by equation 1.4.5; this should result in a metal according to the Hubbard model, as it did in the case of a broad-band semiconductor. In some materials disorder can inhibit metallic behavior, as will be discussed in the next section. A metal-insulator transition initiated by doping is referred to as a filling controlled transition (FC-MIT).(Imada, Fujimori et al. 1998)

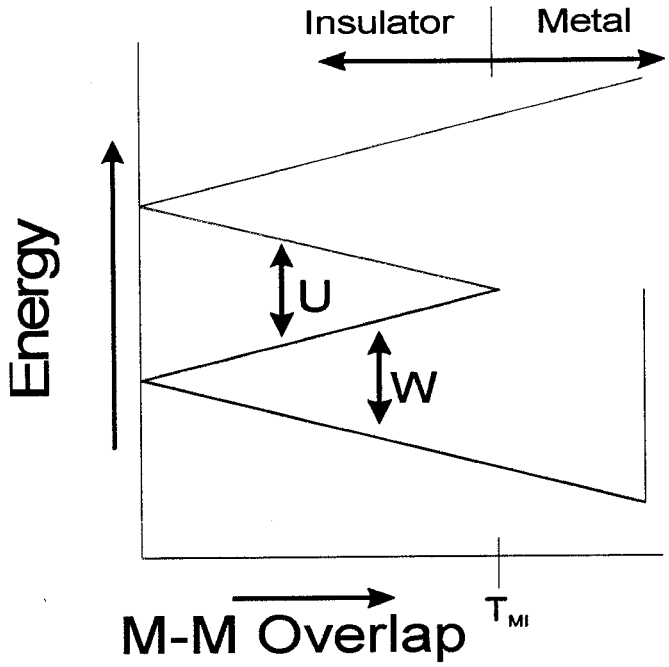


Figure 1.15: Transition ($T_{MI}$) from an insulator to a metal through an increase in bandwidth (W) in the Hubbard model. The x axis shows how an increase in overlap of metal *d* orbitals results in a larger bandwidth. The model illustrates how competition between the effects of the bandwidth and Hubbard U[18] affects conduction in magnetic insulators.

Brinkman and Rice considered a modification of the Hubbard model, such that localized states are formed when $U > U_c \sim W$. One of the main results of this theory is to describe the mass enhancement of correlated electrons that occurs on approaching the metal-insulator transition from the metallic side. At $U = U_c$ the MIT occurs, and the effective mass diverges due to the transformation from band-like to localized states.(Spalek 1990)

---

[17] This MIT is referred to as a Mott-Hubbard metal-insulator transition, due to the contributions of Nevill F. Mott to the study of Coulomb repulsions between electrons.

[18] Note that U as *used in the text* is equivalent to the band gap at *zero* M-M overlap. However, some authors use U as being equivalent to the band gap.

The Hubbard theory was further extended to properly account for the compounds of the heavier transition metals, such as Ni and Cu, by Zaanen, Sawatzky, and Allen. In compounds containing these metals, the *d* band is close to the oxygen 2p band. For large values of the Hubbard U, the oxygen 2p band can reside between the upper and lower *d* bands; in this situation the band gap is now related to the charge-transfer energy (Δ) between the oxygen band and the upper transition metal band (U>Δ). These materials are referred to as charge-transfer insulators.(Zaanen, Sawatzky et al. 1985) In addition, the

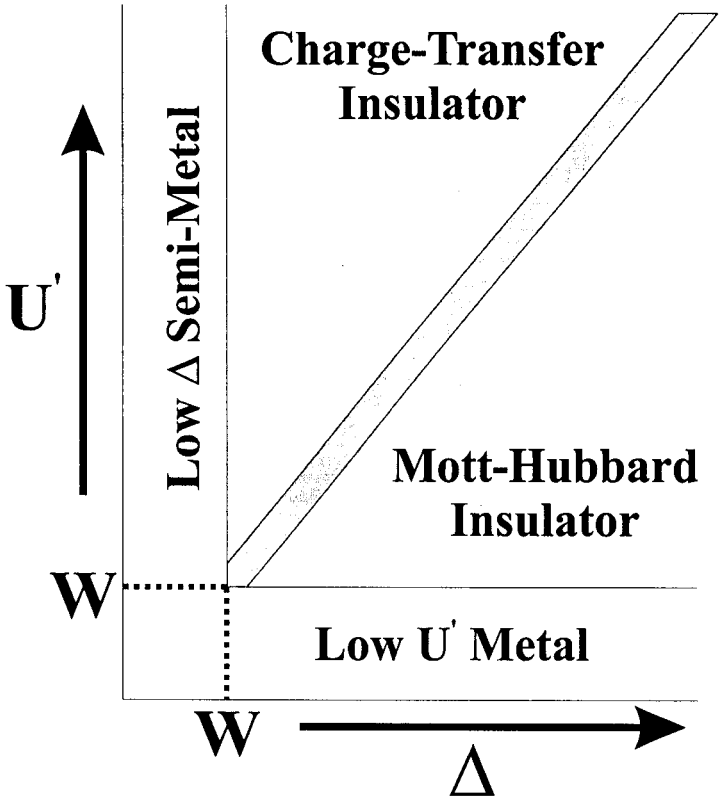


Figure 1.16: A Zaanen-Sawatzky-Allen (ZSA) diagram showing the interplay between the Hubbard-like energy U′ and the charge-transfer energy Δ for transition metal oxides.

metallic phases can be distinguished as a low U′ metal (for large Δ), or a low Δ metal (for large U′)[19]. A diagram used to indicate the region of interest for various metallic and insulating phases in the Zaanen-Sawatzky-Allen framework is shown in figure 1.16.(Torrance, Lacorre et al. 1991)

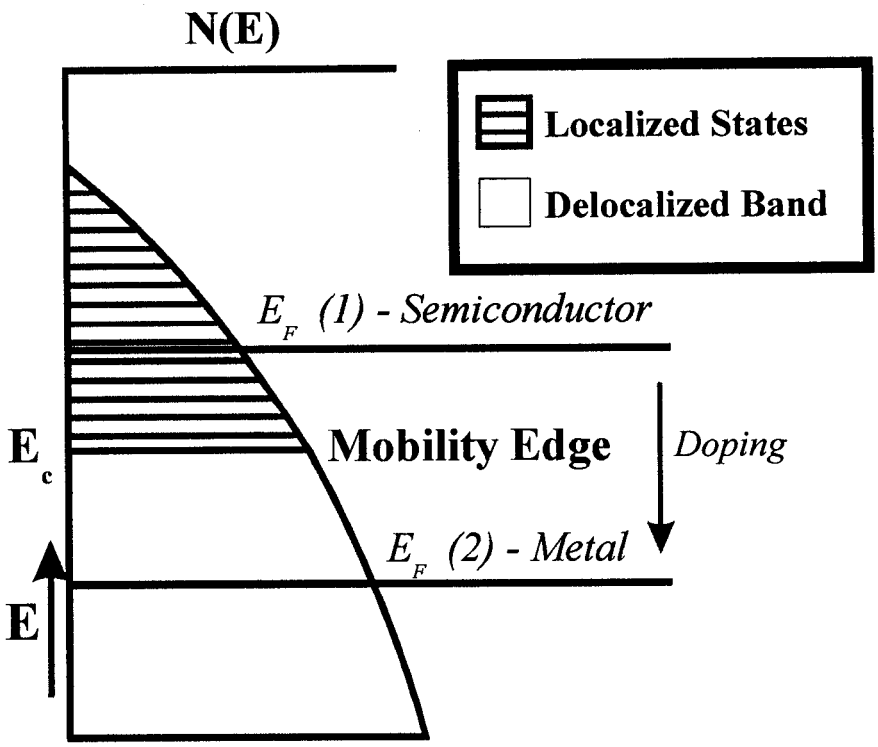


Figure 1.17: The filling controlled metal-insulator transition (Anderson transition). Doping with holes (in this case) brings the Fermi level ($E_F$) from the states localized by a random potential, to the delocalized band states.

### 1.4.4 Carriers Localized by a Random Potential

It has been indicated that for figure 1.14 (d), overlap of the impurity band and the conduction (or valence) band may not initially result in metallic behavior. The

---

[19] The use of U′ indicates that this is not always the Hubbard U.

localization of the electrons arises from the potential created by a random distribution of dopant ions. The random potential will localize the states at the band tails, producing a mobility edge. Shown in figure 1.17 is the case of a lower Hubbard band, with the band edges localized by the random field of the carriers and the random positions of the dopant ions. For metallic behavior to occur, doping must cause the Fermi level to cross the mobility edge; this is referred to as an Anderson transition.[20](Mott 1987)

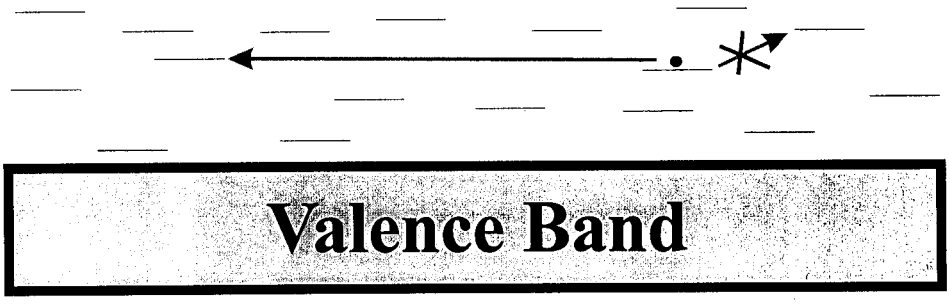


Figure 1.18: Mott variable range hopping (VRH). The carriers hops to a distant site which is close in energy, rather than the close, higher energy site. An equivalent picture can occur close to the conduction band.

### 1.4.4.1 Mott Variable Range Hopping

When carriers are localized by a random site potential, and in the absence of carrier interactions, the hopping is described by Mott variable range hopping (VRH). At sufficiently low temperature it becomes energetically favorable for carriers to tunnel to a distant site of similar energy, rather than a nearest-neighbor site of relatively high energy. This situation is presented in figure 1.18. The energy range of the sites available to the

---

[20] The term 'Anderson transition' is also used to describe the situation in which increasing randomness (with doping) causes the Fermi level to move into the localized region; this is essentially equivalent to the other use of the term, but going through the transition in the other direction.(Ramakrishnan 1994)

carrier is dependent upon the thermal energy of the system; the distance a carrier has to hop also varies with temperature, and therefore is called variable range hopping.

The general case in *d* dimensions was described by Mott as:

$$\sigma = \sigma_o \exp(\frac{-T_o}{T})^{\frac{1}{1+d}} \qquad (1.4.6)$$

where $\sigma_o$ and $T_o$ are constants. $T_o$ is given by:

$$T_o = \frac{\beta}{k_B N(E_F)\alpha^3}. \qquad (1.4.7)$$

The constant β varies depending upon the method used to derive it, but has a value of ~18.1.(Viret, Ranno et al. 1997) The radius of states over which the carrier is localized is given by α, called the localization length.[21] By increasing the localization length, or decreasing the density of states (DOS) at the Fermi level $N(E_F)$, $T_o$ is increased. The Mott VRH law is valid when the DOS is constant at the Fermi level, and the localization length extracted from data is greater than the distance between nearest-neighbor hopping sites.(Mott 1987; Viret, Ranno et al. 1997)

---

[21] In many instances, the localization length is defined as 1/α. As a result, α appears in the numerator of equation 1.4.7.

### 1.4.4.2 Variable Range Hopping with Coulomb Interactions

In the presence of Coulomb interactions between carriers the Mott VRH law must be modified.[22] The Coulomb interactions produce a parabolic behavior of the density of states near the Fermi level: a Coulomb (soft) gap is opened.[23] The formation of a gap may be explained as follows. First place N-1 electrons in a disordered medium, and allow the electrons to minimize the energy of the ground state. Now add another electron to one of two sites whose energies is equivalent, and allow the N electrons to find another minimum energy ground state. After the N electrons have minimized their energy, the two sites are no longer be equivalent; if the Nth electron now hops to the second site an activation energy will be required. This activation energy, as well as the energy difference of the system between N-1 and N electrons, are what cause the Coulomb gap to form.(Pollak 1980)

For the case of single electron, low-energy excitations Efros and Shklovskii (ES) have derived the expression:

$$\sigma = \sigma_o \exp(\frac{-T_o}{T})^{\frac{1}{2}}. \qquad (1.4.8)$$

The constant $T_o$[24] is now

---

[22] This Coulomb interaction may be distinguished from the on-site Hubbard repulsive interaction by the fact that it is long-range.(Rosenbaum and Carter 1990)

[23] The localized states that are occupied in VRH transport cannot carry a current, and therefore do not effectively screen the long-range Coulomb interaction between electrons. For a Coulomb gap, the density of states is depleted at the chemical potential. This is only true for a Hubbard (hard) gap when there are an integral number of electrons per site.

[24] $T_o$ is the generally used to describe the constant in the exponential part of the VRH expression. In cases where both Mott and ES VRH are examined, $T_{Mott}$ and $T_{ES}$ are commonly employed.

$$T_o = \frac{\beta e^2}{\kappa \alpha^3}. \qquad (1.4.9)$$

where β is a constant, κ is the dielectric constant, α is the localization length (as defined above), and *e* is the electron charge.(Efros and Shklovskii 1975)

This behavior is only expected at extremely low temperatures. With increasing temperature the Coulomb interaction is screened; carriers then fill the gap, and a crossover to Mott VRH occurs. There is a great deal of interest in modeling this crossover behavior, and there are a number of reports in which it has been experimentally observed.

The validity of this model has been disputed by Pollak. The main arguments against ES-VRH include: (a) in many cases multi-particle excitations are expected, rather than the single particle excitations of the ES model; (b) Coulomb interactions are only taken into account for pairs of hopping sites, without considering other interactions.(Pollak 1992) It is important to note that while there is still some dispute about the details of the model, examples of this behavior have been found.(Zabrodskii 2001)

#### 1.4.4.3 Prefactor in Variable Range Hopping

There is a significant level of variation in the literature as to the proper prefactor for the variable range hopping expressions. When 1.4.6 and 1.4.8 are not used, two common expressions are:

$$\sigma = \sigma_o T^{-1/2} \exp(\frac{-T_o}{T})^{\frac{1}{4}} \qquad (1.4.10)$$

for Mott VRH, and

$$\sigma = \sigma_o T^{-1} \exp(\frac{-T_o}{T})^{\frac{1}{2}} \qquad (1.4.11)$$

for ES VRH.(Mansfield, Abboudy et al. 1988; Al-Shahrani, Abboudy et al. 1995) It has been suggested that neglecting the temperature dependence of the prefactor during data analysis could lead to the false assignment of a crossover from Mott to ES VRH.(Agrinskaya and Kozub 1994)

### 1.4.5 Polaronic Conduction

In narrow band materials, if the short-range electron-phonon interaction is of sufficient energy to localize a carrier at a particular lattice site, the carrier is now called a small polaron. A general description of this behavior was first given by Holstein for nearest-neighbor hopping of small polarons; this provided an explanation for the occurrence of low mobility materials.(Bottger and Bryksin 1976) There are two main methods of carrier transport: (a) at low temperatures the carrier moves by tunneling through a band of polaron states, and (b) at sufficiently high temperatures a local deformation of neighboring sites results in the transfer of charge.

The polaron band is not equivalent to either the narrow band semiconductor or Hubbard band models described earlier. Due to a large number of equivalent sites, a very

narrow band of states may form.(Jaime, Salamon et al. 1996) In this case the carriers are fully localized at individual lattice sites. Mott has predicted that in the presence of a significant disorder, the carriers will follow the VRH behavior at low temperatures. Therefore, the remainder of this section will focus on hopping related to the local deformation of sites.

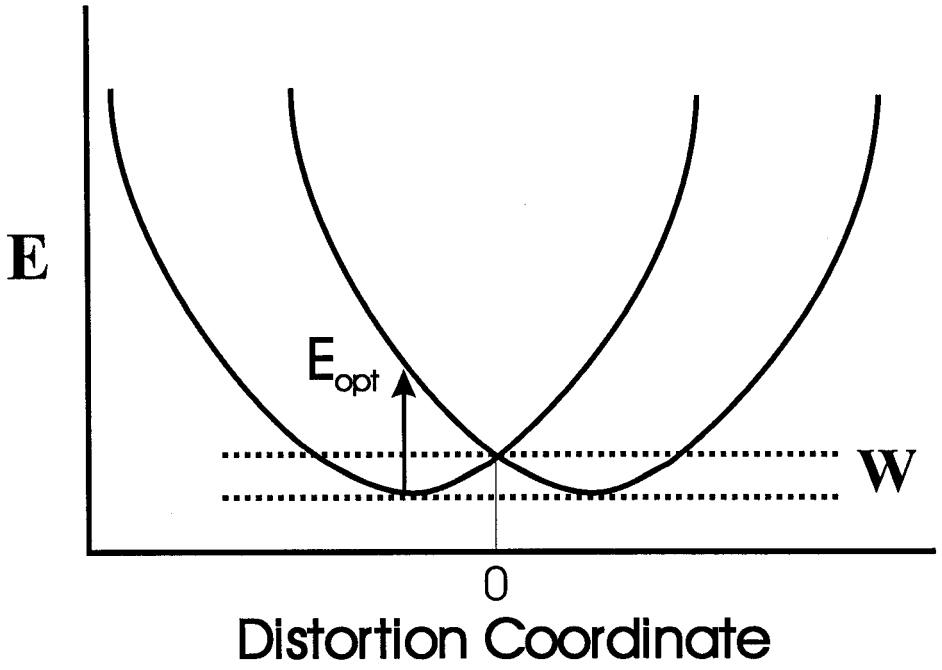


Figure 1.19: Configuration coordinate model for small polaron hopping. When the deformation of the nearest-neighbor sites brings both sites to the same energy (the distortion coordinate equals 0), the carrier can transfer. Each parabola represents the energy of a site with an extra electron, relative to its distortion. The optical transition ($E_{opt}$) occurs when an electron jumps from a *distorted* site (energy minimum) to an *undistorted* site. The energy required for electron transfer via an optical transition is much higher than that for site deformation (W).

The hopping process may be described using the configuration coordinate model, as in figure 1.19. When the energy of nearest-neighbor sites becomes equal, a carrier will transfer from site to site. This energy comes from coupling with one or more lattice

phonon modes. Hopping transitions in which a single phonon is required are important when the maximum phonon energy ($h\omega_D$) is greater than the hopping energy; this is found in the impurity bands of doped, crystalline semiconductors. Where more than one phonon is used, or required, to allow the carrier to transfer, the process is referred to as multi-phonon hopping; this is more common in amorphous semiconductors, where the hopping energy may exceed the maximum phonon energy.(Zvyagin 1991) A further distinction may be made between adiabatic and non-adiabatic hopping: adiabatic hopping occurs when the carrier may travel back and forth between sites during one hop. This requires that the time interval within which two nearest-neighbor sites have equal energy (are 'coincident') is long relative to the time required for an carrier to hop. The opposite case is non-adiabatic hopping; the probability of a hop is low, and so the carrier may only travel in one direction during a single event.(Emin 1975)

#### 1.4.5.1 Polaronic Conduction in Doped Semiconductors

When small polaron hopping occurs in the extrinsic region of a doped semiconductor, there are two different activation energies of interest. First, there is an activation energy associated with exciting the carrier from the dopant ion to the polaron sites ($E_a$). The other activation energy is that required for hopping of the polaron from site to site (W). As in the case of a doped, broad band semiconductor below the exhaustion regime[25], the carrier concentration increases with temperature. The

[25] The exhaustion regime occurs when all of the carriers have been excited from the dopant ions.

conductivity may now be described by equation 1.4.3, with the activation energy for conduction:(Cox 1992)

$$E_\sigma = E_a + W \qquad (1.4.12)$$

### 1.4.5.2 Polaronic Conduction with a Constant Carrier Concentration

There are a number of models which describe polaron hopping in the absence of an activation energy for carrier production. In the model described by Holstein, the adiabatic regime is given by:

$$\sigma = \left(C(1-C)e^2 / kTa\right)\left[\nu_o\right]\exp\left[-\left(W_H - J\right)/kT\right] \qquad (1.4.13)$$

where $C$ is the site concentration of lower oxidation state polarons, $a$ is the average lattice spacing, $\nu_o$ is the characteristic frequency[26], $W_H$ is the activation energy for hopping and 2J is the polaron bandwidth for a rigid one dimensional lattice. The factor (1-C) expresses the fact that the number of sites to which a polaron can hop is reduced by the fraction of sites already occupied by a carrier.

The expression for non-adiabatic hopping is:

$$\sigma = \left(C(1-C)e^2 / akT\right)\left(J^2 / \mathrm{h}\right)\left(\pi / 4kTW_H\right)^{1/2}\left]\exp(-W_H / kT\right).^{27} \qquad (1.4.14)$$

In this case, there is an additional $T^{-1/2}$ dependence in the prefactor. Therefore the adiabatic and non-adiabatic cases can be distinguished by the temperature dependence of

---

[26] Note that this can be considered the attempt-to-escape frequency; in the adiabatic case, $(h/2\pi)\nu_o$ is the energy of the optical phonon that would displace the two neighboring sites such that their energies are equal (the energy at which electron transfer is possible). In the non-adiabatic case, the characteristic frequency determined from this equation is much less than the optical phonon frequency.

[27] In equation 1.4.14, 'h' represents 'h-bar', or Plank's constant divided by $2\pi$ ($h/2\pi$).

the prefactor, which is $T^{-1}$ in the adiabatic case, and $T^{-3/2}$ in the non-adiabatic case.(Elliot 1990; Raffaelle, Anderson et al. 1991)

For amorphous semiconductors, Mott has described a disorder energy ($W_D$) associated with hopping in a random potential. The total hopping energy is therefore given by:

$$W = W_H + \tfrac{1}{2} W_D \quad (1.4.15)$$

At low temperatures $W_D$ predominates, and VRH behavior occurs. In the higher tempera ture range single-phonon assisted conduction is described by:

$$\sigma = \left(C(1-C)e^2 / kTR\right)\left[\nu_o \exp(-2\alpha R)\right]\exp(-W / kT) \quad (1.4.16)$$

where $\nu_o$ is the characteristic phonon frequency, C is the concentration of lower valence polaron states, $\alpha$ is related to the localization of phonon carriers, and W is the hopping energy given in equation 1.4.15.(Ghosh 1994) The factor c(1-c) represents the probability of a carrier finding an available site. At the separation between nearest-neighbor sites increases, the factor exp(-$\alpha$R) lowers the probability of a hop; in the adiabatic regime, this exponential reduces to unity. The final exponential relates to the probability that a carrier will hop from the occupied to the unoccupied site.(Austin and Mott 1969)

### 1.4.5.3 Other Forms of Polaronic Conduction

When long range Coulomb interactions are important, electron-lattice coupling between a carrier and lattice ions[28] can lead to large polaron formation. In this case the carrier is not localized to a specific site, but rather causes the lattice to deform over a number of sites. This type of polaron can be distinguished from a small polaron by examining the temperature dependence and magnitude of the mobility. Small polaron mobility is low ($<<1 cm^2/Vs$) and increases with increasing temperature, as more energy becomes available for lattice deformation. The mobility of a large polaron is larger ($>1 cm^2/Vs$), and decreases with increasing temperature due to scattering by increased atomic vibrations.(Emin 1993)

Another type of polaron has been proposed for magnetic solids, known as the spin (or magnetic) polaron.(Mott 1992) In the paramagnetic regime, carriers on defect sites can polarize the surrounding spins. As the carrier hops, it will drag this polarized spin region (polarization/spin cloud) with it. If the material undergoes ordering with decreasing temperature, or increasing magnetic field, the magnetic polaron will diffuse; a weakly conducting ("dirty") metal will be formed. The details of this model, such as the possible role of lattice distortions, are still under dispute.(Jaime, Salamon et al. 1996)

---

[28] This is referred to as the Fröhlich interaction.

### 1.4.6 Thermoelectric Power

Associated with each of the above models of conduction is a distinctive behavior of the thermoelectric power. After an introduction to the basic theory behind the thermoelectric effect, an expression for the thermopower relating to each of the above models will be discussed.

#### 1.4.6.1 Basic Theory of the Thermoelectric Effect

When a temperature gradient is applied across a sample, under open-circuit conditions a charge buildup occurs at each end of the sample. Carriers at the hot end have a greater kinetic energy than those at the cold end; across a given cross-sectional area (perpendicular to the temperature gradient) there is a net flow of the dominant charge carrier towards the cold end. Steady state conditions are reached when a large enough potential builds up to oppose the flow of carriers, and the net flow of charge is zero. This potential is a characteristic function of a solid at a given temperature, and is called the Seebeck potential ($E_S$). Because the Seebeck potential depends upon the temperature gradient, it is common to report the thermoelectric power, otherwise known as the Seebeck coefficient (S)[29], in which the potential is normalized against the temperature gradient as:

$$S = \frac{\Delta E_S}{\Delta T}. \quad (1.4.17)$$

---

[29] It is common to use the symbols $\alpha$ or Q to represent the Seebeck coefficient.

The sign of the potential is determined by the charge on the dominant carriers: electrons result in a negative Seebeck coefficient, and holes in a positive S. The Seebeck coefficient is composed of two parts, the presence ($S_{presence}$) and the transport term ($S_{transport}$). The presence term is related to the change in the entropy of the system created by placing a charge carrier on a lattice site, and may be divided into three contributions:

$$S_{presence} = \left(\Delta S_{mixing} + \Delta S_{spin} + \Delta S_{vibration}\right)/q \quad (1.4.18)$$

where $\Delta S_{mixing}$ is the entropy-of-mixing associated with adding a carrier to a lattice site, and $\Delta S_{spin}$ is the change in the system's spin entropy upon adding a carrier. The magnitude of $\Delta S_{vibration}$ is related to the fractional shifts in the frequencies of the vibrational modes.(Emin 1999) The transport term is due to the polarization of the lattice around the charge carrier as it moves; it corresponds to the net flow in vibrational energy with a carrier hop, and is temperature dependent[30].(Aselage, Emin et al. 1998) Typically, the transport term is neglected in comparison with the presence term.

The thermopower is essentially a measure of the entropy per carrier ($\Delta S/q$), or heat per carrier divided by the temperature. This is the basic premise on which the characteristic thermopower for various conduction models is calculated.(Chaikin 1990)

---

[30] The transport term is considered the net kinetic energy of the carrier.

### 1.4.6.2 Thermopower of Metals

The thermopower of a metal can be given approximately by the ratio of the electronic specific heat ($c_{el}$) to the charge (q), and is therefore:

$$S \approx \frac{c_{el}}{q} \approx \frac{k}{e}\frac{kT}{\varepsilon_F} \qquad (1.4.19)$$

where $k$ is the Boltzmann constant, $e$ is the electronic charge, and $\varepsilon_F$ is the Fermi energy. From the assumption of a degenerate electron gas (the carriers have a small spread of energies) $\varepsilon_F >> k_B T$; the thermopower of a metal is small, and varies linearly with temperature. This is often referred to as the diffusion thermopower.(Chaikin 1990)

### 1.4.6.3 Thermopower of Doped and Intrinsic Semiconductors

The heat per carrier is essentially the energy a carrier possesses in excess of the chemical potential. If the chemical potential is taken to be the Fermi energy, then for a non-degenerate semiconductor[31] the Seebeck coefficient is

$$S = -\left(\frac{k}{e}\right)\left[\frac{(E_c - E_F)}{kT} + A\right] = -\left(\frac{k}{e}\right)\left[\ln\left(\frac{N_c}{n}\right) + A\right] \qquad (1.4.20)$$

for the case of $n$-type conduction, and for $p$-type conduction is

$$S = +\left(\frac{k}{e}\right)\left[\frac{(E_F - E_v)}{kT} + A\right] = +\left(\frac{k}{e}\right)\left[\ln\left(\frac{N_v}{p}\right) + A\right] \qquad (1.4.21)$$

---

[31] Non-degenerate refers to the situation in which $E_c - E_F >> kT$.

The energy at the conduction band edge is $E_c$, and at the valence band edge is $E_v$. The density of states in the conduction band is $N_c$(valence band is $N_v$), and the concentration of electrons in the conduction band is $n$(valence band is $p$).(Cox 1992) The constant $A$ corresponds to $S_{transport}$, and is usually neglected as it is expected to be $\leq 10\mu V/K$, while Seebeck coefficients on the order of 100-1000μV/K are not uncommon in semiconductors.(Raffaelle, Anderson et al. 1991)

Equations 1.4.20 and 1.4.21 are valid not only for band conduction, but also for polaron conduction when an activation energy for carrier creation ($E_a$) is present. A comparison with equations 1.4.3 and 1.4.12 reveals that as the thermopower is only sensitive to $E_a$, a comparison with $E_\sigma$ obtained from the conductivity data will allow a determination of $W$ (small polaron hopping energy). However, care must be taken in the use of this relationship. While certainly applicable to extrinsic semiconductors, the comparison must be somewhat modified for both localized and delocalized intrinsic semiconductors.(Pai and Honig 1981)

#### 1.4.6.4 Thermopower for Variable Range Hopping Conduction

Starting from a finite density of localized states at the Fermi level, the Seebeck coefficient for Mott variable range hopping is calculated to be:

$$S \propto T^{\frac{d-1}{d+1}} \quad (1.4.22)$$

Thus the thermopower is dependent upon the dimensionality of the system. At low temperatures in a three-dimensional material, $S \propto T^{1/2}$, in two dimensions to $T^{1/3}$, and independent of temperature in one dimension.(Chaikin 1990)

It is interesting to compare this behavior with that of Efros-Shklovskii VRH. It has been shown that near the transition to ES-VRH the thermopower should vary as $T^{-1}$. At the lowest temperatures the thermopower should level off to a constant value. Therefore, the thermopower can be used to distinguish between the two forms of VRH.(Burns and Chaikin 1985)

#### 1.4.6.5 Thermopower of Polarons with a Constant Carrier Concentration

If the carrier concentration is constant, to a first approximation the thermopower should be constant with temperature. A temperature independent thermopower also indicates that the vibrational energy transferred in a hop (a contribution to $S_{transport}$) is small; this occurs if the energy of the sites is nearly identical.(Nagels 1990) The most widely used formula in the literature for this situation is Heikes formula(Heikes and R. W. Ure 1961):

$$S = -\left(\frac{k}{e}\right)\ln\left[\frac{1-p}{p}\right] \qquad (1.4.23)$$

where $p$ is the ratio of carriers to available sites; in a practical application of the formula, $p$ corresponds to the concentration of the lower valence state ion to the number of polaron

hopping sites available. The formula is based solely upon a calculation of the entropy-of-mixing.

In summary, equation 1.4.23 resulted from a number of simplifications, including:

1) the carriers are randomly distributed among the available sites,

2) the distribution in the energy of carrier localization over all sites is small compared with kT,

3) carriers are spinless particles which cannot doubly occupy a site,

4) the kinetic energy of the particles ($qT \times S_{transport}$) is neglected.(Emin 1999) As explained in section 1.4.6.3, $S_{transport}$ is typically neglected in semiconductors.

The choice of spinless particles is highly improbable. To remove the degeneracy of the spins, either a large magnetic field would have to be applied, or the spins would have to be paired to form a bipolaron.(Aselage, Emin et al. 1998) Therefore, at higher temperatures an additional factor of (k/e)ln2 is expected in order to account for the spin degeneracy. Once spin degeneracy is included, it is useful to allow more than one spin to occupy the same site and include the on-site Coulomb repulsion (Hubbard U) effects. The effects of the Hubbard U have been examined by Chaikin and Beni, and are presented in table 1.X for the high temperature ($kT >> U_o$) and low temperature ($kT << U_o$) limits.

Marsh and Parris have considered the effects of orbital degeneracy on the thermopower of 3d transition metal oxide perovskites.(Marsh and Parris 1996) In this

model there are less than three electrons per site, and these electrons are confined to the $t_{2g}$ orbitals on the octahedrally coordinated transition metal site. Furthermore, it is assumed that $U_o$ and $U_1$ (described in section 1.4.3) are much stronger than $U_2$; only parallel spin configurations are considered. Spin interactions between neighboring sites are treated by using two limiting cases: (a) strong coupling results in magnetic ordering, such that the degeneracy of spins is reduced to one; (b) weak coupling in which no spins are aligned, resulting in a degeneracy of $(n + 1)$ for $n$ spins per site. In addition, the low temperature ($kT<<U_2$) and high temperature ($kT>>U_2$) are considered. In the low temperature limit, hopping to a site that already contains an excess of carriers, relative to the average site occupation, has a low probability. The four expressions that result from combining the above four variables are given in table 1.2. A similar model has been applied to carriers in $e_g$ orbitals, but this will not be examined here.(Marsh and Parris 1996)

### 1.4.6.6 Phonon Drag Effects on the Thermopower

Another contribution to the thermopower (in this case to $S_{transport}$) which has not been discussed is phonon drag. This is often observed at low temperatures in metallic compounds, where the phonon drag contribution may be much larger than the diffusion thermopower. However, it can also be observed in pure semiconductors at low temperatures.

The application of a temperature gradient across a sample produces a corresponding phonon current. If significant coupling occurs between electrons and the phonon current, electrons will be "dragged" by the phonon current to the cold end, and thereby contribute to the measured Seebeck potential.(Blatt, Schroeder et al. 1976) At very low temperatures ($T<<\theta_D$) a $T^3$ temperature dependence is observed, which is directly related to the lattice specific heat; this becomes $T^{-1}$ at higher temperatures ($T<\theta_D$).(Chaikin 1990) Due to the effects of phonon-phonon interactions, the phonon drag becomes negligible at high temperatures.(Gratz 1981)

Table 1.2: General Expressions for the Thermoelectric Power

| | Conditions for applicability | Thermopower Expression |
|---|---|---|
| Metal | degenerate electron gas | $S \propto T$ |
| Band Semi. | activation of carriers across a band gap | $S = \frac{-}{+}\left(\frac{k}{e}\right)\left[\frac{(E_c - E_F) or (E_F - E_v)}{kT} + A\right]$ |
| Mott VRH | carriers localized by a random potential | $S \propto T^{\frac{d-1}{d+1}}$ |
| ES VRH | random site potential and Coulomb interactions | Near crossover to ES-VRH: $S \propto T^{-1}$<br>Below the crossover: $S \propto T^{0}$ |
| Small Polaron | spinless carriers | $S = -\left(\frac{k}{e}\right)\ln\left[\frac{1-p}{p}\right]$ |
| Small Polaron | $kT >> U_o$; carriers have spin | $S = -\left(\frac{k}{e}\right)\ln\left[\frac{2-p}{p}\right]$ |
| Small Polaron | $kT << U_o$; carriers have spin | $S = -\left(\frac{k}{e}\right)\ln\left[\frac{2[1-p]}{p}\right]$ |
| Small Polaron | $kT << \lvert U_o \rvert$; spins are paired due to negative $U_o$ | $S = -\left(\frac{k}{2e}\right)\ln\left[\frac{2-p}{p}\right]$ |
| Small Polaron | $kT >> U_2$; weak coupling limit of spins; $3d^{1-3}$ | $S = -\left(\frac{k}{e}\right)\ln\left[\frac{8(3-p)}{(5p-6)+\sqrt{36-12p+9p^2}}\right]$ |
| Small Polaron | $kT >> U_2$; strong coupling limit of spins; $3d^{1-3}$ | $S = -\left(\frac{k}{e}\right)\ln\left[\frac{3-p}{p}\right]$ |
| Small Polaron | $kT << U_2$; weak coupling limit of spins; $3d^{1-3}$ | $S = -\left(\frac{k}{e}\right)\ln\left[\left(\frac{(4-p_o)(p_o+1)}{p_o^2}\right)\left(\frac{1-p_e}{p_e}\right)\right]$ |
| Small Polaron | $kT << U_2$; strong coupling limit of spins; $3d^{1-3}$ | $S = -\left(\frac{k}{e}\right)\ln\left[\left(\frac{4-p_o}{p_o}\right)\left(\frac{1-p_e}{p_e}\right)\right]$ |

S = thermoelectric coefficient; VRH = variable range hopping; $U_o$ = intrasite Coulomb repulsion of antiparallel spins; $U_2$ = intrasite Coulomb repulsion of parallel spins on different orbitals; $E_c/E_v/E_F$ = energy at the bottom of the conduction band/top of the valence band/Fermi level; $p$ = concentration of lower oxidation state polaron sites; $p_o$ = undoped 3d site population; $p_e$ = excess number of 3d electrons per site.

# Chapter 2

# Experimental Methods

## 2.1 X-ray Diffraction

### 2.1.1 Guinier-Hägg Powder X-ray Camera

The Guinier-Hägg powder X-ray camera is useful for obtaining high-resolution data on small samples. For this experiment, a ~5-10mg quantity of polycrystalline sample was spread onto a piece of tape, which was then attached to an aluminum holder. A small quantity of silicon was added as an internal standard, to correct for problems with uneven film shrinkage and stretching during the film development process. This sample was then placed in the camera, as shown in figure 2.1. The line source from a Cu anode sealed X-ray tube was diffracted off a quartz monochromator to produce a convergent Cu-$K_{\alpha 1}$ beam. The high resolution of the Guinier-Hägg geometry is a result of the fact that the beam is focussed on the film, rather than the sample. The zero point, where no diffraction has occurred, corresponds to point A on the diagram. Points B and C are reflection positions, separated from the zero point by an angle in $2\theta$. With the generator set at 40kV and 30mA, a 30 minute exposure time, and a 3 minute period in the developer solution, a good signal to noise ratio was achieved in the resulting film.

Developed film was digitized using a KEJ-LS20 line scanner. Reflection positions, corrected using the internal standard, were obtained using the program SCANPI.(Malmros and Werner 1973) The unit cell constants were calculated from a least-squares fit to the reflection data with the program LSUDF.

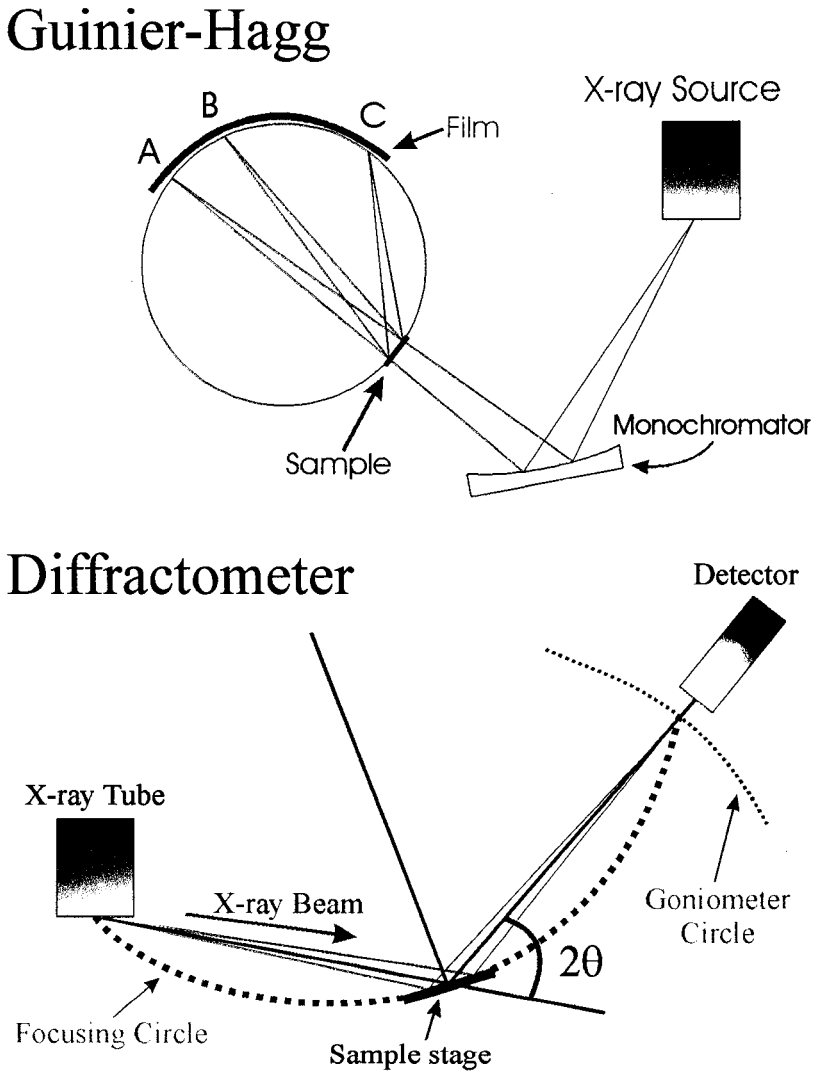


Figure 2.1: Top: Experimental geometry for a Guinier-Hägg powder X-ray diffraction camera. Bottom: Parafocusing Bragg-Brentano diffractometer.

### 2.1.2 Powder X-ray Diffractometer

When larger quantities of polycrystalline material are available (~100-200mg), it is useful to collect diffractometer data. Two different methodologies were used to obtain data from a Bruker D8 Advance powder X-ray diffractometer: (1) a step size of 0.04° 2θ, count time of 10 seconds per step, and 2θ range of 10 to 90°, or (2) a step size of 0.025° 2θ, count time of 13 seconds per step, and 2θ range of 10 to 130°. The first collection scheme was mainly intended for qualitative analysis using the Bruker EVA (EVAluation) search-match software, and the second scheme for collecting data suitable for Rietveld refinement. The peak-width of the diffractometer is slightly higher than that of the Guinier- Hägg camera[1], but the relative intensities are more reliable[2]. Furthermore, the line shape is more easily modeled for the diffractometer.

Material was spread onto the surface of the sample holders. A small amount of ethanol was added, and a glass slide was used to obtain a flat sample surface. The ethanol was evaporated before data collection. Experiments proved that it was essential to wet the sample with a liquid (ethanol in this case) during the flattening step to reduce the level of preferred orientation.[3] The ethanol likely increases the density and randomization of microcrystallites in the packed sample. This has the additional benefit of helping to prevent the sample from falling out of the holder during data collection.

---

[1] By choice of slits, the peak-width for a typical diffractometer setup is usually adjusted to obtain a compromise between resolution and intensity. In effect, as peak overlap becomes more severe with decreasing resolution, the corresponding increase in intensity will improve the signal-to-noise ratio.

[2] The dynamic range of the film is much lower than the scintillation counter.

[3] Microcrystals with an anisotropic shape, such as needles or flat disks, will tend to lie down along the surface of the holder, rather than packing randomly. This situation, called preferred orientation, results in changes to the relative intensities of a powder pattern.

The D8 Advance diffractometer was set up in a Bragg-Brentano (reflection) geometry, shown in figure 2.1. The line source from a Cu anode X-ray tube was diffracted off a sample onto a graphite secondary-beam monochromater, and into a scintillation detector. The beam essentially focusses on the detector, rather than the sample, as was the case for the Guinier- Hägg camera. The graphite monochromator is adjusted to diffract only Cu-$K_\alpha$ radiation, which greatly removes the background due to fluorescence from early 3d transition metal elements in the sample. Measurements are performed by the coupled motion of the sample stage ($\theta$) and detector ($2\theta$), known as a $\theta$-$2\theta$ scan; the sample and detector moves so as to maintain the conditions of Bragg's law (section 1.3.1).(Bish and Post 1989)

### 2.1.3 Single Crystal X-ray Diffraction

Single crystal X-ray diffraction data were collected using a Siemens P4 four-circle diffractometer, with a Mo rotating anode X-ray source, and a 1K charge-coupled device (CCD) area detector. Groups of four pixels were used in combination to improve sensitivity, while reducing the resolution to 512×512 pixels. The X-ray beam was monochromated using a graphite crystal to produce a mixture of Cu-$K_{\alpha1}$ and Cu-$K_{\alpha2}$ radiation on the sample. Samples were limited to dimensions less than 0.05mm, due to collimation of the incident beam to this size. Data were collected using the SMART software, and processed with the SAINT package. Processing included corrections for Lorentz and polarisation effects. Analysis of the raw intensities using RLATT did not indicate the presence of non-merohedral twinning or impurities in any of the crystals

presented in this thesis. Spherical absorption and $\lambda/2$ corrections were performed using the program SADABS; the crystals had been ground into ellipsoidal shapes before measurement to achieve a more accurate absorption correction. Structure solution was performed using the SHELXL97 software package.(Sheldrick 1997) This involved the use of direct methods to obtain an initial model and least-squares refinement against $F^2$ to determine the final model.

## 2.2 Continuous Wave Powder Neutron Diffraction

Since the pioneering work of Brockhouse and Shull, neutron diffraction has become an important tool for solid state science. As discussed in section 1.3.3, continuous wave neutron diffraction experiments can be carried out at reactor sources. Experiments for this thesis have been performed on the high resolution powder diffractometer (C2) in Chalk River, and the high flux instrument D20 at the Institute Laue-Langevin (ILL) in Grenoble.

For experiments at Chalk River, samples of 3-4g size were sealed in thin walled vanadium cans, under ultra-high purity He gas; indium wire was used to ensure a proper seal. The detector at C2 is a curved 800-wire $BF_3$ position sensitive detector, with a range of 80° in $2\theta$ with a 0.1° wire spacing. Data were collected over two angular ranges: low angle from 3°-83°, and high angle from 40°-120°. A monochromator crystal was used to select a wavelength of ~1.329Å to collect data for structural refinement, and ~2.379Å for magnetic structural analysis.

Samples of ~1-1.5g size were sealed in vanadium cans for measurement on D20. The detector is a curved $^3$He microstrip gas-detector (PSD) with an angular range of ~153° in 2θ, and 0.1° spacing between data points. A pyrolytic graphite monochromator was used to select neutrons at a wavelength of 2.4199Å. Data were collected for analysis of magnetic long-range ordering at low temperatures (<45K).

## 2.3 Heat Capacity

The heat capacity of various $BaV_{10}O_{15}$ samples was measured in an Oxford Instruments MagLab measurement system using the relaxation (or time-constant) method at zero magnetic field. Sintered pellets were attached to the sample platform using a known quantity of calibrated material (Wakefield grease)[4] to achieve good thermal contact. The platform is shown in figure 2.2, and consists of a sapphire chip onto which a heater and Cernox thermometer have been attached. The thermometer is connected to the chip using thick gold wires, and the platform to the rest of the apparatus using 20μm gold plated tungsten leads. The sample is shown in the center of the chip to improve the clarity of this figure, but is better placed directly over the heater. Measurements were collected over a temperature range of 2K to 70K.[5](Instruments 2000)

The methods for obtaining low temperature[6] heat capacity data may be broadly separated into two groups: adiabatic and non-adiabatic calorimetry.(Gmelin 1979) A

---

[4] The "Wakefield grease" is actually a suspension of zinc oxide.

[5] The measurements can be carried out above 100K, though the typically large time constant at such temperatures can result in extremely long data collection times. As it was difficult to achieve a proper vacuum in the sample chamber above liquid nitrogen temperature, only data up to 70K has been presented.

[6] For the purposes of this section, the term 'low temperature' will refer to temperatures under 100K.

useful technique for higher temperatures (>~100K) is differential scanning calorimetry, which will be discussed in the next section. In adiabatic calorimetry, a pulse of heat (Q) is applied to the sample, and the change in temperature (ΔT) is measured. This is directly related to the definition of the specific heat, given in equation 2.3.1:

$$C_p = \lim_{\Delta T \to 0}\left[\frac{Q}{\Delta T}\right]. \qquad (2.3.1)$$

Disadvantages of this technique include long measurement times, and the difficulty in achieving sufficiently adiabatic conditions. These problems are balanced by the extremely high accuracy that can be achieved.(Gmelin 1987)

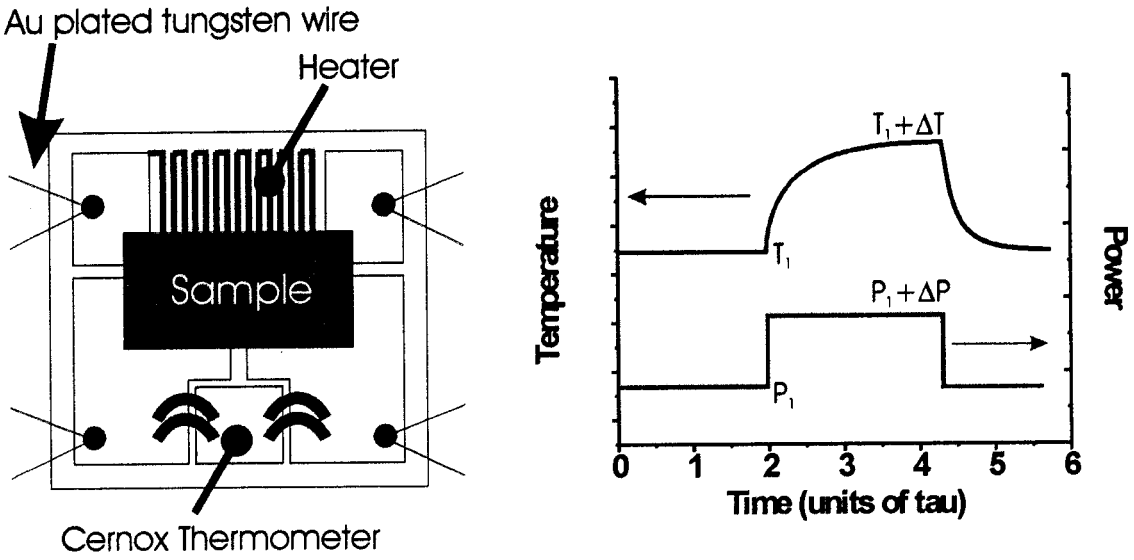


Figure 2.2: Left: Schematic of the sample platform for relaxation method based heat capacity measurements. Right: Plot of one transient pair for the relaxation method.

The relaxation method, which is a common non-adiabatic method, relies upon the type of temperature versus time profile shown in figure 2.2. At a certain time ($t_i$) the power is stepped up to a higher level ($P_1+\Delta P$). The curve between $T_1$ and the final

equilibrium temperature ($T_1+\Delta T_o$), known as a transient, is fitted to the exponential decay function:

$$T = T_1 + \Delta T_o \left( 1 - e^{\frac{-t}{\tau}} \right), \qquad (2.3.2)$$

where $t$ is the measurement time after $t_i$, and $\tau$ is the time constant. This differs from adiabatic calorimetry only in that the power level is only briefly at $P_1+\Delta P$. In addition, the quasi-adiabatic conditions required are easier to achieve than the conditions for adiabatic calorimetry. In the relaxation method, the power level is maintained at the higher level until equilibrium is reached, and the transient fitted. The power level is then stepped down again to $P_1$, and another transient is collected. Heat capacity data on the MagLab system are always collected in pairs of transients, which improves the data quality by using average values of $\tau$ and $\Delta T_o$. Three transient pairs per temperature were collected below ~10K, and two transient pairs above this temperature, due to limitations on measurement time.(Instruments 2000)

The specific heat of the sample, grease and platform is calculated from $\tau$ and $\Delta T_o$ using the expressions:

$$C_p = \frac{\tau}{R_{TH}}, \qquad (2.3.3)$$

and

$$R_{TH} = \frac{\Delta T_o}{\Delta P}, \qquad (2.3.4)$$

where $R_{TH}$ is the effective thermal resistance between the sample and its surroundings. The heat capacity of the sample is obtained by subtracting the contributions from the grease and the addendum, which have been previously measured.(Instruments 2000)

## 2.4 Differential Scanning Calorimetry

Determination of the enthalpy, entropy and temperature of phase transitions can be efficiently carried out using differential scanning calorimetry (DSC). Data have been collected on a TA Instruments DSC 2910 Differential Scanning Calorimeter combined with a TA Instruments 2100 Thermal Analyzer System using, where appropriate, either conventional or modulated DSC. The experimental setup is the same for both methods, and is shown in figure 2.3. A sample of 10 to 30mg size is sealed in a thin aluminum disk and placed in the sample pan. An empty aluminum disk is placed in the reference pan. Temperature measurement is carried out using Alumel and Chromel thermocouple wires, which are attached directly under the reference and sample pans. Heat transfer to the sample and reference pans occurs primarily through the thermoelectric (constantan) disk on which the pans are placed. The apparatus was cooled using a Liquid Nitrogen Cooling Accessory (LNCA), which can access temperatures from –150°C to 500°C. Baseline calibrations were carried out by measuring over the experimental temperature range with empty pans. The cell constant ($K_{Cp}$) and temperature calibration were performed on 10mg of indium, as its heat of fusion and transition temperature are well known.(Instruments 1993)

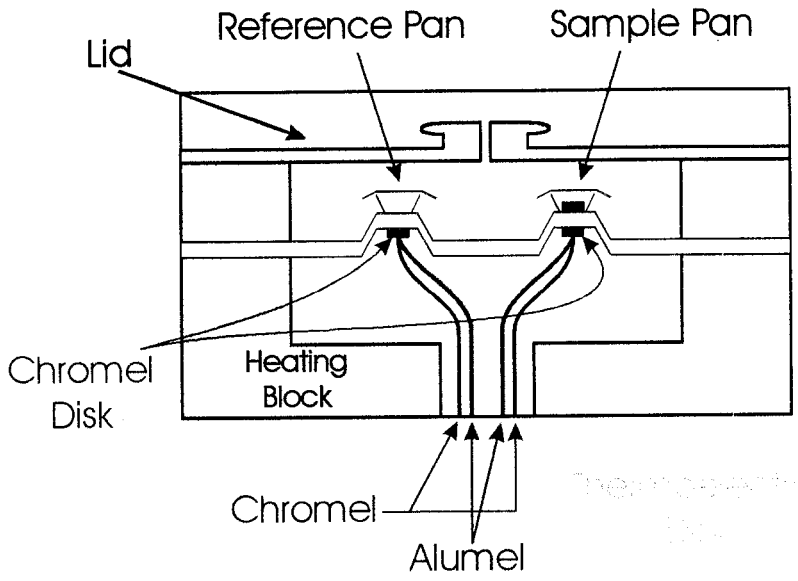


Figure 2.3: Schematic of the cell used to collect data by differential scanning calorimetry (DSC).

Conventional DSC involves raising the temperature of the furnace (or LNCA) in a linear fashion, while heaters under the platform are used to maintain the same heating rate for the sample and reference. As the heat capacities of the reference and sample differ, the heat flow (heater power) will be different for the two pans. The quantity measured in a DSC experiment is therefore the differential heat flow $(dq/dt)$[7], with the manipulated variable being the heating rate $(d\mathrm{T}/dt)$ of the sample associated with that differential heat flow. The ratio of the differential heat flow to the heating rate is directly related to the heat capacity. The chromel-constantan thermocouples in figure 2.3 are used to determine $dq/dt$ and a chromel-alumel thermocouple determines the sample temperature.[8] Furthermore, as the experiment is performed at constant pressure, the heat

---

[7] Heat flow may be plotted in units of mW, or mW/g.

[8] There is a typical systematic error of ~0.3% in the measurement, due to the difference in the heating rate between the sample and reference.(Jin and Wunderlich 1993) Larger errors may result from operator error, if great care is not taken during setup.

flow is related to changes in the enthalpy (ΔH).(White 1984) First-order phase transitions are accompanied by a latent heat, which shows up as a peak in a DSC experiment. A positive peak in the heat flow corresponds to an exothermic transition, and a negative peak to an endothermic transition.[9] When the area of these peaks (for a plot of differential heat flow per gram of material versus tempeature) is integrated, the enthalpy ($\Delta H_{TRANS}$) corresponding to the transition is obtained according to:

$$\Delta H_{TRANS} = \frac{area}{heating\ rate} = \frac{heat\ flow \times temperature}{heating\ rate} = \frac{\frac{JK}{sg}}{\frac{K}{s}} = \frac{J}{g} \quad (2.4.1)$$

As increasing the heating rate can increase the sensitivity of the measurement (while lowering the resolution of individual peaks), scans were performed at 10K/min for most samples, and at 20K/min for samples with weak peaks.(Instruments 1993)

The experimental conditions for modulated DSC are essentially the same as those used in the conventional method, but with a rapid heating rate oscillation added. The total heat flow signal is then separated into reversing, nonreversing, and heat capacity components using a Fourier transform deconvolution process. The various components are described by equation 2.4.2, which gives the total DSC heat flow:

$$\frac{dq}{dt} = \frac{dT}{dt}\left(C_p + f_R(t,T)\right) + f_A(t,T) \quad (2.4.2)$$

---

[9] While the definition of an endothermic (or exothermic) transition is clear, positive peaks in the heat flow are often labeled as endothermic transitions. The TA Instruments software outputs a negative peak in a heat flow versus temperature plot as corresponding to an endothermic transition. Clearly, one must be careful to understand how these peaks are defined in the software.

The variable $t$ refers to time, while $f_R(t,T)$ and $f_A(t,T)$ are functions of time and temperature that are only necessary to describe the kinetic response of a transition. The first function is for a transition that follows the modulation of the heating rate, and is called *reversing*. The second depends on the *absolute* temperature alone, and is referred to as nonreversing.

Using the amplitude of the heat flow oscillations ($q_{AMP}$), heat capacity constant ($K_{Cp}$), the amplitude of the temperature oscillations ($T_{AMP}$) and the period of the temperature modulation, the heat capacity is directly calculated in modulated DSC as:

$$C_p = -K_{Cp} \times \left( \frac{q_{AMP}}{T_{AMP}} \right) \times \left( \frac{Period}{2\pi} \right). \quad (2.4.3)$$

By multiplying $C_p$ by the underlying heating rate, the reversing heat flow is calculated. The total heat flow is obtained from the average over each complete cycle of the raw modulated heat flow signal. The difference between the reversing heat flow and the total heat flow gives the nonreversing heat flow.(Instruments 1993)

## 2.5 DC Magnetic Susceptibility

DC Magnetic susceptibility data were collected on a Quantum Design Superconducting QUantum Interference Device (SQUID) magnetometer. This device is capable of generating fields up to ±5.5T. A SQUID probes the magnetic moment of a sample using the principle of magnetic induction. First, a static field is established by charging a superconducting magnet. Once charged, the current, and thus magnetic field, will persist through the measurement without significant degradation. The DC magnetic

field generates a magnetic moment in the sample. A radio-frequency (rf) SQUID was used, which means that an rf current is applied to the coil to produce a megahertz range oscillation in magnetic flux.(Clarke 1994) The change in magnetic flux due to the presence of the sample in the coil, is then measured by the change in voltage detected by the SQUID. Once the voltage response of the system is calibrated, an accurate measure of the magnetic moment can be obtained.

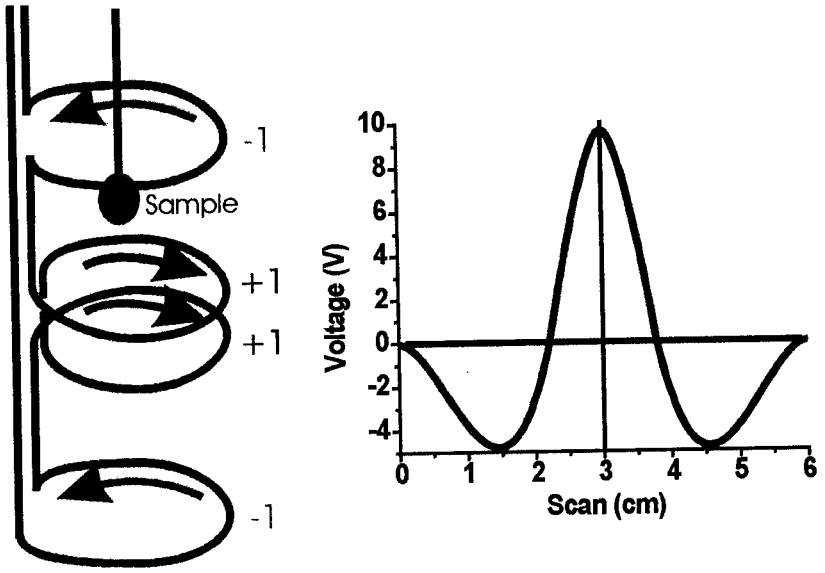


Figure 2.4: Left: Second derivative coil detection system. Right: SQUID response for a 6cm scan.

The detection coil is known as a second-derivative coil, and is a set of three coils of the geometry shown in figure 2.4. This geometry is extremely efficient at minimizing noise. For example, a current that is induced in the center coil, when caused by fluctuations in the applied field, will be cancelled exactly by the currents induced in the upper and lower coils. Two different methods have been applied to measure the magnetic moment of the sample: RSO and DC. In the DC method, the sample was pulled 6cm through the coils by a stepper-motor to produce the voltage response shown on the

right side of figure 2.4. In this case, sample movement is halted during the collection of each data point. For the reciprocating sample option (RSO), the sample is moved rapidly and sinusoidally through the detection coils using a servo motor. The sample does not stop during the measurement. Parameters for the RSO measurements include: a 3cm amplitude of sample movement, 5 cycles per temperature, and a frequency of 0.5-1Hz. For the RSO and DC methods, the sample was placed at the center of the pickup coils for the measurement, and a non-linear least-squares fitting routine (iterative regression) was used to fit the data. RSO measurements have a higher sensitivity ($\sim 5\times10^{-9}$ EMU) than DC measurements.(Design 1999)

At low temperatures (2K to 300K), the sample was contained within a gelatin capsule, which was in turn placed in a straw. The sample masses in this configuration varied between 50 and 200mg. Higher temperature measurements (300K to 600K) were carried out using an oven insert. At high temperatures, samples of 15mg to 30mg size were placed in a quartz tube. The sample masses were limited by availability, and the geometry of the coil system. For sample heights greater than $\approx$0.8cm, it is possible for the sample to induce a significant signal in two coils simultaneously. A cancellation effect can occur if the outer coils are stimulated at the same time as the inner coils, and the moment will appear to be reduced.

## 2.6 AC Magnetic Susceptibility

AC magnetic susceptibility measurements have been carried out with a Quantum Design Physical Property Measurement System (PPMS) fitted with the Model P500,

AC/DC Magnetometry System (ACMS). The system consists of a superconducting magnet for producing DC magnetic fields, a primary excitation field coil, and secondary pickup coils connected to a Digital Signal Processor (DSP). The DC magnetic field ($H_{DC}$) can be varied between –9T and 9T. AC excitation fields ($H_{AC}$) from 0.002Oe to 15Oe, at driving frequencies ($\omega$) from 10Hz to 10kHz, are accessible. The sample can be measured at temperatures ranging from 1.9K to 350K. (Design 1999) Sintered pellets were placed in a plastic capsule partially filled with grease, which prevented the sample from shifting. Sample masses were typically in the range of 100mg to 300mg, depending upon the mass required to achieve a strong signal.

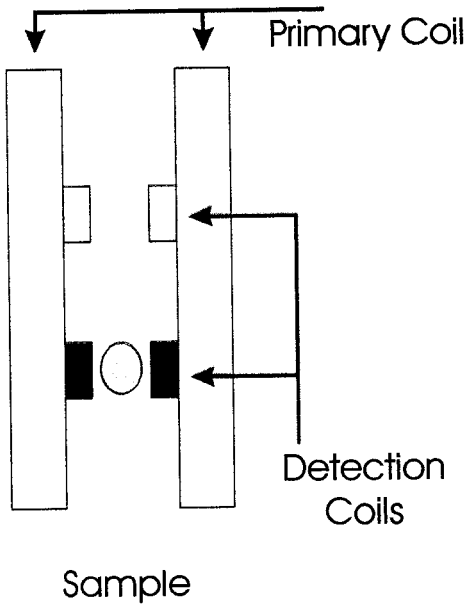


Figure 2.5: Schematic of detection coil array for AC magnetic susceptibility measurements.

An experiment involves first centering the sample in one of the pickup coils, shown in figure 2.5. An AC driving field is then applied using the primary coil, which induces a time-varying magnetization in the sample. The variation in sample

magnetization induces a signal in the secondary pickup coil, which is measured using the DSP. This technique hinges on the fact that the impedance of the lower coil in figure 2.5 is changed relative to the upper coil. In the absence of a sample, the upper and lower secondary coils have an identical impedance. It is the difference in the induced voltage between the secondary coils in the presence of a sample that is measured. To correct for imbalances in the coil system, the sample is also positioned in the upper pickup coil and measured. It is the average of AC waveforms from the two secondary coils that is analyzed to obtain the sample moment.(Instruments 2000)

For small AC fields, the induced moment ($M_{AC}$) is:

$$M_{AC} = \left(\frac{dM}{dH}\right) H_{AC} \sin(\omega t) = \chi_{AC} H_{AC} \sin(\omega t), \quad (2.6.1)$$

where $t$ is time.(Design 2002) It is clear from equation 2.6.1 that the AC susceptibility ($\chi_{AC}$) represents the local slope of the sample's magnetization curve M(H). The experiment not only measures the susceptibility, but can detect a phase shift ($\varphi$) in the magnetization of the sample, if it falls behind the modulation of the excitation field. These quantities can be converted in to an in-phase (real) component $\chi'$, and an out-of-phase (imaginary) component $\chi''$ using the expressions:

$$\chi' = \chi_{AC} \cos\varphi, \quad (2.6.2)$$

and

$$\chi'' = \chi_{AC} \sin\varphi. \quad (2.6.3)$$

A significant magnitude of $\chi''$ indicates that the time constant ($\tau$) for relaxation of the spins is long compared with the frequency of the driving field, and therefore that the sample is absorbing energy from the AC field.(Carlin and Duyneveldt 1977) As a result, AC magnetic susceptibility measurements provide information about the magnetization dynamics of an induced sample moment. This is possible due to the alternating AC driving magnetic field, which differs from the static field used in DC magnetic susceptibility measurements.

The calibration of the inductance of the sensing coils is a crucial step in AC susceptibility measurements. A slight miscalibration can lead to a phase shift in the measured moment, and to errors in $\chi''$ and $\chi'$. For any instrument, there is a finite delay time between the applied field and the measured signal. The instrument dependent phase shift is measured for each data point collected by the ACMS, using a low-inductance calibration coil array that is placed at the center of each secondary coil.(Design 1999)

## 2.7 Muon Spin Relaxation

Production of muons typically involves striking a target with high energy protons. A nuclear reaction occurs between the incident protons and protons/neutrons in the target to produce pions ($\pi^+$). The pions in turn decay into muons ($\mu^+$)[10], which are directed towards the sample. The muons implant into the sample, rapidly lose their kinetic energy (thermalize), and stop at an interstitial site.

---

[10] While both $\mu^+$ and $\mu^-$ can be produced, only measurements utilizing $\mu^+$ are presented in this thesis ($\mu^+$SR). As $\mu^-$ beams are typically ~80% spin polarized, the use of $\mu^+$ is advantageous.

As the muon has a magnetic moment, it precesses around the effective field created at the interstitial site by the local magnetic ions. In a zero-field (ZF) muon spin relaxation (μSR) experiment the muon is allowed to depolarize in the absence of an applied magnetic field. Due to the fact that the initial muon beam is 100% spin polarized, and that the implanted spins rapidly thermalize, the depolarization in the local fields can be effectively monitored. To detect the average muon spin polarization at time *t* (defined as the muon spin relaxation function G(*t*)), the experimental geometry shown in figure 2.6 is assembled. The measurement of time for a data point begins after a muon passes the trigger. The forward and backward counters detect the positron emitted when the muon decays. As the positrons are emitted preferentially along the muon spin direction, the spin orientation can be detected. The normal positron decay curve initially collected is converted into the spin relaxation function.(Lee, Kilcoyne et al. 1999)

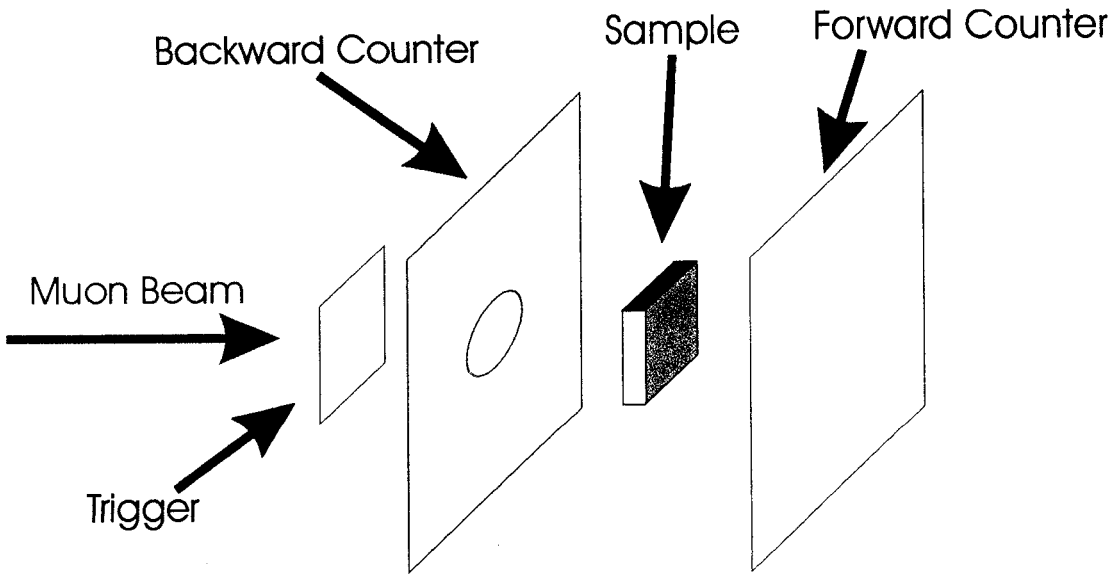


Figure 2.6: Schematic of the setup for a muon spin relaxation experiment.

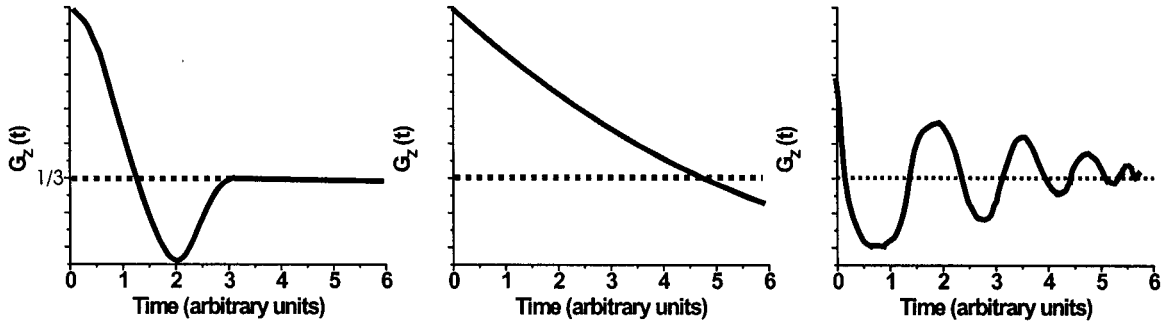


Figure 2.7: Relaxation functions ($G_Z$ (t)) for various magnetic systems from muon spin relaxation data. Left: The Gaussian Kubo-Toyabe relaxation function for static, concentrated random spin systems. Middle: Exponential relaxation for fluctuating spins. Right: Oscillation is present due to long range magnetically ordered spins.

The field distribution resulting from a dense, strongly disordered frozen spin arrangement is expected to be nearly Gaussian. The spin relaxation which occurs as a result of this field distribution can be fitted using a Gaussian Kubo-Toyabe (KT) relaxation function for zero-field conditions(Noakes and Kalvius 1997)[11]:

$$G_Z^G(t) = \frac{1}{3} + \frac{2}{3}(1-\Delta^2 t^2)\exp(-\Delta^2 t^2/2) \quad . (2.7.1)$$

After an initial drop related to the halfwidth of the Gaussian distribution ($\Delta$) of local fields, the polarization recovers to 1/3 of its initial value. This reflects the fact that the local field is static. In the limit of dilute moments, the field distribution is expected to become Lorentzian. When the spins fluctuate rapidly enough to change the local field of an implanted muon during an experiment, the polarization gradually decreases with time, and is eventually lost. For static ordered spins, a significant precession around the ordered spin direction should result in an oscillation of the polarization function. The

[11] Equation 2.7.1 represents the *exact* form for a isotropic Gaussian field distribution at the muon site.

relaxation functions for each these cases are illustrated in figure 2.7. Therefore, on the time scale of the muon spin relaxation experiment, one can distinguish between fluctuating, static ordered, and static disordered spins.(Noakes and Kalvius 1997)

## 2.8 DC Resistivity

DC resistivity measurements have been performed on both an Oxford Instruments MagLab measurement system and a Quantum Design Physical Property Measurement System (PPMS). In each case, silver leads were anchored to sintered pellets using silver epoxy.[12] The sintered pellets had been previously cut into long, thin rods using a diamond saw. Four leads were placed according to the standard four-probe geometry, illustrated in figure 2.8. The four-probe geometry requires the application of current leads on the ends of the sample; the ends must be thoroughly covered with silver epoxy to ensure a uniform potential field. The silver leads used to measure the sample potential are electrically insulated from the current leads; as a negligibly small current flows through the measurement leads, the effects of contact resistance ($R_{C3}$ and $R_{C4}$ in figure 2.8) are greatly minimized.[13](Hong, Ford et al. 1997)

The measured potential ($V_{SI}$) is converted to resistance ($R_{SI}$) based upon the excitation current ($I$):

---

[12] Silver epoxy has similar electrical characteristics to silver paste, but the mechanical properties of the epoxy are superior. If leads are not firmly anchored to the sample, a significant contact resistance will be present. After an overnight period to allow proper setting, the leads attached with epoxy can only be removed with significant force.

[13] Corrections to the measured potential may be required in the event that the sample and/or contact resistances reach the same order of magnitude as the instrument impedance.(Hong, Ford et al. 1997) For example, errors exceed 1% above a sample resistance of 4MΩ for the PPMS system.(Design 1999)

$$V_{S1} = IR_{S1}. \quad (2.8.1)$$

The resistivity (ρ) is calculated from $R_{S1}$ according to equation 2.8.2:

$$\rho = \frac{R_{S1}A}{l}, \quad (2.8.2)$$

where $A$ is the cross-sectional area perpendicular to the current direction, and $l$ is the distance between the potential leads.(Design 1999) For equation 2.8.2 to be used, it is necessary to determine that equation 2.8.1 is valid for the current applied to the sample. A linear plot of current versus voltage ($I$-$V$) can confirm this behavior, though in practice a plot of current versus resistance is more sensitive to non-Ohmic behavior. If the applied current is too small, a large error will result - it will be difficult to obtain reliable estimates of conduction parameters (such as the activation energy of conduction) from the data. Large excitation currents for resistive samples will often lead to a non-Ohmic response. As a result, for samples in which the resistivity changes by orders of magnitude over the temperature range under investigation, it is necessary to employ a number of currents to obtain the optimum data.

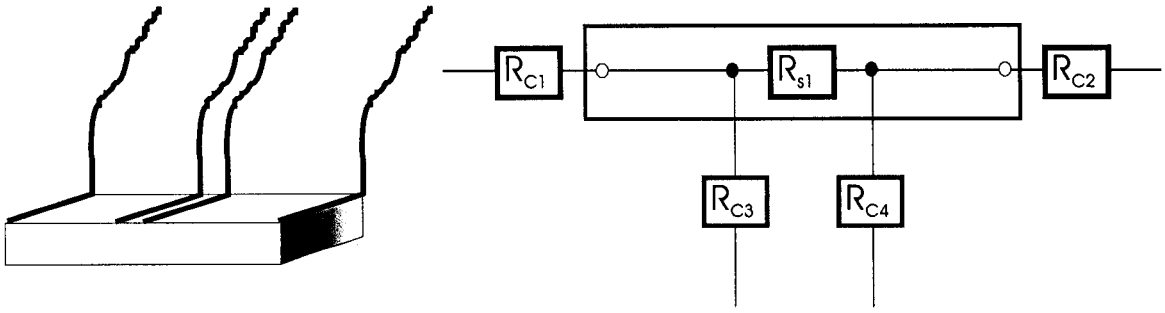


Figure 2.8: Left: experimental setup for four-probe resistivity measurements. Right: Schematic diagram of the contact ($R_C$) and sample ($R_S$) resistances in the four-probe geometry.

The input impedances of the digital multimeters installed in the MagLab and PPMS systems is greater than $10^7$ Ω. The high input impedance, in combination with applied currents in the range of 0.01 to 100μA, made it possible to measure the relatively insulating materials examined in this thesis over a wide range of temperature. The lower limit of temperature for each sample was marked by extremely large resistances, to the extent that only currents below 0.01μA produced Ohmic behavior. For such small currents, the error was typically too large to obtain high quality data.

For all measurements, an average of the potential for a forward and reverse bias of the current was reported. This compensates for DC offsets; these can often arise from thermoelectric effects caused by small thermal gradients on the sample.(Hong, Ford et al. 1997)

## 2.9 Thermopower

When a material is placed under a temperature gradient, a potential develops known as the Seebeck potential ($\Delta E_S$). The ratio of the Seebeck potential over the temperature gradient (ΔT) gives the Seebeck coefficient (*S*), a characteristic quantity for any compound. This is properly defined by the equation:

$$S = -\lim_{\Delta T \to 0} \frac{\Delta E_S}{\Delta T}. \qquad (2.9.1)$$

There are two common DC methods for measuring this quantity: the constant ΔT method, and the "steady-state straddle" method.[14](Hong, Ford et al. 1997) In the constant ΔT method, a constant temperature gradient between the ends of the sample is maintained while sweeping the average temperature. This is well suited to the study of phase transitions, and is more rapid than the straddle method. However, the experimental setup is complicated by the requirement for a tandem measurement with a standard material. This is necessary to compensate for any DC offsets that may be present.

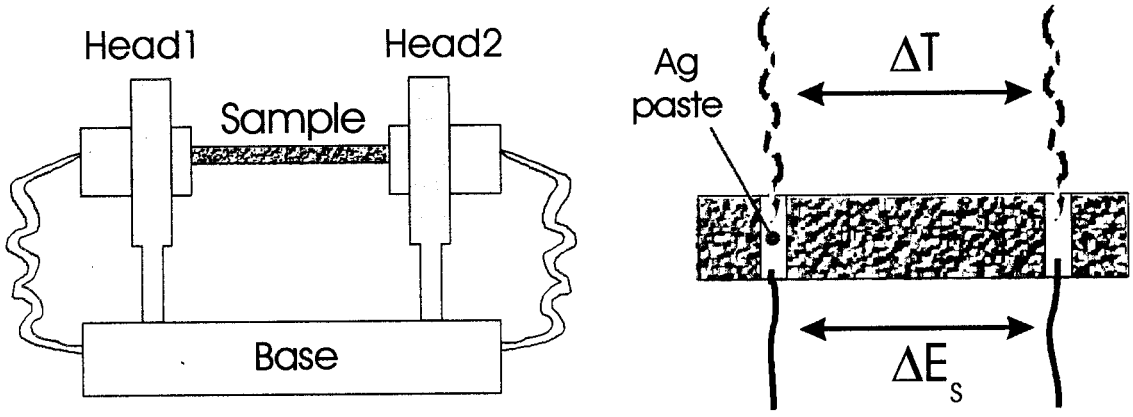


Figure 2.9: Left: Simplified view of experimental setup for thermopower measurements. The sample is placed between two heads with independent temperature control, such that any temperature gradient can be created across the sample. Right: Thermocouple leads are placed directly across from the potential (Cu) leads. Silver paste is used to create good thermal and electrical contact between the leads and the sample.

The steady-state straddle method involves holding one end of the sample at a constant temperature (using head 1) while varying the temperature of the other end (using head 2), relative to the diagram shown in figure 2.9. An apparatus has been built at McMaster University to determine Seebeck coefficients using the steady-state straddle

[14] AC thermoelectric measurements involve applying an oscillating temperature profile to one end of the sample.

method. Cooling is provided from below the base using a CTI Inc. Model 21C closed cycle refrigerator. The two copper heads are in thermal contact with (though electrically isolated from) the base. The heads can be programmed to create a wide range of temperature gradients, though gradients across the sample were held below ±5K for all measurements to ensure compatibility with equation 2.9.1. The greatest error in this method arises from the measurement of ΔT.(Hong, Ford et al. 1997) To minimize this error, it is crucial that the thermocouple leads be placed opposite the potential (Cu) leads, as illustrated on the right side of figure 2.9. Moreover, silver paste is used to create good thermal contact between the leads and the sample, and a band of silver paste is painted around the entire sample to promote more uniform potential lines between the measurement leads.

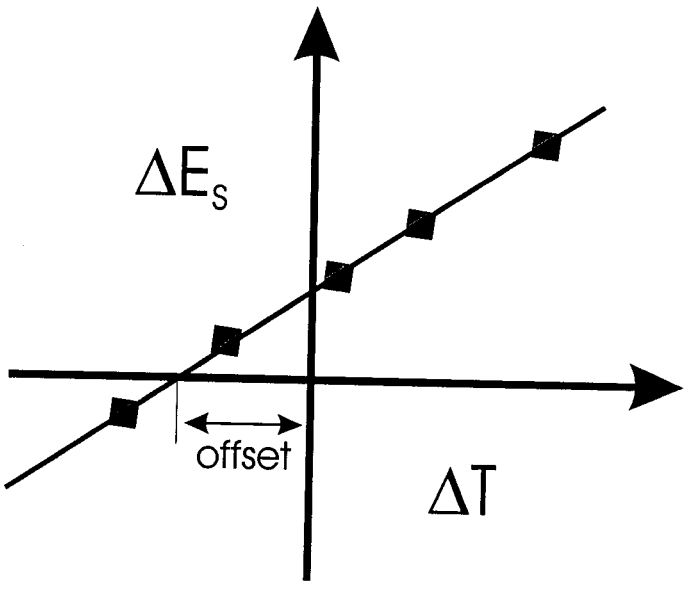


Figure 2.10: A plot of $\Delta E_S$ versus $\Delta T$ data, collected by the "steady-state straddle" method, is shown. The slope of this plot is equal to the Seebeck coefficient. This method can compensate for small DC offset errors.

Data points are collected with the temperature of head 2 both above and below that of head 1. The measured potential is corrected for the thermoelectric contributions from the copper leads and silver paste to obtain the Seebeck potential of the sample. When the corrected data are plotted as $\Delta E_S$ versus $\Delta T$ (figure 2.10), the Seebeck coefficient can be determined from the slope. As many data points are collected for one value of *S*, the measurement is quite slow. However, the quality of the data can be readily judged from the least-squares fit of the $\Delta E_S$ versus $\Delta T$ data. Furthermore, relatively small offsets can be readily determined by the intercept of the linear fit, and do not affect the slope. Systematic errors (represented by the offset) can be a result of (1) asymmetry of the two copper heads, (2) contamination of the thermocouple junctions, or (3) small differences in the cold junction temperatures of the thermocouple wires. The small offsets generally obtained during the steady-state straddle experiments conducted for this thesis suggest that these errors are negligible for the data that has been collected.

# Chapter 3

# $BaV_{10}O_{15}$

## 3.1 Introduction

The fascinating properties of pure and doped vanadium sesquioxide have recently led to interest in the related series $AB_{10}O_{15+X}$, where A = Ba, Sr, B = V, Cr, and x has been found to range from ~0.08 to ~0.78. These materials were reported initially by Müller-Buschbaum in 1980, in which the details of the preparation and crystal structure of $BaV_{10}O_{15}$ were described.(Beaulieu and Müller-Buschbaum 1980) Rewriting the composition as ("$Ba_xV_2O_3$" where x = 0.2), it is possible to consider that this material is barium-doped $V_2O_3$. The structural relationship of this compound to $V_2O_3$ will be elaborated upon in section 3.3. Recently, Liu and Greedan reported the magnetic properties of the isostructural $SrV_{10}O_{15}$ and $BaCr_{10}O_{15}$ compounds.(Liu and Greedan 1996) In addition, the crystal structure of $BaCr_{10}O_{15}$ was reinvestigated at temperatures ranging from 5 to 298K by powder neutron diffraction, while the structure of $BaV_{10}O_{15}$ was refined using single crystal X-ray diffraction at room temperature. In this thesis, further examination of $BaV_{10}O_{15}$ at low temperature has revealed the existence of a crystallographic phase transition. It does not appear that this structural transition is present in the other members of the $AB_{10}O_{15}$ series.

This chapter extends previous studies with respect to the crystallography,

magnetism and transport properties of $BaV_{10}O_{15}$. It is proposed that the low temperature structural phase transition is characterized by homopolar bonding among a subset of the vanadium cations. The magnetic ground state is an unusual mixture of long range order and spin glass-like behavior. Resistivity and thermopower data are shown to be qualitatively consistent with two different models at high temperatures, and variable range hopping at low temperatures.

## 3.2 Sample Preparation

Three different methods of preparation were used for this compound in an attempt to obtain, reproducibly, a phase pure product, namely the tube furnace, tri-arc furnace and induction furnace methods.

### 3.2.1 Tube Furnace

The characteristics of the tube furnace are long reaction times, a moderate temperature range (25-1350°C), and the ability to create an atmosphere of inert or reactive gases. Into the furnace were placed stoichiometric amounts of $BaCO_3$ (99.7% from Baker Chemical Co.) and $V_2O_3$. The $V_2O_3$ was prepared from $V_2O_5$ (Aldrich, 99.6%) in a quartz tube under $H_{2(g)}$ at 700°C for 24 hours.

$$V_2O_5 \xrightarrow{700^\circ C / H_2 / 24hrs} V_2O_3 \qquad (3.2.1)$$

$BaV_{10}O_{15}$ was made by grinding stoichiometric amounts of the powders in an agate mortar under acetone, which provided intimate mixing, followed by pressing 3/8"

diameter pellets. The pelletized mixture was then reacted within a molybdenum boat using a temperature program which involved heating from room temperature to 1350°C at 150°C/hr, followed by soaking at 1350°C for 24 hours. and ending with shutting off the power such that the maximum cooling rate is obtained.

$$BaCO_3 + 5V_2O_3 \xrightarrow{1350^\circ C\,/\,H_2\,/\,24hrs} BaV_{10}O_{15} + H_2O + CO_2 \qquad (3.2.2)$$

The products were examined using a Guinier-Hägg camera with a Cu-$K_{\alpha 1}$ radiation source. All preparations from the tube furnace were found to contain varying amounts of rock salt-type $VO_{1\pm X}$ impurity. The impurity was evident from the appearance of the samples which were either entirely golden in appearance, or simply had a golden surface. Regrinding and refiring the sample under the same conditions resulted in the disappearance of lines corresponding to $BaV_{10}O_{15}$. The remaining pattern consisted of $VO_{1\pm X}$ plus lines which did not correspond to any compound present in the Powder Diffraction Files (PDF). The mullite tube was examined for cracks by fully evacuating the tube; no leaks were found, which suggests that the decomposition of the sample was not related to oxidation. Therefore, the ability to prepare pure product using the Tri-Arc welder and induction furnace may be related to the higher temperatures, and more rapid quenching of the reaction, achieved with those methods.

### 3.2.2 Tri-Arc Furnace

A preparation with the tri-arc furnace is advantageous with respect to the speed of the reaction, which is complete over a time scale of seconds to minutes. The main disadvantage is the danger of losing material. This can occur by evaporation,

decomposition, or occasionally sputtering caused by local heating. The first (and by experience the most serious) problem was minimized by keeping reaction times down. Decomposition was not significant if the arc power was kept to a minimum, and sputtering was avoided by spinning the sample to distribute the heat on the sample more evenly.

$BaCO_3$ was not used for this reaction as it would decompose violently due to the rapid nature of the heating process. As well, it would not be possible to reduce the product in the same manner as the tube furnace preparations. So, different reagents were needed. Toward this end, $Ba_3V_2O_8$ was prepared from $BaCO_3$ and $V_2O_5$. Intimate mixing of stoichiometric amounts of the reagents in an alumina ball mill which contained acetone, followed by firing in air for 24 hours at 950°C in a platinum boat, produced the final product.

$$BaCO_3 + V_2O_5 \xrightarrow{950^\circ C/air} Ba_3V_2O_8 \qquad (3.2.3)$$

Preparations on the order of 2 grams of $BaV_{10}O_{15}$ involved intimate mixing of $Ba_3V_2O_8$ and $V_2O_3$ and co-melting with an appropriate weight of vanadium metal (A.D. Mackay 99.5%). A pellet of the $Ba_3V_2O_8/V_2O_3$ mixture and the metal were placed in a short molybdenum crucible that was open on one end. After several flushing and filling steps in the tri-arc a useful argon atmosphere was obtained. The crucible was then heated vigorously with an arc plasma until the reagents melted and the products were formed according to the reaction:

$$Ba_3V_2O_8 + {}^{10}\!/_{3}\,V + {}^{37}\!/_{3}\,V_2O_3 \xrightarrow{20\,seconds-2\,minutes} 3BaV_{10}O_{15} \qquad (3.2.4)$$

Some of the samples contained very weak peaks - never greater than a few percent of the sample's strongest peaks - which could not be indexed on the $BaV_{10}O_{15}$ cell. As well, these peaks could not be assigned to any compound in the PDF database. The cell constants and magnetic properties of these samples were not reproducible, though they were prepared under exactly the same conditions and so this approach was also abandoned.

### 3.2.3 Induction furnace

In order to achieve higher temperatures than the tube furnace, and more reproducible results than the tri-arc furnace, the induction furnace was used. Both reactions 3.2.4 and 3.2.5 were utilized in the induction furnace preparations. For reaction 3.2.5, $VO_x$ (where $\bar{x} \cong 1$) was prepared by arc melting of the proper amounts of vanadium metal and $V_2O_5$. Oxidative weight gain by thermogravimetric analysis (TGA) in air showed that the stoichiometry was $VO_{1.0}$ within the error of the measurement. Films taken with the Guinier-Hägg showed diffuse, broad peaks for all preparations, indicating that in fact a range of stoichiometries (e.g. $VO_{0.8\text{-}1.2}$) was present. This is typical for arc preparations of this material and the average of $VO_{1.0}$ was used in calculations, based upon the TGA result. In later preparations, the VO reagent was purchased from Cerac (99.5%).

Mixing of $Ba_3V_2O_8$, VO and $V_2O_3$ was done using the same procedure as above for the preparation of $Ba_3V_2O_8$. The mixture was sealed in a molybdenum crucible under a ½ atmosphere of "HP+" argon gas using a mono-arc welder. Next the crucible was

surrounded by a W wire, and placed in a BN cylinder (sealed at one end) within the furnace. The tungsten wire was present to prevent a reaction between the BN and molybdenum crucible at high temperatures. The temperature was brought up over 7 hours to 1500°C, according to a pyrometer placed directly over the sample position. The temperature listed in the reaction below is 50-100°C above this value, as experience has shown that the pyrometer typically underestimates the true temperature by this amount. The sample was held at this temperature for 17 hours, then cooled slowly over 6 hours to ~1400°C to allow for crystal growth, followed by quenching of the reaction to room temperature.

$$Ba_3V_2O_8 + 10VO + 9V_2O_3 \xrightarrow{1550-1600^{o}C/17hrs} 3BaV_{10}O_{15} \qquad (3.2.5)$$

The product was pure according to Guinier film results. The product melted at the temperatures used for the reaction, and crystals on the order of 0.1-0.5mm in size were found in the melt. The crystals were of a sufficient size and quality to perform single crystal x-ray diffraction measurements. For most of the preparations listed below, the temperature was maintained below the melting point such that sintered pellets would be obtained for measurement of the transport properties. It was necessary in most of these cases to regrind, pelletize, and refire the sample to obtain a pure product, though in some cases a pure product was not obtained with repeated refiring. All of the samples examined in this chapter were found to be pure by powder X-ray diffraction and, in some cases, powder neutron diffraction methods.

The induction furnace was determined to be the optimum equipment to use for preparation of $BaV_{10}O_{15}$. While various samples demonstrated a range of properties, it

was also possible in some cases to obtain pure product from different preparations that showed the same physical properties. One example of this is shown by the DC magnetic susceptibility data in figure 3.4 in which two of the samples exhibit the same behavior.

## 3.3 Crystal Structure

### 3.3.1 High Temperature Crystal Structure of $BaV_{10}O_{15}$

Data were collected using a Siemens Mo rotating-anode generator with a P4 diffractometer and a SMART CCD detector. Data processing and analysis were performed using the SHELXTL software package. Absorption corrections were provided by the SADABS program, including a $\lambda/2$ correction. Low temperatures were achieved using a 700 series cryostream cooler from Oxford Cryosystems. As determined by DC susceptibility measurements, which will be described in section 3.5, a crystallographic transition occurs in this preparation at a temperature of 125K. Data were first collected above the transition, at a temperature of 130K. The space group and structural details are consistent with the results of earlier studies, which were performed at room temperature.(Beaulieu and Müller-Buschbaum 1980; Liu and Greedan 1996) These are presented in tables 3.1 to 3.4. Anisotropic displacement parameters are given in appendix A.

Table 3.1: Details of the single crystal X-ray diffraction experiment at 130K

| | | | |
|---|---|---|---|
| Space group | Cmca | Refinement | |
| a (Å) | 11.6015(9) | R1 ($I > 2\sigma(I)$) | 0.0213 |
| b (Å) | 9.9186(7) | wR2 ($I > 2\sigma(I)$) | 0.0527 |
| c (Å) | 9.3940(7) | R1 (all) | 0.0229 |
| V (Å$^3$) | 1081.0(1) | wR2 (all) | 0.0533 |
| Temperature (K) | 130 | Goodness of fit | 1.244 |
| Radiation type | Mo $K_\alpha$ | | |
| Colour | Black | No. of reflections | 1340 |
| Index ranges | $-19 \leq h \leq 18$ | No. of parameters | 68 |
| | $-16 \leq k \leq 11$ | Extinction | 0.0054(2) |
| | $-15 \leq l \leq 12$ | Mean shift/su | 0.000 |

Table 3.2: Final Atomic and Isotropic Displacement Parameters in Cmca at 130K
$T = \exp(h^2a^{*2}U^{11}+... +2hka^*b^*U^{12}+... )$

| Site | x | y | z | Ui/Ue(Å$^2$) |
|---|---|---|---|---|
| Ba1 | 0 | 0.5 | 0 | 0.00468(7) |
| V1 | 0.5 | 0.67623(4) | 0.13922(4) | 0.00320(9) |
| V2 | 0.37097(3) | 0.40976(3) | 0.13548(3) | 0.00667(8) |
| V3 | -0.24606(3) | 0.67201(3) | 0.10991(3) | 0.00464(7) |
| O1 | -0.2541(2) | 0.5 | 0 | 0.0066(3) |
| O2 | 0.1185(1) | 0.2472(2) | 0.0022(1) | 0.0063(2) |
| O3 | 0.25 | 0.3257(2) | 0.25 | 0.0046(3) |
| O4 | 0.6298(1) | 0.5887(1) | 0.2446(1) | 0.0041(2) |
| O5 | 0.5 | 0.3429(2) | 0.2477(2) | 0.0045(3) |
| O6 | 0.5 | 0.5 | 0 | 0.0054(4) |

Table 3.3: Selected Bond Distances for $BaV_{10}O_{15}$ in Cmca at 130K (Å)

| | Bond Length | | Bond Length | | Bond Length |
|---|---|---|---|---|---|
| Ba-O5 (×2) | 2.836(2) | V1-O5 | 1.965(2) | V3-V3 [a] | 2.5819(6) |
| Ba-O2 (×4) | 2.860(2) | V1-O4 (×2) | 2.000(1) | V3-V3 [b] | 2.6336(6) |
| Ba-O1 (×2) | 2.949(2) | V1-O2 (×2) | 2.010(2) | ***V2-V3*** [c] | ***2.7317(5)*** |
| Ba-O4 (×4) | 2.966(1) | V1-O6 | 2.183(1) | ***V2-V3*** [d] | ***2.8410(5)*** |
| Mean | **2.903** | Mean | **2.028** | V1-V3 [e] | 2.9592(4) |
| | | | | ***V2-V3*** [f] | ***2.9872(5)*** |
| V2-O5 | 1.947(1) | V3-O2 | 1.986(2) | V2-V2 [g] | 2.9939(7) |
| V2-O3 | 1.9551(9) | V3-O1 | 1.9964(3) | V1-V2 [h] | 3.0377(5) |
| V2-O2 | 2.028(2) | V3-O2 | 2.012(2) | V1-V2 [i] | 3.1028(5) |
| V2-O4 | 2.049(1) | V3-O3 | 2.014(2) | | |
| V2-O1 | 2.063(2) | V3-O4 | 2.088(1) | | |
| V2-O6 | 2.1591(3) | V3-O4 | 2.091(1) | | |
| Mean | **2.034** | Mean | **2.031** | | |

Table 3.4: Selected Bond Valence Sums for $BaV_{10}O_{15}$ in Cmca at 130K (in v.u.)

| Atom | Bond Valence* | Atom | Bond Valence |
|---|---|---|---|
| Ba | 2.266 | O1 | 1.975 |
| V1 | 2.760 | O2 | 2.130 |
| V2 | 2.724 | O3 | 2.043 |
| V3 | 2.710 | O4 | 1.841 |
| Mean Bond Valence<br>V = 2.726<br>O = 1.971 | | O5 | 1.888 |
| | | O6 | 1.866 |

*Note : The bond valences listed above represent weighted averages based upon the condition that the $V^{2+}$ and $V^{3+}$ cations are randomly distributed on the available sites. The value of $R_o$ for $V^{2+}$ was obtained from the VaList program.(Wills and Brown 1999)

$BaV_{10}O_{15}$ is composed of close packed layers (alternating hcp and cubic close packed (ccp) layers) of oxygen perpendicular to the *a-b* plane, in which 5/8 of the octahedral sites are filled by vanadium ions (figure 3.1(a)). This is similar to the room temperature structure of $V_2O_3$, known as the corundum structure, which is composed of a hexagonal close packing (hcp) of oxygen atoms, with 2/3 of the octahedral sites filled.(Ueda, Kosuge et al. 1980; Wold and Dwight 1991) The $Ba^{2+}$ ion sits within every second oxygen layer and directs the site occupation of the vanadium ions such that within a single layer, edge-shared triangular $V_5$ clusters are effectively formed. When two such layers are considered, $V_{10}$ clusters are observed (figure 3.1(b,c)). These bi-layer clusters are connected through edge-shared octahedra within a layer, and stack in an ..ABAB.. fashion. The sublattice contains both triangular and tetrahedral motifs, either of which can satisfy the requirements for geometrical magnetic frustration described in section 1.2.4. The $VO_6$ octahedra are minimally distorted from a regular coordination in spite of the fact that there are few symmetry constraints on the vanadium sites. The octahedra are linked together through corner, edge and face-sharing.

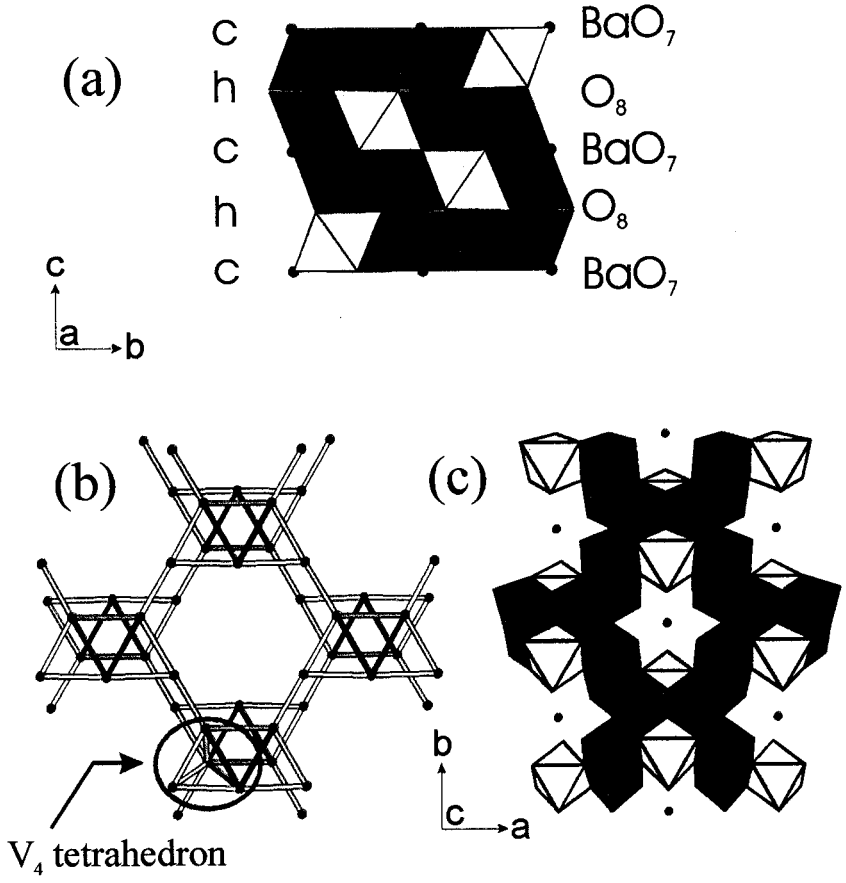


Figure 3.1: Structure of $BaV_{10}O_{15}$. (a) the direction of the $VO_6$ octahedra in alternate layers indicates that the oxygen packing is ..hchc.., (b,c) view down the [001] direction which illustrates ordering of the vanadium sublattice due to $Ba^{2+}$ site occupation. The $Ba^{2+}$ cations in (c) are at z=0. In (a) and (c) the filled circles are $Ba^{2+}$, and the different colors for octahedra represent different vanadium sites; in (b) the filled circles represent vanadium cations.

The shortest vanadium-vanadium distances, 2.5819(6) and 2.6336(6)Å, occur between V(3) cations. These distances are for edge- and face-sharing octahedra, respectively. It is somewhat surprising that the edge-sharing distance is shorter than the face-sharing, but the results do not differ greatly from those at room temperature. At room temperature these distances are reported to be 2.618(2) and 2.604(2), respectively.(Liu and Greedan 1996) This study contains the first reported structural

information below room temperature, and it appears that contrary to expectation, the edge-sharing distance decreases with decreasing temperature while the face-sharing distance increases. No explanation can currently be given for this, and it may be necessary to engage in a theoretical study of this material to provide a satisfactory answer.

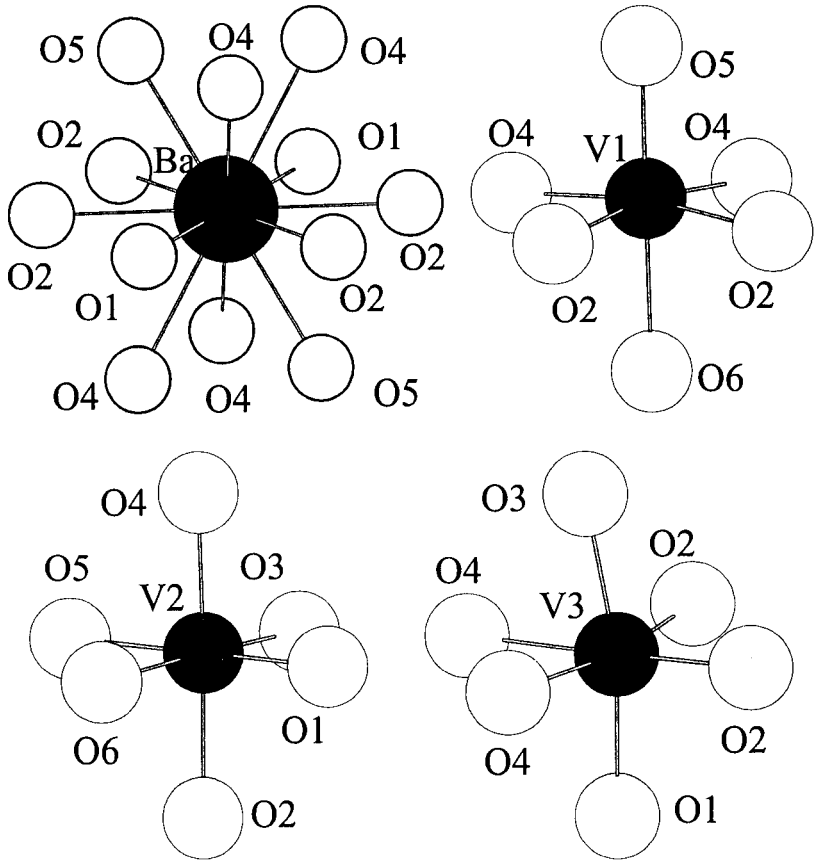


Figure 3.2: Coordination of barium and vanadium cations.

It is interesting to note that the vanadium bi-layers mentioned above are connected in three dimensions through corner and face-sharing. The face-sharing distance, again between two V(3) ions, is by far the shortest vanadium-vanadium separation between the bi-layers. The next-shortest distance is corner-sharing between

V(1) and V(2), at ~3.48Å. The vanadium-vanadium separations within the bi-layers are listed in table 3.3, and are between edge- and face-sharing octahedra. The barium cations are 12-fold coordinated by oxygen to form a cuboctahedron. The coordination of barium and vanadium cations is illustrated in figure 3.2.

Bond valence analysis of the vanadium sublattice is consistent with a random distribution of $V^{2+}$ and $V^{3+}$ – a mean bond valence for all vanadium cations of 2.726 v.u.[1], compared with an expected value of 2.8 v.u.. In the structure, vanadium ions occupy one eight-fold (V1) and two sixteen-fold (V2/V3) sites. The ratio of $V^{2+}$:$V^{3+}$ is 1:4 in $BaV_{10}O_{15}$, for a total of eight $V^{2+}$ cations in the unit cell. As a result, only the V1 site can be filled by $V^{2+}$ alone. This is not the case, as bond valence analysis gives a result of 2.512 v.u. for a calculation involving only $V^{2+}$, and 2.822 v.u. for $V^{3+}$ on that position.

### 3.3.2 Low Temperature Crystal Structure of $BaV_{10}O_{15}$

Details of the data collection and processing for the low temperature structure are identical to those given in section 3.3.1 for the high temperature structure. The results are presented in tables 3.5 to 3.8, with the exception of anisotropic displacement parameters – these are listed in appendix A.

[1] v.u. stands for 'valence units'

Table 3.5: Details of the single crystal X-ray diffraction experiment at 100K

| | | | |
|---|---|---|---|
| Space group | Pbca | Refinement | |
| a (Å) | 11.6155(9) | R1 ($I > 2\sigma(I)$) | 0.0227 |
| b (Å) | 9.8735(7) | wR2 ($I > 2\sigma(I)$) | 0.0536 |
| c (Å) | 9.4178(7) | R1 (all) | 0.0278 |
| V (Å$^3$) | 1080.1(1) | wR2 (all) | 0.0600 |
| Temperature (K) | 100 | Goodness of fit | 1.200 |
| Radiation type | Mo $K_\alpha$ | | |
| Colour | Black | No. of reflections | 2556 |
| Index ranges | $-18 \leq h \leq 19$ | No. of parameters | 122 |
| | $-16 \leq k \leq 11$ | Extinction | 0.0029(1) |
| | $-12 \leq l \leq 15$ | Mean shift/su | 0.000 |

Table 3.6: Final Atomic and Isotropic Displacement Parameters in Pbca at 100K

$T = \exp(h^2a^{*2}U^{11}+... +2hka^*b^*U^{12}+... )$

| Site | x | y | z | Ui/Ue(Å$^2$) | Δ(Ui/Ue)(%) |
|---|---|---|---|---|---|
| Ba | 0 | 0.5 | 0 | 0.00323(5) | 31 |
| V1 | 0.50407(3) | 0.67522(4) | 0.14202(4) | 0.00201(7) | 37 |
| V2 | 0.37552(3) | 0.41157(3) | 0.13676(3) | 0.00246(7) | 63 |
| V3 | -0.24143(3) | 0.67945(3) | 0.11246(3) | 0.00226(7) | 51 |
| V2B | 0.63553(3) | 0.09703(4) | 0.63208(3) | 0.00274(7) | 59 |
| V3B | 0.24878(3) | 0.82959(3) | 0.60593(3) | 0.00219(7) | 53 |
| O1 | -0.2566(2) | 0.5039(2) | 0.0023(1) | 0.0038(3) | 42 |
| O2 | 0.1141(1) | 0.2505(2) | 0.0064(2) | 0.0036(2) | 43 |
| O2B | 0.8793(1) | 0.2545(2) | 0.5040(2) | 0.0033(2) | 48 |
| O3 | 0.2512(1) | 0.3279(2) | 0.2481(1) | 0.0033(2) | 28 |
| O4 | 0.6332(1) | 0.5884(2) | 0.2451(2) | 0.0032(2) | 22 |
| O4B | 0.3725(1) | 0.9116(2) | 0.7444(2) | 0.0031(2) | 24 |
| O5 | 0.5017(1) | 0.3426(2) | 0.2438(2) | 0.0033(2) | 27 |
| O6 | 0.5 | 0.5 | 0 | 0.0038(4) | 30 |

Table 3.7: Selected Bond Distances for $BaV_{10}O_{15}$ in Pbca at 100K (Å)

| | Bond Length | | Bond Length | | Bond Length |
|---|---|---|---|---|---|
| Ba-O2 (×2) | 2.798(2) | V1-O5 | 1.973(2) | V3B-V3 [a] | 2.5378(5) |
| Ba-O5 (×2) | 2.870(2) | V1-O4 | 1.981(2) | V3B-V3 [b] | 2.6561(5) |
| Ba-O2B (×2) | 2.877(2) | V1-O4B | 2.000(2) | ***V3B-V2*** [c] | ***2.7997(5)*** |
| Ba-O4B (×2) | 2.958(2) | V1-O2B | 2.002(2) | ***V3-V2B*** [c] | ***2.5334(5)*** |
| Ba-O1 (×2) | 2.981(2) | V1-O2 | 2.016(2) | ***V3B-V2B*** [d] | ***2.7120(5)*** |
| Ba-O4 (×2) | 2.986(2) | V1-O6 | 2.1873(4) | ***V3-V2*** [d] | ***2.9567(5)*** |
| Mean | **2.912** | Mean | **2.027** | V3-V1 [e] | 2.9696(5) |
| | | | | V3B-V1 [e] | 2.9851(5) |
| V2-O5 | 1.905(2) | V3-O3 | 1.971(2) | ***V3B-V2*** [f] | ***2.9636(5)*** |
| V2-O3 | 1.967(2) | V3-O2 | 1.980(2) | ***V3-V2B*** [f] | ***3.0869(5)*** |
| V2-O4B | 2.019(2) | V3-O2B | 2.009(2) | V2B-V2 [g] | 3.0217(6) |
| V2-O2B | 2.041(2) | V3-O1 | 2.028(2) | V1-V2 [h] | 3.0014(5) |
| V2-O1 | 2.078(2) | V3-O4B | 2.092(2) | V2B-V1 [h] | 3.0929(5) |
| V2-O6 | 2.1241(4) | V3-O4 | 2.119(2) | V2-V1 [i] | 3.0958(5) |
| Mean | **2.022** | Mean | **2.033** | | |
| V2B-O3 | 1.905(2) | V3B-O2B | 1.994(2) | | |
| V2B-O5 | 1.969(2) | V3B-O1 | 2.002(2) | | |
| V2B-O1 | 2.014(2) | V3B-O2 | 2.010(2) | | |
| V2B-O2 | 2.015(2) | V3B-O3 | 2.052(2) | | |
| V2B-O4 | 2.118(2) | V3B-O4B | 2.103(2) | | |
| V2B-O6 | 2.2233(4) | V3B-O4 | 2.104(2) | | |
| Mean | **2.041** | Mean | **2.044** | | |

Table 3.8: Selected Bond Valence Sums for $BaV_{10}O_{15}$ in Pbca at 100K (in v.u.)

| Atom | Bond Valence | Atom | Bond Valence |
|---|---|---|---|
| Ba | 2.245 | O1 | 1.956 |
| V1 | 2.774 | O2 | 2.164 |
| V2 | 2.812 | O2B | 2.119 |
| V3 | 2.708 | O3 | 1.741 |
| V2B | 2.724 | O4 | 1.893 |
| V3B | 2.621 | O4B | 1.821 |
| Mean Bond Valence<br>V = 2.728<br>O = 1.966 | | O5 | 2.099 |
| | | O6 | 1.864 |

*Note : The bond valences listed above represent weighted averages based upon the condition that the $V^{2+}$ and $V^{3+}$ cations are randomly distributed on the available sites. The value of $R_o$ for $V^{2+}$ was obtained from the VaList program.(Wills and Brown 1999)

Data below the transition contain weak reflections at $h + k = 2n + 1$, which violate the C-centering condition in Cmca. In addition, the mirror plane perpendicular to the *a*-axis has been lost. The remaining absences indicate the space group Pbca, a maximal isomorphic subgroup of Cmca. The loss of symmetry reduces the multiplicity of the general position from 16 to 8. Atoms on general positions, including V2, V3, O2 and O4 are split into two crystallographic sites (labeled with the suffix B). A further indication of the lowered symmetry comes from the displacement[2] parameters. In fact, displacement parameters for all ions decrease significantly through the transition from Cmca to Pbca. The oxygen displacement parameters decrease nearly 36%, from a mean value of 0.0053 to 0.0034Å$^2$. The vanadium parameters range from 0.0048 to 0.0023Å$^2$ (52%), and for barium, from 0.0047 to 0.0032Å$^2$ (31%). However, the most notable decrease is observed for the V2 (61%),V3 (52%), O1 (42%) and O2 (45%) sites.

Significant changes occur in the cell constants through the transition. With decreasing temperature, the *a* axis increases by 0.014(1)Å, the *b* axis decreases by 0.045(1)Å, and the *c* axis increases by 0.024(1)Å. A series of data sets were obtained first with decreasing, and then increasing temperature on the single crystal of $BaV_{10}O_{15}$, which are presented in figure 3.3. The presence of temperature hysteresis is shown clearly by the variation of the *b* axis parameter on the bottom right of this figure. Each of the points represents a 30 minute data collection time at low angle, and thus the error bars are rather large. While the shift along the *a* axis is difficult to observe, the two full data

[2] Displacement parameters are also referred to as thermal parameters. The use of 'displacement' is currently preferred due to the fact that it may represent both static incoherent and dynamic atomic displacements. The term 'thermal' suggests atomic vibration alone.

sets collected at 130K and 100K clearly indicate an increase in this parameter with decreasing temperature. The volume change is from 1080.1(1) to 1081.0(1) $Å^3$, a difference of only 0.9(2)$Å^3$ (or 0.08(2)%). This can be compared with the almost 3.5% change in volume observed at 160K in $V_2O_3$ during the metal-insulator transition.(Yethiraj 1990)

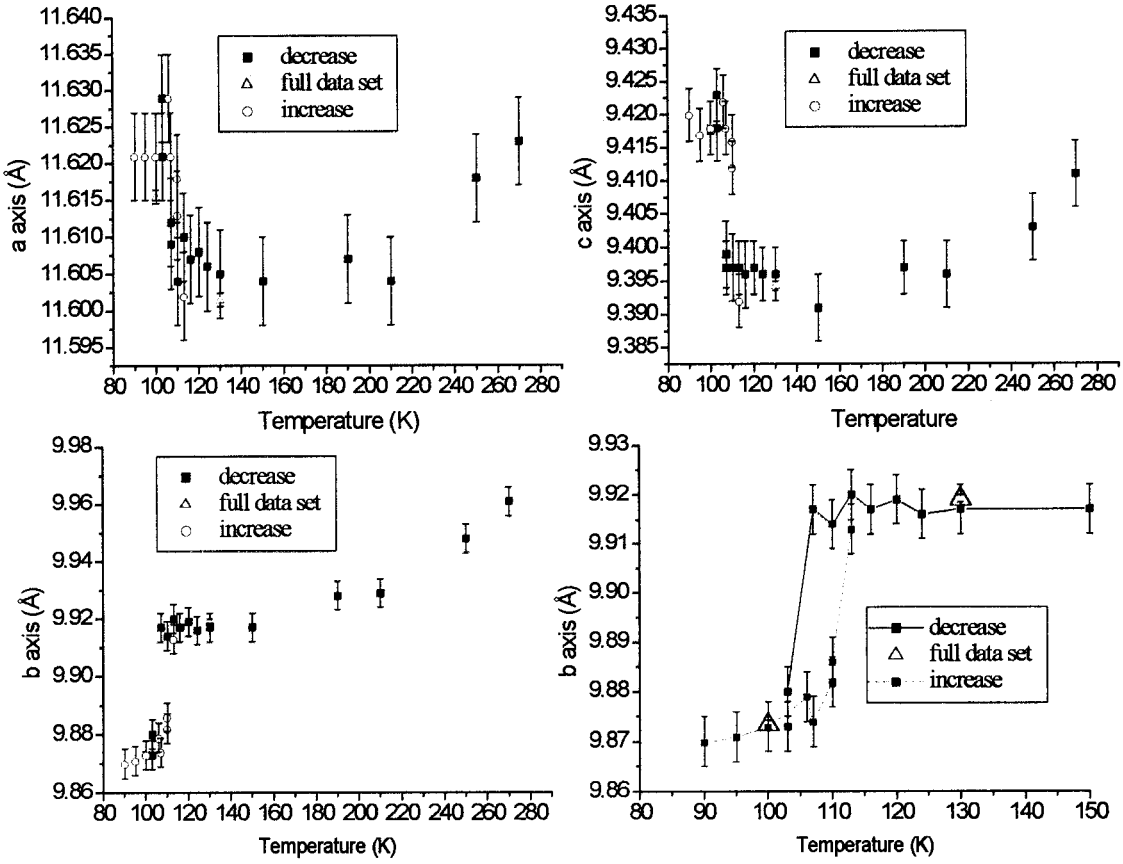


Figure 3.3: Variation of cell constants with temperature for the single crystal of $BaV_{10}O_{15}$.

The O1 and O2 positions are in the $BaO_7$ planes, and are coordinated to barium in that plane. The principal mean square atomic displacement along the *a* axis direction ($U_a$) for O1 changes from 0.0120 to 0.0063$Å^2$. For O2, $U_a$ decreases from 0.0111 to

0.0042/0.0043Å$^2$ (O2/O2B). Also in the $BaO_7$ plane, O6 ions are octahedrally coordinated by vanadium atoms and have relatively isotropic displacement parameters both above and below the transition. A naïve conclusion might be that the anisotropic oxygen displacement parameters are related to coordination with barium. It is perhaps surprising, then, that the changes in displacement parameters are not reflected in the bond valence analysis. The bond valence sums for O1, O2 and Ba shift on the order of 1%, indicating that the coordination sphere of these atoms has little influence on the transition.

The principal mean square atomic displacements (U) are also elongated for the V2 and V3 positions along the *a* axis direction. The displacement along that axis for V2 decreases from 0.0134 at 130K, to 0.0035/0.0044 (V2/V2B)Å$^2$ at 100K. For V3, this decrease is from 0.0073 to 0.0029/0.0028 (V3/V3B)Å$^2$. There is also no evidence of correlation between changes in the vanadium displacement parameters and results from the bond valence analysis. At 100K, bond valence analysis of the vanadium sublattice is again consistent with a random distribution of $V^{2+}$ and $V^{3+}$. The mean bond valence for all vanadium cations is 2.728 v.u., compared with 2.726 v.u. at 130K. In Pbca, vanadium resides on five sites (all of which are general positions), and any of these sites could be fully occupied by $V^{2+}$. However, the results in table 3.8 do not indicate that charge ordering has occurred. It is presumed that the deviation of the bond valence results may range up to 10%, and still indicate agreement with expected values. With such an error it is not possible to state conclusively that the distribution is entirely random, though we may be sure that none of the sites is fully occupied by $V^{2+}$ in this unit cell. In addition,

there are no superstructural reflections present that would suggest charge ordering in conjunction with a larger chemical cell. Certainly charge ordering in this case, between ions which differ in their total electron count by one, and are both typically coordinated by oxygen in relatively regular octahedra, would be very difficult to detect by standard X-ray diffraction methods.

Discussion of possible reasons for the crystallographic transition is left until the end of this chapter, after effects of the structure change upon magnetic and transport properties have been presented.

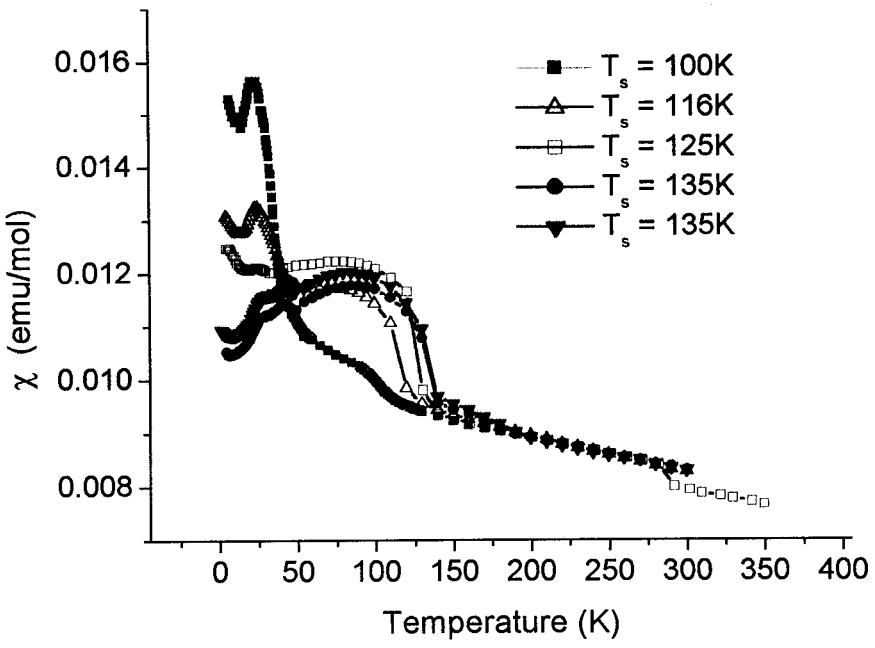


Figure 3.4: Discontinuity in the DC magnetic susceptibility reveals the variation of the structural transition temperature with preparation. These data were collected from 2K to 300K (350K) after initially cooling in the absence of an external field (ZFC). The applied field during measurement was 1000 Oe for all samples.

## 3.4 Physical Properties at the Crystallographic Transition

### 3.4.1 DC Magnetic Susceptibility Near the Transition

Previous reports of the compound $BaV_{10}O_{15}$ did not include DC magnetic susceptibility.(Beaulieu and Müller-Buschbaum 1980; Liu and Greedan 1996) The reason for the lack of these data involved difficulties in developing a preparative route that would consistently produce a given set of properties. During the course of this investigation, a remarkable feature in the susceptibility has been found to occur in the temperature range 105-135K, shown in figure 3.4. This feature, which was not observed in the DC susceptibility measurements of $BaCr_{10}O_{15}$ or $SrV_{10}O_{15}$(Liu and Greedan 1996), corresponds to the structural phase transition described in section 3.3. The temperature at which the transition occurs is sample dependent, and in the absence of diffraction data at low temperatures for all samples, it is necessary to define the temperature based upon the DC magnetic susceptibility data. As this transition is somewhat broad in the susceptibility data, the extremum in the derivative of the product ($\chi$T) with temperature is used to define the structural phase transition temperature ($T_S$). This derivative has been defined by Fisher as approximating the variation of the magnetic specific heat, and is typically used to determine the Néel temperature of an antiferromagnet according to equation (3.4.1).(Fisher 1962)

$$C_M(T) = A\frac{\partial}{\partial T}(\chi(T)T) \,. \qquad (3.4.1)$$

The use of this equation is not intended to imply that this is an antiferromagnetic transition, but rather provides a means for comparison between the samples. As there is

hysteresis exhibited in the susceptibility (described later in this section), the inflection point in the data elucidated by this relationship should be closer to the true transition temperature. In particular, it should be closer than either the endpoint or start of the transition, as for all samples the data were collected with increasing temperature. Plots of $d(\chi T)/dT$ are presented as insets in figure 3.9, and the derived values of $T_S$ are listed in table 3.9.

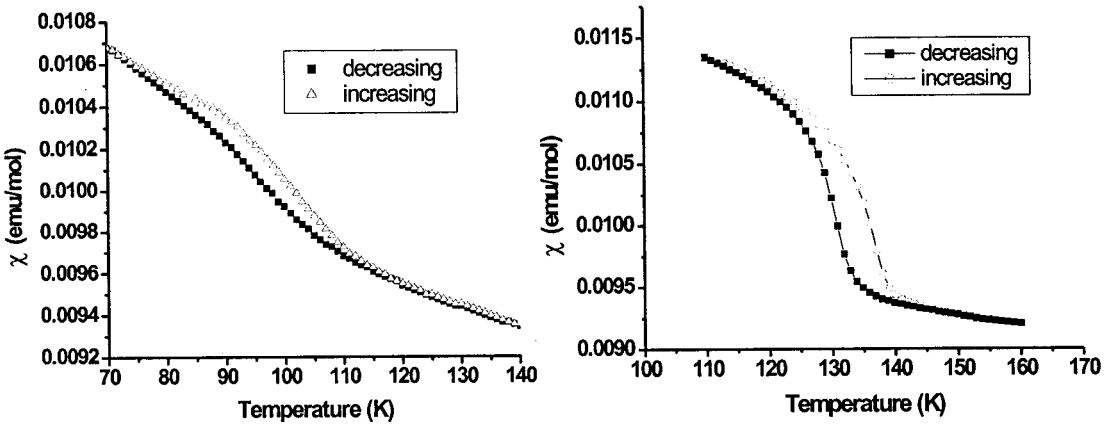


Figure 3.5: Temperature hysteresis in the DC magnetic susceptibility. Left: $T_S$ = 105K sample. Right: $T_S$ = 135K sample.

Additional measurements were performed with both increasing and decreasing temperature for the $T_S$ = 105K and 135K samples. The results presented in figure 3.5 demonstrate a marked temperature hysteresis. The width of this hysteresis was estimated by taking the derivative of $\chi$ versus temperature with increasing and decreasing temperature, and then taking the difference between the maxima of the resulting peaks. This is similar to the procedure used above. The width for the $T_S$ = 105K sample is ~5K, and for the $T_S$ = 135K is ~7K. Appearance of this hysteresis is indicative of a nucleation

process occuring at the transition. This is expected for a first-order transition.(Vainshtein, Fridkin et al. 1994)

### 3.4.2 Latent Heat at the Transition

The enthalpy (H) is discontinuous at a first-order transition, which results in a latent heat.(Collins 1989) Various samples have been measured by differential scanning calorimetry (DSC), and all samples, with the exception of the $T_S$ = 105K sample, exhibit an endothermic peak at the structural phase transition. Transitions near 100K are not within the experimentally accessible temperature range for the instrument. The transition temperatures are determined as the intercept of the projected baseline and the low temperature slope of the peak, and are shown in table 3.9.(Williams and Chamberland 1969) These are in good agreement with the values derived from DC magnetic susceptibility. Measurements have been performed for the $T_S$ = 135K sample that have elucidated a hysteresis with heating (133.30K) and cooling (130.60K). This is shown in figure 3.6, along with data for a reverse-modulated DSC run for the $T_S$ = 125K sample. A temperature hysteresis of this type was also observed in DC magnetic susceptibility (section 3.4.1) and single crystal X-ray diffraction (section 3.3.2) measurements. The presence of hysteresis and latent heat at the transition are sufficient evidence to state that the transition is first-order. It is important to note that the change in crystal symmetry at the transition can indicate the order of the transition. In a critical (second-order) transition the symmetry of one phase is necessarily a subgroup of the second phase. The low temperature phase of $BaV_{10}O_{15}$ is described by the symmetry of Pbca, which is a

subgroup of the symmetry found in the high temperature phase, Cmca. However, this does not define the transition as second-order, merely that symmetry cannot exclude the possibility of a second-order transition, as the symmetry at a first-order transition changes arbitrarily.(Vainshtein, Fridkin et al. 1994)

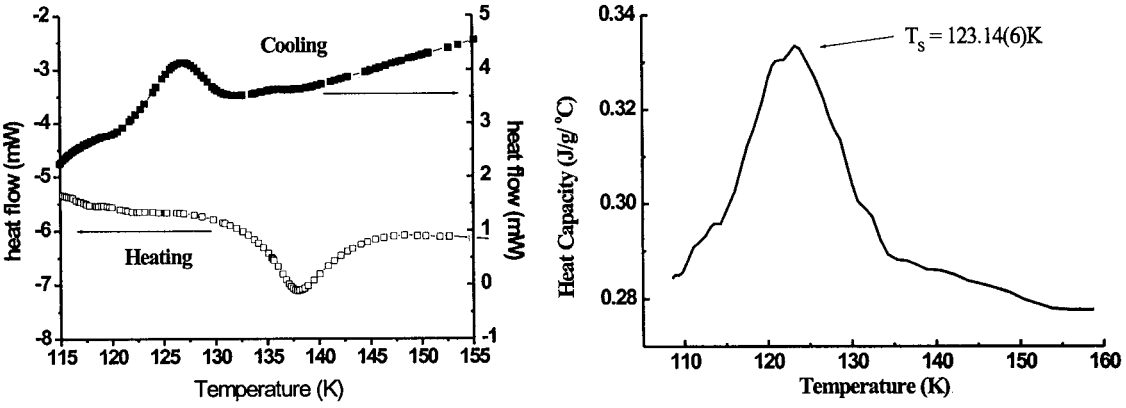


Figure 3.6: Differential scanning calorimetry (DSC) plots for $BaV_{10}O_{15}$. Left: Temperature hysteresis at the structural phase transition for the $T_S$ = 135K sample. Transition temperatures correspond to 133.3K while heating, and 130.6K during cooling. Right: Heat capacity measured by reverse-modulated DSC (RMDSC) for the $T_S$ = 125K sample. Peak temperature is determined here to be 123.14(6)K.

For each sample, a baseline was determined by extrapolating from the high and low temperature sides of the peak, and then the peak area was integrated to obtain the change in enthalpy at the transition ($\Delta H_{TRANS}$). The entropy at the phase transition has been determined by equation (3.4.2)

$$\Delta S_{TRANS} = \frac{\Delta H_{TRANS}}{T_S}. \qquad (3.4.2)$$

This is valid under constant pressure conditions, and under the assumption that the transition is primarily isothermal.(White 1984; Atkins 1990) In addition, the volume change is extremely small (section 3.3.2), and therefore will not significantly contribute

to the observed entropy change. The change in entropy expected for a two configuration model of the lattice (entropy due to the repositioning of atoms between the Pbca and Cmca models ) is estimated as Rln(2) = 5.8 J/mol-K. This compares with experimentally determined values of 2.2 to 8.3 J/mol-K. The lowest transition temperature measured, 116K, coincides with the smallest entropy removal (2.2J/mol-K), while the other samples are generally above this theoretical value. The small amount of entropy removal for prep#5 is unexpected in comparison with similar samples, and may indicate that caution should be taken in comparing results from reverse-modulated and standard DSC. Rather than assuming the two configuration model, it is instructive to fit the entropy data with Rln($s$), where $s$ is the number of possible configurations. The range of configurations, from 1.30 to 2.71, may indicate that the assumption of Rln(2) is unjustified with respect to the sample dependent behavior of $BaV_{10}O_{15}$. The implications of the DSC data for the structural phase transition will be explored further at the end of this chapter, in section 3.10.

### 3.4.3 Relationship Between Cell Constants, Volume, Oxygen Content and the Structural Phase Transition Temperature

A comparison of the room temperature cell constants for various preparations with the transition temperature is given in figure 3.7. The overall trend suggests that a decrease in $T_S$ coincides with an increase along the $b$ axis, and decrease along the $a$ and $c$ axes. This is opposite to the trend in cell constants with temperature observed in figure 3.3.

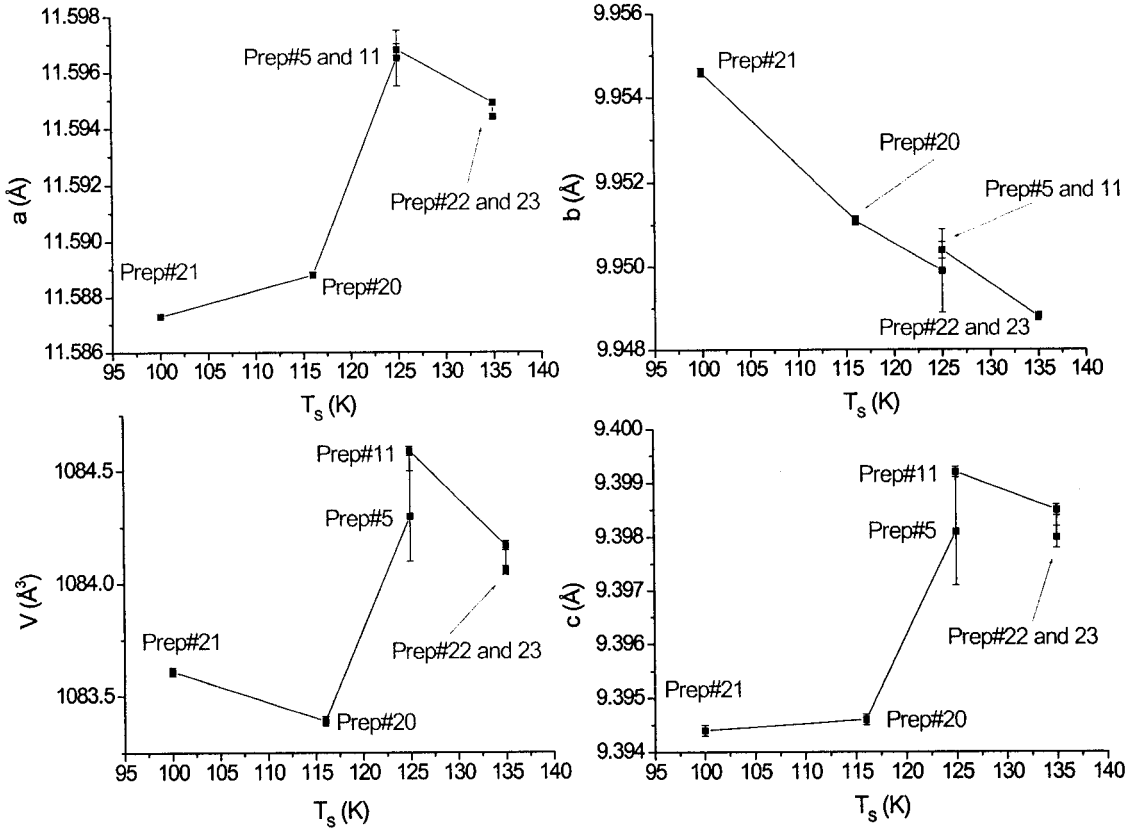


Figure 3.7: Relationship between the room temperature cell constants and volume, and the structural phase transition temperature for various preparations. All data points were obtained using powder X-ray diffraction. Data for preparation #5 was collected on a Guinier-Hagg camera, and for all others on a Bruker D8 Advance diffractometer.

Changes in cell constants are frequently related to the oxidation state of the transition metal cation. Earlier work on the compound $BaCr_{10}O_{15}$ suggested that it was possible to oxidize this compound to $BaCr_{10}O_{15+x}$.(Liu and Greedan 1996) However, the exact oxygen content was not specified, presumably due to the fact that the weight gain was from both oxidation and contamination by impurity phases. The most significant evidence for oxidation is in the cell volume, which decreases from 1080.16(1) to 1053.60(1)$Å^3$. The reported volume change for the oxidation of $BaCr_{10}O_{15}$ is far greater

than any observed for $BaV_{10}O_{15}$ in this study. For $BaV_{10}O_{15}$, a range of only 1083.39(2) (preparation #20) to 1084.59(2)Å$^3$(preparation #11), corresponds to a range of oxygen content from 15.08 to 15.78 (table 3.9). The cell constants for $BaCr_{10}O_{15}$ are $a$ = 11.4537(5), $b$ = 10.0926(5), $c$ = 9.3441(4)Å, compared to $a$ = 11.3894(4), $b$ = 10.0040(5), $c$ = 9.2470(4)Å for $BaCr_{10}O_{15+x}$, which are much greater shifts than any observed in figure 3.7. In addition, the trend for $BaCr_{10}O_{15}$ with oxidation is for all cell constants to decrease, whereas for $BaV_{10}O_{15}$ the $b$ axis length actually increases.

The cell constant data used in the above argument have all been obtained from fits to Bruker D8 Advance diffractometer data, with the exception of preparation #5, which was collected using a Guinier-Hägg camera. These data are self-consistent, from the point of view of the trend in figure 3.7, but the results from the single crystal measurements do not fit neatly into this picture. The cell constants at 270K from single crystal X-ray diffraction are $a$ = 11.623(6), $b$ = 9.961(5), $c$ = 9.411(5)Å in this study, and $a$ = 11.584(4), $b$ = 9.946(3), $c$ = 9.383(4)Å from Liu and Greedan.(Liu and Greedan 1996) This does not invalidate the earlier discussion, but rather illustrates the potential difficulties associated with comparing results from different powder and single crystal techniques.

A comparison of the change in $T_S$ with oxygen content is listed in table 3.9. The lowest observed $T_S$, 105K, coincides with the most oxidized product, but there is no apparent trend for $T_S$ in the range 125 to 135K. The structural implications of this oxidation have not been fully addressed in this or the study of Liu and Greedan.(Liu and Greedan 1996) There is no evidence from diffraction data to indicate that oxygen

occupies interstitial positions in the structure; the defect levels may simply be too low to detect by these means. The structure itself is devoid of any favorable sites for this excess oxygen. This suggests that defect chemistry may be important to the interpretation of these results, such as a deficiency on the barium or vanadium sites. The results from inductively-coupled-plasma mass spectrometry (ICPMS) indicate that a slight amount of barium deficiency is present. However, this deficiency is not sufficient to account for the observed TGA result without also including oxygen excess, and a mixture of the two is probable.

Table 3.9: $BaV_{10}O_{15}$ cell, TGA, and DSC data for various preparations

| $T_S$ | Prep. # | Weight Gain (%) | Ba:V ratio (ICPMS) | x[A] | $\Delta H_{TRANS}$ (J/mol) | $\Delta S_{TRANS}$ (J/mol-K) | $s$[B] | $T_S$,[C] (K) |
|---|---|---|---|---|---|---|---|---|
| 135 | 23 | 19.67 | 0.975(6):10 | 0.10 | 791.2 | 5.909 | 2.04 | 133.90 |
| 135 | 22 | 19.24 | 0.978(4):10 | 0.29 | 978.1 | 7.338 | 2.42 | 133.30 |
| 125 | 11 | 19.12 | - | 0.34 | 1054 | 8.276 | 2.71 | 127.36 |
| 125 | 5 | 19.6 | 0.941(6):10 | 0.15 | 558[D] | 4.53 | 1.72 | 123.14[D] |
| 116 | 20 | - | - | - | 254.5 | 2.176 | 1.30 | 116.94 |
| 105 | 21 | 18.18 | 0.973(4):10 | 0.79 | -[E] | - | - | - |

Note that error estimates are not given as the values were obtained by integration, rather than a least-squares fitting procedure.

[A] additional oxygen content of $BaV_{10}O_{15+X}$ based upon TGA result, and including ICPMS result where appropriate

[B] possible configurations ($s$) determined from a fit to $\Delta S_{TRANS} = R\ln(s)$

[C] structural transition temperature determined from DSC data

[D] obtained by reverse-modulated DSC; other data were collected by standard DSC

[E] 100K is too low a temperature to obtain DSC data

Though all of the samples presented in this chapter exhibit this structural phase transition (as evidenced by the DC magnetic susceptibility data), a number of samples have been prepared which do not show this transition. The susceptibility data for one

sample is shown in figure 3.8. None of these samples has been explored in detail as it is not clear that any of them is pure. For the example given, the presence of $V_2O_3$ was detected by X-ray powder diffraction, and a crude estimate based upon peak height suggests that it represents approximately 4% of the pattern. The presence of $V_2O_3$ does not correlate directly with the loss of a structural phase transition, as $V_2O_3$ has been identified in various samples exhibiting a jump in the magnetic susceptibility. The unit cell constants for this sample are in agreement with the trends expected for a low $T_S$ from figure 3.7, in that the *b* axis is larger (9.9644(1)Å), and *a* (11.5823(2)Å) and *c* (9.3939(1)Å) axes smaller than any given on that graph. In particular, the *b* axis is far larger than in other samples, and as a result the volume (1084.15(2) $Å^3$ for this sample) is slightly larger than might be expected for a more oxidized sample.

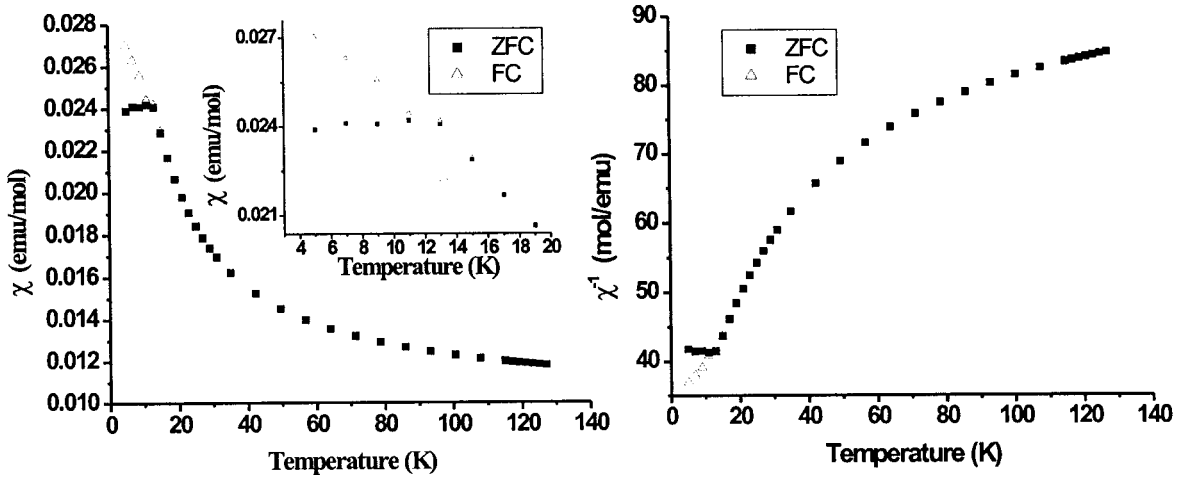


Figure 3.8: DC magnetic susceptibility results for a sample of $BaV_{10}O_{15}$ which does not exhibit any sign of a structural phase transition.

No further analysis will be attempted on these samples, as the impurity severely limits the possibilities for an accurate determination of oxygen content or Ba:V ratio for

the $BaV_{10}O_{15}$ phase. Preparation of pure samples will be essential to examine this behavior, that may represent an end-member for this series of $BaV_{10}O_{15}$ samples, in which the structural phase transition may be entirely absent.

## 3.5 Bulk Magnetic Properties

### 3.5.1 DC Magnetic Susceptibility

The DC magnetic susceptibility of polycrystalline $BaV_{10}O_{15}$ was measured on a Quantum Design SQUID magnetometer at an applied field of 1000 Oersted for a number of samples from 2K to 300K. Data were collected after first cooling in the absence of a magnetic field (ZFC), and then after cooling in the presence of a 1000 Oe applied field (FC). These data were partially analyzed in section 3.4.1 with respect to the structural phase transition, and are now presented here, and in figure 3.9, with a focus on the magnetic properties. The data for the temperature region ~250K to 300K have been fitted to the Curie-Weiss law (equation 1.2.9). Data obtained above 300K for the samples of interest all exhibited a strange displacement with respect to the low temperature data that can be attributed to experimental difficulties. Measurements conducted in the past found that the temperature range from ~250K to ~450K could be fitted to the Curie-Weiss law, and so the data above 300K are unnecessary in the present case. When plotted as $\chi^{-1}$ versus T there was no evidence for curvature of the data in the fitted region, and thus a temperature independent term was not included. The Curie constants for various preparations, summarized in table 3.10, are close to the expected value of 11.75 emuK/mol. The close agreement supports the use of this model over the temperature region examined, and indicates that the vanadium 3d electrons are acting as Curie-Weiss

spins. The expected value is calculated based upon contributions from 2 (S=3/2) + 8 (S=1) magnetic ions per formula unit. The θ values are very large and negative, indicating strong antiferromagnetic correlations. The onset of magnetic order is taken here to be $T_D$, the temperature at which the ZFC and FC magnetic susceptibilities diverge, as this is in close agreement with the results of AC susceptibility, heat capacity, and powder neutron diffraction experiments that are described in later sections.

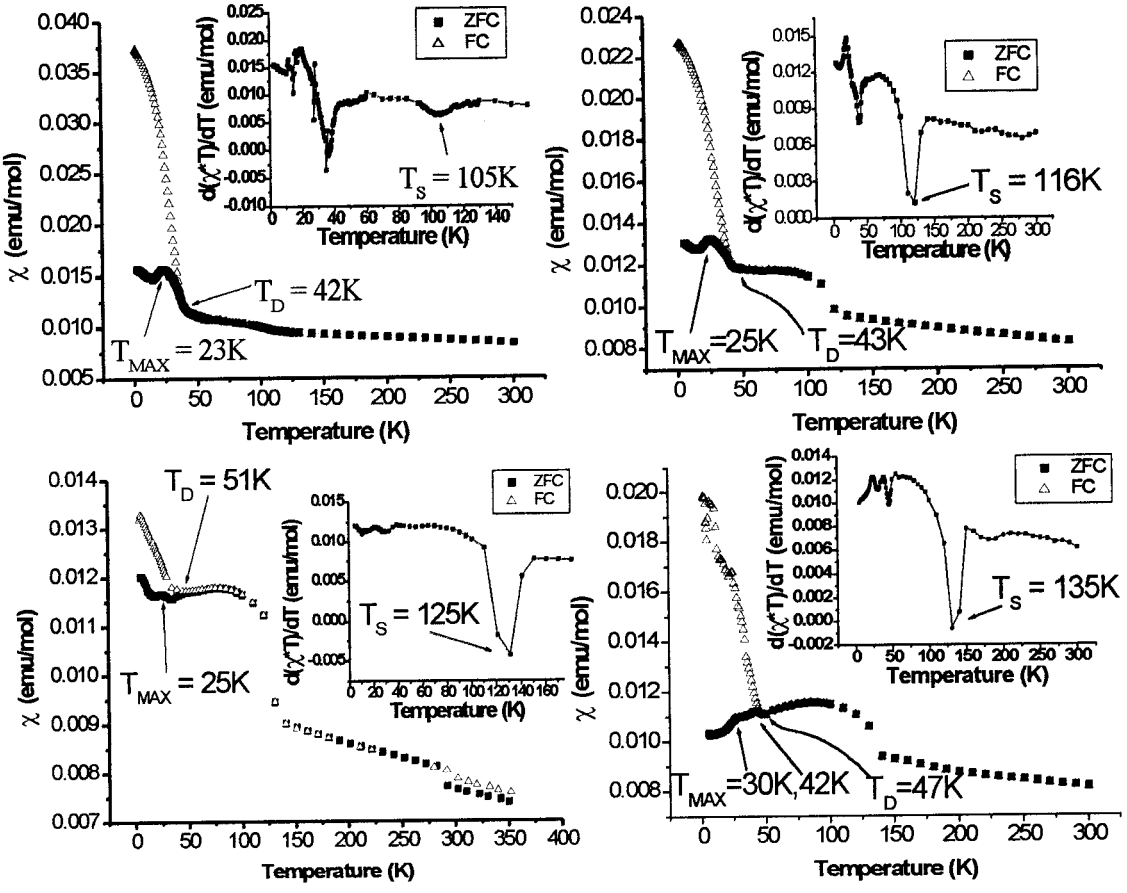


Figure 3.9: DC magnetic susceptibility data collected on a SQUID magnetometer at 1000Oe for samples with different structural transition temperatures. $T_S$ refers to the structural phase transition, $T_D$ to the temperature at which the ZFC/FC divergence occurs, and $T_{MAX}$ to peaks in the ZFC data below $T_D$.

The ratio of θ to the onset of magnetic ordering is often given as a measure of the frustration present in a material. Values in the range 1-4 or 5 are expected for conventional ordering, while values in the range of 10 to 20 or higher are expected for frustrated materials.(Ramirez 1994) The $\theta/T_D$ values are therefore quite large (24 - 26) and indicate a high degree of magnetic frustration. A summary of various other features of the DC magnetic susceptibility are also presented in table 3.10: $T_S$ refers to the structural phase transition, and $T_{MAX}$ to maxima in the ZFC data below $T_D$.

The low temperature data exhibit hysteresis for all samples. Hysteresis can be symptomatic of spin glass-like behavior (found in frustrated materials), spin canting, or superparamagnetic clusters. The divergence of the ZFC and FC magnetic susceptibility alone does not distinguish among these possibilities. The sharp rise in the FC data below the divergence temperature is indicative of a ferromagnetic component, and is not expected for conventional spin glass ordering. Curiously, the magnitude of this ferromagnetic component appears to be especially weak in the case of the $T_S$ = 125K sample though all data were collected using the same applied field. This is a reproducible phenomenon that is not currently understood.

Additional experiments have been performed which involve measuring the susceptibility versus time at a fixed temperature and field. The sample was first cooled in zero field to the base temperature, and left to 'age' at this temperature for 30 minutes. The field was then set to 0.1T and the measurement started. Without the aging period the data were determined to be unacceptably noisy, and so the same procedure was used to collect all of the data presented. Samples were heated to room temperature between

measurements to remove any memory effects. All examined samples exhibited relaxation effects at low temperature. The results for $T_S$ = 105K are shown in figure 3.10. The increase in susceptibility with time indicates a relaxation of the spins towards their FC values.

A related experiment was also performed at 2K and 5K. At 2K, after the above relaxation measurement was completed, the field was switched off and data collection immediately recommenced. An identical experiment was conducted at 5K. This is a measurement of the isothermal remnant magnetization (IRM), which is expected, roughly, to follow a logarithmic time dependence over large time scales for a spin glass. This behavior is observed for $\chi_{IRM}$ in this material, and is also presented in figure 3.10.

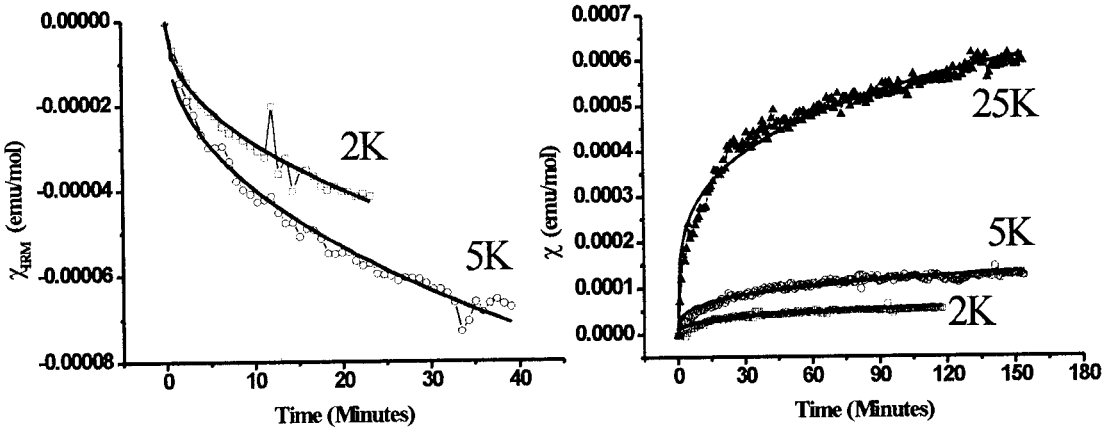


Figure 3.10: Relaxation measurements using DC magnetic susceptibility for the $T_S$ = 105K sample. Left: Isothermal remnant magnetization - relaxation after removal of the applied field. Right: Relaxation in the presence of an applied field. The data have been scaled to an initial value of zero.

In spin glass materials the ZFC and FC susceptibilities are expected to be field dependent, which can be observed experimentally by a shift in $T_D$.(Kimura, Li et al. 2000; Kmety, Huang et al. 2000) The divergence between the ZFC and FC curves is seen

to decrease dramatically from an applied field of 110 Oe to 5000 Oe for the $T_S$ = 125K sample in figure 3.11. However, $T_D$ remains apparently unaffected by the field in the range of 110 Oe to 1000 Oe, at a temperature of ~51K. At 5000 Oe the divergence temperature shifts to 38K, which implies the presence of spin glassy behavior.

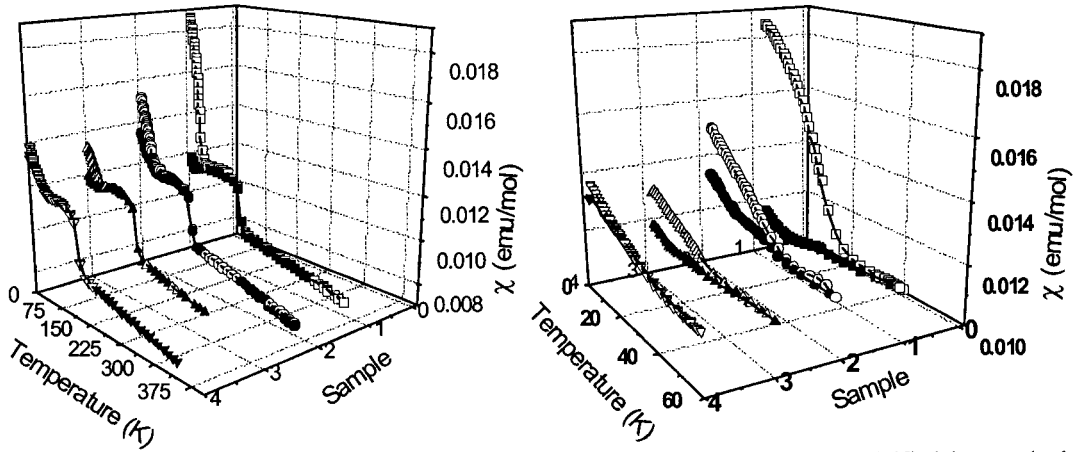


Figure 3.11: Field dependence of the zero-field cooled(ZFC)/field cooled (FC) divergence for the $T_S$ = 125K sample. Samples 1, 2, 3 and 4 refer to 110, 500, 1000 and 5000Oe respectively. The jump at the structural phase transition is insensitive to applied field, as illustrated in the left plot.

Isothermal magnetization measurements have been carried out between 10 Oe and 5T, and are shown in figure 3.12. For the $T_S$ = 125K sample, a ferromagnetic component is present in the 5K and 30K data which is not present at higher temperatures. This component is particularly strong at 5K. Hysteresis loops were collected at 25K, 110K and 150K for the $T_S$ = 135K sample, and indicate the presence of a small ferromagnetic component in the 25K data which has a coercive field of ~0.062T in this measurement. The small ferromagnetic component is also present at 5K in the $T_S$ = 116K sample, with a coercive field of ~0.056T. Clearly these samples show a ferromagnetic component that is only present below the divergence temperature for the FC and ZFC data.

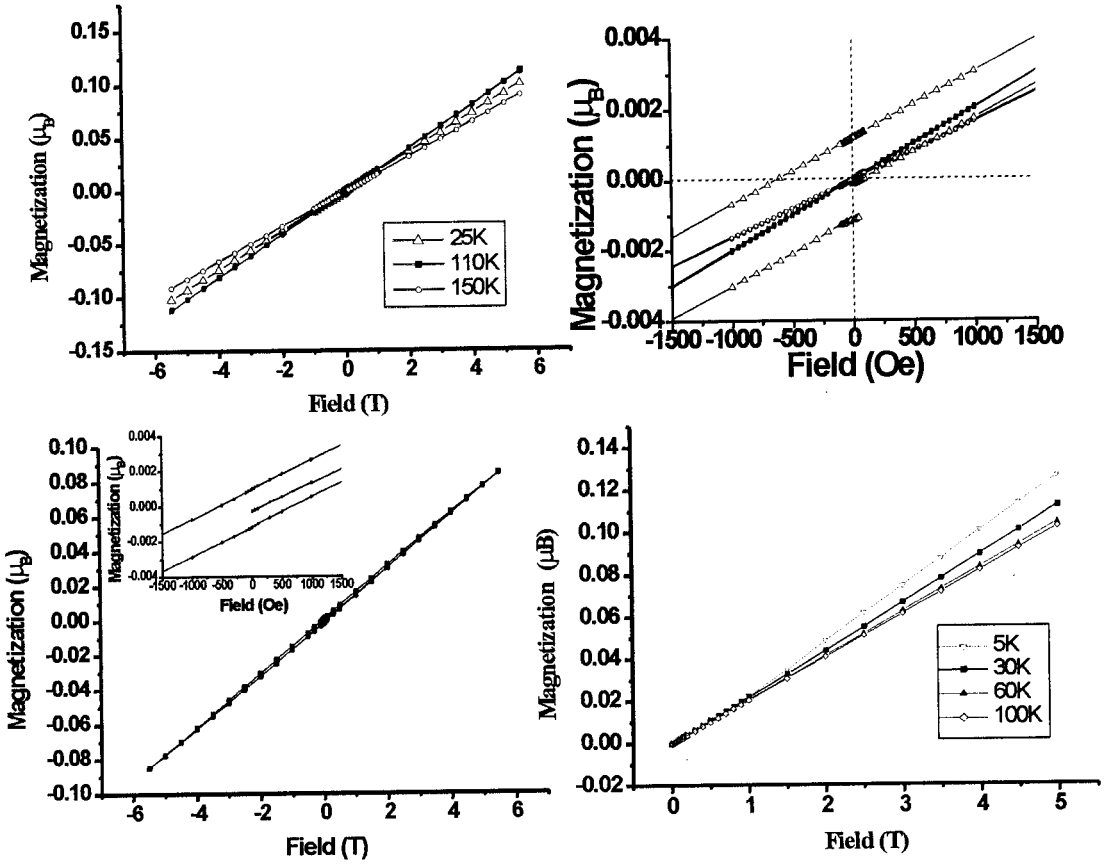


Figure 3.12: Isothermal magnetization as a function of applied field for samples with different structural phase transition temperatures. Top: $T_S$ = 105K sample at 25K, 110K and 150K. Bottom Left: $T_S$ = 116K sample at 5K. Right: $T_S$ = 125K sample at 5K, 30K, 60K, and 100K.

Table 3.10: Bulk DC magnetic susceptibility results for various preparations of $BaV_{10}O_{15}$

| $T_S$ (K) | $T_{MAX}$ (K) | $T_D$ (K) | C (emuK/mol) | θ (K) | $\theta/T_D$ |
|---|---|---|---|---|---|
| 135 | 30,42 | 47 | 11.8(2) | -1141(23) | -24 |
| 125 | 25 | 51 | 11.43(2) | -1126(3) | -22 |
| 116 | 25 | 43 | 11.0(3) | -1027(30) | -24 |
| 105 | 23 | 42 | 11.6(2) | -1095(26) | -26 |

*$T_S$ = structural phase transition temperature; $T_D$ = divergence temperature; $T_{MAX}$ = maximum in susceptibility below $T_D$; C = Curie constant; θ = Weiss temperature; $\theta/T_D$ = index of frustration

### 3.5.2 AC Magnetic Susceptibility

Sintered pellets were measured in a Quantum Design Physical Property Measurement System (PPMS) for the $T_S$ = 105K and 135K samples, and are presented in figure 3.13. The $T_S$ = 135K sample was measured with a 4 Oe driving field, in the presence of a 5 Oe static field, at frequencies ranging from 10 to 10000 Hz, and over a temperature range of 2 to 80K. Measurements were carried out at a constant rate of 1 second per frequency, which resulted in noisy data for the lower frequency range. Useful data were obtained above 1000 Hz, which are presented on the left side of the figure.

The in-phase component, $\chi'$, is nearly identical to the DC magnetic susceptibility result. There are peaks at ~43K and ~30K, although the lower temperature peak is considerably broadened relative to the result from DC measurements. A frequency dependence is observed for $\chi'$ below ~45K, causing the susceptibility to decrease with increasing frequency. The imaginary part, $\chi''$ , increases rapidly below ~51K, reaches a maximum near 29K, then decreases until ~17K where it levels off. No frequency dependence can be discerned between 1000 Hz and 4641 Hz for the out-of-phase component, which is likely due to the quality of the data. At 10000 Hz the maximum in $\chi''$ is shifted to higher temperatures. However, this result is suspect due to the observation that at lower temperatures for this frequency the susceptibility is negative, which is an unphysical result.[3]

---

[3] A negative result for $\chi''$ suggests that energy is being *created*, rather than dissipated.

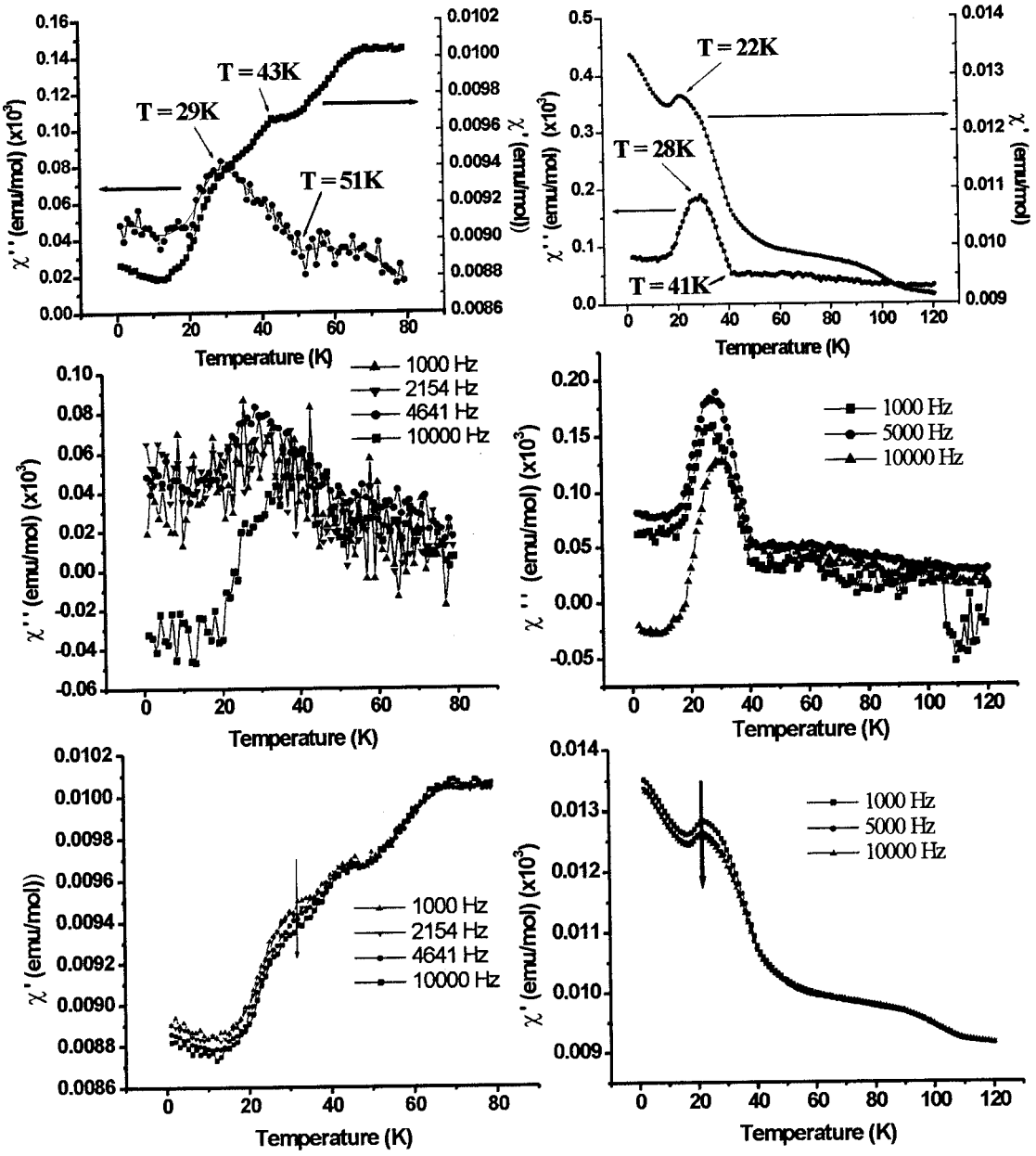


Figure 3.13: AC magnetic susceptibility data for two different $BaV_{10}O_{15}$ samples. Left: Susceptibility for $T_S$ = 135K sample with a 5 Oe static applied field, 4 Oe driving field. Top Left: Data collected at 4641Hz. A curve is drawn through the $\chi''$ data as a guide to the eye. Right: Susceptibility for $T_S$ = 105K sample. Top Right: Data collected at 5000Hz.

Results for the $T_S$ = 105K sample are shown on the right side of figure 3.13. The sample was measured with a 10 Oe driving field, in the presence of a 100 Oe static field, at frequencies of 1000, 5000, and 10000 Hz, and over a temperature range of 2 to 120K. The data quality relative to the $T_S$ = 135K sample was somewhat improved by increasing the count time to 5 seconds per frequency. A maximum is observed in $\chi'$ near 22K. The out-of-phase component experiences a change in slope at 41K, followed by a broad peak with qualitatively similar features to the peak in $\chi''$ for the $T_S$ = 135K sample. The data was of sufficient quality that at 1000Hz and 5000Hz, the peak position in $\chi''$ was extracted by fitting to a Lorentzian function. The maximum at 1000Hz is 27.4(1)K, and 28.0(1)K at 5000Hz. Again at 10000Hz, the $\chi''$ data is negative at low temperatures, and is therefore disregarded.

The presence of an imaginary component is indicative of a relaxation process. This can be found in both superparamagnetic and spin glassy materials. The most straightforward method for distinguishing between these is the shift of the maximum in $\chi'$ with frequency.(Mydosh 1993) This shift is predicted to be much larger in superparamagnets than spin glasses, and is expressed by the quantity $K$ (3.5.1)

$$K = \frac{\Delta T_{MAX}}{T_{MAX}\Delta(\log f)}. \qquad (3.5.1)$$

Here $T_{MAX}$ is the maximum in $\chi'$, and $f$ is the frequency of the alternating field.(Maignan, Sundaresan et al. 1998) A value of 0.28 for $K$ has been observed in the superparamagnet a-$(Ho_2O_3)(B_2O_3)$, while less that 0.1 is expected for spin glasses.(Mydosh 1993) For the $T_S$ = 105K sample K= 0.03(1), as determined by fitting the 1000Hz and 5000Hz $\chi''$ data,

as opposed to the $\chi'$; the reason for using $\chi''$ is explained below. This value of K falls within the range expected for a spin glass.

A peculiar result from the AC magnetic susceptibility measurements, is that there is no clear shift in $T_{MAX}$ for $\chi'$ in either the $T_S$ = 105K or 135K samples, though a clear shift is observed in $\chi''$ for the $T_S$ = 105K sample. Moreover, the maxima in $\chi'$ and $\chi''$ are expected to approximately coincide, but for the $T_S$ = 105K sample, $T_{MAX}$ occurs at 22K in $\chi'$ and at ~28K in $\chi''$. The strange behavior of $\chi'$ reflects the fact that this is not a conventional spin glass.

### 3.5.3 Summary of Bulk Magnetic Properties

The results of DC magnetic susceptibility data are suggestive of spin glassy behavior or superparamagnetic clusters, rather than spin canting; AC susceptibility measurements further rule out superparamagnetic behavior. The most conclusive evidence against spin canting is provided by the field dependence of the divergence temperature. A weak ferromagnetic component has been identified in all samples. The lack of field dependence of the susceptibility at the structural phase transition suggests that it is not driven by magnetic correlations, which will be again discussed in section 3.7 using μSR measurements.

AC susceptibility measurements have shown that spin glass behavior is more consistent with the results than superparamagnetic behavior. The inability to discern a shift in $T_{MAX}$ for $\chi'$ with frequency indicates that this is an unconventional spin glass, as will be clearly demonstrated by heat capacity and powder neutron diffraction

measurements. With decreasing temperature, the point at which a transition in $\chi''$ occurs is very close to the values of $T_D$ extracted from the DC magnetic susceptibility data. This supports the conclusion that spin freezing occurs at this temperature.

## 3.6 Specific Heat

The heat capacity of various $BaV_{10}O_{15}$ samples was measured in an Oxford Instruments MagLab measurement system using the relaxation (or time-constant) method at zero magnetic field. Sintered pellets were attached to the sample platform using a known quantity of calibrated material (Wakefield grease) to achieve good thermal contact. The specific heat of the sample is extracted from the measured quantity by subtracting the contribution from the grease and the addendum. Measurements were collected over a temperature range of 2K to 140K, but due to problems with maintaining a proper vacuum in the sample chamber above liquid nitrogen temperature only data up to 70K will be presented.

A sharp, λ-shaped peak is observed for the $T_S$ = 125K and 135K samples at 42 and 43K, respectively. This corresponds to the onset of long range magnetic ordering. However, this feature is not observed in the $T_S$ = 105K sample. The absence of a peak could be interpreted as the absence of long range order, but powder neutron diffraction results in section 3.6.2 will show that long range magnetic order is present. Therefore, the reason that a peak is not observed is that only a small amount of entropy is removed during the transition to long range order.

The measured heat capacity is the sum of a number of components, including the nuclear, lattice, and electronic contributions. There are no features of the data consistent with nuclear or magnetic Schottky contributions.(Gopal 1966) As indicated in section 3.9, these samples are insulating at low temperature, and so the electronic contribution is magnetic alone. To isolate the magnetic contribution to the heat capacity it is necessary to subtract the lattice component. A common method of achieving this is to measure a diamagnetic, insulating sample that is isostructural with the compound of interest, and to take this as the lattice contribution. Toward that end, attempts were made to prepare $BaMg_2Al_8O_{15}$ and $BaMg_2Ga_8O_{15}$, which were unsuccessful. The products were multiphasic, and no evidence for a phase isostructural with $BaV_{10}O_{15}$ was found.

Therefore the lattice contribution was taken to be that of $BaV_3Ti_7O_{15}$. These titanium substituted compounds will be discussed in detail in chapter 4. This compound is only weakly semiconducting, and the DC magnetic susceptibility results suggest that there is no collective magnetic behavior down to 2K. However, it is evident from the plot of $C_m/T$ versus T in figure 3.14, that entropy removal occurs in $BaV_3Ti_7O_{15}$ below 13K. The entropy removal may indicate the onset of collective magnetic behavior. As a result, data for this compound was only used as an estimate of the lattice contribution down to 13K. The magnetic entropy ($\Delta S$) extracted using $BaV_3Ti_7O_{15}$ as a lattice standard may be considered only as a lower estimate of the total entropy removal ($\Delta S^A$ in table 3.11). To obtain a upper estimate of the magnetic entropy, data was simulated up to 70K based upon a $T^3$ temperature dependence of the lattice heat capacity, which is predicted by the Debye model. The Debye temperature for this estimate was obtained by scaling the high

temperature part of the simulated data to the raw data ($\Delta S^B$ in table 3.11). Based upon the fact that the samples match in the region above ~55K, where it appears that the lattice contribution dominates, the $T^3$ simulated data was calculated up to this temperature, and scaled to match the raw data.[4]

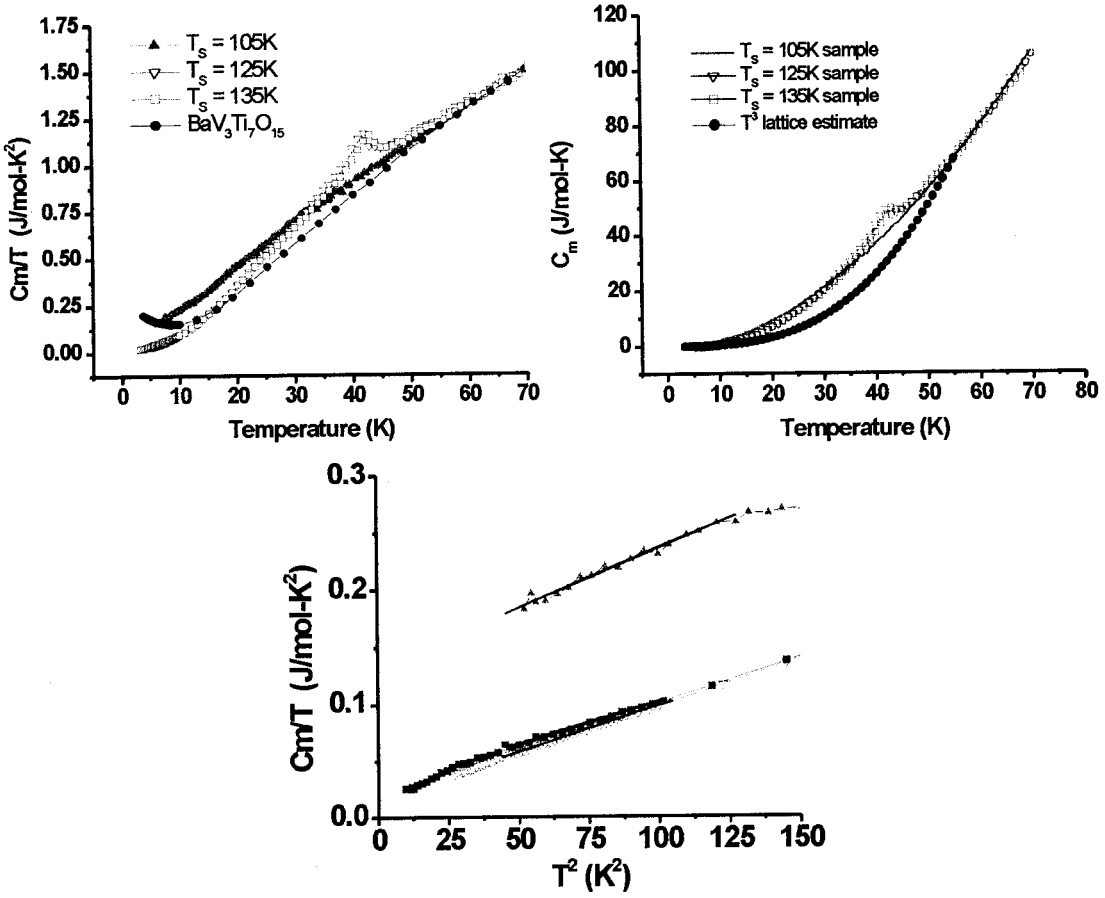


Figure 3.14: The heat capacity of $BaV_{10}O_{15}$ measured by the relaxation method for $T_S$ = 105K, 125K and 135K. The upper plots compare the raw data with the lattice standard $BaV_3Ti_7O_{15}$ (left) and a $T^3$ (lattice term) calculation (right). The bottom figure shows the low temperature fit to equation 3.6.2. The large linear term for the $T_S$ = 105K sample is evident from this plot.

[4] It is important to note that while the $T_S$ = 135K, $T_S$ = 105K, and $BaV_3Ti_7O_{15}$ samples all have a nearly identical high temperature heat capacity, the heat capacity of the $T_S$ = 135K sample required a scaling factor of 1.05 to match up with the other samples. This is considered acceptible in light of the similar heat capacity for the other samples, which suggests that the lattice component dominates in that temperature range. The error is likely a weighing error, related to the extremely small masses used.

Plots of $C_m/T$ versus T are used to extract the magnetic entropy according to equation (3.6.1):

$$S_m = \int_0^T \frac{C_m}{T} dT \,. \qquad (3.6.1)$$

This integration is properly performed down to zero kelvin. Therefore, the results for $\Delta S^A$ and $\Delta S^B$ include a linear extrapolation to 0K (figure 3.15). The entropy removed is far less than the expected value for eight $V^{3+}$ and two $V^{2+}$ ions, of Rln(3)*8+Rln(4)*2 = 96.12 J/mol-K.(Gopal 1966) This corresponds to a range from ~5% ($\Delta S^A$) to ~13% ($\Delta S^B$) of the total magnetic entropy, and suggests that much of the entropy is removed above the transition temperature. This is a result expected for a spin glass.(Mydosh 1993) However, the sharp, λ-type peaks observed in the $T_S$ = 125K and 135K samples are not typically observed in spin glasses, which suggests that a mixture of spin glassy behavior and long range order is present.

To further illustrate that only a small fraction of the magnetic entropy removal is observed, the data were integrated over the entire temperature range *without* first subtracting an estimate of the lattice component. Even if all of the entropy removal below 70K could be considered magnetic in origin, only ~50% of the predicted magnetic entropy could be accounted for.

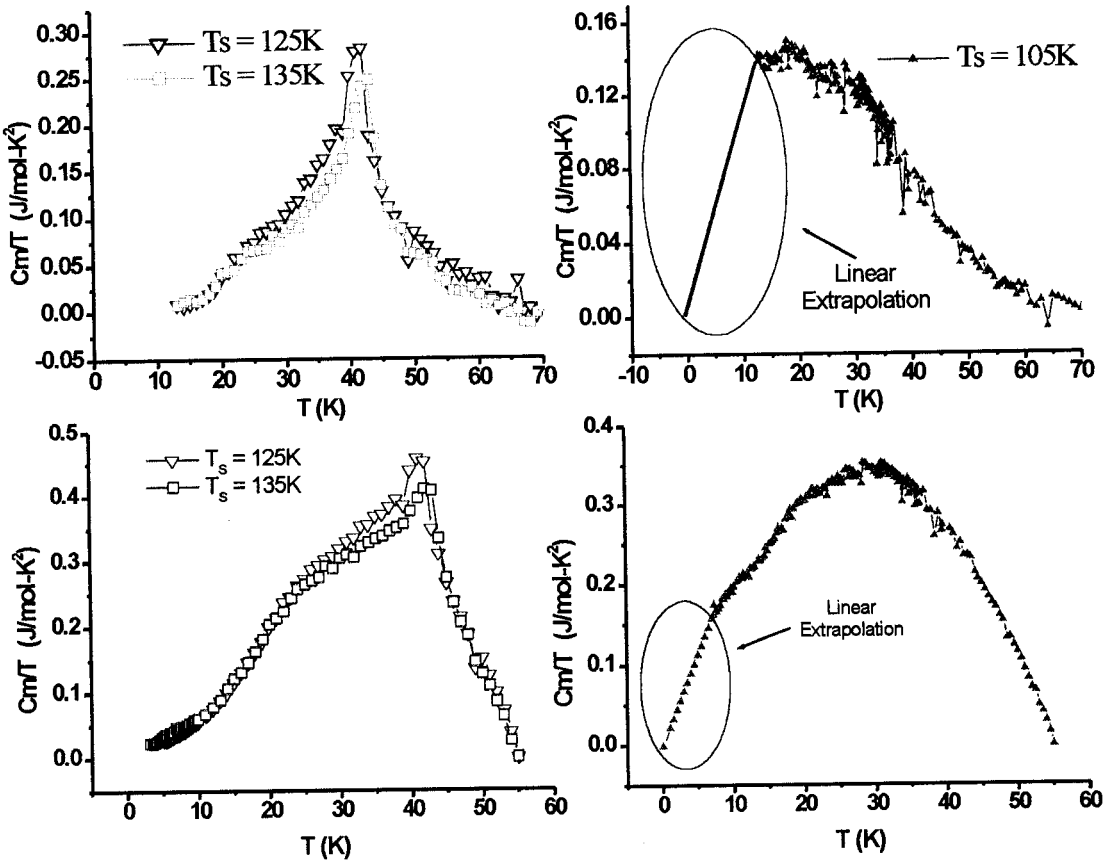


Figure 3.15: Estimates of the magnetic contribution to the heat capacity for the $T_S$ = 105K, 125K and 135K samples of $BaV_{10}O_{15}$. The top figures show the removal of magnetic entropy at low temperature with $BaV_3Ti_7O_{15}$ as the lattice standard. For the bottom figures, the simulated $T^3$ data was used as the lattice standard.

The data below 11K were fitted to equation (3.6.2):

$$C_m = \gamma T + \beta T^3, \qquad (3.6.2)$$

where $\gamma$ is related to the electronic component, and $\beta$ to the lattice component of the heat capacity. When the heat capacity data are plotted as $C_m/T$ versus $T^2$, the $\gamma$ and $\beta$ coefficients can be extracted (bottom plot in figure 3.14). The $\beta$ coefficients range from 7.4(2)E-4 to 1.03(4)E-3 J/molK$^4$. The linear contribution can arise from the spin glassy component of the sample.(Mydosh 1993)

Table 3.11: Heat capacity results for various preparations of $BaV_{10}O_{15}$

| $T_s$ (K) | $T_c$ (K) | $\Delta S^A$* (J/molK) | $\Delta S^B$ (J/molK) | $\Delta S^C$ (J/molK) | $\gamma$ (J/molK$^2$) | $\beta$ (J/molK$^4$) |
|---|---|---|---|---|---|---|
| 135 | 43 | 4.02 | 10.6 | 53.7 | 0.0280(1) | 7.4(2)E-4 |
| 125 | 42 | 4.73 | 11.1 | 54.4 | 0.0185(5) | 8.06(7)E-4 |
| 105 | - | 5.06 | 12.3 | 55.8 | 0.133(3) | 1.03(4)E-3 |

$\Delta S^A$ = linear extrapolation to zero kelvin from 13K with $BaV_3Ti_7O_{15}$ data as lattice standard; $\Delta S^B$ = theoretical $T^3$ data as lattice standard, plus linear extrapolation to zero kelvin; $\Delta S^C$ = integrate over all available data *without* lattice subtraction; $T_C$ = maximum in $\lambda$-type peak which corresponds to long range magnetic ordering
*the expected value is 96.12 J/mol-K

The data suggest that the $T_S$ = 105K sample has a much larger $\gamma$, and thus spin glass contribution, than the other two samples. We may therefore summarize the results as showing that magnetic ordering in $BaV_{10}O_{15}$ is a combination of spin glassy and long range ordering, and that the fraction of each component can vary. The sample in which the structural transition temperature is 105K has a larger fraction of the spin glassy component than the samples with a larger structural transition temperature.

## 3.7 Muon Spin Relaxation

Muon spin relaxation ($\mu$SR) measurements were performed at the TRIUMF facility in Vancouver using the M20 surface $\mu^+$ beamline. Data were collected over a temperature range of 3.85K to 152K in zero field (ZF) on the $T_S$ = 105K sample, and are presented in figure 3.16. Between temperatures of 152K and 48.3K there is no change in the relaxation behavior. Over this temperature range the relaxation data are fit well by a

Gaussian Kubo-Toyabe type function in which the distribution of local fields ($\Delta$) is small and temperature-independent. This is consistent with paramagnet behavior.

The 30.2K data exhibit a two component relaxation, showing that there are quasi-static moments, but the minimum (visible at 3.85K and 10.2K) isn't visible. This is evidence for partial freezing, and coincides with the maximum in the out-of-phase component of the AC susceptibility (section 3.5.2). The data have been fit with a Gaussian Kubo-Toyabe type function with fluctuations, evidenced by a rapid drop in the asymmetry followed by a 1/3 recovery. This behavior is typically found in dense, spin glassy materials.(Noakes and Kalvius 1997) It may also be encountered for samples in which several muon sites are available (resulting in a broadened distribution function). The form of the muon spin relaxation spectra resulting from multiple muon sites is slightly different from that of spin glasses, so the distinction between these possibilities is made on the basis of which has a better fit to the data. For the $T_S$ = 105K sample of $BaV_{10}O_{15}$, the spin glass model provides a better fit.

At longer times, the 30.2K, 10.2K and 3.85K data are equivalent. The presence of long range magnetic order results in muon spin precession for zero field conditions. This should result in oscillations in the asymmetry that are not apparent in the data. However, the long range ordering described in section 3.8 represents too small a fraction of the sample to have this effect on the data. The majority of the sample rather has a spin glass-like behavior.

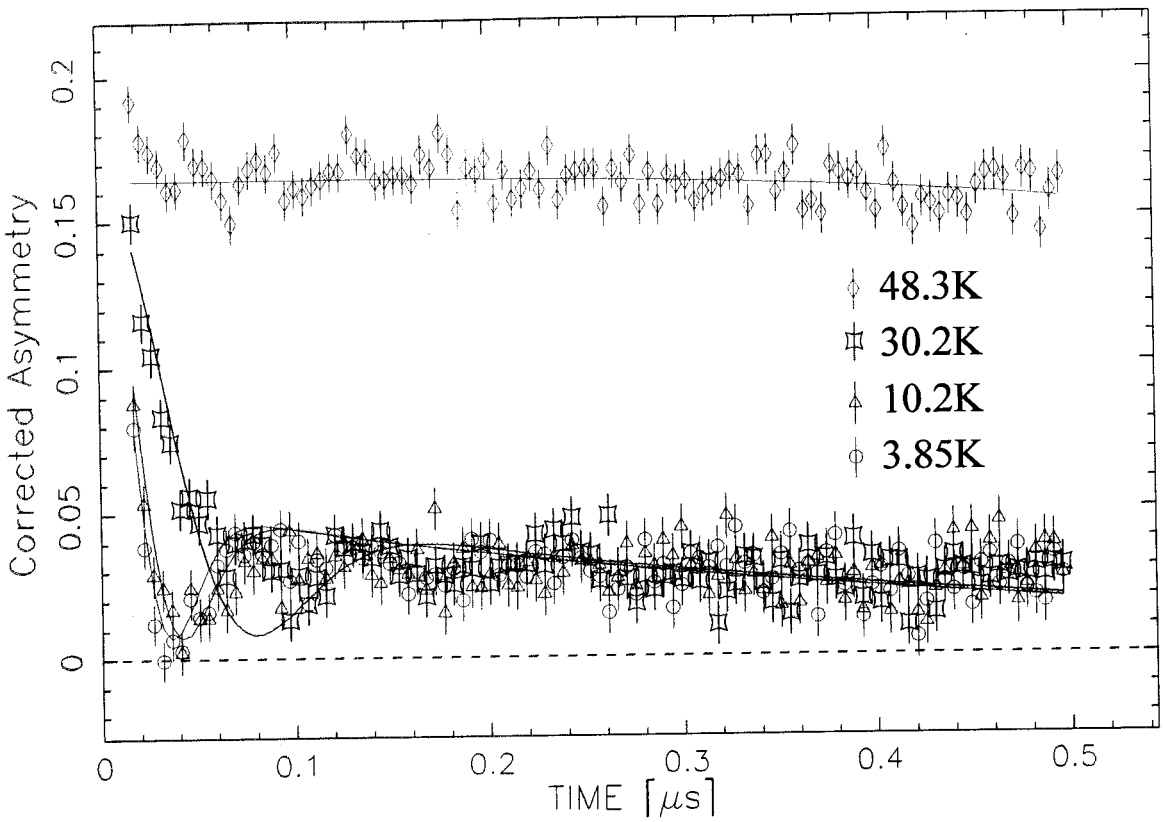


Figure 3.16: Muon spin relaxation spectra for the $T_S$ = 105K sample of $BaV_{10}O_{15}$. The first 0.5μs are shown from 3.85 to 48.3K. Two data sets were collected at 90.8K and 152K, but are not shown as they are identical to the 48.3K data set.

## 3.8 Powder Neutron Diffraction

### 3.8.1 Long-Range Magnetic Order

Powder neutron diffraction patterns were collected on the D20 diffractometer with λ = 2.4199Å at the ILL in Grenoble. The instrument is situated close to the reactor core, and is optimized for high flux measurements. The use of D20 was necessary to obtain good intensity statistics for the magnetic peaks, which are extremely weak. These peaks are on the order of 1% and less of the most intense peaks in the $BaV_{10}O_{15}$ pattern. Three different samples have been examined, corresponding to structural transition

temperatures ($T_S$) of 105, 125, and 135K. Results for the $T_S$ = 125 and 135K samples will be presented before the 105K sample. The powder neutron diffraction pattern for the 125K sample is shown in figure 3.17. The crosses represent data points, the line through these points is the calculated pattern, and the difference between the calculated and observed is shown at the bottom. High resolution neutron diffraction data will often provide significantly improved estimates of atomic positions and displacement parameters over X-ray diffraction results; this is due largely to the stronger scattering in neutron diffraction at high angles. However, due the poor resolution of this instrument, the calculated pattern cannot be significantly distinguished from the low-temperature single crystal X-ray refinement. The vanadium positions were taken directly from the single crystal X-ray results (and were not refined), due to the extremely weak scattering of neutrons by vanadium.

There are at least seven magnetic reflections, with the possibility of ten additional weak peaks. The weakest peaks are close to 0.05% intensity relative to the strongest peak in the pattern, which makes conclusive identification difficult. Figure 3.18 shows the evolution of the stronger magnetic reflections, along with their associated Miller indices, over a temperature range of 4K to 67K. The magnetic peaks can be indexed by doubling the *a* axis length, requiring a lattice translation vector (**k**)[5] of (1/2, 0, 0). The (110) (15.2°) and (121)[6] (32.4°) peaks were integrated at each temperature, and a plot of this intensity versus temperature shows that the transition occurs between 39 and 43K. This corresponds closely with the λ-shaped peak in the heat capacity, which has a

[5] this is also referred to as the propagation vector

maximum at a temperature of 42K. Attempts were made to extract a critical exponent from the intensity versus temperature data, however the data were not of sufficient quality close to the transition for this analysis to be valid.(Gronvold 1976; Collins 1989)

The magnetic ordering in the $T_S$ = 135K sample is nearly identical to that of the 125K sample, with peaks disappearing between 40.5 and 46.5K. Figure 3.19 illustrates the temperature dependent neutron diffraction patterns for the $T_S$ = 135K sample. The appropriate lattice translation vector is again (1/2, 0, 0). However, due to a smaller mass of sample the signal-to-noise ratio is lower than for the 125K sample, and therefore the weakest peaks are not observed. The major difference in the long range magnetic ordering between these two samples is the presence of the (010) magnetic reflection in the 135K sample.

The $T_S$ = 105K sample is shown in figure 3.20. This sample is qualitatively quite different from those previously described. First, there are only three magnetic peaks that can be distinguished from the noise level. These are the (010), (011), and (111) reflections. Of these, the (010) reflection has been observed in the $T_S$ = 135K sample, but not the 125K sample. The other two magnetic reflections, the (011) and (111), are unique to this sample, and both have structural contributions that are visible in the 80K and 160K diffraction patterns.[7] Second, all of the peaks can be indexed on the chemical cell. The (011) peak should be systematically absent due to the *b* glide perpendicular to the *a* axis in Pbca. This reflection should also be absent in the higher symmetry, room temperature Cmca structure. Therefore, the presence of this peak in the 160K powder

---

[6] The Miller indices given here - (110) and (121) - are defined relative to the doubled chemical unit cell.

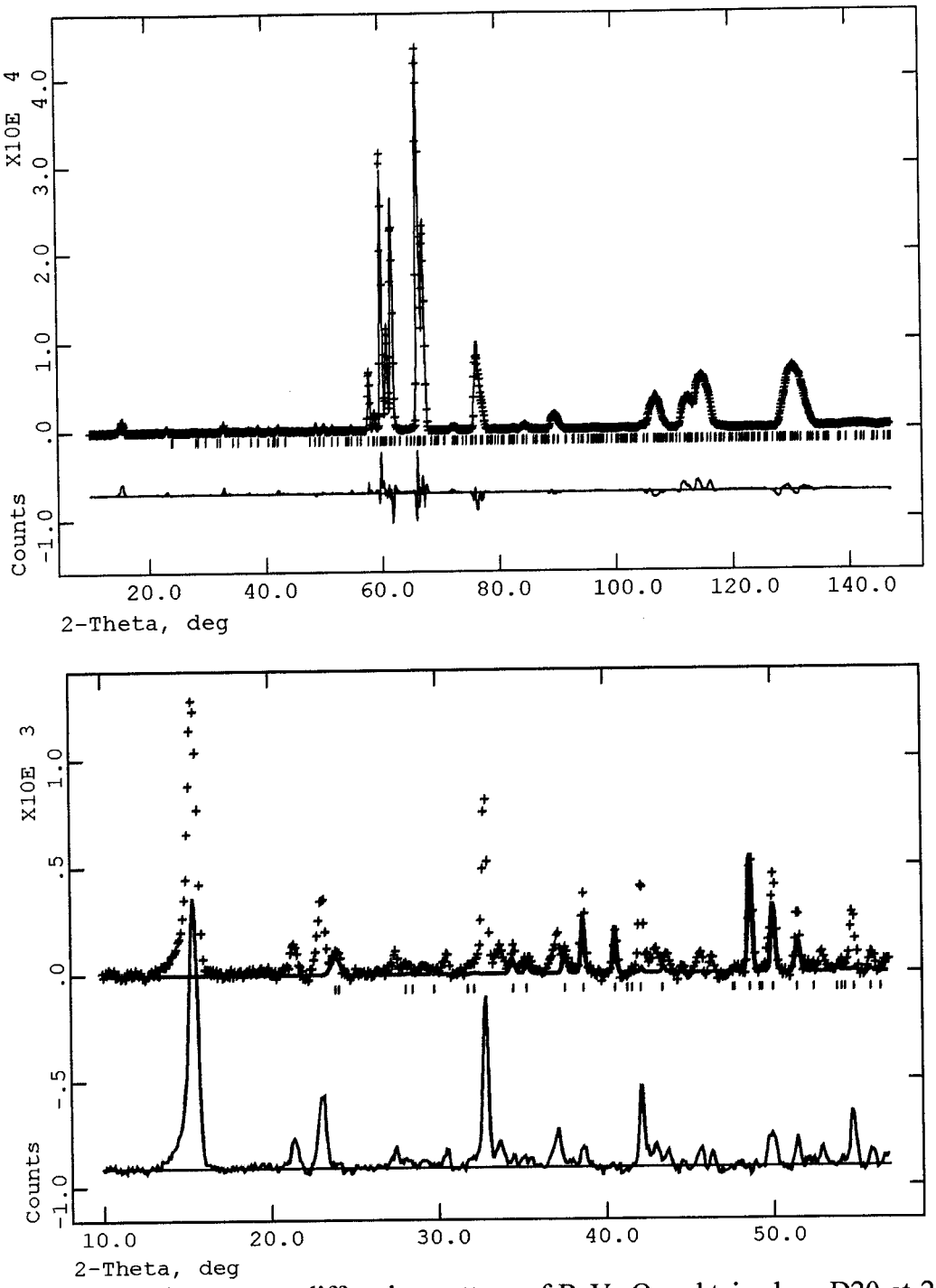


Figure 3.17: Powder neutron diffraction pattern of $BaV_{10}O_{15}$ obtained on D20 at 2K for the $T_S$ = 125K sample. Reflection markers refer to the chemical cell. In the lower figure, the difference pattern at the bottom of the figure represents the pattern due to magnetic long-range ordering.

[7] The structural contribution to the (111) reflection is visible in all $BaV_{10}O_{15}$ samples.

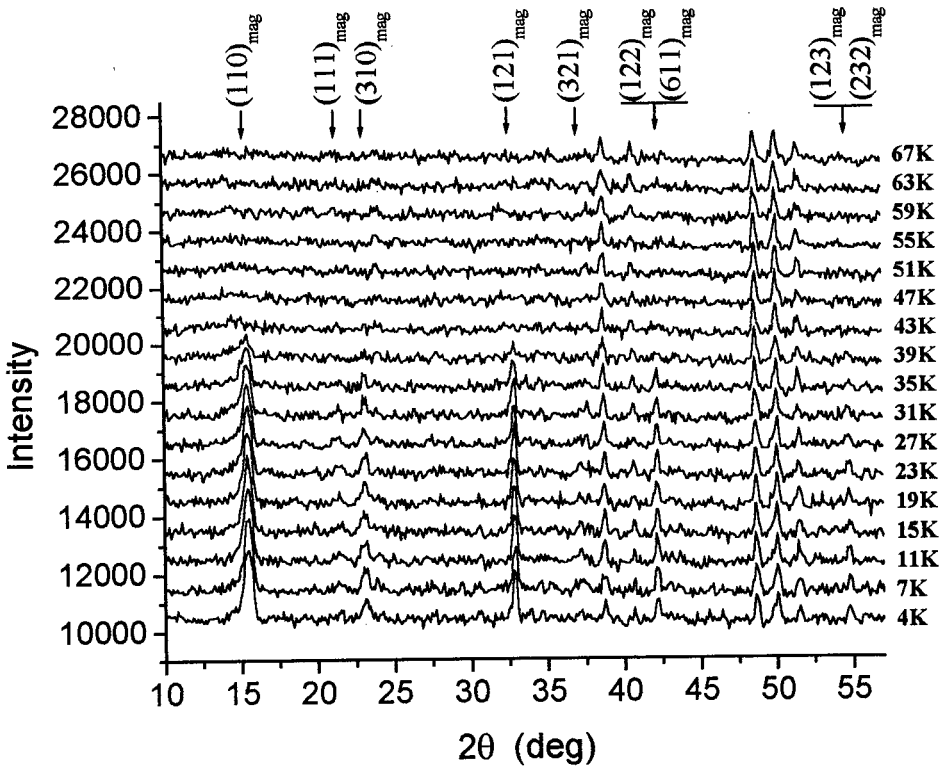


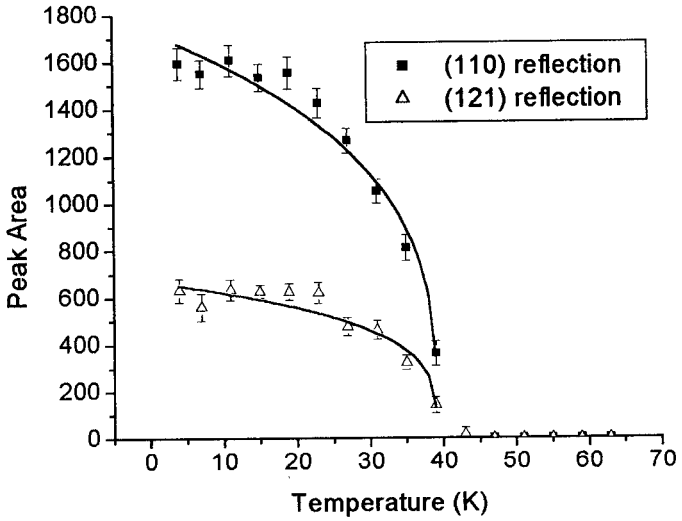


Figure 3.18: Top: Powder neutron diffraction pattern of $BaV_{10}O_{15}$ versus temperature for the $T_S$ = 125K sample. Two of the higher angle peaks cannot be indexed unambiguously in the absence of a magnetic structural model. Bottom: The variation in peak intensity versus temperature for the (110) and (121) reflections. The lines are guides to the eye.

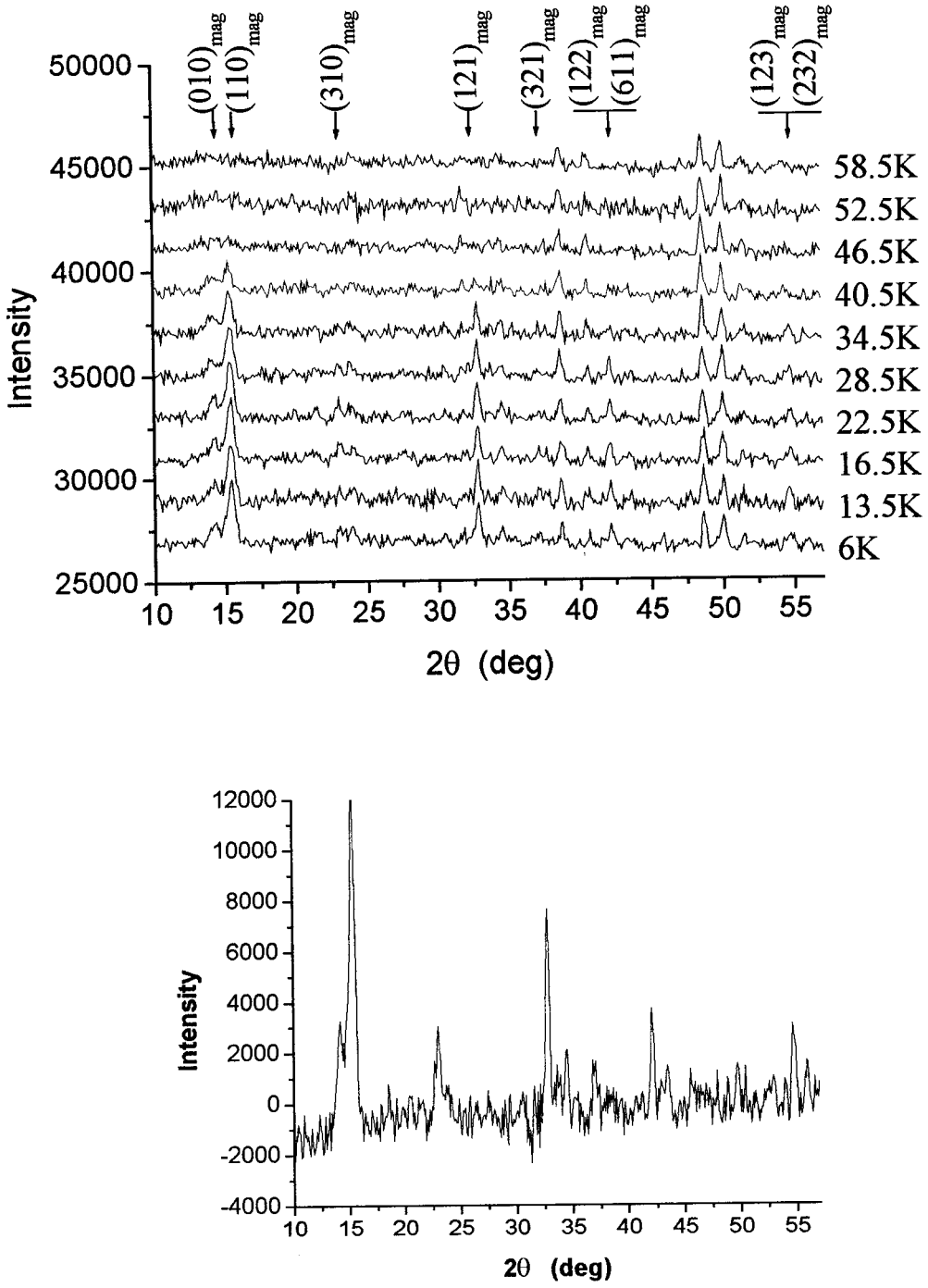


Figure 3.19: Top: Powder neutron diffraction pattern of $BaV_{10}O_{15}$ versus temperature for the $T_S$ = 135K sample. Two of the higher angle peaks cannot be indexed unambiguously in the absence of a magnetic structural model. Bottom: Difference pattern (2K-100K dataset) corresponding to magnetic long range ordering in the $T_S$ = 135K sample.

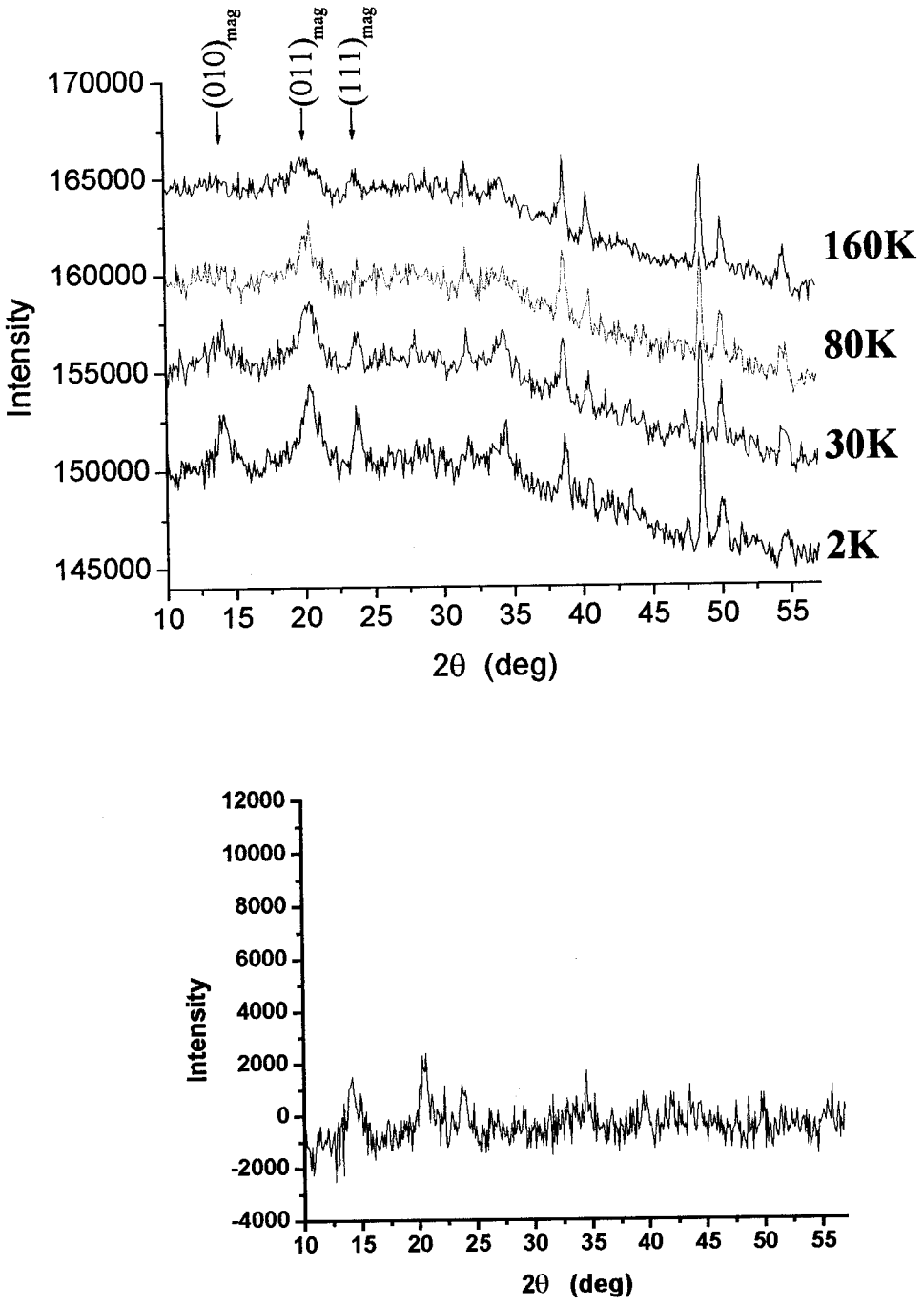


Figure 3.20: Top: Powder neutron diffraction pattern of $BaV_{10}O_{15}$ versus temperature for the $T_S$ = 105K sample. Bottom: Difference pattern (2K-160K dataset) corresponding to magnetic long-range ordering in the $T_S$ = 105K sample. The intensity has been scaled to be identical with the difference pattern for the $T_S$ = 135K sample.

pattern shows that its appearance is not related to the structural phase transition at 105K. There is no evidence in the room temperature X-ray powder diffraction pattern of this sample for impurities or for reflections that violate the Cmca space group symmetry. X-ray diffraction is sensitive to shifts in the vanadium or barium positions, whereas neutron diffraction is insensitive to the vanadium atoms. In summary, the (011) structural peak is a result of small distortions of the oxygen sublattice. Due to the poor resolution of this instrument, as well as the large wavelength used for this experiment, this distortion has not been refined.

The long-range magnetic order appears between 30K and 60K in the $T_S$ = 105K sample. These peaks are extremely weak, which may explain why a λ-type peak is not observed in the heat capacity results for this sample. The transition temperature may be estimated from the divergence temperature in the DC magnetic susceptibility, as 42K.

Magnetic peak intensities for each sample have been extracted by integrating over each peak after subtracting the background. This information, as well as the intensities normalized to the integrated intensity of the (222) structural reflection (chosen as there are no overlapping reflections at that peak position), is presented in table 3.12. A comparison of the relative peak intensities for the $T_S$ = 125K and 135K samples shows that the ordering is nearly identical, with the exception of the $(010)_{MAG}$ reflection in the $T_S$ = 135K sample. The sum of the integrated, normalized magnetic intensity for each sample is also presented. This indicates that the moment is reduced in the $T_S$ = 135K sample relative to the $T_S$ = 125K sample. Though the magnetic structure must be

significantly different in the $T_S$ = 105K sample, the total magnetic intensity (3.27) implies that the moment is smallest in this sample.

Table 3.12: A comparison of magnetic peak intensities for various samples of $BaV_{10}O_{15}$

| | $T_S$ = 135K sample | | $T_S$ = 125K sample | | $T_S$ = 105K sample | |
|---|---|---|---|---|---|---|
| (hkl) Reflection | I | $I_{MAG}/I_{(222)}$ | I | $I_{MAG}/I_{(222)}$ | I | $I_{MAG}/I_{(222)}$ |
| $*(010)_{MAG}$ | 230 | 0.82 | - | - | 310 | 1.51 |
| $(110)_{MAG}$ | 1004 | 3.59 | 1005 | 6.28 | - | - |
| $*(011)_{MAG}$ | - | - | - | - | 250 | 1.22 |
| $*(111)_{MAG}$ | - | - | 70 | 0.44 | 110 | 0.54 |
| $(310)_{MAG}$ | 220 | 0.79 | 235 | 1.46 | - | - |
| $(121)_{MAG}$ | 335 | 1.20 | 335 | 2.09 | - | - |
| $(321)_{MAG}$ | 100 | 0.36 | 105 | 0.66 | - | - |
| $(122)/(611)_{MAG}$ | 156 | 0.56 | 135 | 0.84 | - | - |
| $(123)/(232)_{MAG}$ | 129 | 0.46 | 115 | 0.72 | - | - |
| Total | - | 7.78 | - | 12.49 | - | 3.27 |
| $(222)_{STRUC}$ | 280 | 1 | 160 | 1 | 205 | 1 |

*Note: indexing of the 105K sample is based on the chemical cell (which is equivalent to the magnetic cell), while for the 135K and 125K samples, the magnetic cell (doubled *a* axis) is used. I = intensity in arbitrary units; $I_{MAG}/I_{(222)}$ = ratio of the intensity of the magnetic reflection to the (222) structural reflection.

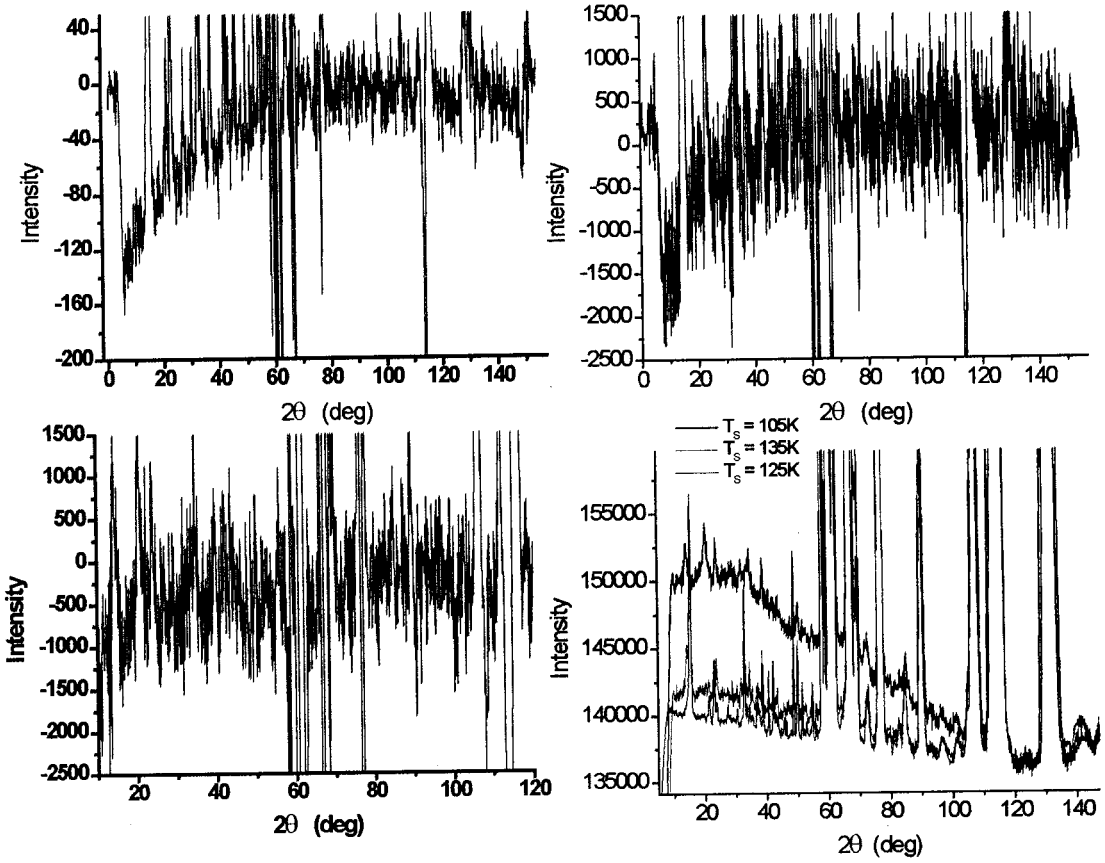


Figure 3.21: Paramagnetic background above the transition to magnetic long range order for $BaV_{10}O_{15}$. Top Left: Difference powder neutron diffraction pattern for the $T_S$ = 125K sample (2K-100K dataset). Top Right: Difference powder neutron diffraction pattern for the $T_S$ = 135K sample (2K-100K dataset). Bottom Left: Difference powder neutron diffraction pattern for the $T_S$ = 105K sample (2K-160K dataset). Bottom Right: Powder neutron diffraction patterns for the $T_S$ = 105K, 125K and 135K samples at 2K.

### 3.8.2 Background Analysis

The background of the $T_S$ = 105K sample diverges below ~120° from the other two samples, and increases significantly more. This is true at all temperatures, indicating that this is not a magnetic feature. This suggests the possibility that a fraction of the sample is amorphous, or disordered. The presence of this background is made clearer by the comparison with other samples at 2K shown in figure 3.21.

The background was carefully examined in all samples for the presence of short-range order, typically identified as a broad, temperature-dependent asymmetric peak. No conclusive evidence was found for short-range order in any sample. However, in all samples a paramagnetic contribution to the background is seen above the long-range magnetic ordering temperature. This is most clear for the $T_S$ = 125K and 135K samples, seen in figure 3.21, but is also present in the 105K sample.

### 3.8.3 Representational Analysis

For cases in which only a small number of magnetic ions are present in the unit cell, the magnetic structure is typically solved by a trial and error method.(Rossat-Mignod 1987) The $T_S$ = 125K and 135K samples require **k** = (1/2, 0, 0), which results in a magnetic unit cell containing 80 magnetic vanadium ions. The use of group theory to limit the number of possible solutions is essential, though it remains unlikely that a unique solution can be found for such a complicated magnetic cell. The group theoretical calculations are referred to as representational analysis (RA).(Bertaut 1968; Bertaut 1981)

The program SARAh* has been used to calculate the irreducible representations and associated basis vectors for $BaV_{10}O_{15}$.(Wills 2000) The initial conditions used for the calculation include the translation vector **k** = (1/2, 0, 0), the paramagnetic space group Pbca, and the five crystallographically independent vanadium ions present in the asymmetric unit of the nuclear cell. The magnetic $V^{2+}/V^{3+}$ ions are on general positions,

* SARAh stands for simulated annealing (SA) and representational analysis (RA)

which have a multiplicity of 8 in Pbca. The ions are assumed to be randomly distributed on these sites, as discussed in section 3.3.2, such that an average magnetic moment may be refined. The decomposition of the magnetic representation for each vanadium ion is identical (as they are all on the same Wykoff position), and is given by

$$\Gamma_{Mag} = 6\Gamma_1^2 + 6\Gamma_2^2, \qquad (3.8.1)$$

where the representation $\Gamma_{Mag}$ is described by six occurrences of irreducible representation one ($\Gamma_1^2$), and the same number of $\Gamma_2^2$. The superscript indicates the order of the irreducible representation, which is two (two-dimensional) in this case. However, these have been further split into twelve one-dimensional basis vectors ($\psi_i$). These are given in appendix B, where the first twelve basis vectors correspond to $\Gamma_1^2$, and the last twelve to $\Gamma_2^2$. The irreducible representations differ only in that the moment direction is reversed in the last four atoms.

There are two groups of basis vectors within each irreducible representation. Basis vectors 1-3 and 10-12 describe the moment for atoms 1, 3, 5 and 7 (group A), and basis vectors 4-9 describe the moment for 2, 4, 6 and 8 (group B). There are a number of rules which can further simplify the assignment of basis vectors to individual atoms for a given vanadium site. First, an appropriate model for the magnetic structure requires that at least one basis vector be assigned to each atom, so the model must include at least one basis vector from each group (A and B). Second, the same basis vector cannot be used more than once. Third, basis vectors that both define the same component for the same atom, such as basis vectors 1 and 10, cannot be used simultaneously. Fourth, we shall

assume here that the symmetry breaking associated with the transition to magnetic long-range order is second-order. If so, then according to Landau theory only one of the irreducible representations will become critical at the transition.(Rossat-Mignod 1987)

Due to the third rule, no more than 6 basis vectors can be used for a single vanadium site. The total number of allowed combinations when choosing from 2 to 6 basis vectors, and from a total of 12 basis vectors per irreducible representation, is shown in table 3.13. The calculations for the total number of allowed combinations are explained in detail in appendix B. The table clearly reveals the extent of this problem. Any linear combination of these basis vectors is a possible solution, and thus the solution is not restricted by this theory to a simple structure.

Table 3.13: The total number of allowed combinations of basis functions for one irreducible representation of the space group Pbca with **k** = (1/2, 0, 0)

| $n$ | 2 | 3 | 4 | 5 | 6 |
|---|---|---|---|---|---|
| $t_{BV}$ | 36 | 144 | 240 | 192 | 64 |

$n$ = number of basis vectors per vanadium site;
$t_{BV}$ = total number of allowed basis vector combinations

It is labor intensive to test all of these possibilities, and at the time of writing no model has been found that can account for all of the observed intensity. Rietveld refinement of the magnetic structure was carried out with the program GSAS (General Structure Analysis System) (Larson and Dreele 1994) for magnetic structure factor calculation, and the program SARAh (Wills 2000) for selection of the basis vectors. For refinement, a further assumption was that the same basis vectors be used for each vanadium atom. The mixing coefficients were optimized using a reverse-Monte Carlo

(RMC) algorithm until a global minimum in the $\chi^2$ parameter was reached.(Wills 2001) In addition, the magnetic moment was refined using three least-squares cycles for each RMC cycle. Initially, the crystal structure was refined in order to provide a calibration for the magnetic moment. However, all variables other than the magnetic moment were held constant during the refinement of the magnetic structure.

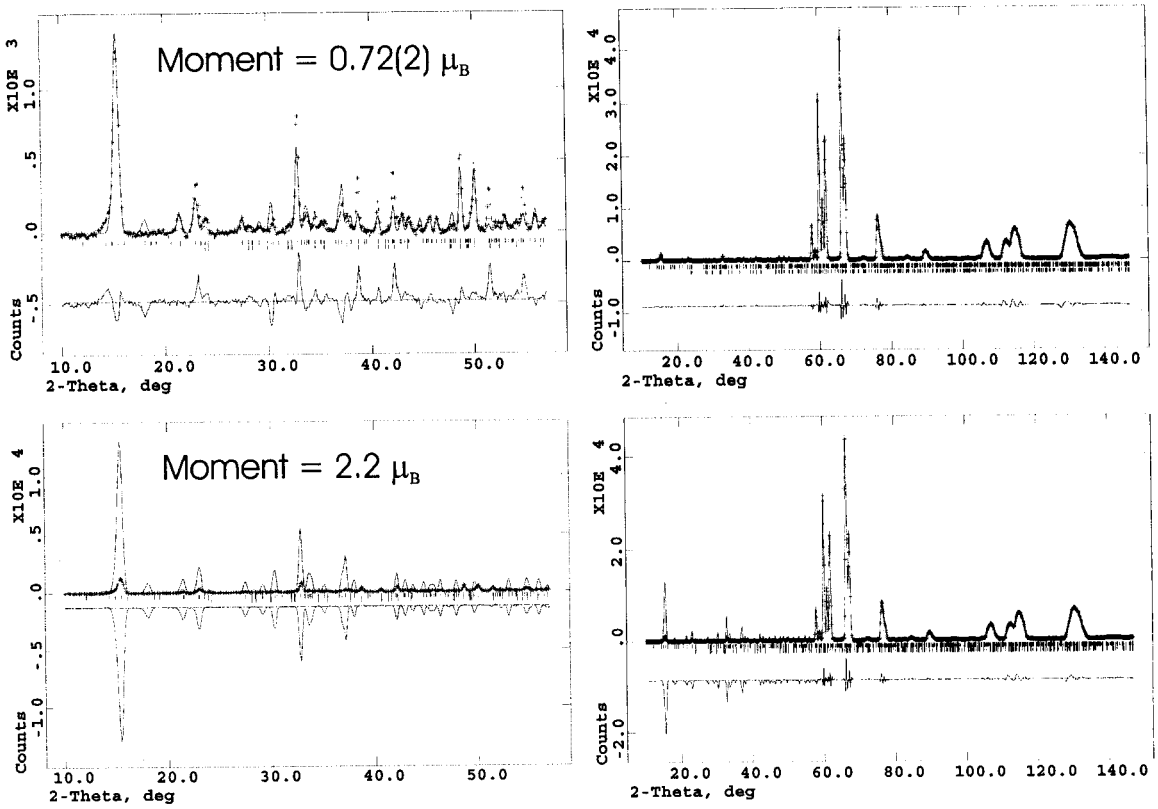


Figure 3.22: Estimate of the magnetic moment for the long range ordered fraction of the $T_S$ = 125K sample. The magnetic structural model is not quite correct, but is useful for illustrating that the moment is reduced from the expected value. Top: refined moment. Bottom: Moment is set at the expected value of 2.2$\mu_B$.

### 3.8.4 Estimated Magnetic Moment

The average maximum saturated moment for each site, based upon the 4:1 ratio of $V^{3+}$:$V^{2+}$, is expected to be 2.2$\mu_B$. One of the refinements from the last section for the $T_S$ = 125K sample is presented in figure 3.22. Though it is clearly not the correct structure, as not all of the magnetic peaks have been properly modeled, this is one of the best fits which has been achieved thus far. The moment on the vanadium site was refined to a value of 0.72(2)$\mu_B$. This is compared with profile of the expected moment in the lower figure for the same magnetic model. It is clear that the moment is reduced significantly from the expected value. An identical conclusion may be drawn for the $T_S$ = 135K sample, which has similar, though weaker, magnetic peaks to the $T_S$ = 125K sample. Due to uncertainty about the structural details, no attempt was made to refine the moment of the $T_S$ = 105K sample.

### 3.8.5 Absence of Structural Transition at the Magnetic Long Range Order Transition

The transition to magnetic long-range order occurs between ~39 and ~46K for all of the samples measured by powder neutron diffraction. To ensure that a structural transition is not associated with any of the weak, low angle peaks observed in the powder neutron diffraction experiment, it is useful to perform a powder x-ray diffraction experiment at low temperature. Due to the fact that the magnetic diffraction peaks found

in X-ray diffraction are a factor of about $10^{-4}$ to $10^{-8}$ smaller than the normal scattering[8], it can be assumed that any peaks observed are non-magnetic in origin.(Greedan 1994) Powder X-ray diffraction data have been collected at above (58K) and below (15K) the transition to magnetic long range order, and are presented in figure 3.23. Experiments were conducted at low temperature using a helium closed-cycle refrigerator in reflectivity mode, off the surface of a sintered $T_S$ = 135K pellet. There is no evidence to indicate that additional peaks are present at low angle in this sample. The angular regions for this experiment were chosen under the assumption that the weak peaks observed in the powder neutron diffraction experiment would occur at a similar position using X-ray diffraction, if such peaks could be attributed to a change in the crystal structure. Within the error limits of this experiment, these data suggest that the phase transition in the region of ~39K to ~45K is purely magnetic.

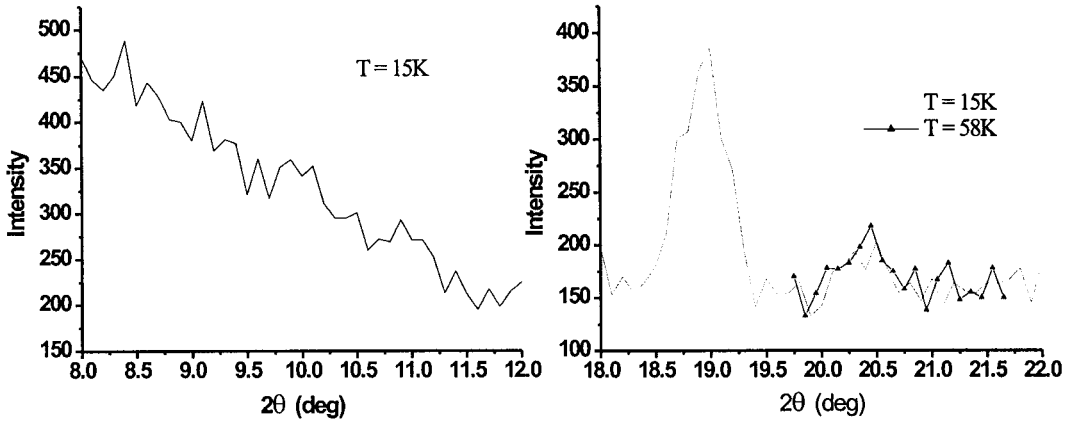


Figure 3.23: Low temperature powder X-ray diffraction on the $T_S$ = 135K sample. Left: Data collected between 8 and 12 degrees 2θ show no evidence for a peak. Right: Peaks observed at 18.4 and 20.5 degrees 2θ are both structural.

[8] this is true for a standard experiment, though a technique called resonant X-ray scattering may increase

## 3.9 Transport properties

### 3.9.1 DC resistivity measurements

DC resistance data were collected on an Oxford Instruments MagLab measurement system ($T_S$ = 105K sample) or Quantum Design PPMS ($T_S$ = 135K sample) over the available temperature range using a four-probe geometry. The samples were sintered at high temperatures in pellet form, and then were cut using a diamond-saw into the shape of a rod. Silver wire was attached using silver epoxy, and then left overnight to dry to ensure that the leads were firmly anchored on the sample. Data were not corrected for sample porosity, as this correction is expected to be negligible for well sintered pellets. It is furthermore assumed that any contribution from resistive grain boundaries is negligible, or if present, exhibits the same temperature dependence as the bulk resistance. These are not evaluated separately in this study, as AC impedance spectroscopy (AC-IS) is the only reliable way to separate the contributions from the grain boundaries and grain bulk.(Hong, Ford et al. 1997)

#### $T_S$ = 105K Sample at High Temperatures

The resistance varied over nearly six orders of magnitude for the $T_S$ = 105K sample, presented in figure 3.24. It was necessary to collect data over four separate regions, with currents of 0.08μA, 10μA, 50μA, and 200μA, to obtain good quality data over the entire temperature range. Data collection began at 35K, 65K, 115K, and 195K for the four ranges, with some overlap to facilitate data merging. At each of the initial

---

the intensity of magnetic scattering by as much as $10^4$

temperatures, a plot of resistance versus current was collected to check for ohmic response. The current required below 35K to achieve an ohmic response was too low to obtain useful data.

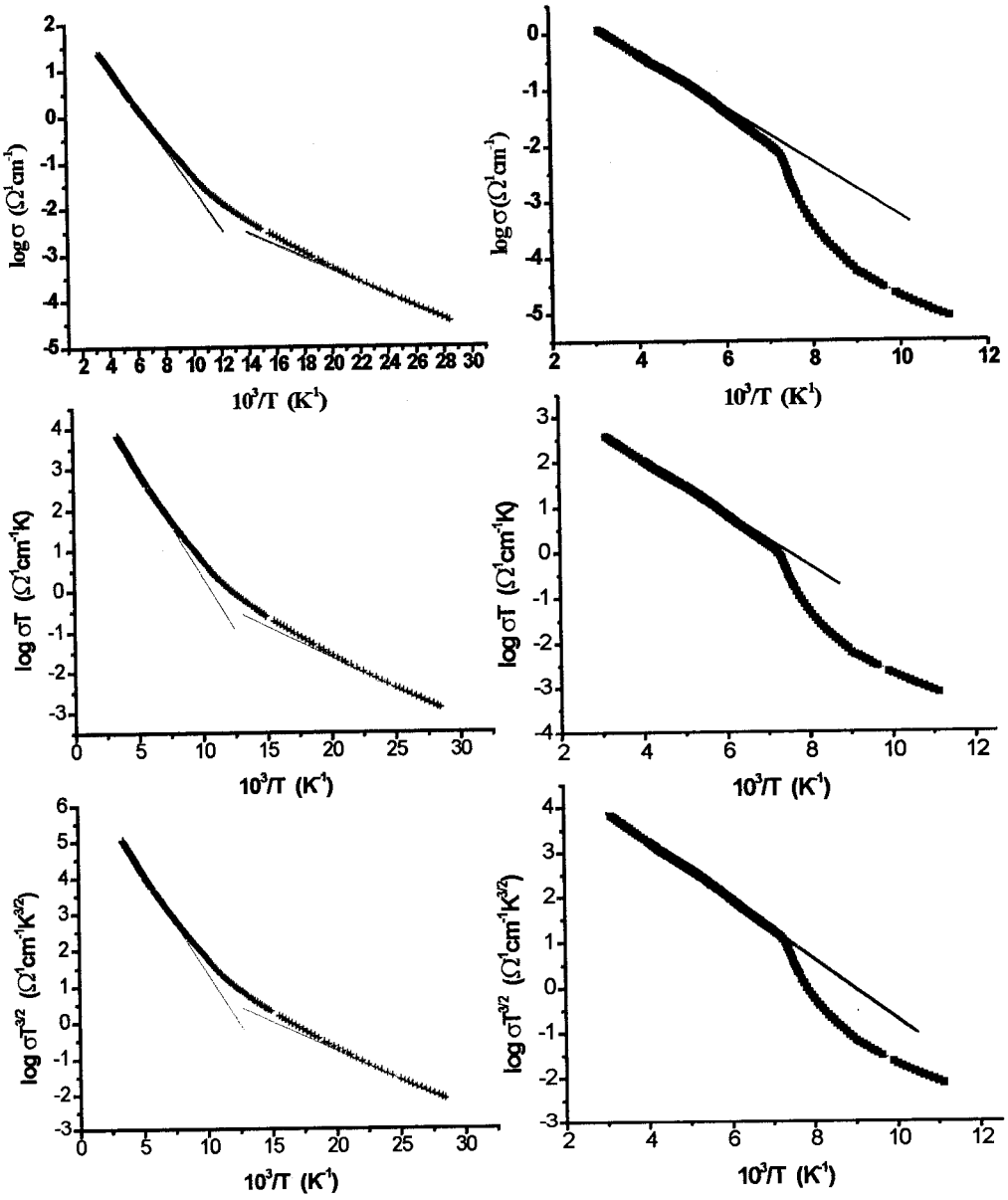


Figure 3.24: DC resistivity data for $BaV_{10}O_{15}$. Plots on the left are for the $T_S$ = 105K sample, and on the right for the $T_S$ = 135K sample. Top: Plotted according to the models for band or polaronic conduction. Middle: Holstein adiabatic hopping, Mott adiabatic hopping, and Mott nonadiabatic hopping. Bottom: Holstein nonadiabatic hopping.

A plot of $\log(\sigma)$ vs $T^{-1}$ (Arrhenius plot) yields two regions of linearity. This implies that over these linear regions the activation energy required for conduction ($E_\sigma$) is constant. As discussed in section 1.4.2, $E_\sigma$ may be due to a sum of contributions - the energy required to produce free carriers ($E_a$), and the polaron hopping energy (W). Measurements of the thermoelectric power can resolve these contributions, and will be discussed in the next section. The activation energy ($E_\sigma$) has been extracted by fitting to the Arrhenius equation (equation 1.4.3). The results, presented in table 3.14 suggest that the activation energy decreases from a value of 0.0886(2)eV at high temperature (180K to 290K), to 0.0266(2)eV low temperature (35K to 46K). The trend is consistent with the earlier report of 0.045 eV at high temperature and 0.016 eV at low temperature, though the magnitude is somewhat greater.(Liu and Greedan 1996)

Other expressions have been derived for the DC conductivity, based upon the assumption that the number of carriers is constant with temperature. These expressions are valid at high temperatures, and are discussed in section 1.4.5. One model for small polaronic hopping was derived by Mott for transition metal oxide glasses, in which the constant (W) corresponds to the hopping activation energy. Both the high and low temperature results listed in table 3.14, for the Arrhenius equation and the Mott equation, were fitted over the same temperature range. The high temperature range extends from 180K to 290K, and the low temperature range from 35K to 46K. At low temperatures ($T<\theta_D/4$) in the Mott model, the contribution from disorder to the hopping activation energy ($W_D$) is expected to dominate. In this case variable range hopping (VRH) is expected, and so the small polaron model used at higher temperature would no longer be

appropriate. We shall discuss VRH in more detail below; for the sake of comparison with the Arrhenius equation, the low temperature region has been fitted with the small polaron model. We can see in table 3.14 that the temperature dependence of the prefactor has little effect on the activation energies ($E_\sigma$ and W) derived from the conductivity data. Moreover, the fit to the data is of similar quality for both the Arrhenius and the Mott models, and thus the conductivity data alone cannot distinguish between these models. A plot which compares the data with the Holstein non-adiabatic model (a $T^{-3/2}$ factor included) has been added to provide a comparison with the other models; the quality of the fit is similar to the Mott and Arrhenius models. The constant part of the prefactor, which corresponds to the y-intercept obtained from each fit, is listed for each model in appendix C.

It is useful to differentiate between adiabatic and non-adiabatic hopping in the Mott model. The tunneling term in the non-adiabatic limit ($\exp(-2\alpha R)$) reduces to unity in the adiabatic case. Experimental evidence suggests that small polaron hopping is usually adiabatic.(Emin 1993) The decision for a particular compound requires knowledge of the optical phonon frequency ($\omega_o$), which is commonly estimated from infrared spectroscopy, and the effective dielectric constant ($\varepsilon_p$), obtained from Cole-Cole plots of the complex dielectric constants.(Ghosh 1991) In particular, a comparison between the optical phonon frequency and the characteristic hopping frequency (section 1.4.5.2) is useful.(Raffaelle, Anderson et al. 1991) Here we shall take the adiabatic limit, and estimate the characteristic hopping frequency using the derivation of Mott (equation 1.4.16). An estimate of the fraction of sites occupied by the polaron (C) is 0.2, taken as

the ratio of the $V^{2+}$ concentration to the total concentration of vanadium ions. The average site separation is given by the average of vanadium-vanadium distances listed in table 3.3, a value of 2.874Å. The hopping energy (W) is taken from the high temperature region. From these parameters a hopping frequency of $4.93(3)\times10^{13}s^{-1}$ is derived[9], which is comparable with values typically obtained for optical phonon frequencies in vanadate glasses ($\sim10^{13}$).(Ghosh 1991) It is clearly difficult to distinguish between adiabatic and non-adiabatic behavior with the available data, as this characteristic frequency is on the transition region separating the two behaviors.

Table 3.14: Estimates of conduction parameters from several different models of charge transport for the $T_S$ = 105K sample

| T | Arrhenius | Mott Polaron | Mott VRH | | ES VRH | |
|---|---|---|---|---|---|---|
| (K) | $E_\sigma$ (eV) | W (eV) | $T_{Mott}$-pre (K) | $T_{Mott}$ (K) | $T_{ES}$-pre (K) | $T_{ES}$ (K) |
| 180-290 | 0.0886 (2) | 0.1083 (2) | - | - | - | - |
| ~35-65 | 0.0266 (2) | 0.0300 (2) | 3.57 $(2)\times10^7$ | 4.63 $(2)\times10^7$ | 2.430 $(9)\times10^3$ | 1.002 $(4)\times10^4$ |

T = temperature range (the low temperature range varies slightly with the model being fitted); $E_\sigma$ = activation energy for conduction from the Arrhenius equation; W = activation energy for Mott model of polaronic hopping; $T_o$-pre/$T_o$ = characteristic temperature derived with/without a temperature dependent of the prefactor for the Mott and Efros-Shklovskii (ES) models of variable range hopping

### $T_S$ = 105K Sample at Low Temperatures

In semiconductors containing a significant level of atom scale disorder, conduction at low temperatures is often modeled by variable range hopping of charge

[9] The y-intercept of the fit (listed in appendix C) was used to calculate the phonon frequency.

carriers. There are two standard models for this behavior, Mott VRH and Efros-Shklovskii (ES) VRH. As discussed in section 1.4.4, the exact temperature dependence of the prefactor is disputed. The conductivity data have been evaluated with, and without a temperature dependent prefactor for both VRH models. It is significant that Mott VRH in one dimension will give a temperature dependence of $T^{-1/2}$, which is equivalent to the ES VRH model. Based upon the structure of $BaV_{10}O_{15}$, it is unlikely that 1D behavior need be considered. The results are given in table 3.14 and figure 3.25. A temperature region from 35K to 60K has been fitted in each case. It is difficult to distinguish between these models from the fit alone, as all are acceptable. The prefactor has a significant effect on the values extracted from the data, but not upon the quality of the fit.

To determine the appropriate model, whether $T^{-1/4}$ (Mott) or $T^{-1/2}$ (ES), it is necessary to first define the activation energy as the gradient of an Arrhenius plot, as shown in equation 3.9.1.(Hill 1976; Zabrodskii 1977)

$$\Delta E = -k\frac{d(\ln\sigma)}{d(1/T)} \quad (3.9.1)$$

Here $\Delta E$ is the activation energy[10], $\sigma$ is the conductivity and T is temperature. More details of this method are presented in appendix D. A plot of log($\Delta E$) against log (T) will give an exponent of -1/4, -1/2, or 1, though in practice the exponent can be intermediate between these values.(Zabrodskii 2001) The exponent determined from the $T_S$ = 105K sample is 0.46(1). The fit is shown in figure 3.26. The dashed line corresponds to Mott

[10] $\Delta E$ is also referred to as the local activation energy(Yakimov, Dvurechenskii et al. 1997), or reduced activation energy.(J.A.Reedijk, Martens et al. 1999)

VRH, and the solid line to ES VRH. A linear region is observed below ~65K, for which an exponent of $\sim T^{-1/2}$ is appropriate.

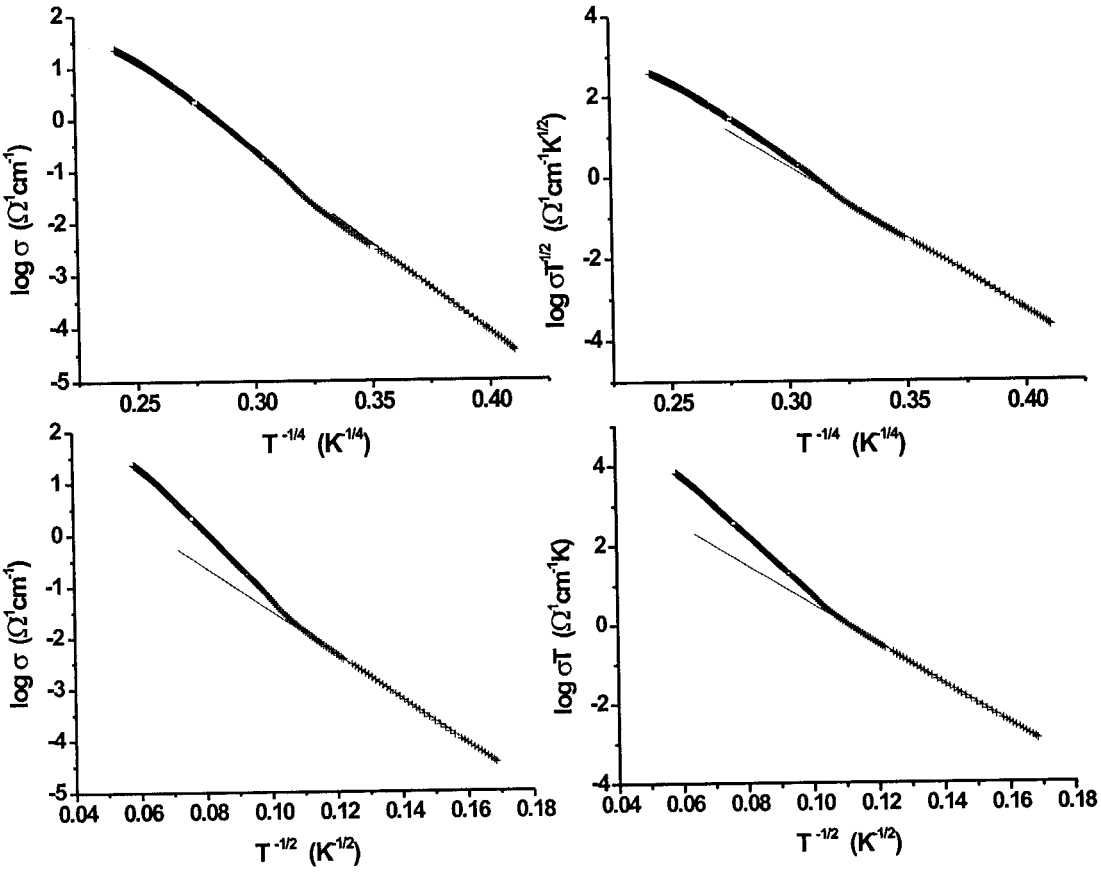


Figure 3.25: DC resistivity data for $BaV_{10}O_{15}$, $T_S$ = 105K sample. Top: Plotted according to the model for Mott variable range hopping. Bottom: Efros-Shklovskii variable range hopping. The figures on the right side consider the effect of a temperature dependent prefactor on the fitting results.

The values of $T_{ES}$ obtained from fits to the Efros-Shklovskii VRH model are in the range of $2\times10^3$ to $1\times10^4$, which is much higher than expected from the model. Values are typically vary from $10^0$ to $5\times10^2$K.(Rosenbaum 1991; Lisunov, Arushanov et al. 2000) In addition, the $T^{-1/2}$ behavior is usually found below ~10K, whereas the

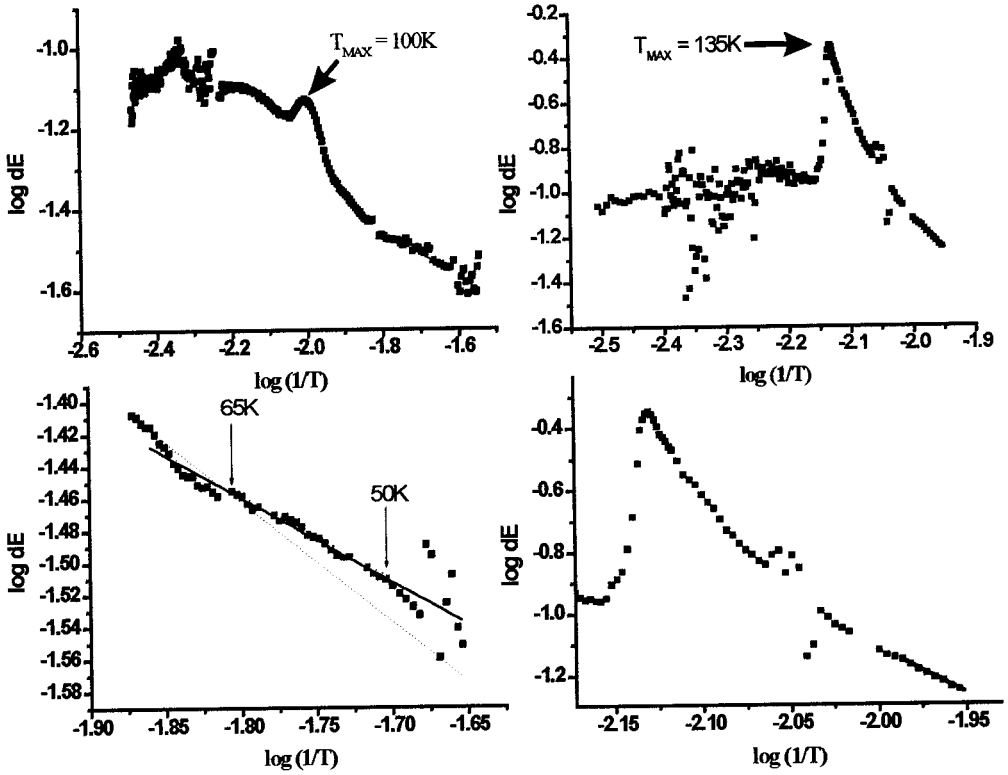


Figure 3.26: Hill analysis of DC resistivity data for $BaV_{10}O_{15}$. Plots on the left are for the $T_S$ = 105K sample, and on the right for the $T_S$ = 135K sample. Top: Plots of the local activation energy. Maxima which are labeled correspond closely to the structural phase transition temperature. The solid line in the bottom left plot is the fit, the dashed line corresponds to an exponent of -1/4.

linear region extends to 65K in $BaV_{10}O_{15}$ for the $T_S$ = 105K sample. The observation of a $T^{-1/2}$ law implies the presence of a soft Coulomb gap around the Fermi energy ($E_F$). It is expected that as the temperature is raised crossover from ES to Mott VRH hopping will occur as the width of the hopping energy becomes comparable to the Coulomb gap width.(Shlimak 2001) The large gap implied by the extension of $T^{-1/2}$ behavior up to higher temperature, and in particular the magnitude of $T_{ES}$, are anomalous; there is no clear precedent in the literature for this behavior. An unusually large Coulomb gap has

been proposed for the ferromagnetic, layered cobalt oxide $Sr_2Y_{0.5}Ca_{0.5}Co_2O_7$.(Yamaura, Young et al. 2001) In this case, however, $T_{ES}$ is still much lower (~300K) than observed in $BaV_{10}O_{15}$, and the $T^{-1/2}$ dependence is only found up to 30K. A crossover to $T^{-1/2}$ has been observed near 52K in amorphous $In_xO_y$ films, but $T_{ES}$ = 352K, which is significantly lower than observed here.(Rosenbaum 1991)

Though the results of the local activation energy plot suggest a $T^{-1/2}$ dependence, it is useful to consider the magnitude of $T_o$ found using the Mott VRH model ($T^{-1/4}$), which is on the order of $10^8$K. This is unrealistic for the Mott hopping model, for which values on the order of $10^5$ or less are expected.(Mott 1979) Small polaron conduction, via multiphonon-assisted hopping between deep states, has been proposed by Emin to exhibit a $T^{-1/4}$ dependence at low temperatures.(Emin 1974) The values for $T_o$ are predicted to be in the range $10^7$-$10^{10}$ in the model of Emin. This has been proposed as the mechanism of conduction in other transition metal oxides, such as $Fe(Nb_{1-x}W_x)O_4$ ($T_o \approx 2\times10^9$)(Schmidbauer 1998), and $Fe_3O_{4-x}F_x$ ($T_o \approx 10^8$)(Mott 1979).

## $T_S$ = 135K Sample at High Temperatures

As was the case for the $T_S$ = 105K sample, a number of different excitation currents were used to obtain high quality data over the entire measured temperature range (figure 3.24). As well, the lower limit of data collection was determined by the point at which the resistance became too large to obtain useful data.

The structural phase transition has a much more pronounced effect on the resistivity than observed for the $T_S$ = 105K sample. There is a sharp change in slope near

135K, which corresponds to a maximum in the local activation energy plot (figure 3.25). The activation energies suggested for band and Mott small polaron hopping in the high temperature region are slightly higher than observed for the $T_S$ = 105K sample. This may be interpreted in the band case as a larger band gap, and in the small polaron case as involving a higher activation energy for carrier creation or mobility. The conductivity data alone cannot distinguish between these possibilities, as noted above.

If the Mott model of small polaron hopping is assumed, an estimate of the characteristic hopping frequency may be derived from the high temperature data. If the adiabatic limit is assumed, a frequency of $2.93(3)\times10^{12}s^{-1}$ is obtained.[11] This suggests that this sample is closer to the non-adiabatic limit of small polaron hopping. One concern for this analysis is that the room temperature resistivity is nearly an order of magnitude higher for the $T_S$ = 135K sample than the $T_S$ = 105K sample. This difference could possibly be explained by a variation in grain boundary resistance, rather than in the bulk. In the absence of impedance spectroscopy data, it is necessary to assume that the grain boundary is similar in both samples, and thus the difference in room temperature resistance is a bulk effect. In this case, the lower hopping frequency can be interpreted as a lower carrier hopping rate in the $T_S$ = 135K sample.

### $T_S$ = 135K Sample at Low Temperatures

Data were collected down to 35K for the $T_S$ = 105K sample, and in the lowest temperature region a $T^{-1/2}$ temperature dependence was observed. To the minimum

temperature (90K) accessed for the $T_S$ = 135K sample, this behavior was not observed. A fit to the low temperature data using the analysis of Hill (equation 3.9.1) produced an exponent of ~-1.9 (fitted slope of -2.91(7)), which has no clear physical meaning. There is no clear model with which to perform a quantitative analysis of the low temperature data, though it is possible that at even lower temperatures, a $T^{-1/2}$ temperature dependence would again be found.

Table 3.15: Estimates of conduction parameters from the Arrhenius band and Mott small polaron models of charge transport for the $T_S$ = 135K sample

| T | Arrhenius | Mott Polaron |
|---|---|---|
| (K) | $E_\sigma$ (eV) | W (eV) |
| 250-320 | 0.0955 (5) | 0.1197 (4) |

T = temperature range; $E_\sigma$ = activation energy for conduction from the Arrhenius equation; W = activation energy for Mott model of polaronic hopping

A range of models have been explored. However, it is not possible from conductivity data alone to distinguish between these models. To provide further insight into the conduction mechanism in $BaV_{10}O_{15}$, it is necessary to examine the temperature dependence of the thermopower.

### 3.9.2 Thermoelectric measurements

Thermoelectric measurements have been performed on the $T_S$ = 105K sample, as well as two different $T_S$ = 135K samples, and are presented in figure 3.27. The error

[11] The same estimates of the average site separation and fraction of occupied sites were used to analyze these data as were used for the $T_S$ = 105K sample.

listed for the observed thermopower is the statistical uncertainty associated with the least-square fit of Seebeck voltage ($\Delta E_S$) versus temperature difference across the sample ($\Delta T$) data at each set temperature. The error given for the other quantities corresponds to the worst case bound in each case. Repeated measurements of a particular sample over the entire temperature range eventually resulted in an overall decrease in the magnitude of the thermopower; this was later followed by obvious cracking of the pellet. As the sample is under pressure while mounted in the instrument, cycling through the structural phase transition degrades, and eventually destroys the pellet. The data which are presented are from initial runs on a given sample.

There are four important results from these measurements:

(1) The thermopower is positive over all temperatures, indicating that conduction occurs primarily through holes.

(2) All samples approach a small, essentially temperature-independent thermopower at high temperatures.

(3) Below ~250K the thermopower increases rapidly with decreasing temperature.

(4) A change in slope occurs near the structural phase transition.

A constant thermoelectric response is observed between ~250K to 325K, and is expected to remain constant up to much higher temperatures. Two models will be used to discuss this behavior. The first involves fully localized carriers (small polarons). For small polaron hopping the number of carriers is constant with temperature (only the mobility is activated), and a $T^0$ temperature dependence results. The second model involves delocalized carriers (band conduction). The standard model of band conduction

# NOTE TO USERS

Page(s) not included in the original manuscript and are unavailable from the author or university. The manuscript was scanned as received.

165

This reproduction is the best copy available.

UMI®

C = 0.2. The expected thermoelectric power for C = 0.2 is -119μV/K, based upon Heikes formula. The contribution from the transport term to the thermopower, which typically takes values <10μV/K, has been assumed to be zero in this analysis, as is commonly done.(Goodenough 1970) Clearly, this cannot account for the observed thermopower at high temperatures, which ranges from 0.34(1) to 1.19(3)μV/K for various samples.

Chaikin and Beni developed models that consider spin degeneracy of charge carriers with negligible Coulomb interactions ($C_{kT>U}$), spin degeneracy with strong on-site repulsive Coulomb interactions ($C_{kT<U}$), and spin degeneracy in the presence of electron-electron attractive Coulomb interactions ($C_{kT<|-U|}$).(Chaikin and Beni 1976) These models have been fitted to the data, but none are found to be in accord with the expected result: C = 0.2. The estimated $V^{2+}$ concentration from these fits, and for each model, is given in table 3.16. Results of $C \approx 1$ imply that only the lower oxidation state is present (or that each site contains a polaron), and $C \approx 0.5$ suggests that $V^{2+}$ and $V^{3+}$ are present in equal numbers. Goodenough has used the concept of intermediate-size polarons ("molecular" clusters) to explain the thermopower behavior in $M_xV_2O_5$-β phases (Goodenough 1970), the vanadium spinels $A_{1-x}^{2+}Li_x[V_2]O_4$ and $Mg[B_x^{2+}V_{2-x}]O_4$ (A = Mg or Zn; B = Mg or Ni) (Goodenough 1970), and $Fe_3O_4$. In the case of $Fe_3O_4$, this model has been rejected by Mott on the basis that it violates one of the assumptions on which Heikes formula is based, namely the requirement of an infinite Hubbard Coulomb correlation ($U_0$).(Mott 1979) The basis for the rejection does not seem to apply to the vanadium spinels or $M_xV_2O_5$-β phases. Through the formation of clusters, characterized

Table 3.16: Analysis of the high temperature thermopower data with various models of polaronic conduction

| $T_S$ | $S_{obs}$ | $C_{Heikes}$ | $C_{kT>U}$ | $C_{kT<U}$ | $C_{kT<\|-U\|}$ | $P_{HW}$ | $P_{HS}$ | $P_{LW}$ | $P_{LS}$ |
|---|---|---|---|---|---|---|---|---|---|
| | μV/K | | | | | | | | |
| 105 | 1.19 (3) | 0.5035 (1) | 1.0069 (2) | 0.6697 (1) | 1.0138 (4) | 1.8091 (3) | 1.5104 (3) | 2.9319 (2) | 2.2526 (1) |
| 135 | 0.41 (3) | 0.5012 (1) | 1.0024 (2) | 0.6677 (1) | 1.0048 (4) | 1.8032 (3) | 1.5036 (3) | 2.9261 (2) | 2.2509 (1) |
| 135 | 0.34 (1) | 0.5010 (1) | 1.0020 (1) | 0.6675 (1) | 1.0040 (1) | 1.8026 (1) | 1.5030 (1) | 2.9256 (1) | 2.2507 (1) |

$S_{obs}$ = Seebeck coefficient observed at high temperature (data was obtained at ~300K); C = concentration of the lower valence state ($V^{2+}$) from analysis for a model with spinless (Heikes formula) carriers, carriers with spin, with spin and on-site repulsion, and with spin and on-site attraction of the charge carriers. A value for C of 0.2 is expected. P = average number of *d* electrons per site in the high temperature-weak limit (HW), high temperature-strong limit (HS), low temperature-weak limit (LW), and low temperature-strong limit (LS). A value for P of 2.2 is expected. Numbers in the brackets indicate statistical uncertainties given by the least-squares analysis for $S_{obs}$, and the worst-case bound for the calculated values.

by collective orbitals, it is proposed in these compounds that the number of sites available for polaron hopping is reduced. It would superficially seem that the number of available sites in $BaV_{10}O_{15}$ is 10. However, if the model of molecular polarons is applied, such that the number of sites is reduced to four and C = 0.5, the results would be compatible with the predictions of Heikes formula.

In the model of Marsh and Parris the variable of interest is the average number of *d* electrons per site (P), as discussed in section 1.4.6.5.(Marsh and Parris 1996) For $BaV_{10}O_{15}$, this is equal to 2.2 electrons per site. The results differ significantly from the expected value, although the low temperature, strong coupling limit provides a relatively close value of ~2.25 electrons per site. Use of the low temperature limit (kT<<U) is

justified, as a large Coulomb energy is not unexpected in narrow band, 3d transition metal oxides. However, the strong magnetic coupling limit corresponds to the complete removal of spin degeneracy (i.e. magnetic ordering); it is not valid at room temperature for this material. To a first approximation the models of Marsh and Parris, and those of Chaikin and Beni, cannot account for the observed temperature-independent thermopower. Perhaps by invoking the formation of molecular polarons, the data in the high temperature region can be accounted for quantitatively.

## Conduction within a Localized Band

As discussed above, the small polaron hopping model has great difficulty in explaining the small thermoelectric response of $BaV_{10}O_{15}$ at high temperature. In this section, a model based upon conduction within a localized band will be explored. The magnitude of the thermopower can be used in favorable cases to distinguish between itinerant (<40μV/K) and localized (>40μV/K) carriers at small doping levels for extrinsic conductors.(Zhou, Chan et al. 1993) For the case of intrinsic semiconductors, the situation is complicated by the significant levels of both hole and electron carriers. The total thermopower that results is expressed as the conductivity weighted sum of the two carriers:

$$S = \frac{-|S_e|\sigma_e + S_h\sigma_h}{\sigma_e + \sigma_h}, \qquad (3.9.2)$$

where $S_e$ and $S_h$ are the partial Seebeck coefficients and $\sigma_e$ and $\sigma_h$ are the partial conductivities of the electrons and holes respectively. For an intrinsic conductor in which

the mobilities of the electrons and holes are similar, the net thermopower is essentially zero and temperature-independent. This has been proposed for $NiS_{2-x}Se_x$ for $x \leq 0.44$, which exhibit a small, temperature-independent thermopower in low temperature regions where the resistivity is large. With increasing temperature, carriers are excited from the sulfur $(3p)\sigma^*$ states to the nickel $(3d)e_g^*$ band. As the mobility of holes (and therefore the conductivity) in the relatively broad $(3p)\sigma$ band is higher than the mobility of the $(3d)e_g^*$ electrons, the holes begin to dominate the total Seebeck coefficient. At higher temperatures, the density of holes increases sufficiently to cause a decrease in the thermopower. Therefore, a plot of $S$ versus $T$ should exhibit a broad maximum at intermediate temperatures, in addition to the temperature-independent behavior at low temperatures.(Spalek and Honig 1998)

The absence of this broad maximum for $BaV_{10}O_{15}$ thermoelectric data can be explained on the basis of the Zaanen-Sawatzky-Allen framework (section 1.4.3).[12] The *d* band is significantly removed from the oxygen 2p band in the case of vanadium oxide materials, and so excitations involve mainly *d-d* transitions in the temperature range examined. A simplified schematic diagram for the Hubbard sub-bands in the low temperature phase of pure $V_2O_3$ is shown in figure 3.28(A). This material should be an intrinsic semiconductor, as equal numbers of hole and electron carriers are created by excitation across the band gap.

This model is further complicated by the fact that a non-integral number of electrons per vanadium site are present; from standard Mott-Hubbard theory, $BaV_{10}O_{15}$

should be a metal as the *d* band is partially occupied. If $BaV_{10}O_{15}$ is treated simply as Ba-doped $V_2O_3$, the additional *d* electrons should occupy the lower edge of the upper Hubbard sub-band in figure 3.28(A). To account for the observed semiconducting behavior, it is reasonable to assume that the disordered occupation of the $V^{2+}/V^{3+}$ cations could create Anderson-type localization at the *d* band edges, inhibiting metallic conduction (figure 3.28(B)). At higher temperatures, conduction would be dominated by excitations to the delocalized region of the band. This would produce mainly *n*-type carriers, and a $T^{-1}$ temperature dependence of the thermopower, which is not observed. Therefore, for the band model to be successful in describing the experimental results, the band gap must occur at the Fermi level, such that equal numbers of electrons and holes are produced by carrier excitation.

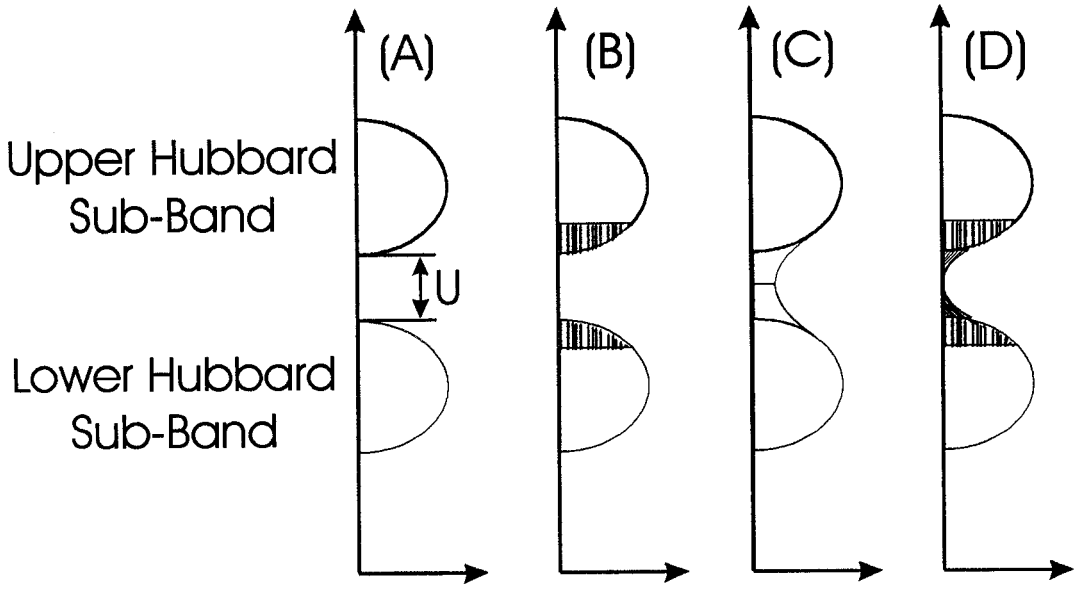


Figure 3.28: Various schematic diagrams for the density-of-states of a material in which large Hubbard U-type correlations are present between conduction electrons. Models A to D are described in the text.

[12] It is possible that at higher temperatures, the broad maximum would be observed in agreement with the results for $NiS_{2-x}Se_x$.

It is useful to compare the doping of $V_2O_3$ with chromium to the present case of barium doping. The simplest explanation for the behavior of $(V_{1-x}Cr_x)_2O_3$ is based upon the assumption that chromium exerts a negative pressure on the lattice. In doing so, an increase in chromium doping effectively decreases the orbital overlap between adjacent vanadium sites, and narrows the bandwidth to the point that the two Hubbard sub-bands split. This corresponds to a transition from figure 3.28(C) to 3.28(A), at a 3% (or higher) level of chromium doping. At high temperatures, the thermopower for chromium doped samples is small and positive. As the temperature is lowered the band gap increases rapidly, which in turn causes the thermopower to become large and positive. This is interpreted to indicate that the hole mobility becomes increasingly dominant over the electron mobility, as a result of the changes in the band structure with decreasing temperature.(Kuwamoto, Honig et al. 1980)

$BaV_{10}O_{15}$ is iso-electronic with 20% chromium doped $V_2O_3$. This is a much higher chromium doping level than has been discussed in the literature, with respect to the transport properties. In addition, the structure of $BaV_{10}O_{15}$ differs from that of $V_2O_3$ (corundum). Nevertheless, the qualitative behavior of the thermoelectric response for $BaV_{10}O_{15}$ is remarkably similar to that observed for chromium doping levels up to ~10%. The band structure may have the qualitative features shown in figure 3.28(D). A small band gap exists at the Fermi level at room temperature, with disorder localizing the band edges. This model will be expanded upon with respect to titanium doping effects in the next chapter.

## Variable Range Hopping at Low Temperatures

The possible existence of a Coulomb (soft) gap, as evidenced by a $T^{-1/2}$ dependence of the conductivity, was discussed in section 3.9.1. The rapid increase in thermopower with decreasing temperature near the structural phase transition could indicate that carriers are created by excitation across the Coulomb gap. In this model a non-Arrhenius temperature dependence of the conductivity is expected, as is observed below ~180K. The thermopower is predicted in the ES model to increase with decreasing temperature until $T<<T_c$, below which a constant, non-zero value is obtained.(Burns and Chaikin 1985) However, the presence of such a gap ($T^{-1/2}$ dependence) is not evident from the conductivity data near the structural transition, and effects associated with a soft gap are not likely to be felt at such high temperatures (~100K). The driving force for the structural phase transition is unlikely to be the formation of a Coulomb gap.

Due to the large resistance of $BaV_{10}O_{15}$ samples, the thermopower is extremely noisy below ~60K, and cannot be used to distinguish between the Mott VRH and ES VRH models in this temperature range. Therefore, the possibility of a Coulomb gap cannot be excluded at low temperatures.

## Thermopower near the Structural Phase Transition

It is interesting to note that a change in slope occurs in the thermopower near the structural phase transition. Exact determination of the inflection point from a plot of dS/dT is difficult from the available data, but is within 10K of the transition (figure 3.27).

The increase in the thermopower below ~250K indicates, as interpreted within the framework of the small polaron model, that the number of available charge carriers is decreasing (trapping out of mobile polaron holes). The rapid decrease in atomic displacement parameters below the transition (section 3.3.2.) could then be related to a decrease in the mobility of the polarons. Structurally, this would correspond to the removal of dynamic disorder below the transition. The change in slope would therefore be linked to the freezing out of mobile holes with a change in structure.

This could also be consistent with the band model if, as a result of changes in the band structure near the structural phase transition, the hole contribution to the thermopower is enhanced. The curvature of the Arrhenius plot below ~180K, discussed in the last section, indicates that the activation energy for conduction is changing with temperature. This is not expected for simple activation across a constant band gap. To be consistent with the jump in the resistivity, significant changes must occur in the band structure near the transition.

## 3.10 Origin of the Structural Phase Transition

Based upon the evidence that has been presented, it is valuable to speculate about the driving force behind the structural phase transition. This work shows that the jump in DC susceptibility at $T_S$ is a secondary effect of the transition, based upon μSR and DC magnetization data. Questions remain in the analysis of the transport properties. However, the structural and thermodynamic data may provide a possible model.

Careful analysis of the single crystal X-ray diffraction data suggests that the transition may be due to vanadium-vanadium bond formation. One layer of vanadium ions from the *ab* plane is presented in figure 3.29. The alternation in vanadium ion separation between V2 and V3 atoms along the *b* axis shifts from ·····2.73-2.99-2.73-2.99····· in Cmca, to ·····2.53-3.09-2.53-3.09····· (V3-V2B) and ·····2.80-2.96-2.80-2.96····· (V3-V2) in Pbca. The most significant changes in V-V separation are occurring between the V2B and V3 atoms, which connect the $V_{10}$ clusters described in section 3.3.1. The decrease in separation between V3 and V2B, from 2.7317(5) to 2.5334(5), is striking; bond formation is proposed between these ions. There is relatively little change in the bond distances between the V3 and V2 ions, which suggests that bonding occurs preferentially between V3 and V2B ions. These ions account for 16 of 40 vanadium ions in the unit cell, requiring 8 bonds; the bonding occurs in a zigzag fashion along the *b* axis.

Displacements of these ions towards one another is not expected: on the basis of electrostatic arguments a repulsive force is present between the two cations. A situation in which electronic charge is concentrated between the cations in the form of bonds would reduce this repulsion. In addition, an alternation of long and short bond lengths is expected due to the decrease in electronic charge between the remaining V3-V2B interactions. As the bond lengths along this direction are not equivalent in the high temperature phase, the bonding merely increases the difference between the long and short bonds; homopolar bonding in this case does not require a doubling of the *b* axis length.

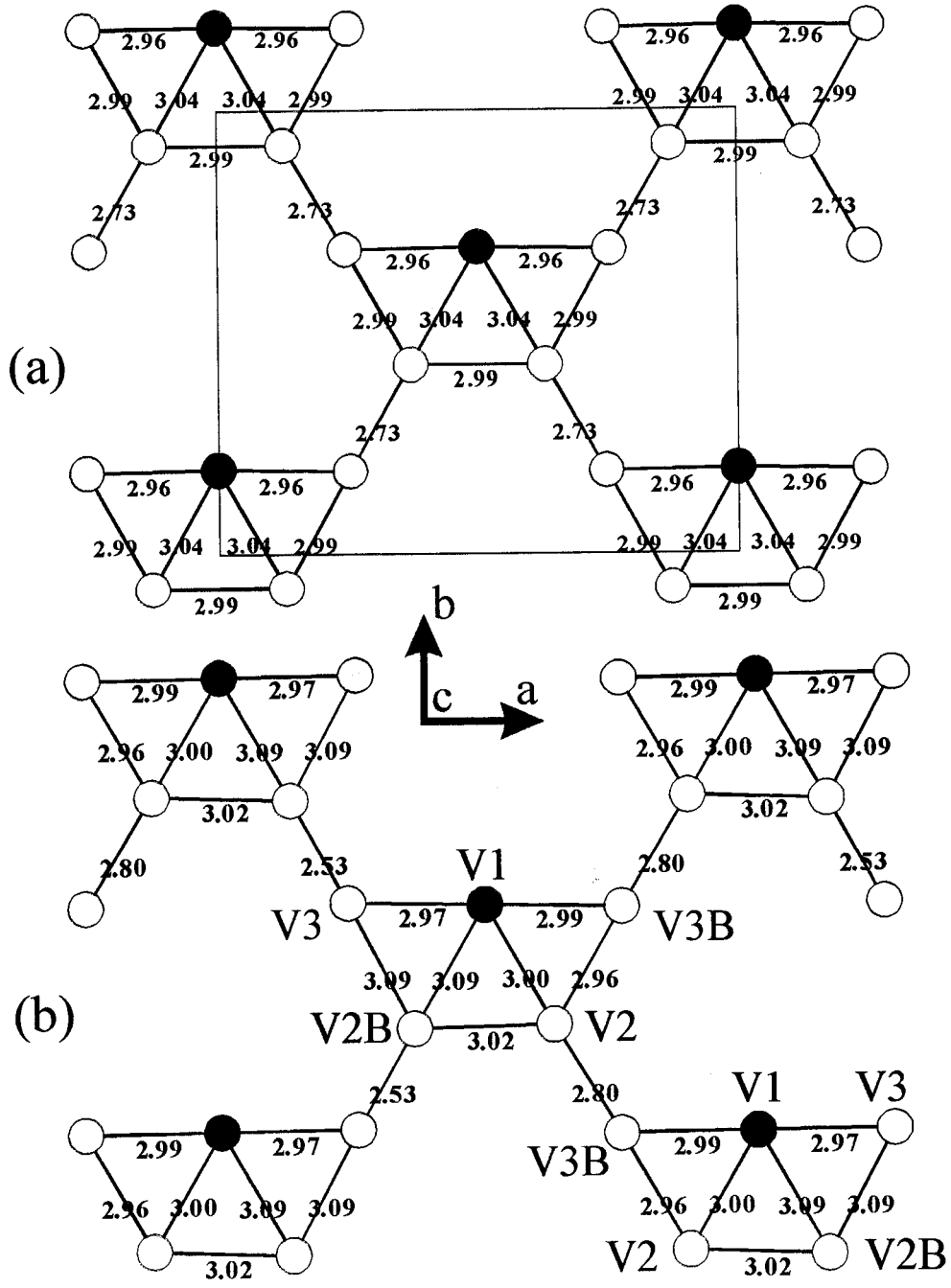


Figure 3.29: View of vanadium sublattice perpendicular to the c axis for $BaV_{10}O_{15}$ at (a) 130K, and (b) 100K. An outline of the unit cell is shown in the upper figure. There are four such planes of vanadium atoms per unit cell, the orientation of which switches 180° along the b axis for each successive layer.

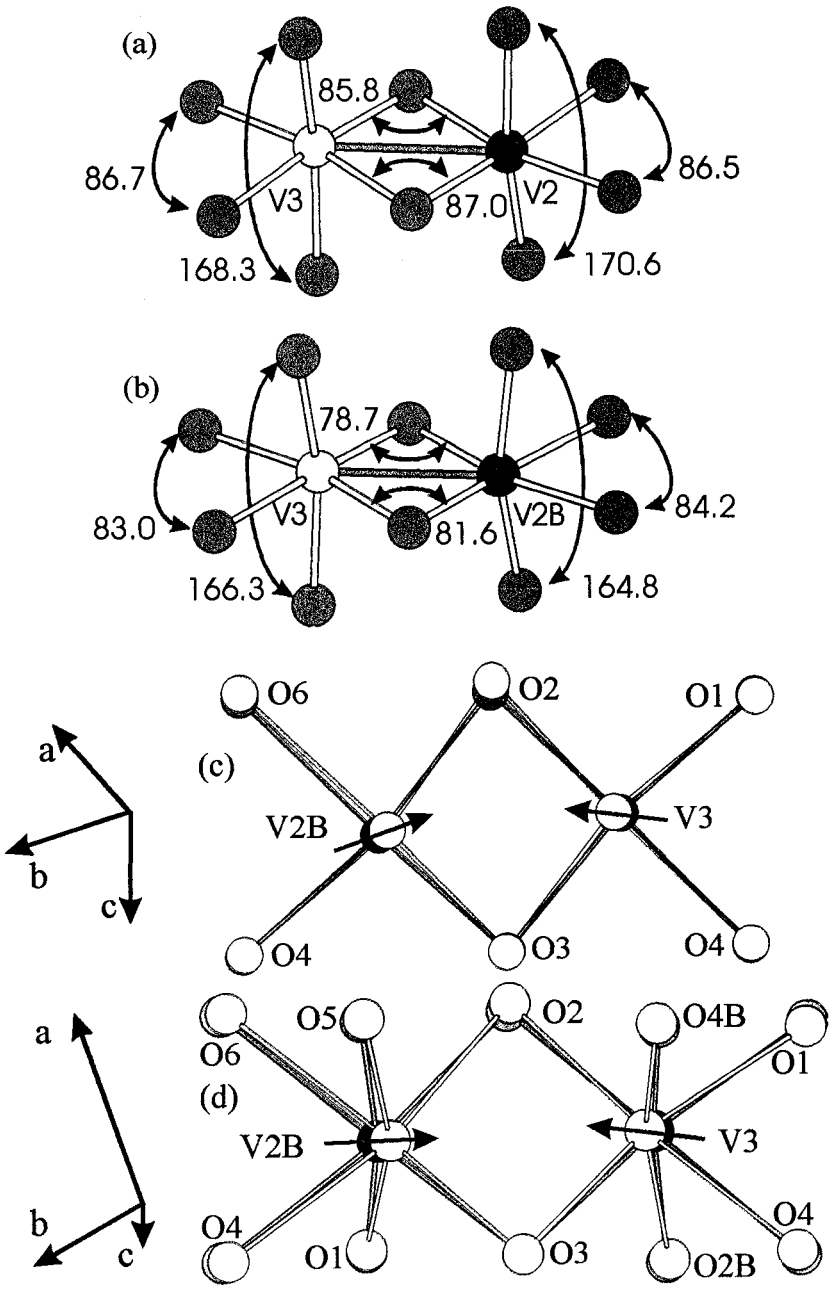


Figure 3.30: View of coordination sphere around vanadium atoms which are proposed to undergo metal-metal bonding, at temperatures of (a) 130K, and (b) 100K. Both (c) and (d) are perspectives in which the Pbca phase (clear atoms) is on top of the Cmca phase (dark atoms). Perspective (c) is from above the octahedra, and oxygen anions above and below the vanadium cations have been removed for clarity. The V-V distance changes from ~2.73Å in the Cmca phase to ~2.53Å in the low temperature phase.

The orbital interactions required to stabilize metal-metal bonding occur more commonly in 4d and 5d compounds than in 3d materials. This is due to the larger radial extent of the 4d and 5d orbitals.(Baird 1968) For the same reason, 3d transition metals occurring earlier in the period are more likely to exhibit metal-metal bonding. Goodenough has described a semi-empirical expression to distinguish between localized and itinerant 3d electrons in oxides which is based upon the room temperature critical separation ($R_c$). The critical separation is predicted to be 2.94Å for $V^{3+}$, and 2.92Å for $V^{2+}$.(Goodenough 1971) Some, though not all, of the V-V separations in $BaV_{10}O_{15}$ are significantly lower than either $R_c$ at room temperature. In particular, the distance between V3 and V2B is much lower than this value. At low temperature, the bonding separation is less than the intermetallic distance in vanadium metal (2.622Å); this suggests strong interactions between the cations.(Baird 1968)

An empirical parameter ($\alpha$) has been defined for edge-sharing octahedra that is based upon the ratio between the bridging edge length and the average of the remaining interanionic separations among octahedral edges. The criterion for metal-metal bonding is $\alpha>1$; the result of this calculation for V2B is 1.05, and for V3 is 1.06. It is clear that in conjunction with various crystallographic data, various (semi-)empirical parameters support the claim of bonding in this 3d transition metal oxide.(Rogers, Shannon et al. 1969)

Metal-metal bonding has been observed in $VO_2$ below ~340K. In this material, the symmetry changes from a high temperature tetragonal ($P4_2/mnm$) rutile structure to a low temperature monoclinic ($P2_1/c$) structure. The V-V separation changes from 2.87Å

to alternating 2.65Å and 3.12Å distances along the monoclinic *a* axis.(Goodenough 1971) More recent theoretical calculations on the electronic and crystal structure of $VO_2$ have predicted distances of 2.52Å and 3.14Å in the low temperature phase.(Wentzcovitch, Schulz et al. 1994) As in $BaV_{10}O_{15}$, the bonding occurs between edge-sharing octahedra; these separations in $VO_2$ are comparable with the bonding (~2.53Å) and antibonding (~3.09Å) distances in $BaV_{10}O_{15}$.

In light of the proposed bonding, it is somewhat surprising that a discontinuous change in the thermoelectric power is not observed. The relatively small amount of latent heat associated with the transition (255 to 1054J/mol) compared with that observed in $VO_2$ (4690J/mol)(Chandrashekhar, Barros et al. 1973), reaffirms that only a fraction of the atoms are involved in the bonding. The endothermic nature of the first-order transition in $BaV_{10}O_{15}$ with increasing temperature is not inconsistent with the claim of bonding, as energy is required to break the bond. In the case of $VO_2$, the transition involves all of the vanadium ions, and an antiferroelectric-to-paraelectric component is present in addition to the homopolar bonding.(Goodenough 1971) For these reasons, it is not unexpected that the transition should be weaker in $BaV_{10}O_{15}$ than in $VO_2$.

There are a variety of possible causes for the lattice distortion observed at the transition, and many of these can be readily excluded from the available data. To do this, it is useful to examine the local distortion of the vanadium octahedra. Various perspectives on the local coordination sphere of V3 and V2B are shown in figure 3.30. Both above and below the transition the vanadium ions are not at the center of symmetry of the octahedron, as expected from a Jahn-Teller type distortion.(Goodenough 1967;

Goodenough 1967) Ferro- and antiferroelectric distortions, in which cations displace in the direction of one or more nearest-neighbor anions, are ruled out by the fact that a non-centrosymmetric space group is required; both Pbca and Cmca are centrosymmetric. The displacement of the vanadium ions occurs predominantly toward each other. This is a characteristic feature of a transition from itinerant to localized electrons (i.e. from metal to insulator), and often is found in conjunction with low dimensional behavior.(Canadell 1998) While the high temperature phase is not metallic, it does appear that the transition results in a localization of charge density between vanadium cations which are in close contact.

## 3.11 Summary of Magnetic Properties

Evidence from various measurements suggests that a rather exotic magnetic ground state is present at low temperatures in $BaV_{10}O_{15}$. Bulk magnetic susceptibility data indicate that unconventional spin glass-like behavior is present. Powder neutron diffraction data reveal weak magnetic long-range ordering below ~40K in all samples. A sharp peak is observed in the heat capacity at the transition to magnetic long-range order for samples with a relatively high temperature structural phase transition; on the other hand, a peak was not observed in the heat capacity data for the $T_S$ = 105K sample, which suggests spin glass-like behavior. Muon spin relaxation measurements reaffirm that for the $T_S$ = 105K sample, the predominate form of ordering is spin glass-like. The sum of this evidence provides a model in which long-range order and spin glass-like behavior coexist; the relative proportion of each ground state varies depending upon the sample.

The low temperature magnetic properties appear correlated with the structural phase transition. At $T_S$, a jump in the susceptibility occurs which results from a disruption of the frustrated interactions that had reduced the moment. Thus spin glass-like behavior is more prominent in the $T_S$ = 105K sample, for which a relatively small jump occurs at the transition. The $T_S$ = 105K sample contains differences in both the crystal and magnetic structural details from the other samples; further work will be required to properly clarify these differences. The $T_S$ = 125K and 135K samples have a similar, though not identical, magnetic neutron diffraction patterns.

The range of possible magnetic long range ordered ground states has been determined for the **k** = (1/2, 0, 0) wave vector, which was found in the $T_S$ = 125K and 135K samples, using representational analysis. Based upon the relatively low symmetry (Pbca) of the crystal structure, the presence of five crystallographically independent vanadium ions in the asymmetric unit, and the constraint that all of these five ions have the same choice of basis vectors, a total of 676 basis vector combinations (magnetic structures) have been identified. This represents a minimum number, as the five vanadium ions are not required by symmetry to have the same basis vectors.

The bond disorder created by the random distribution of the $V^{2+}$ and $V^{3+}$ ions on the vanadium sublattice is accentuated by the topological frustration, and results in the unusual magnetic ordering at low temperatures. Materials which exhibit a mixture of long range magnetic order and spin glass behavior are known, and are usually termed semi-spin glasses, or reentrant spin glasses. One example is the semi-spin glass spinel phase $Co_2TiO_4$, in which a ferrimagnetic longitudinal component and a spin-glass

transverse component are observed a low temperature.(Hubsch and Gavoille 1982) For reentrant spin glasses, the term reentry implies that a transition occurs first to a long range ordered state, followed by the appearance of spin glass behavior at low temperature. A large number of experiments have found that the long range order is destroyed at the transition to spin glass behavior. However, there are examples in which coexistence of the long range and spin glass order occur, such as the dilute Ising antiferromagnet $Fe_{0.55}Mg_{0.45}Cl_2$.(Wong, Molnar et al. 1985) Coexistence of long range antiferromagnetic order and spin glass-like behavior have similarly been identified in $BaV_{10}O_{15}$.

## 3.12 Conclusions

This work has shown that $BaV_{10}O_{15}$ exhibits a variety of interesting phenomena. A first-order structural phase transition occurs at intermediate temperatures (~100 to 135K), below which homopolar bonding is observed between a fraction of the vanadium cations. The compound is semiconducting, and two different models have been proposed to account for the higher temperature data: one based upon small polaron hopping, and another on band conduction of an intrinsic semiconductor. The low temperature data indicates variable range hopping in the presence of a Coulomb gap. The magnetic ground state is a complicated mixture of long range magnetic order and spin glass behavior.

# Chapter 4

# $BaV_{10-x}Ti_xO_{15}$

## 4.1 Introduction

Mixed titanium-vanadium containing systems have been extensively reported in the literature; this is not unexpected, due to the similar size of titanium and vanadium cations. Examples of solid solutions including these elements are $(V_{1-x}Ti_x)_2O_3$, $LnV_{1-x}Ti_xO_3$(Yoshii and Abe 2001), $Sr(V_{1-x}Ti_x)_6O_{11}$(Kanke, Izumi et al. 1991), $Sr(V_{1-x}Ti_x)O_3$, $Ca(V_{1-x}Ti_x)O_3$, $V_{1-x}Ti_xO_2$, $(V_{1-x}Ti_x)_4O_7$, $Ba(V_{1-x}Ti_x)S_3$, $Ba(V_{1-x}Ti_x)_8O_{16}$, $(V_{1-x}Ti_x)O$ and more. Solid solutions of this type have aroused a great deal of interest for the opportunity to tune structural, magnetic, and electronic transitions. For example, the highly correlated metallic phase of $V_2O_3$ is stabilized down to the lowest available temperatures at a titanium doping level of ~5%; the parent $V_2O_3$ undergoes a MIT with temperature near ~160K.(Yethiraj 1990) The ability to alter the *d* electron concentration, or width of the *d*-like bands, in these materials without changing the structure is an important tool to study the electronic ground state. Furthermore, in the case of $(V_{1-x}Ti_x)_2O_3$, the magnetic properties exhibit a progression from antiferromagnetic, to mixed spin glass (or cluster glass) and antiferromagnetic, to spin glass order with increasing titanium content (from 0-95%).(Dumas and Schlenker 1979)

In this chapter the effect of titanium substitution upon the magnetic properties and transport properties of $BaV_{10}O_{15}$ will be examined. This constitutes the first study of the effects of substitution for this structure type.

## 4.2 Sample Preparation

Members of the solid solution $BaV_{10-x}Ti_xO_{15}$ were prepared in polycrystalline form using the tube furnace, mono-arc and induction furnace methods.

### 4.2.1 Tube Furnace

$BaTiO_3$ starting material was prepared by firing a pressed pellet containing stoichiometric quantities of $BaCO_3$ (99.7% from Baker Chemical Co.) and $TiO_2$ (99.9% from Cerac) in air at ~1350°C for 24 hours, according to the reaction

$$BaCO_3 + TiO_2 \longrightarrow BaTiO_3 \,. \qquad (4.2.1)$$

A number of later reactions used $BaTiO_3$ purchased from Cerac (99.98%). Attempts to form the titanium end-member $BaTi_{10}O_{15}$ were based on the reaction

$$BaTiO_3 + 3TiO + 3Ti_2O_3 \xrightarrow{H_2} BaTi_{10}O_{15}. \qquad (4.2.2)$$

The reagents were ground in an agate mortar under acetone, and then were pressed into 3/8" diameter pellets. The TiO was prepared by arc melting a mixture of titanium metal and $Ti_2O_3$; the oxygen content of the TiO was characterized by TGA. The pelletized mixtures were reacted within a molybdenum boat using a variety of

temperature programs for 24 hours. after which the power was shut off such that the maximum cooling rate was obtained.

The products were examined using a Guinier-Hägg camera with a Cu-$K_{\alpha 1}$ radiation source. All preparations below ~1100°C contained starting material in addition to a range of impurities; preparations above ~1100°C resulted in varying amounts of $TiO_x$, $BaTi_5O_{11}$, $Ba_4Ti_{13}O_{30}$, and other unidentified lines. The impurities were readily apparent from the appearance of the pellets which typically had a surface cover of blue material, and an inner golden brown material. As powder patterns of the blue material contained reflections from the starting material and the inner golden brown material, it seems that the surface covering was an intermediate mixture in the reaction; powder patterns of the blue surface layer were highly multiphasic. Regrinding and refiring did not result in the formation of $BaTi_{10}O_{15}$; typically a layer of blue material would reappear. In no preparation was there any evidence for formation of $BaTi_{10}O_{15}$. The mullite tube was examined for cracks by fully evacuating the tube; no leaks were found, which suggests that the decomposition of the sample was not related to oxidation.

Reactions to form mixed titanium-vanadium containing materials were also attempted in the tube furnace. Starting materials included vanadium metal (99.7% from Cerac), $V_2O_3$ was prepared according to reaction 3.2.1, VO as discussed in section 3.2.3, and $Ti_2O_3$ from Cerac (99.9%). Different reactions were examined as a route to pure samples, such as:

$$BaCO_3 + 4V_2O_3 + Ti_2O_3 \xrightarrow{H_2} BaV_8Ti_2O_{15} + H_2O \qquad (4.2.3)$$

or

$$Ba_3V_2O_8 + 10VO + 3V_2O_3 + 6Ti_2O_3 \xrightarrow{H_2} 3BaV_6Ti_4O_{15} \quad (4.2.4)$$

or

$$Ba_3V_2O_8 + \frac{13}{3}V + \frac{4}{3}V_2O_3 + \frac{21}{2}Ti_2O_3 \xrightarrow{H_2} 3BaV_3Ti_7O_{14.5}. \quad (4.2.5)$$

Reactions based on the reagents in reaction 4.2.3 were impure. Typically, varying amounts of $TiO_x$ and/or $VO_x$ were found, as evidenced by a golden layer of material on the surface of the pellet. The second reaction resulted in a blue surface layer with a golden brown interior, which appeared similar to the reactions discussed above for the formation of $BaTi_{10}O_{15}$. Reactions of the third type were theoretically for a slightly reduced product. It was hoped that if impurity formation in the tube furnace was related to oxidation, then the product would be pure if a slightly reduced sample was prepared. However, impurities were formed; in this case, the impurity lines were significant, and likely corresponded to $Ba_2Ti_{13}O_{22}$. Regrinding and refiring was attempted, but did not result in pure product for any of the reactions. The tube furnace was clearly unsuitable for forming the titanium-substituted products.

### 4.2.2 Mono-Arc Furnace

Reactions similar to (4.2.5) above were carried out in the mono-arc furnace. One example of such a reaction is

$$Ba_3V_2O_8 + V + \frac{3}{2}V_2O_3 + \frac{5}{2}Ti_2O_3 \longrightarrow BaV_4Ti_6O_{15}. \quad (4.2.6)$$

In this case the reaction was calculated for a stoichiometric product (no oxygen deficiency). After thorough mixing in an agate mortar, pellets were pressed, and then were placed in a short molybdenum crucible that was open on one end. Several flushing and filling steps with argon gas were performed. The plasma arc was then drawn directly over the pellet until melting occurred; the melt was maintained for ~30 seconds to ensure a complete reaction. Weak impurities were present in some products that could not be assigned to any compound in the PDF database. Concern over the stoichiometry of the products under the extreme conditions of the plasma arc led to the use of the induction furnace for the majority of $BaV_{10-x}Ti_xO_{15}$ preparations.

### 4.2.3 Induction furnace

Reactions of the type given by equations 4.2.4 and 4.2.6 were performed in the induction furnace. An identical procedure was used to that which was described in section 3.2.3 for reactions in the induction furnace: pellets were first sealed in a molybdenum crucible, then were fired at high temperatures with an optical pyrometer in position to measure the temperature. The products obtained by this method were generally pure, according to Guinier film results; occasionally, weak peaks from $TiO_x$, $VO_x$, $V_2O_3$, or unidentified phases were observed. In instances where products containing weak impurities have been measured, this is indicated along with the result of the measurement in the following sections.

Both the induction furnace and mono-arc methods were determined to be useful, although the induction furnace is preferred due to the greater control over the final stoichiometry of the products.

### 4.2.4 Crystal Growth

In some cases, slow cooling of melted products in the induction furnace resulted in crystal growth. However, in no case was a good quality single crystal found with this method for the solid solution $BaV_{10-x}Ti_xO_{15}$. Therefore another method was examined to obtain crystals: Czochralski growth using a modified tri-arc furnace.(Reed and Pollard 1968) First, a small boule (~3g) of material was placed on a water-cooled copper hearth. Due to the relatively low conductivity of these materials (discussed in section 4.5.1) the material has a tendency to jump away from the plasma arc - a small sample is more easily controlled. Two of the arcs were struck, and these were used to synthesize the product prior to crystal growth; the melted sample was flipped and then melted again to ensure a complete reaction.[1] In the next stage, the copper hearth was rotated with the sample at the center, and heated by two arcs with sufficient power to barely melt the material (this ensures that little evaporation occurs). A cooled rod was lowered into the sample; material which solidified on the rod was polycrystalline. The rod was then pulled up at a rate of ~45mm/hr - a slower rate could have allowed a number of grains to persist in the growth. There were three regions produced during this growth: upper and lower regions containing polycrystalline material, and a single crystal region in the middle. Analysis of

[1] In some cases the starting materials were first reacted in the mono-arc.

the different regions using film collected on a Guiner-Hagg camera indicate that the various regions contained identical material: no significant change in stoichiometry from the crystal growth could be detected.

## 4.3 Crystallographic Structures

### 4.3.1 Powder X-ray Diffraction and TGA Results for $BaV_{10-x}Ti_xO_{15}$

The phase purity and cell parameters have been examined in this solid solution using a Guinier-Hägg camera with $CuK_{\alpha 1}$ radiation, and a Bruker D8 Advance Bragg-Brentano diffractometer with a $CuK_{\alpha}$ source. Evolution of the unit cell parameters for a large number of preparations based upon Guinier-Hägg data is presented in figure 4.1.[2] The *b* axis increase is approximately linear with titanium substitution; though there is some variation between the different preparations, a trend is easily discerned due to the relatively large variation of this axis over the range of substitution (~0.18Å). The scatter in the *c* axis plot is quite large due to the relatively small change in this parameter with substitution; there is an overall increase in the *c* axis length with increasing titanium content. The *a* axis appears to exhibit a change in slope above ~40% titanium content, though this is difficult to quantify due to scatter in the plot. The cause of this change in slope is presently unclear, as refinements of powder X-ray diffraction data using the Rietveld method do not indicate any significant change in the structural model with substitution. The proposed change in slope of the *a* axis is not sufficiently pronounced to

[2] Lines present on the figures are merely guides to the eye.

have an obvious effect on the change in cell volume with substitution; the increase in cell volume is nearly linear.

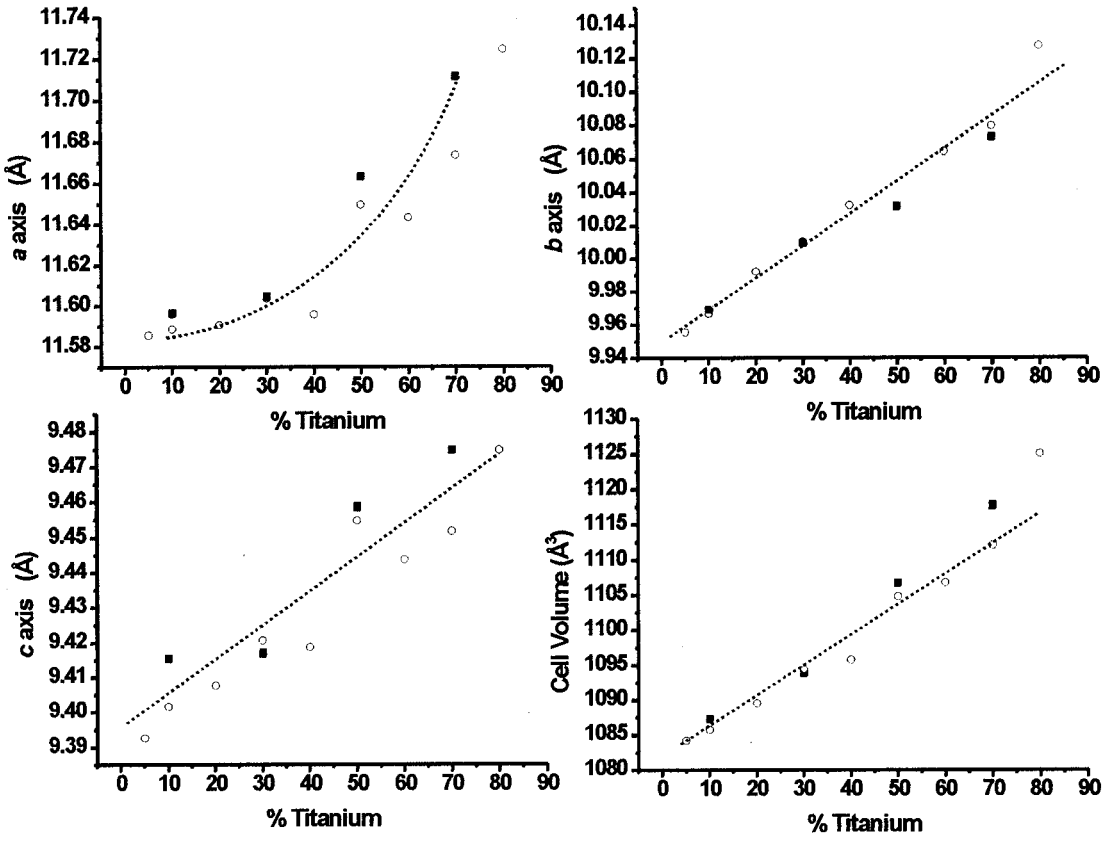


Figure 4.1: Change in cell constants and cell volume for $BaV_{10-x}Ti_xO_{15}$ with titanium content. The open circles were collected using a Guinier-Hägg camera. The filled squares correspond to other preparations analyzed using a D8 Advance diffractometer. Dotted lines are guides to the eye.

In the course of this study it became clear that the difficulties encountered in obtaining pure samples became more pronounced with increased titanium substitution. Low levels of impurities were observed in all of the $BaV_3Ti_7O_{15}$ and $BaV_2Ti_8O_{15}$ preparations. An attempt to form $BaV_2Ti_8O_{15}$ resulted in a multiphase product - evident

from the multicolored nature of the pellet (black, with streaks of brown and orange) - with no evidence for a $BaV_{10}O_{15}$-type structure. For the $BaV_5Ti_5O_{15}$ preparation used in the transport property measurements described in section 4.5, there is a small fraction of the compound $Ba_2Ti_{13}O_{22}$ (~2%).[3] This compound is structurally related to some of the reaction products found in the attempts to synthesize $BaTi_{10}O_{15}$ - namely $BaTi_5O_{11}$ and $Ba_4Ti_{13}O_{30}$.(Akimoto, Gotoh et al. 1994) These reduced barium titanates are all members of a family in which barium resides within hexagonally close-packed layers of oxygen. Titanium occupation of the holes between the layers is dictated by the distribution of barium, due to the electrostatic repulsion of the cations. Clearly, these titanates are also related to the $BaV_{10-x}Ti_xO_{15}$ series; as discussed in section 3.3.1, the vanadium (and titanium) ions occupy the space between the $BaO_7$ close-packed layers in such a manner as to minimize the interaction with barium ions. The different transition metal sublattice observed in these structures stems from the significantly larger fraction of barium present in the titanates. In consideration of the structural similarities between the impurities and the intended product, it is not surprising that these impurities would be obtained.

The TGA results for the samples used in the transport property measurements are presented in table 4.1. These suggest that it is possible to accommodate both oxygen excess and oxygen deficiency in the structure.

[3] It is difficult to identify an impurity with such weak peaks (two peaks were observed). However, other preparations with impurity peaks at the same positions contained larger amounts of this phase (~10-20%); these fit to the compound $Ba_2Ti_{13}O_{22}$.

Table 4.1: TGA results for $BaV_{10-x}Ti_xO_{15}$

| Compound | Weight Gain (%) | Oxygen[A] (x moles) |
|---|---|---|
| $BaV_9TiO_{15}$ | 18.65[B] | +0.17 |
| $BaV_7Ti_3O_{15}$ | 16.58[B] | +0.35 |
| $BaV_5Ti_5O_{15}$ | 14.36[B] | +0.59 |
| $BaV_3Ti_7O_{15}$ | 14.21[B] | -0.33 |

Note that error estimates are not given as the values were obtained by integration, rather than a least-squares fitting procedure.
[A] oxygen content of $BaV_{10-x}Ti_xO_{15\pm X}$ calculated from TGA result (with the transition metal site fully occupied)
[B] sample used in transport property measurements

### 4.3.2 Single Crystal X-ray Diffraction Results for $BaV_9TiO_{15}$

Good quality single crystals were obtained from a crystal growth in a tri-arc welder that was modified for Czochralski growth (see section 4.2.4). A number of these crystals were ground into spheres to improve the absorption correction, and one was selected for data collection. Data were collected using a Siemens Mo rotating-anode generator with a P4 diffractometer and a SMART CCD detector. Data processing and analysis were performed using the SHELXTL software package. Absorption corrections were provided by the SADABS program, including a $\lambda/2$ correction. The results are presented in tables 4.2 to 4.5; anisotropic displacement parameters are given in appendix A.

Table 4.2: Details of the single crystal X-ray diffraction experiment at Room Temperature on $BaV_9TiO_{15}$

| | | | |
|---|---|---|---|
| Space group | Cmca | Refinement | |
| a (Å) | 11.6322(1) | R1 ($I > 2\sigma(I)$) | 0.0251 |
| b (Å) | 10.0022(1) | wR2 ($I > 2\sigma(I)$) | 0.0573 |
| c (Å) | 9.4380(1) | R1 (all) | 0.0284 |
| V (Å$^3$) | 1098.09(2) | wR2 (all) | 0.0584 |
| Temperature (K) | 298 | Goodness of fit | 1.244 |
| Radiation type | Mo $K_\alpha$ | | |
| Colour | Black | No. of reflections | 1598 |
| Index ranges | $-20 \leq h \leq 16$ | No. of parameters | 68 |
| | $-17 \leq k \leq 17$ | Extinction | 0.0073(2) |
| | $-16 \leq l \leq 16$ | Mean shift/su | 0.000 |

Table 4.3: Final Atomic and Isotropic Displacement Parameters in Cmca at 300K for $BaV_9TiO_{15}$

$T = \exp(h^2a^{*2}U^{11}+... +2hka^*b^*U^{12}+... )$

| Site | x | y | z | Frac | Ui/Ue(Å$^2$) |
|---|---|---|---|---|---|
| Ba1 | 0 | 0.5 | 0 | 1.0 | 0.01077(6) |
| V1 | 0.5 | 0.67806(4) | 0.13878(4) | 0.9 | 0.00676(8) |
| V2 | 0.37064(3) | 0.41004(3) | 0.13536(3) | 0.9 | 0.00850(7) |
| V3 | -0.24589(3) | 0.67127(3) | 0.11059(3) | 0.9 | 0.00741(7) |
| Ti1 | 0.5 | 0.67806(4) | 0.13878(4) | 0.1 | 0.00676(8) |
| Ti2 | 0.37064(3) | 0.41004(3) | 0.13536(3) | 0.1 | 0.00850(7) |
| Ti3 | -0.24589(3) | 0.67127(3) | 0.11059(3) | 0.1 | 0.00741(7) |
| O1 | -0.25372(18) | 0.5 | 0 | 1.0 | 0.0090(3) |
| O2 | 0.11882(12) | 0.24686(13) | 0.00164(14) | 1.0 | 0.0088(2) |
| O3 | 0.25 | 0.32570(18) | 0.25 | 1.0 | 0.0075(3) |
| O4 | 0.62904(11) | 0.58849(13) | 0.24374(13) | 1.0 | 0.0073(2) |
| O5 | 0.5 | 0.34238(19) | 0.2498(2) | 1.0 | 0.0079(3) |
| O6 | 0.5 | 0.5 | 0 | 1.0 | 0.0073(4) |

Table 4.4: Selected Bond Distances for $BaV_9TiO_{15}$ in Cmca at 300K (Å)

| | Bond Length | | Bond Length | | Bond Length |
|---|---|---|---|---|---|
| Ba-O5 (×2) | 2.839(2) | *S1-O5 | 1.951(2) | S3-S3 [(a)] | 2.6167(6) |
| Ba-O2 (×4) | 2.885(1) | S1-O4 (×2) | 2.009(1) | S3-S3 [(b)] | 2.6332(6) |
| Ba-O1 (×2) | 2.951(2) | S1-O2 (×2) | 2.015(1) | ***S2-S3*** [(c)] | ***2.7560(4)*** |
| Ba-O4 (×4) | 2.981(1) | S1-O6 | 2.2107(4) | ***S2-S3*** [(d)] | ***2.8558(4)*** |
| Mean | **2.920** | Mean | **2.035** | S1-S3 [(e)] | 2.9686(3) |
| | | | | ***S2-S3*** [(f)] | ***2.9980(4)*** |
| S2-O3 | 1.9626(8) | S3-O2 | 1.994(1) | S2-S2 [(g)] | 3.0094(7) |
| S2-O5 | 1.972(1) | S3-O1 | 2.0081(3) | S1-S2 [(h)] | 3.0744(5) |
| S2-O2 | 2.037(1) | S3-O2 | 2.026(1) | S1-S2 [(i)] | 3.1201(5) |
| S2-O4 | 2.057(1) | S3-O3 | 2.030(1) | | |
| S2-O1 | 2.071(1) | S3-O4 | 2.093(1) | *S1 = V1/Ti1 | |
| S2-O6 | 2.1693(3) | S3-O4 | 2.103(1) | S2 = V2/Ti2 | |
| Mean | **2.045** | Mean | **2.042** | S3 = V3/Ti3 | |

Table 4.5: Selected Bond Valence Sums for $BaV_9TiO_{15}$ in Cmca at 300K (in v.u.)

| Atom | Bond Valence* | Atom | Bond Valence |
|---|---|---|---|
| Ba | 2.179 | O1 | 1.925/1.950 |
| S1 | 2.725/2.763 | O2 | 2.059/2.086 |
| S2 | 2.638/2.675 | O3 | 1.982/2.010 |
| S3 | 2.628/2.666 | O4 | 1.796/1.819 |
| Mean Bond Valence<br>S = 2.664/2.701<br>O = 1.898/1.923 | | O5 | 1.834/1.857 |
| | | O6 | 1.789/1.814 |

*Note : The bond valences listed above represent weighted averages based upon the condition that the cations are randomly distributed on the transition metal sites (S1-3); the left value corresponds to a bond valence analysis using $V^{2+}$ and $V^{3+}$ cations, and the right value to the inclusion of $Ti^{3+}$ randomly distributed on S1-3. The value of $R_o$ for $V^{2+}$ was obtained from the VAlist program.(Wills and Brown 1999)

Attempts to refine the ratio of titanium to vanadium in the sample, both with the total occupancy of the transition metal (TM) site constrained and without this constraint, were unsuccessful; the difference between titanium and vanadium scattering factors is too small to distinguish these cations in a standard X-ray diffraction experiment. Refinement of the transition metal site occupancy with the Ti:V ratio held constant at 1:9, and while holding the barium and oxygen fractional occupancy at 1 and 15 respectively, resulted in

a small, but significant decrease in the site occupation. If the barium fractional occupancy is also included in the refinement, the TM site occupancy is further reduced; the barium fractional occupancy also decreases minimally. However, if the fractional occupancy of all sites are refined, including oxygen, the stoichiometry of the product is $Ba_1(V_9Ti)_1O_{15}$ within error; this is related to the overall increase in uncertainty (error) from including oxygen, which is a relatively weak scatterer. In general, the refinement of site occupation minimally affected the atomic displacement parameters, but did not significantly affect the atomic positions. The results suggest that the presence of defects on the barium and transition metal sites is possible, but cannot be definitely concluded from the available X-ray diffraction data alone. In the final refinement the Ti:V ratio was held constant at 1:9, and the stoichiometry was held at $Ba_1(V_9Ti)_1O_{15}$.

The space group and structural details are similar to the results of earlier room temperature studies on $BaV_{10}O_{15}$.(Beaulieu and Müller-Buschbaum 1980; Liu and Greedan 1996) The cation-anion and TM-TM distances are compared in table 4.6; results for $BaV_9TiO_{15}$ come from this study, while the $BaV_{10}O_{15}$ data comes from the paper by Liu and Greedan.[4] The results are not substantially different between the titanium-substituted and vanadium end-member compounds. This may be expected from the similar, though slightly larger ionic radius of the $Ti^{3+}$ ion (0.670Å) compared with that of the $V^{3+}$ cation (0.640Å).(Shannon 1976) We can see that there is a slight increase in the average TM-TM distances from ~2.877Å in $BaV_{10}O_{15}$ to ~2.982Å with 10% titanium substitution. This can be compared with an overall volume change from 1081.1(7)Å$^3$ for

[4] The V-V distances from $BaV_{10}O_{15}$ at 130K, which are taken from chapter 3, are provided for comparison.

$BaV_{10}O_{15}$, to 1098.09(2)Å$^3$ in $BaV_9TiO_{15}$. The results are consistent with substitution of titanium for vanadium in the structure.

The shorter S2-S3 distances of 2.7560(4)Å and 2.8558(4)Å are surprisingly close to the corresponding distances in $BaV_{10}O_{15}$, which are 2.756(1)Å and 2.864(2)Å. These correspond to the V2-V3 ions proposed to undergo metal-metal bonding in chapter 3. The distances indicate that significant interactions between TM cations on these positions can be expected at low temperatures, as found in the vanadium end member.

A bond valence analysis of the single crystal data for $BaV_9TiO_{15}$ is given in table 4.5. For bonds involving vanadium, two values have been given: the first value corresponds to the use of $V^{2+}$ and $V^{3+}$ bond valence parameters, and the second value to the substitution of one vanadium cation by $Ti^{3+}$. The results which consider titanium substitution are closer to the expected values: 2.701 for the transition metal site versus the expected value of 2.8, and 1.923 versus the expected value of 2.0 for oxygen. We may consider the left value equivalent to assuming that if substituted titanium is in the 2+ oxidation state, then the bond valence parameter is the same as for $V^{2+}$. A bond valence parameter for $Ti^{2+}$ is not currently available, though it will likely be larger than the parameter for $V^{2+}$ (1.7Å) and smaller than the parameter for $Ti^{3+}$ (1.791Å). Therefore, the result based on $Ti^{3+}$ substitution is more appropriate. In fact, the difference in the result between the two bond valence parameters is on the order of ~1%, which is hardly significant. An improved, though still somewhat naive, approximation would be to estimate the value for $Ti^{2+}$ using the difference between the $V^{2+}$ (1.7Å) and $V^{3+}$ (1.743Å) parameters. This provides an estimate of ~1.748Å for $Ti^{2+}$, from a $Ti^{3+}$ parameter of

Table 4.6: Compare Bond Distances for $BaV_9TiO_{15}$ and $BaV_{10}O_{15}$ in Cmca at 300K (Å)

| $BaV_9TiO_{15}$ | Bond Length | $BaV_{10}O_{15}$ | Bond Length | $BaV_9TiO_{15}$ | Bond Length |
|---|---|---|---|---|---|
| S1-O5 | 1.951(2) | V1-O5 | 1.974(5) | Ba-O5 (×2) | 2.839(2) |
| S1-O4 (×2) | 2.009(1) | V1-O4 (×2) | 2.009(4) | Ba-O2 (×4) | 2.885(1) |
| S1-O2 (×2) | 2.015(1) | V1-O2 (×2) | 2.014(4) | Ba-O1 (×2) | 2.951(2) |
| S1-O6 | 2.2107(4) | V1-O6 | 2.183(1) | Ba-O4 (×4) | 2.981(1) |
| Mean | **2.035(2)** | Mean | **2.034(4)** | Mean | **2.920(2)** |
| | | | | | |
| S2-O3 | 1.9626(8) | V2-O3 | 1.954(2) | | |
| S2-O5 | 1.972(1) | V2-O5 | 1.937(4) | | |
| S2-O2 | 2.037(1) | V2-O2 | 2.020(4) | $BaV_{10}O_{15}$ | |
| S2-O4 | 2.057(1) | V2-O4 | 2.035(3) | Ba-O5 (×2) | 2.826(6) |
| S2-O1 | 2.071(1) | V2-O1 | 2.058(4) | Ba-O2 (×4) | 2.891(4) |
| S2-O6 | 2.1693(3) | V2-O6 | 2.159(1) | Ba-O1 (×2) | 2.964(6) |
| Mean | **2.045(1)** | Mean | **2.027(3)** | Ba-O4 (×4) | 2.963(4) |
| | | | | Mean | **2.916(5)** |
| S3-O2 | 1.994(1) | V3-O2 | 1.981(4) | | |
| S3-O1 | 2.0081(3) | V3-O1 | 1.998(1) | | |
| S3-O2 | 2.026(1) | V3-O2 | 2.008(4) | | |
| S3-O3 | 2.030(1) | V3-O3 | 2.016(4) | | |
| S3-O4 | 2.093(1) | V3-O4 | 2.076(4) | | |
| S3-O4 | 2.103(1) | V3-O4 | 2.077(4) | | |
| Mean | **2.042(1)** | Mean | **2.026(4)** | | |
| | | | | $BaV_{10}O_{15}$ at 130K | |
| S3-S3 [a] | 2.6167(6) | V3-V3 [a] | 2.604(2) | V3-V3 [a] | 2.5819(6) |
| S3-S3 [b] | 2.6332(6) | V3-V3 [b] | 2.618(2) | V3-V3 [b] | 2.6336(6) |
| ***S2-S3*** [c] | ***2.7560(4)*** | ***V2-V3*** [c] | *2.756(1)* | ***V2-V3*** [c] | ***2.7317(5)*** |
| ***S2-S3*** [d] | ***2.8558(4)*** | ***V2-V3*** [d] | *2.864(2)* | ***V2-V3*** [d] | ***2.8410(5)*** |
| S1-S3 [e] | 2.9686(3) | V1-V3 [e] | 2.954(1) | V1-V3 [e] | 2.9592(4) |
| ***S2-S3*** [f] | ***2.9980(4)*** | ***V2-V3*** [f] | *2.978(1)* | ***V2-V3*** [f] | ***2.9872(5)*** |
| S2-S2 [g] | 3.0094(7) | V2-V2 [g] | 2.979(2) | V2-V2 [g] | 2.9939(7) |
| S1-S2 [h] | 3.0744(5) | V1-V2 [h] | 3.038(2) | V1-V2 [h] | 3.0377(5) |
| S1-S2 [i] | 3.1201(5) | V1-V2 [i] | 3.102(2) | V1-V2 [i] | 3.1028(5) |
| Mean | **2.982(1)** | Mean | **2.877(2)** | Mean | **2.874(1)** |

1.791Å. With this estimate the difference in the calculation between $Ti^{2+}$ and $Ti^{3+}$ lowers to ~0.1%. This analysis illustrates how the consideration of titanium substitution in the

bond valence analysis can be used to identify the presence of titanium, though the analysis provides no distinction between $Ti^{2+}$ and $Ti^{3+}$ substitution.

### 4.3.3 Powder Neutron Diffraction Results for $BaV_9TiO_{15}$

The C2 powder diffractometer at Chalk River was used to collect data at room temperature and 30K, for the compound $BaV_9TiO_{15}$, using a wavelength of 1.3282Å. These data are presented in figure 4.2. There are three regions which have been excluded in the lower temperature data set due to instrument contributions; the instrument related peaks are ~3-5% of the height of the maximum peak in the pattern. As the instrument contribution is less in the higher temperature data, not all of the weak peaks have been excluded during the refinement.[5] For the 30K refinement the high and low angle patterns were not merged before refinement; both patterns were refined simultaneously using the program GSAS.(Larson and Dreele 1994)

These data indicate that there is no magnetic contribution to the pattern at 30K. Although we note that this temperature may not be low enough to observe ordering, as the only feature in the low temperature DC susceptibility data is a zero-field cooled (ZFC)/field-cooled (FC) divergence near ~13K. The quality of the Rietveld refinement for the two data sets is similar. As there is no evidence to indicate a phase change occurs (such as splitting of peaks, or the appearance of new peaks) with temperature, the structure is determined to be identical at both temperatures. Thus, the crystallographic

[5] As the experimental setup is different for the room temperature and 30K runs, the misalignment which causes the instrument peaks to appear may shift, causing the peak intensity to change.

phase transition observed for $BaV_{10}O_{15}$ appears to be suppressed by ~10% titanium substitution.

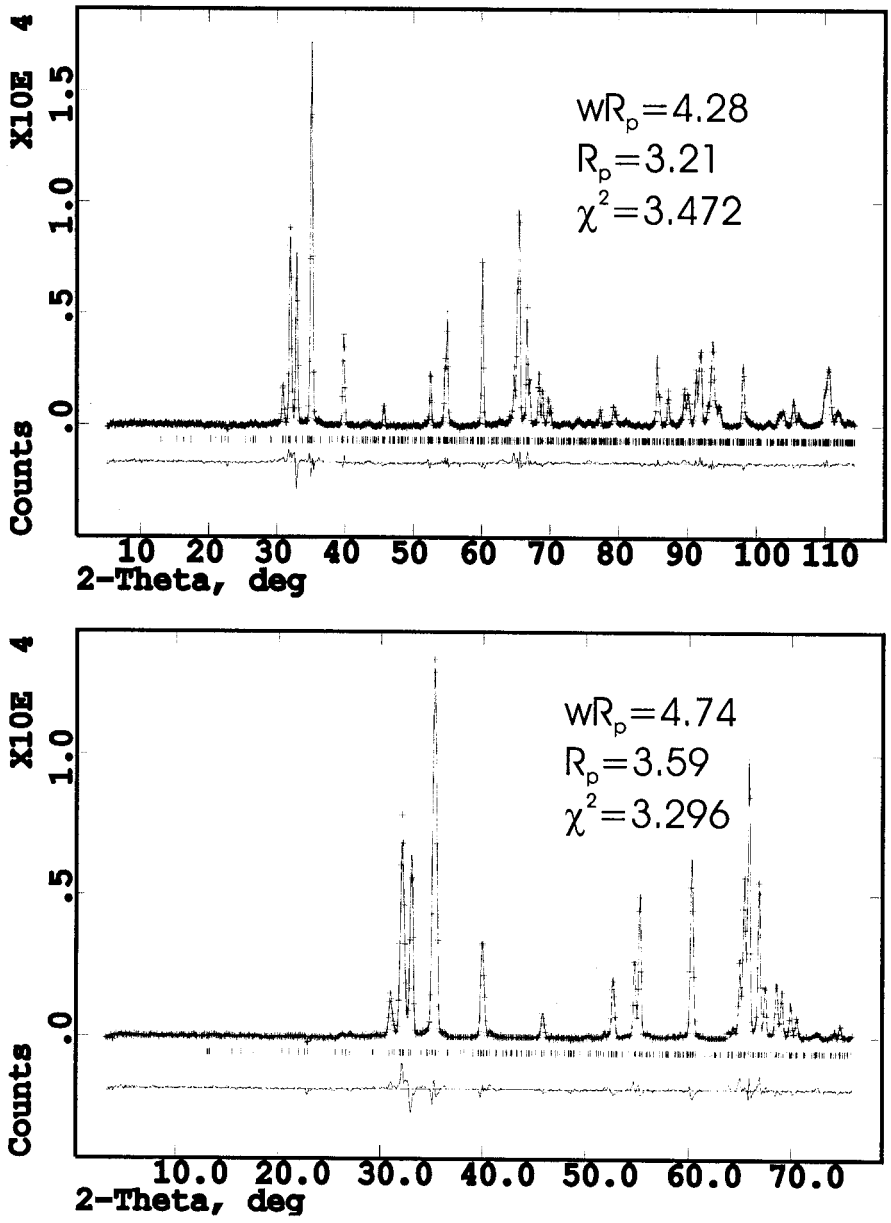


Figure 4.2: Powder neutron diffraction data collected using the C2 powder diffractometer for $BaV_9TiO_{15}$ at a wavelength of 1.3282Å. The top data were collected at room temperature, and the bottom data at 30K. Some regions have been excluded at both temperatures due to instrument contributions. The 30K data were not merged before refinement, and only the low angle range is presented for comparison.

## 4.4 Magnetic Susceptibility

### 4.4.1 Bulk DC Susceptibility

A Quantum Design Squid Magnetometer was used to collect DC magnetic susceptibility data over a temperature range from 5 to 600K. The applied field was 1000Oe for all measurements. Where possible the data were fitted using the Curie-Weiss law (equation 1.2.9). A transition representing cooperative magnetic behavior is indicated by a divergence between the field cooled (FC) and zero-field cooled (ZFC) data. The temperature at which a ZFC/FC divergence occurs ($T_D$), along with results from the Curie-Weiss law fits, are presented in table 4.7. Plots of the susceptibility data are shown in figures 4.3 to 4.5. The fact that the experimentally derived Curie constants ($C_{exper}$) agree well with the expected spin-only values ($C_{calc}$) suggests that the fit is appropriate for this region. The divergence temperature decreases with increasing substitution above 20% titanium doping. As discussed in section 3.5.2 for $BaV_{10}O_{15}$, the divergence can be attributed to a number of different effects. As will be corroborated by other data later in this section, the divergence in this case can be assigned to spin glass behavior. The frustration index ($\theta/T_D$) is extremely high for these materials, and increases with increasing doping. Therefore, these data suggest that the increase in disorder from titanium substitution is causing an increase in the level of frustration in these materials. This frustration results from a combination of chemical disorder and geometric frustration on the transition metal sublattice.

Curie-Weiss behavior can be identified up to a doping level of 30%. The curvature of the $\chi^{-1}$ versus T plots increases with increasing doping, possibly shifting the

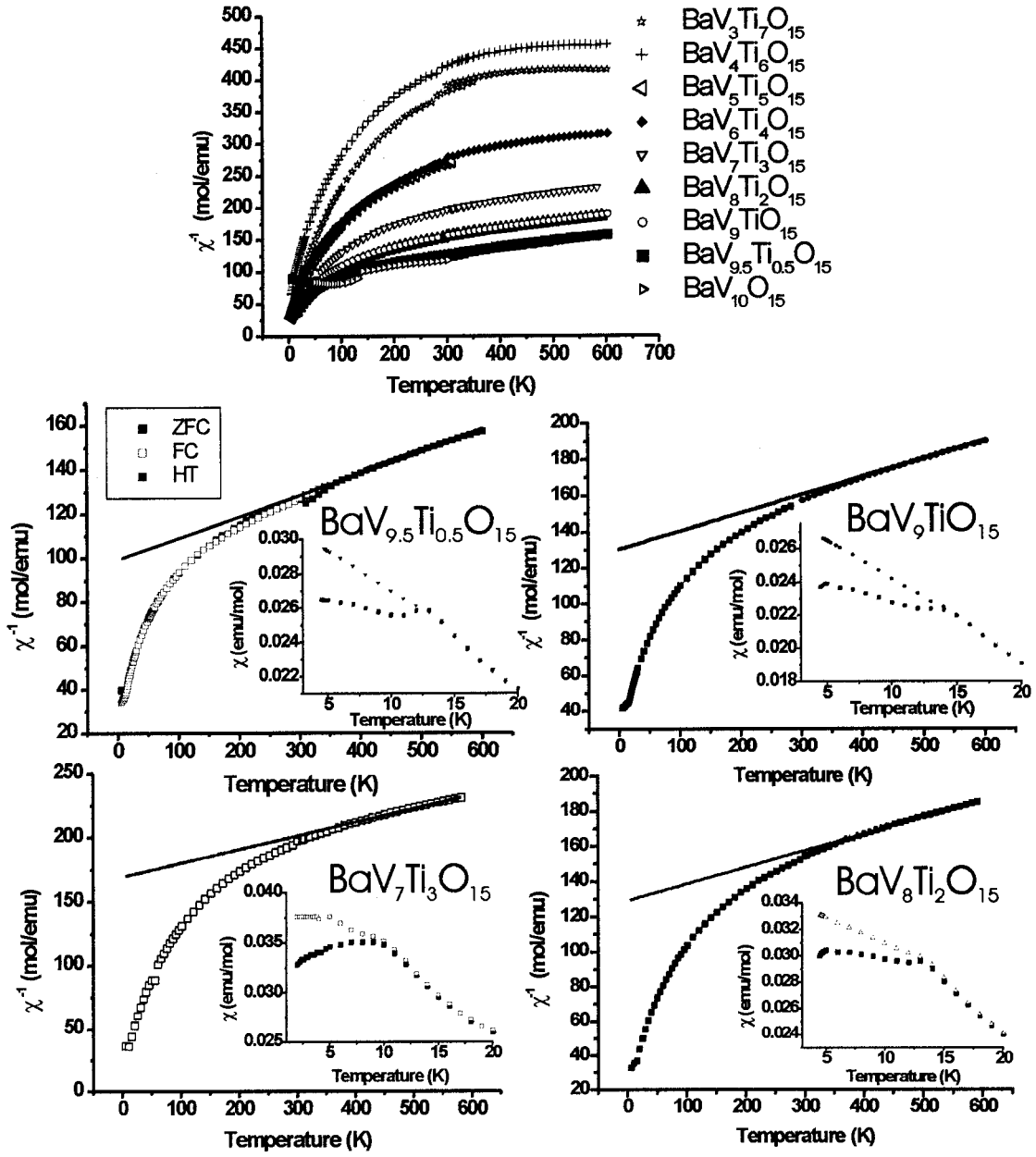


Figure 4.3: DC susceptibility data for $BaV_{10-x}Ti_xO_{15}$ ($x$=0.5-3). In addition, the trend in susceptibility with titanium doping is shown in the top plot. In each of the lower plots, the fit to the Curie-Weiss law is indicated by a solid line. HT refers to data collected with an oven insert in the SQUID magnetometer (temperature range 300K to 600K). The insets show the divergence of the FC and ZFC data at low temperatures using a $\chi$ versus temperature plot.

Curie-Weiss region up to higher temperatures (top plot in figure 4.3). The disappearance of Curie-Weiss behavior, and the corresponding prominence of a temperature-independent paramagnetism (TIP) at high doping levels, is not clearly understood. The resistive behavior identified by transport property measurements (section 4.5) readily discounts the possibility of Pauli TIP paramagnetism. However, is it possible that if the sample is near to a metal-insulator transition, doping could eventually result in overlap of Hubbard sub-bands (in the presence of Anderson localization effects) without a transition to metallic behavior. The finite, but localized, density-of-states at the Fermi level may be responsible for the temperature-independent character of the paramagnetism at high temperatures in the highly doped samples. In addition, the large Curie component at low temperatures indicates the presence of local moments. This model will be examined further in section 4.5.2 with respect to the transport properties.

Table 4.7: DC susceptibility data results for the series $BaV_{10-x}Ti_xO_{15}$

| Compound | $C_{calc}$ (emuK/mol) | $C_{exper}$ (emuK/mol) | $\theta$ (K) | $T_D$ (K) | $\theta/T_D$ |
|---|---|---|---|---|---|
| $BaV_{9.5}Ti_{0.5}O_{15}$ | 11.313-11.438 | 10.7(1) | -1091(±14) | 13 | 84 |
| $BaV_9TiO_{15}$ | 10.875-11.125 | 10.8(1)[a] | -1322(±20)[a] | 15[a] | 88 |
| $BaV_8Ti_2O_{15}$ | 10.0-10.5 | 10.6(1) | -1369(±17) | 14 | 98 |
| $BaV_7Ti_3O_{15}$ | 9.375-9.875 | 9.5(1)[b] | -1629(±30)[b] | 12 | 136 |
| $BaV_6Ti_4O_{15}$ | 8.75-9.25 | n/a | n/a | 8 | - |
| $BaV_5Ti_5O_{15}$ | 8.125-8.625 | n/a | n/a | 4.8[a] | - |
| $BaV_4Ti_6O_{15}$ | 7.5-8.0 | n/a | n/a | - | - |
| $BaV_3Ti_7O_{15}$ | 6.875-7.375 | n/a | n/a | - | - |
| $BaV_2Ti_8O_{15}$ | 6.25-6.75 | n/a | n/a | - | - |

C is the Curie Constant; $C_{calc}$ is based upon spin-only calculations for $M^{2+}/M^{3+}$ (M = V,Ti); $\theta$ = Weiss temperature; $T_D$ = divergence temperature; $\theta/T_D$ = index of frustration; n/a = $\chi^{-1}$ never seemed to reach a linear region vs temperature up to 600K

[a] results from two samples were averaged to get this result

[b] one preparation could be fitted; two other preparations never reached a linear region (n/a)

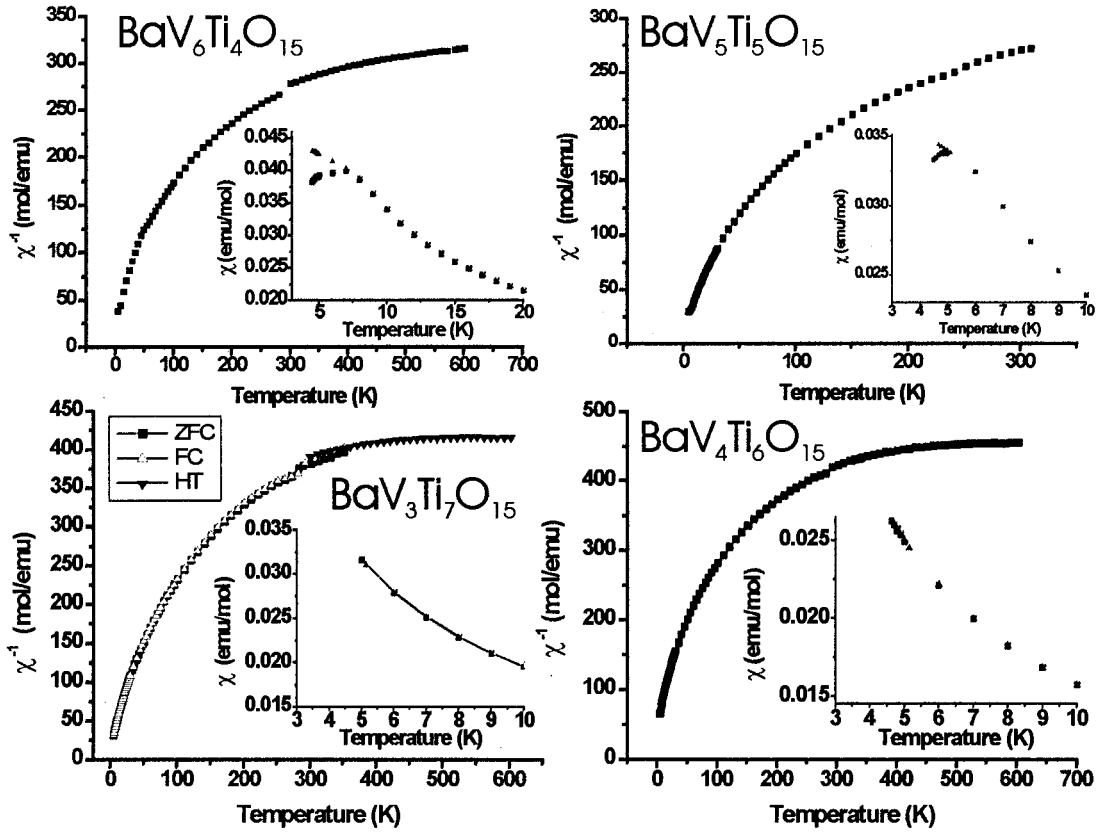


Figure 4.4: DC susceptibility data for $BaV_{10-x}Ti_xO_{15}$ ($x$=4-7). The curvature of these plots suggests that the Curie-Weiss is not accessed over the temperature range investigated in these samples. Data after cooling in zero field (ZFC), in the presence of a field (FC) and at high temperature (HT) are shown for $BaV_3Ti_7O_{15}$. The insets show the divergence of the FC and ZFC data (up to $BaV_5Ti_5O_{15}$) at low temperatures using a $\chi$ versus temperature plot.

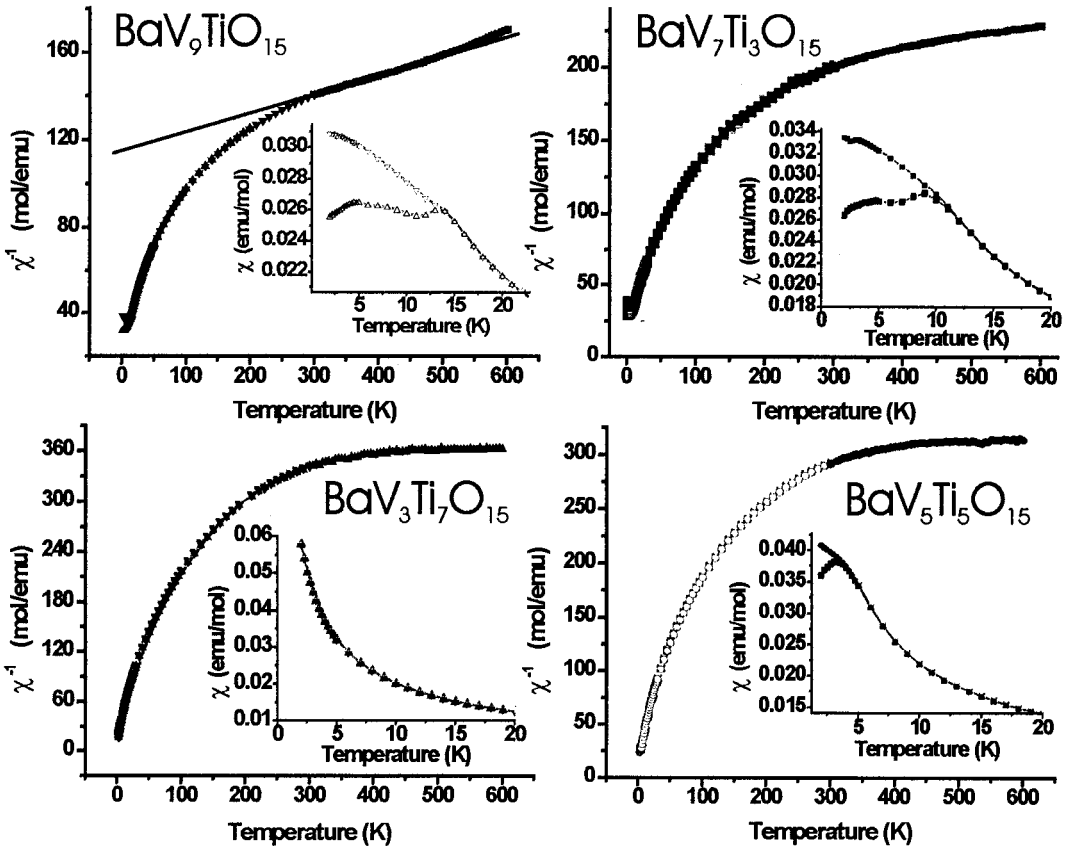


Figure 4.5: DC susceptibility data for $BaV_{10-x}Ti_xO_{15}$ ($x$=1,3,5,7) samples used in the transport property measurements. Data after cooling in zero field (ZFC), in the presence of a field (FC) and at high temperature (HT) are shown for all samples. The curvature of these plots suggests that a fit to the Curie-Weiss is only possible in the $BaV_9TiO_{15}$ sample. The insets show the divergence of the FC and ZFC data (up to $BaV_5Ti_5O_{15}$) at low temperatures using a $\chi$ versus temperature plot.

### 4.4.2 Relaxation Measurements

Measurements of susceptibility versus time were performed for a number of samples below the divergence temperature, and are presented in figure 4.6. The procedure for measuring these samples involved cooling to the measurement temperature in zero field, waiting for 30 minutes, setting a field of 0.1T, and then measuring for approximately 2.5 hours. It was found that if the 30 minute delay was not included, it

was difficult to obtain a smooth relaxation curve; the reason for greater fluctuations in the measurements without the delay is not clear, but may be related to the complex aging process which occurs in these materials. No attempt is made here to explain the change in magnitude of this relaxation with measurement temperature or sample. The presence of relaxation is consistent with the sample history dependent behavior of spin glass-like compounds, as observed in the end-member $BaV_{10}O_{15}$.

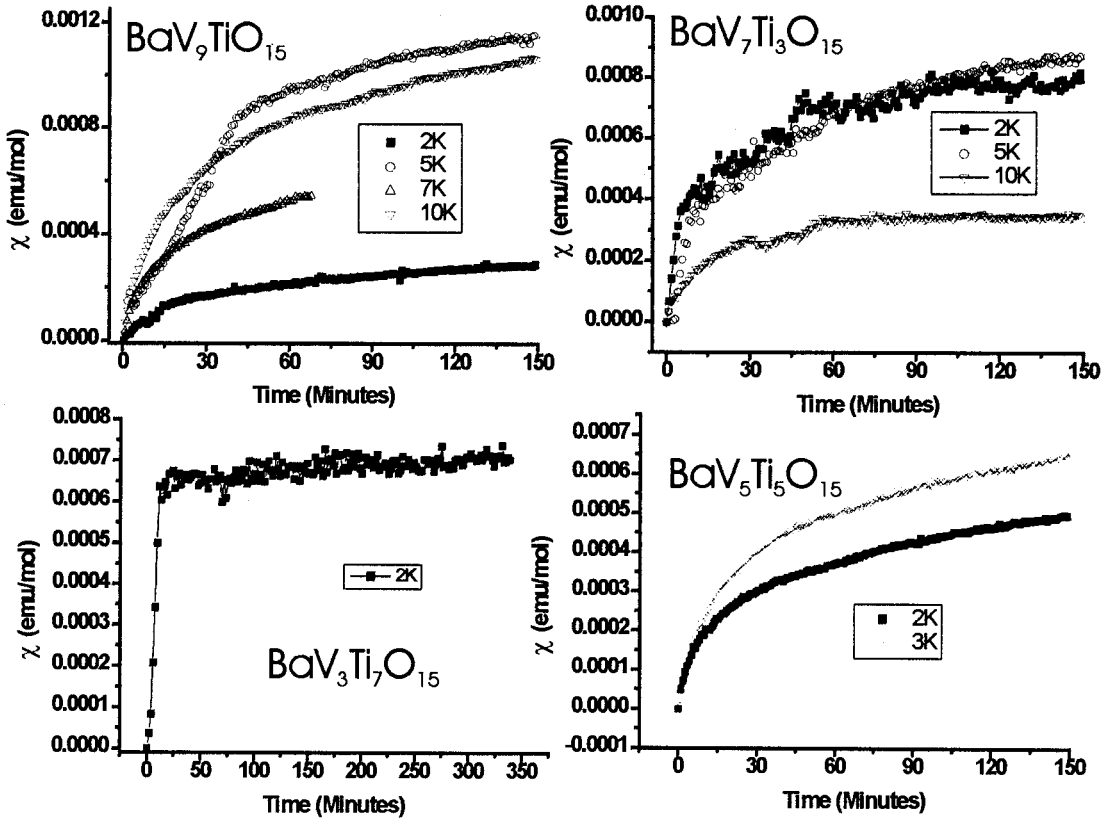


Figure 4.6: Relaxation measurement from DC susceptibility data for $BaV_{10-x}Ti_xO_{15}$ ($x$=1,3,5,7) samples used in the transport property measurements. All samples were cooled in zero field before starting the measurement.

### 4.4.3 Bulk AC Susceptibility

A sintered pellet of $BaV_9TiO_{15}$ was measured in a Quantum Design Physical Property Measurement System (PPMS); the results are presented in figure 4.7. The parameters for the measurements include: a 10 Oe driving field; 100 Oe static field; frequencies of 1000Hz, 5000Hz, and 10000Hz; a temperature range of 2 to 20K; a data collection rate of 5 seconds per frequency. Data for all three frequencies were collected sequentially, rather than measuring over the entire temperature range at a given frequency. As encountered with AC susceptibility measurements of $BaV_{10}O_{15}$, the out-of-phase component ($\chi''$) is negative over a range of temperatures; the reason for this is miscalibration of the secondary coils. When compared with the DC susceptibility data, we see that maximum $\chi'$ occurs at nearly the same temperature as $T_D$. A frequency dependence of the maximum in $\chi'$ is found; this occurs at 15.26(6), 15.42(7), and 15.49(7), for the 1000Hz, 5000Hz, and 10000Hz data, respectively.[6] While the errors are too large to distinguish between the last two maxima, the difference between the 1000Hz and 10000Hz data can be used to estimate the magnitude of K (described in section 3.5.1); a value for K of 0.015 is obtained. This is much less the value ($K > 0.1$) expected for a superparamagnetic compound; it is in the range expected for a spin glass.(Mydosh 1993) The lower two plots in figure 4.7 demonstrate that the maxima in $\chi'$ and $\chi''$ are not coincident, which is another criterion for a spin glass.(Yoshii and Abe 2001) As the

[6] The peaks were fitted to a Gaussian function to extract the maxima. This gives a reasonable estimate of the peak position, with an associated error.

features of the DC magnetic susceptibility data are similar with titanium substitution, it is reasonable to assume that similar behavior is found in the other members of this series.

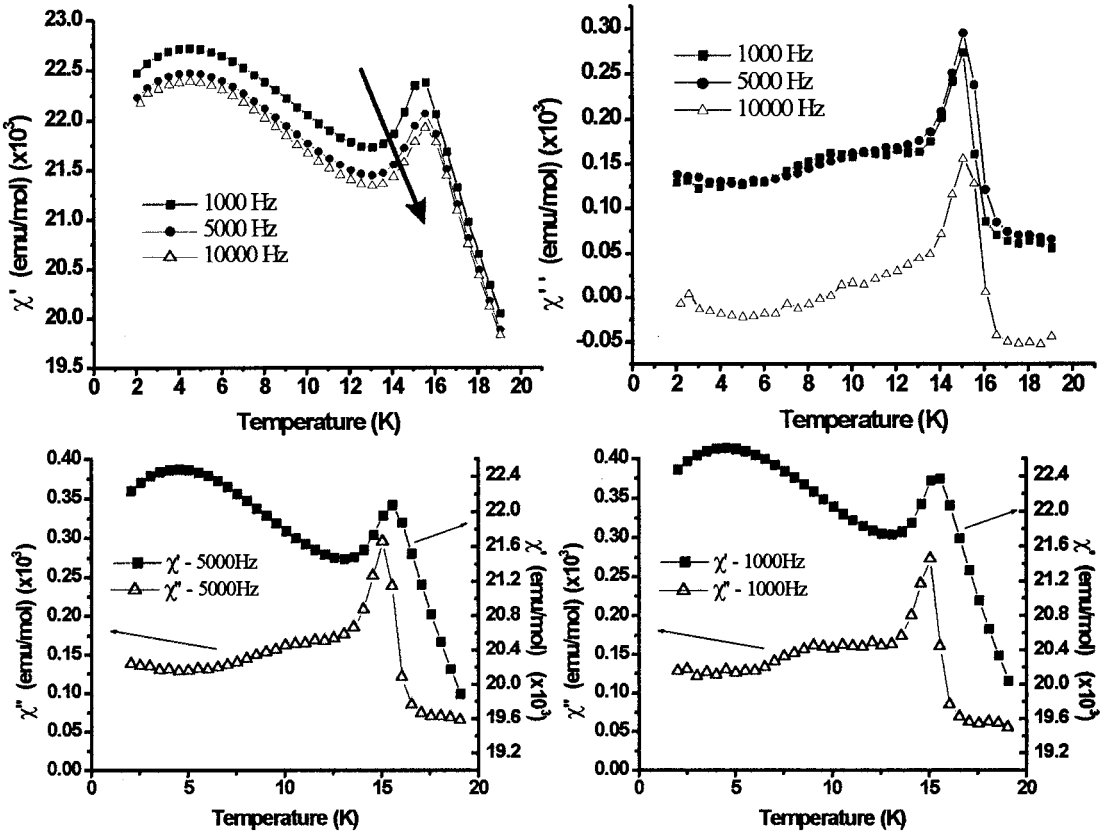


Figure 4.7: AC susceptibility data for $BaV_9TiO_{15}$; this sample was used for the transport property measurement discussed in this section. The top plots show the in-phase ($\chi'$) and out-of-phase ($\chi''$) components at 1000Hz, 5000Hz and 10000Hz. The bottom plots compare $\chi'$ and $\chi''$ at 1000Hz and 5000Hz.

## 4.5 Transport properties

### 4.5.1 DC resistivity measurements

DC resistance data were collected on an Oxford Instruments MagLab measurement system over the available temperature range using a four-probe geometry. Details of the sample preparation and data collection are identical to those described in

section 3.9.1. As is the case of the $BaV_{10}O_{15}$ measurements, it was necessary to obtain data over a few different temperature regions due to the large resistance of the samples. Four different titanium substituted compounds were chosen for these measurements, due to their high level of purity, and the fact that they span a range of doping levels: $BaV_9TiO_{15}$, $BaV_7Ti_3O_{15}$, $BaV_5Ti_3O_{15}$, and $BaV_3Ti_7O_{15}$. These are plotted together in figures 4.8 and 4.10, and individual plots which include fits to the data are given in figures 4.11 to 4.14. There is a general trend toward an increase in the conductivity with doping. However, the room temperature conductivity of $BaV_7Ti_3O_{15}$ is higher than expected from this general trend. In the case of $BaV_9TiO_{15}$, the room temperature conductivity is lower than expected. This can be due to differences in the grain boundary contribution to the conductivity, or to contact resistance. However, after removing the leads, cleaning off the sample, and attaching fresh leads, the resistivity of $BaV_9TiO_{15}$ was essentially identical in magnitude and trend to the first run. Each of the samples was tested for a linear current-voltage response (or constant resistance versus applied current); in all cases the sample response was Ohmic. If a non-Ohmic response were found, this could indicate that the contact resistance is significant; it is expected that the four-probe geometry of the experiment will minimize the effects of the contact resistance.(Hong, Ford et al. 1997) The reproducibility of the runs, as well as the Ohmic response of the I-V plots, indicates that a poor contact between the leads and the sample is not responsible for the trend in the room temperature resistance with substitution. As all of the samples were prepared under the same conditions, it is also unlikely the grain boundary effects are

responsible, but this cannot be ruled out without impedance spectroscopy measurements. It is probable that the trends are related to the bulk properties of the solution series.

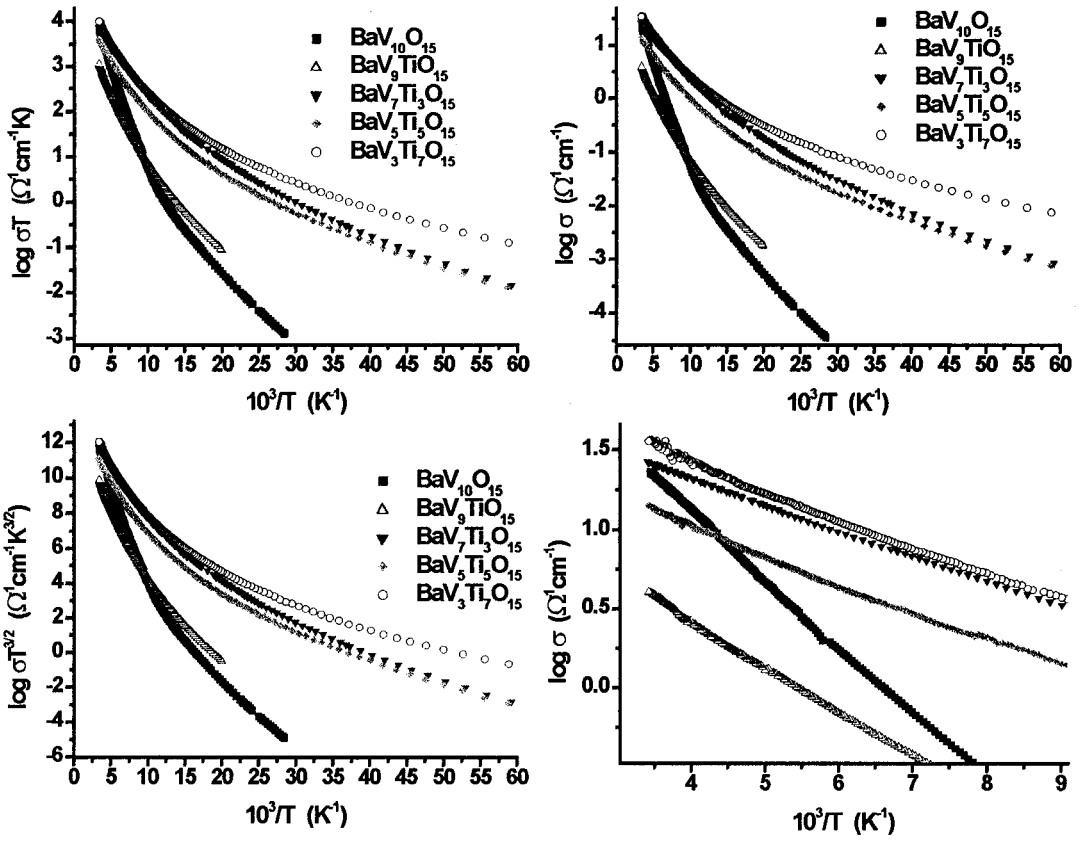


Figure 4.8: DC resistivity data for $BaV_{10-x}Ti_xO_{15}$ ($x$=0,1,3,5,7). The $BaV_{10}O_{15}$ data, presented using black squares, is for the $T_S$ = 105K sample. Different models of conduction are represented by the different plots. Top left: Small polaron hopping by the Mott model. Top right: Arrhenius band conduction. Bottom left: Small polaron hopping by the Holstein non-adiabatic model. Bottom right: High temperature region of Arrhenius plot.

## High Temperature Region

It is clear from figure 4.8 that over most of the temperature range investigated, the titanium substituted samples exhibited a changing activation energy for conduction with temperature; it was only above ~250K that a linear region in the Arrhenius plot could be

found in these samples. With the exception of the result for $BaV_7Ti_3O_{15}$, the activation energy for conduction decreases with increasing titanium content. From the perspective of a simple band model it is difficult to explain the occurrence of a low activation energy for 30% titanium substitution, relative to the compounds with higher titanium content; it is expected that the number of charge carriers would increase, until the density of charge carriers is sufficient for a crossover into metallic behavior. The possibility of band conduction will be examined further in the next section, using thermoelectric measurements.

It is somewhat complicated to describe the titanium substituted series on the basis of a small polaron hopping model. In section 3.9.1 the Mott equation for small polaron hopping (equation 1.4.14) was used to extract the characteristic hopping frequency for $BaV_{10}O_{15}$. To do this, it was necessary to estimate the fraction of sites (C) in the lower oxidation state as the concentration of $V^{2+}$. In the substituted compounds the situation could be complicated by the presence of titanium on the transition metal sublattice. The energy of a polaron present on a titanium cation will be different from a polaron on a vanadium cation. If the energy difference is sufficiently large, it will dominate the mechanism of conduction in this material. If the energies of the $Ti^{2+}/V^{2+}$ and $Ti^{3+}/V^{3+}$ states are identical, such that

$$Ti^{3+} + V^{2+} \rightarrow V^{3+} + Ti^{2+} \qquad (4.5.1)$$

and

$$Ti^{2+} + V^{3+} \rightarrow V^{2+} + Ti^{3+} \qquad (4.5.2)$$

are equivalent to hopping between different oxidation states of the same element, it would suggest that C does not change from a value of 0.2 over the entire range of titanium doping. Moreover, as the energy required for hopping ($W_H$) is related to the energy gain from placing a carrier on a transition metal site ($W_P$), and $W_P$ is assumed to be equal, there might be little reason to expect the conductivity to change with substitution.[7]

If we allow a significantly different $W_P$ between the sites containing different elements, but maintain a sufficiently large overlap between these sites such that the probability of electron transfer is high (adiabatic hopping), it is possible for the conductivity to gradually increase with increasing cation substitution. An explanation of this type is given for the conductivity in $La_{0.8}Sr_{0.2}Co_{1-y}Fe_yO_{3-\delta}$ (y = 0-1), where the iron centers are lower in energy than the cobalt centers.(Lankhorst and Elshof 1997) There is a clear change in conductivity with substitution in $BaV_{10-x}Ti_xO_{15}$, which leads to the possibility that the average $W_H$ seen by the carrier decreases with substitution, while the polaron concentration remains constant.

Another possibility is that a large energy difference exists between the different cation centers. In this case, $W_H$ contains contributions from four different sources: hopping between equivalent cation centers ($W_{S1\text{-}S1}$, $W_{S2\text{-}S2}$), and between cation centers which are not equivalent ($W_{S1\text{-}S2}$, $W_{S2\text{-}S1}$). The latter possibilities are illustrated above in equations 4.5.1 and 4.5.2. For example, the spinel $Co_{3-x}Fe_xO_4$ is considered to undergo a

[7] Note that in the model for small polaron behavior in which the carrier concentration does not change with temperature, as is assumed by the Mott equation for small polaron hopping, the total *d* electron count of a

transition from small polaron transport between cobalt ions on the octahedral site for x<2, to small polaron transport between iron cations on the same site for x>2; conduction occurs on the octahedral site, and exclusively between like ions in this material.(Cox 1992) By the overall increase in the conductivity with titanium doping in $BaV_{10-x}Ti_xO_{15}$, we can conclude that the energy of a polaron on a titanium ion is lower than that of a vanadium ion. In the temperature range covered by the data, the hopping rate is expected to be exponentially higher for hopping from vanadium sites onto titanium sites (equation 4.5.1) than the reverse (equation 4.5.2).(Raffaelle, Anderson et al. 1991) As a result, at low doping levels the titanium cations may act as traps for the carriers; the conductivity will be greatly reduced due to the low mobility of the trapped carriers. This is referred to as "trap-limited diffusion". At a certain critical concentration of the doping, there will be a path available through the solid via nearest-neighbor hopping between only titanium cations. The material then enters the percolation regime, in which transitions between titanium and vanadium cations decrease rapidly in significance. With further titanium doping the conductivity should increase progressively until the other end-member of the series is reached. This type of behavior has been observed in the material $LaCr_{1-x}Mn_xO_3$; the lower energy polaron site is associated with manganese ions.(Raffaelle, Anderson et al. 1991) This type of behavior can be used to explain the rapid decrease in conductivity at room temperature when doping $BaV_{10}O_{15}$ with titanium to form $BaV_9TiO_{15}$. The general increase in resistance with doping can be explained by the occurrence of trap-

---

material does not enter into the equation for conductivity. The concentration of polarons, and the concentration of available polaron sites, are the important factors.

limited diffusion. However, the reason for the low conductivity and activation energy of $BaV_7Ti_3O_{15}$ remains unclear, as it should be entering the percolation regime.

Though the Mott and Holstein models of small polaron conduction have been derived on the basis of hopping between equivalent sites, we may apply these as a first approximation to derive the activation energy for hopping. The hopping energy for the adiabatic and non-adiabatic models is taken from the high temperature region, and presented in table 4.8. The fitting procedure is identical for the Mott model (adiabatic and non-adiabatic) and the adiabatic Holstein model, however the hopping energy ($W_H$ is not identical in both cases unless the polaron bandwidth (J) is zero in the Holstein case. An independent measure of the bandwidth is not available, so these cases cannot be distinguished. The average site separation is taken to be the average of vanadium-vanadium distances listed in table 3.3, a value of 2.874Å. By fitting to the Mott formula with the assumption of adiabatic behavior, the characteristic phonon frequencies for the series have been calculated and are presented in table 4.8. The frequencies are somewhat reduced from that calculated for $BaV_{10}O_{15}$ ($4.93\times10^{13}s^{-1}$), but remain comparable with values typically obtained in vanadate glasses ($\sim10^{13}$).(Ghosh 1991) As is the case for $BaV_{10}O_{15}$, the titanium substituted samples are near the border between adiabatic and non-adiabatic behaviors. It is important to note that the frequencies listed in table 4.8 have been calculated on the basis of a phonon concentration of 0.2. As the above discussion has observed, and the thermopower data in the next section will show, this is not necessarily the case.

There is an inflection point near 300K in the high temperature data for $BaV_5Ti_5O_{15}$, as is shown by the upper-right plot in figure 4.13. The data above and below this point have been fitted to the Arrhenius, Mott and Holstein models - in each case the higher temperature slopes and intercepts are ~5% higher than the low temperature fits. There is no evidence from the DC susceptibility or thermopower measurements that a transition of any sort is occurring at this temperature, and none of the above discussion is affected. Therefore, the lower temperature (~250 to 300K) fit has been given in the table; this corresponds to the temperature over which the other members of the $BaV_{10-x}Ti_xO_{15}$ series have been fitted.

Table 4.8: Estimates of conduction parameters for various models of conduction at high temperatures in $BaV_{10-x}Ti_xO_{15}$

| | Arrhenius | Mott Polaron | | | Holstein Polaron | |
|---|---|---|---|---|---|---|
| x (%) | $E_\sigma$ (eV) | W (eV) | $\nu_{MA}$ ($s^{-1}$) | $W/h\nu_{MA}$ | $W_H$-J (eV) | $W_H$ (eV) |
| 10 | 0.071 (1) | 0.094 (1) | 5.0(2) $\times10^{12}$ | 4.6 | 0.094 (1) | 0.106 (1) |
| 30 | 0.0338 (3) | 0.0570 (3) | 7.3(2) $\times10^{12}$ | 1.9 | 0.0570 (3) | 0.0687 (4) |
| 50 | 0.0420 (1) | 0.0655 (1) | 5.53(1) $\times10^{12}$ | 2.89 | 0.0655 (1) | 0.0773 (1) |
| 70 | 0.0409 (1) | 0.0620 (1) | 1.10(1) $\times10^{13}$ | 1.37 | 0.0620 (1) | 0.0726 (4) |

x = percent of titanium doping; $E_\sigma$ = activation energy for conduction from the Arrhenius equation; W = activation energy for Mott model of polaronic hopping; $\nu_{MA}$ = characteristic polaron frequency in Mott adiabatic hopping; $W_H$-J/$W_H$ = activation energy for Holstein model of adiabatic/non-adiabatic polaronic hopping.

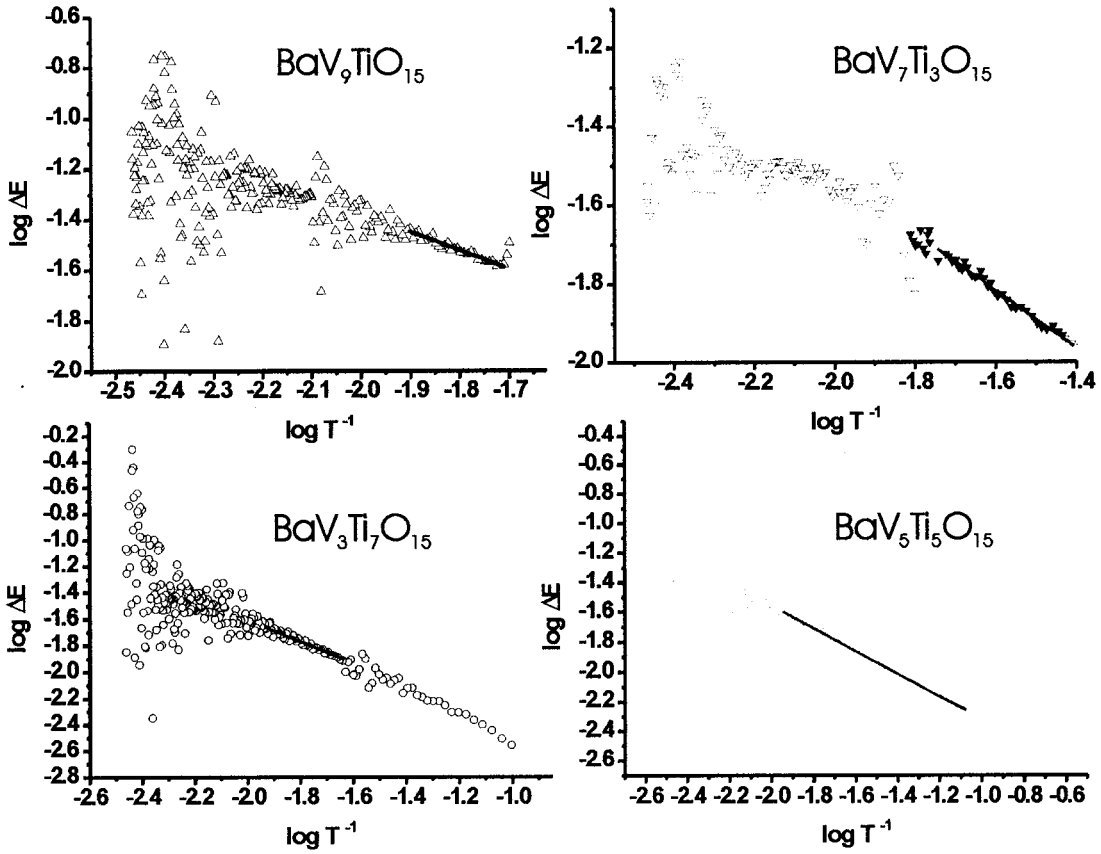


Figure 4.9: Plots of the local activation energy from the analysis of $BaV_{10-x}Ti_xO_{15}$ ($x$=1,3,5,7) DC resistivity data.

## Low Temperature Region

In order to determine the nature of the low temperature conduction, the exponent of the conductivity was determined according to the analysis of Hill (described in section 3.9.1). The results are given in figure 4.9 and table 4.9. There are intermediate sections of these plots in which the scatter in the plot appears to be quite high. This scatter occurs at areas of overlap between the different temperature regions over which the conductivity was collected, and is not a characteristic feature of the samples. The exponents vary from 0.18(4) to 0.27(5), and with the exception of $BaV_3Ti_7O_{15}$, all agree within error with the

$T^{-1/4}$ value expected for Mott VRH. In practice it is not unexpected to find exponents which differ from the -1/2 or -1/4.(Hill 1976) However, for the sake of comparison with other titanium substitution levels, the $BaV_3Ti_7O_{15}$ sample will be fitted to this model.

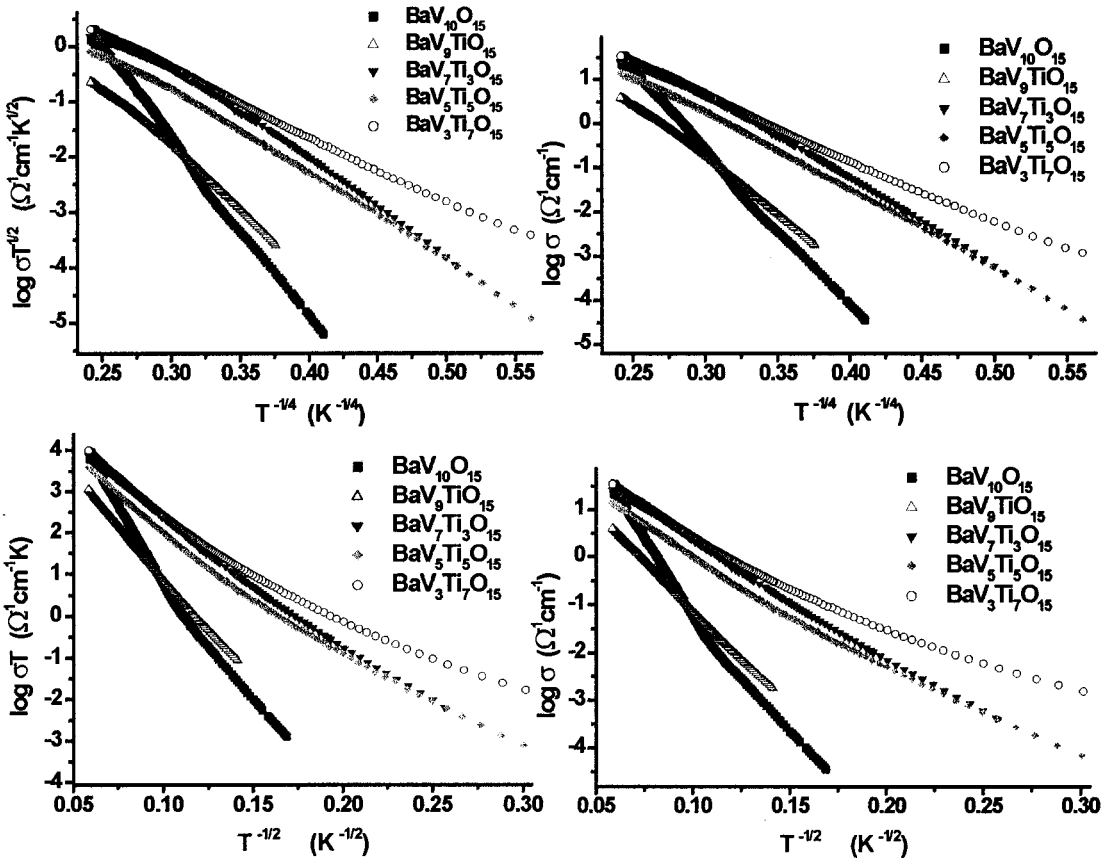


Figure 4.10: DC resistivity data for $BaV_{10-x}Ti_xO_{15}$ ($x$=0,1,3,5,7) as plotted for the analysis of VRH models. The $BaV_{10}O_{15}$ data, presented using black squares, is for the $T_S$ = 105K sample. Different models of conduction are represented by the different plots. Top: Mott Variable Range Hopping. Bottom: Efros-Shklovskii Variable Range Hopping.

The plots show that for the $BaV_9TiO_{15}$ and $BaV_7Ti_3O_{15}$ samples the quality of fit obtained is similar for the ES and Mott VRH models. For these compounds the result from the local activation energy plot will be used; that is, Mott VRH model is taken to be the appropriate model. In the case of $BaV_3Ti_7O_{15}$, it is clear from the plots that the ES

VRH model does not fit the data at low temperature; while the high temperature part of the plot can be fitted, this is well above the temperature range in which this model is expected to be valid, and therefore no result is listed in table 4.9. The $BaV_5Ti_5O_{15}$ sample is particularly interesting, as it appears to show a crossover from Mott to ES VRH with decreasing temperature. This is evident from the plots in figure 4.13, and from the local activation energy plot (figure 4.9). An exponent of 0.56(2) was obtained below 11K, which is close to the value expected for ES VRH. Crossovers from Mott to ES VRH have been noted in the literature(Agrinskaya and Kozub 1994; Lien and Rosenbaum 1998; Khondaker, Shlimak et al. 1999; Capoen, Biskupski et al. 2000), and have been observed to occur with decreasing temperature in a number of materials. Examples of this behavior include insulating, compensated n-CdSe(Zhang, Dai et al. 1990), and the layered cobalt oxide $Sr_2Y_{0.5}Ca_{0.5}Co_2O_7$(Yamaura, Young et al. 2001). A similar crossover, or a related decrease in the density of states at the Fermi level, may also occur in the $BaV_9TiO_{15}$ and $BaV_7Ti_3O_{15}$ samples. Due to the rapid increase in resistivity of these samples with decreasing temperature, data could not be collected down to liquid helium temperatures in order to confirm this possibility.

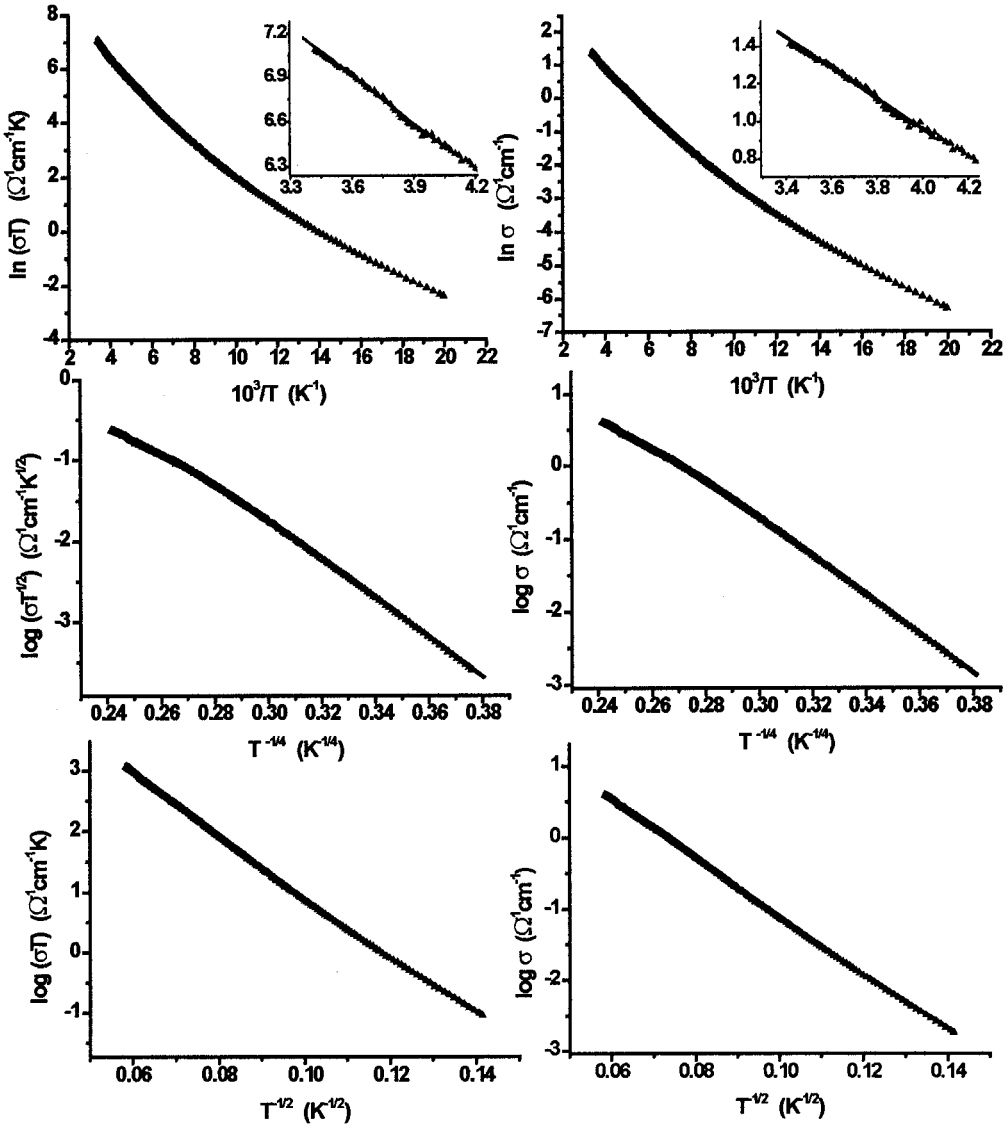


Figure 4.11: Fitted DC resistivity data for $BaV_9TiO_{15}$. Different models of conduction are represented by the different plots. Top left: Small polaron hopping. Top right: Arrhenius band conduction. Middle : Mott Variable Range Hopping. Bottom: Efros-Shklovskii Variable Range Hopping.

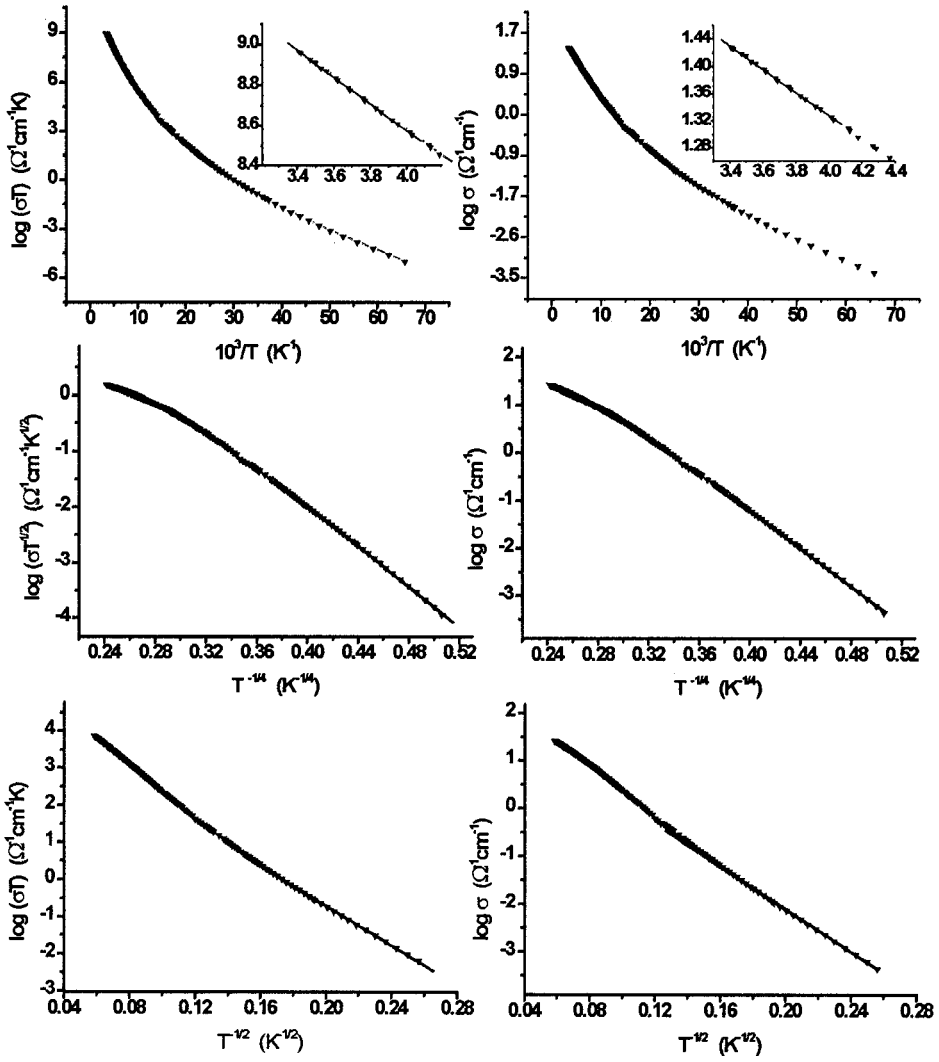


Figure 4.12: Fitted DC resistivity data for $BaV_7Ti_3O_{15}$. Different models of conduction are represented by the different plots. Top left: Small polaron hopping. Top right: Arrhenius band conduction. Middle : Mott Variable Range Hopping. Bottom: Efros-Shklovskii Variable Range Hopping.

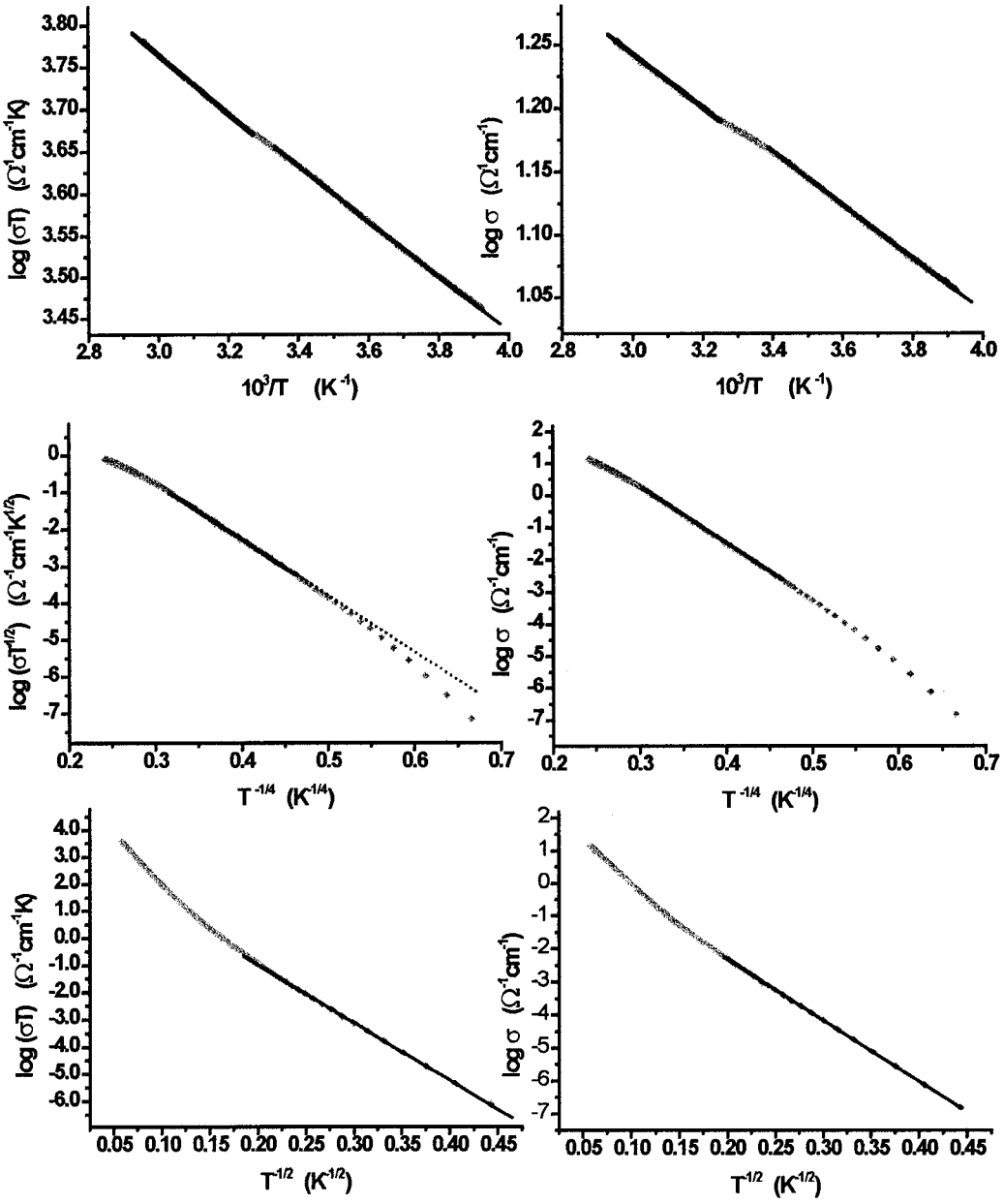


Figure 4.13: Fitted DC resistivity data for $BaV_5Ti_5O_{15}$. Different models of conduction are represented by the different plots. Top left: Small polaron hopping. Top right: Arrhenius band conduction. Middle : Mott Variable Range Hopping. Bottom: Efros-Shklovskii Variable Range Hopping.

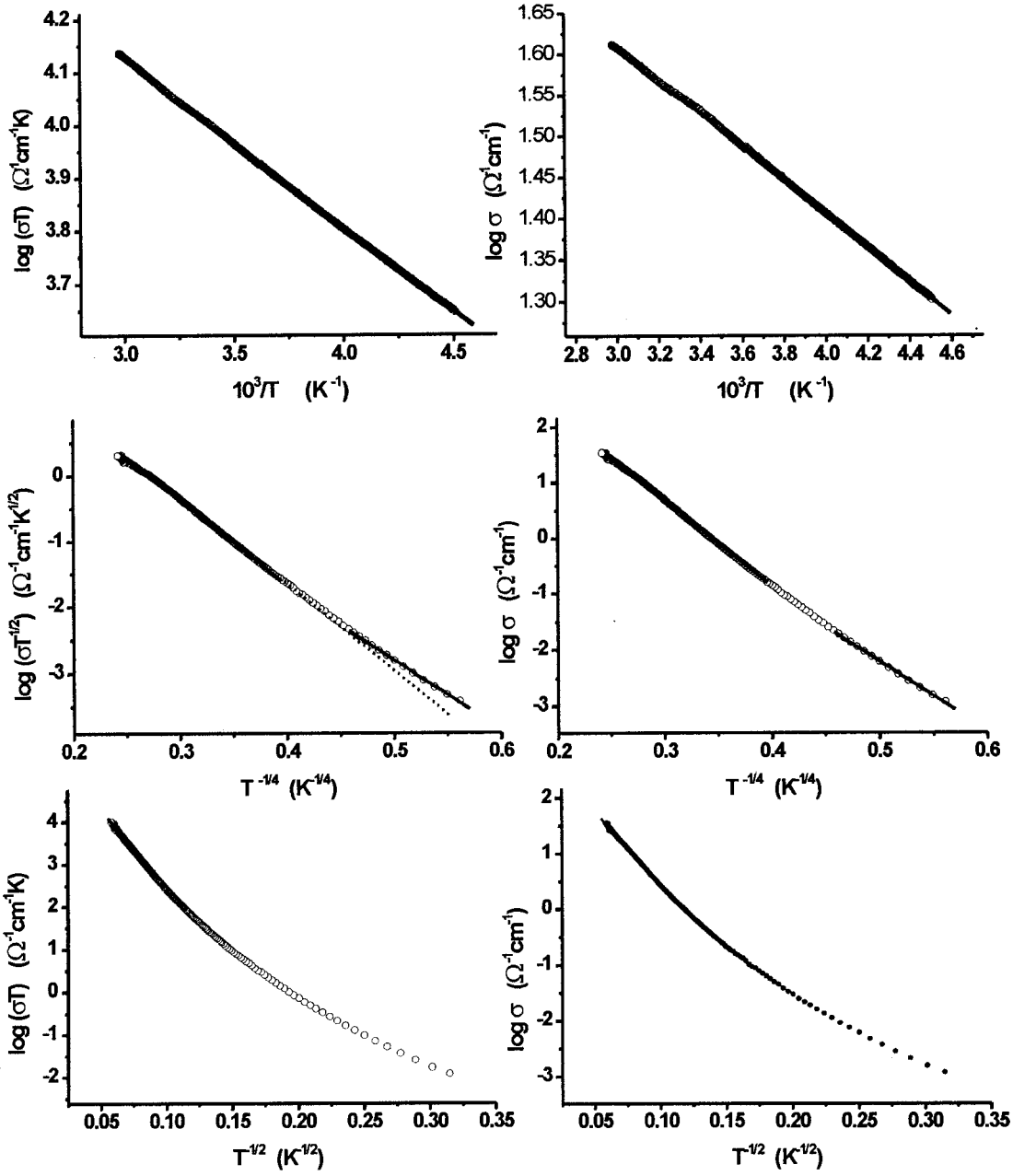


Figure 4.14: Fitted DC resistivity data for $BaV_3Ti_7O_{15}$. Different models of conduction are represented by the different plots. Top left: Small polaron hopping. Top right: Arrhenius band conduction. Middle : Mott Variable Range Hopping. Bottom: Efros-Shklovskii Variable Range Hopping.

Table 4.9: Estimates of conduction parameters for various models of conduction at low temperatures in $BaV_{10-x}Ti_xO_{15}$

| | Mott VRH | | ES VRH | | Exponent |
|---|---|---|---|---|---|
| x (%) | $T_{Mott}$-pre (K) | $T_{Mott}$ (K) | $T_{ES}$-pre (K) | $T_{ES}$ (K) | |
| 10 | 1.031 (5)×$10^7$ | 1.497 (5)×$10^7$ | 1.040 (6)×$10^4$ | 7.52 (3)×$10^3$ | 0.27(5) |
| 30 | 3.20 (6)×$10^6$ | 4.76 (8)×$10^6$ | 3.76 (4)×$10^3$ | 2.81 (2)×$10^3$ | 0.27(2) |
| 50 | 1.50 (2)×$10^6$ | 2.63 (2)×$10^6$ | 2.40 (2)×$10^3$ | 1.81 (1)×$10^3$ | 0.24(5) |
| 70 | 8.49 (4)×$10^5$ | 1.76 (1)×$10^6$ | - | - | 0.18(4) |

x = percent of titanium doping; $T_{Mott}/T_{ES}$ = characteristic temperature for the Mott/Efros-Shklovskii (ES) models of variable range hopping (VRH) - the suffix 'pre' indicates that a temperature-dependent pre-exponential factor was used in the fit; Exponent = low temperature hopping exponent derived from the data.

The characteristic temperature ($T_{Mott}$) is found to decrease steadily with increasing titanium substitution (figure 4.15). For the series, the values of $T_{Mott}$ are intermediate between the magnitude expected for Mott VRH (~$10^5$), and that proposed for multiphonon-assisted hopping between deep states by Emin (~$10^7$-$10^{10}$), though the results are closer to those expected for the model of Emin. It is difficult, based upon these data, to decide with certainty upon the correct model; this will be discussed further with respect to the thermopower of the series. The decrease in $T_{Mott}$, as well as the overall increase in conductivity at low temperature, can nevertheless be explained by an approach to an Anderson transition (section 1.4.4). The progressive hole doping with titanium brings the Fermi level closer to the mobility edge. The conductivity remains localized at all substitution levels in this series. Mott has predicted that when the Fermi

level ($E_F$) is coincident with the conduction band edge ($E_C$), a characteristic minimum metallic conductivity ($\sigma_{MIN}$) on the order of ~$10^2$ $\Omega^{-1}cm^{-1}$ is expected. Though subsequent theoretical efforts have shown that $\sigma_{MIN}$ may only have a physical significance for liquids(Mott 1987), it has been found that many solid materials exhibit a conductivity on this order of magnitude near the metal-insulator transition.(Cox 1992) For the $BaV_{10-x}Ti_xO_{15}$ series, even at 70% titanium doping the conductivity at low temperatures is orders of magnitude below the typical $\sigma_{MIN}$ values; the Fermi level is still well removed from the mobility edge.

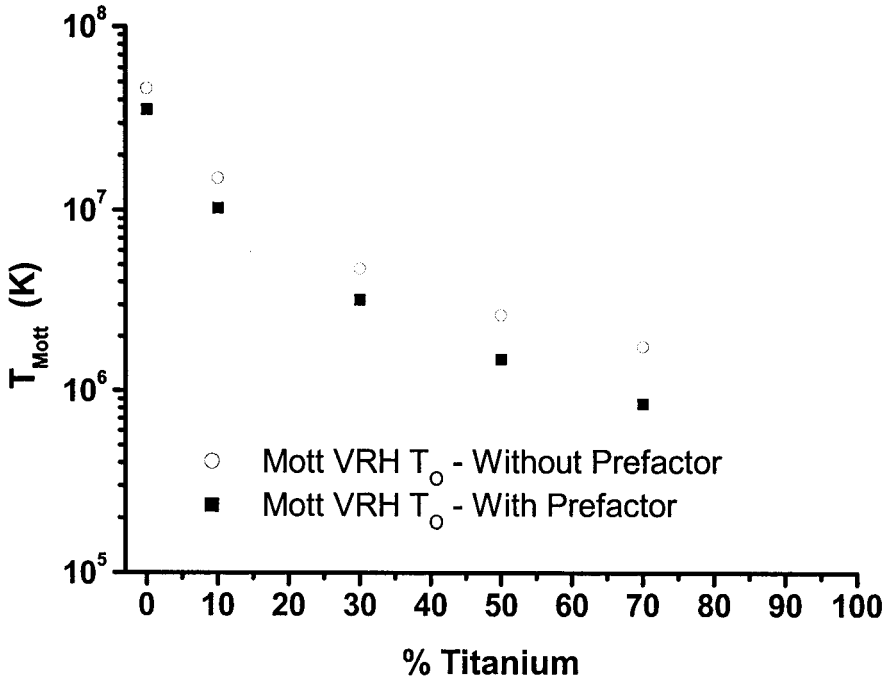


Figure 4.15: Variation in the characteristic temperature ($T_{Mott}$) from fits to the Mott variable range hopping model on DC resistivity data in the series $BaV_{10-x}Ti_xO_{15}$ ($x$=1,3,5,7). The error in the values in on the order of the size of the points. Data for fits with and without a temperature dependent prefactor are presented.

Thermoelectric measurements will now be considered, in order to understand better the mechanism of conduction in this series of compounds.

### 4.5.2 Thermoelectric measurements

Thermoelectric measurements have been performed on the same samples as were examined in the last section: $BaV_9TiO_{15}$, $BaV_7Ti_3O_{15}$, $BaV_5Ti_3O_{15}$, and $BaV_3Ti_7O_{15}$. These data are presented in figure 4.16. The error listed for the observed thermopower is related to a least-square fit of the raw data; for the other quantities the worst case bound is listed. Repeated measurements of a particular sample over the entire temperature range did not result in cracking of the pellet, as occurred in $BaV_{10}O_{15}$. This supports the proposal that a structural phase transition does not occur in these materials, as proposed by the lack of a jump in the DC susceptibility data over the entire temperature range, and the results of powder neutron diffraction on $BaV_9TiO_{15}$. The important qualitative results from these measurements include:

(1) The thermopower is positive over all temperatures, indicating that conduction occurs primarily through holes.

(2) Each member of the series exhibits a small, roughly temperature-independent thermopower over the range investigated, in sharp contrast to undoped $BaV_{10}O_{15}$.

The first point was also observed in the end member $BaV_{10}O_{15}$., indicating that at no point in the series does *n*-type conduction become dominant.

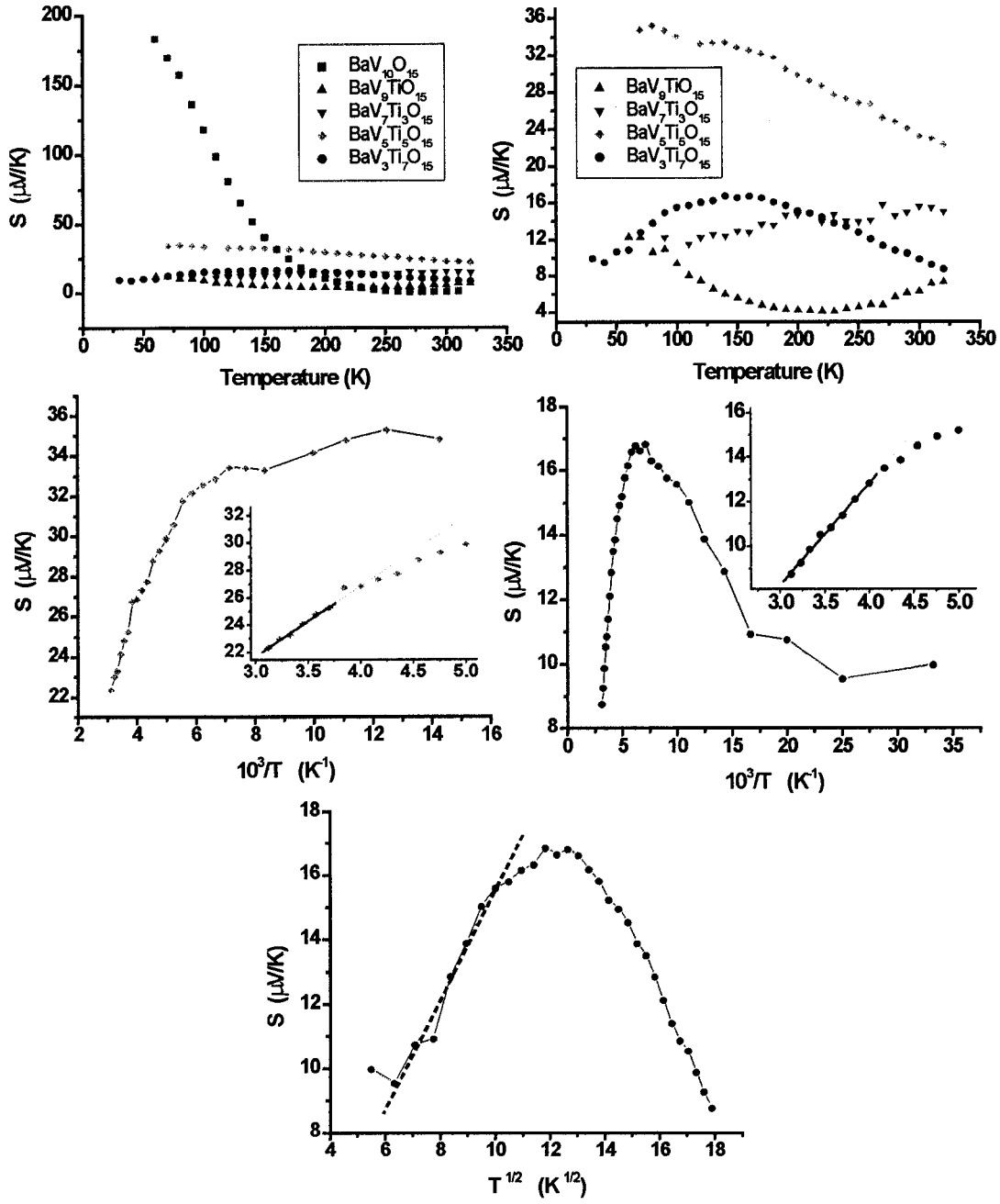


Figure 4.16: Thermoelectric power data for $BaV_{10-x}Ti_xO_{15}$ ($x$=1,3,5,7). Top left: Data for $BaV_{10-x}Ti_xO_{15}$ *including* the $T_S$ = 105K sample of $BaV_{10}O_{15}$. Top right: $BaV_{10-x}Ti_xO_{15}$ *without* $BaV_{10}O_{15}$ data. Middle Left: Plot of $BaV_5Ti_5O_{15}$ thermopower data to determine the activation energy for carrier creation. Middle right: $BaV_3Ti_7O_{15}$. Bottom: Plot of $BaV_3Ti_7O_{15}$ with the model of Mott Variable Range Hopping.

The temperature dependence of the thermoelectric response does not vary in a simple fashion with substitution. It is clear that in the absence of a structural phase transition, the rapid increase in thermopower with decreasing temperature disappears. A hint of this may be present in the $BaV_9TiO_{15}$ data, with the gradual increase at low temperatures; there is no direct evidence for a structural transition in this material at low temperatures, but there may be residual effects from the interactions which caused a transition in $BaV_{10}O_{15}$. The thermopower of $BaV_7Ti_3O_{15}$ increases with temperature over the entire range; the magnitude only changes by ~4μV/K over the temperature range from 90K to 320K. The slope changes at 50% titanium content, such that the thermopower decreases with increasing temperature from 70K to 320K. At a 70% titanium substitution level, a maximum is observed at ~160K. A shift occurs with substitution from a minimum, to an approximately linear increase, to an approximately linear decrease, to a maximum in the temperature dependence.

Based upon arguments initially presented in section 3.9.2 for the transport properties of $BaV_{10}O_{15}$, two models will be proposed as a basis for understanding the thermopower data of the $BaV_{10-x}Ti_xO_{15}$ series. One model based upon localized carriers (small polaron hopping), and another model which involves band theory.

## Evidence for Hopping Conduction

Based upon the activation energies extracted from Arrhenius plots of the conductivity data, a significant $T^{-1}$ temperature dependence is expected from the band (extrinsic semiconductor) model. The thermopower data for $BaV_5Ti_5O_{15}$ and $BaV_3Ti_7O_{15}$

have been fitted above 250K to a $T^{-1}$ dependence (equation 1.4.21); the extracted activation energies are 0.0051(3) eV and 0.0046(1) eV, respectively. For itinerant electron conduction in band states the activation energies from the thermopower measurement should ideally be the same as $E_\sigma$, obtained from the conductivity data. This is clearly not the case, as the activation energies are 0.0420(1) eV for 50% titanium substitution, and 0.0409(1) eV for 30% substitution. For these samples, the weak temperature dependence may be taken to indicate that conduction is via small polaron hopping. The nearly linear temperature dependence observed for $BaV_7Ti_3O_{15}$ is predicted for metallic conduction, but the conductivity data for this sample clearly demonstrates that the material is a semiconductor. Therefore, a small polaron hopping model would be more consistent with the weak temperature dependence. At low temperatures in $BaV_9TiO_{15}$, the rise in the thermopower cannot be explained on the basis of conventional band behavior, as the conductivity indicates a temperature dependent activation energy in this region; the weak temperature dependence again suggests polaron hopping as the conduction mechanism. The data suggest that the conduction mechanism for the substituted compounds is not inconsistent with small polaron hopping.

The small magnitude of the thermopower for all samples is striking. For small polaron conductors with a nearly temperature independent thermopower, the data are typically analyzed using the Heikes formula, or related expressions. The concentration of cations in the upper valence state has been calculated based upon these formulae, and the results are given in table 4.10. This table offers little in the way of guidance as to the conduction mechanism in this material, except to indicate that the standard models of

small polaron hopping in the regime characterized by a constant carrier concentration cannot account quantitatively for the observed behavior. The results in table 4.10 suggest that the carrier concentration changes very little with titanium substitution. As found in $BaV_{10}O_{15}$, the results from Heikes formula suggest that the 2+ and 3+ oxidation states are present in almost equal amounts. This has been observed in $LaCr_{1-x}Mn_xO_3$: at small manganese doping levels the thermopower briefly increases, then decreases with further doping until $LaMnO_3$. For $LaMnO_3$, a value for C of 0.51(3) was determined from a thermopower which is nearly independent of temperature over a range from ~350K to ~1550K. The explanation suggested proposes a disproportionation of $Mn^{3+}$ into $Mn^{2+}$ and $Mn^{4+}$.(Raffaelle, Anderson et al. 1991) It is highly unlikely that a disproportionation of this type would occur in the $BaV_{10-x}Ti_xO_{15}$ series; there is no crystallographic evidence to suggest that higher oxidation state titanium or vanadium cations are present, as these would likely result in a distorted octahedral coordination for any significant concentration.(Zavalij and Whittingham 1999; Schindler, Hawthorne et al. 2000) Another reason must be found to explain why the thermoelectric power is so much less than the expected value for C = 0.2 of -119eV/K, based upon Heikes formula. Perhaps the intermediate-size polaron ("molecular" clusters) model described by Goodenough (used in section 3.9.2) is required to explain the low absolute magnitude of the thermopower.(Goodenough 1970)

Table 4.10: Analysis of the high temperature thermopower data with various models of polaronic conduction for $BaV_{10-x}Ti_xO_{15}$

| x | $S_{obs}$ | $C_{Heikes}$ | $C_{kT>U}$ | $C_{kT<U}$ | $C_{kT<\|-U\|}$ | $P_{HW}$ | $P_{HS}$ | $P_{LW}$ | $P_{LS}$ |
|---|---|---|---|---|---|---|---|---|---|
| x (%) | μV/K | μV/K | μV/K | μV/K | μV/K | μV/K | μV/K | μV/K | μV/K |
| 10 | 7.42 (3) | 0.5215 (1) | 1.0430 (1) | 0.6855 (1) | 1.0859 (4) | 1.8565 (2) | 1.5646 (3) | 2.9790 (2) | 2.2665 (1) |
| 30 | 15.13 (3) | 0.5438 (1) | 1.0876 (1) | 0.7045 (1) | 1.1742 (4) | 1.9142 (2) | 1.6314 (3) | 3.0389 (2) | 2.2844 (1) |
| 50 | 22.40 (3) | 0.5646 (1) | 1.1293 (1) | 0.7218 (1) | 1.2543 (3) | 1.9677 (2) | 1.6939 (3) | 3.0970 (2) | 2.3018 (1) |
| 70 | 8.77 (2) | 0.5254 (1) | 1.0509 (1) | 0.6889 (1) | 1.1015 (2) | 1.8667 (2) | 1.5763 (2) | 2.9894 (2) | 2.2696 (1) |

$S_{obs}$ = Seebeck coefficient observed at high temperature (data was obtained at ~320K); C = concentration of the higher valence state ($V^{2+}$) from analysis for a model with spinless (Heikes formula) carriers, carriers with spin, with spin and on-site repulsion, and with spin and on-site attraction of the charge carriers. P = average number of *d* electrons per site in the high temperature-weak limit (HW), high temperature-strong limit (HS), low temperature-weak limit (LW), and low temperature-strong limit (LS). Numbers in the brackets indicate statistical uncertainties given by the least-squares analysis for $S_{obs}$, and the worst-case bound for the calculated values.

The transition from "trap-limited diffusion" to the percolation regime, discussed in the last section, predicts that at small levels of doping the thermopower should increase due to the fact that the carrier concentration is effectively reduced. As the doping level increases beyond the percolation regime the thermopower should drop rapidly and continuously until the end-member is reached. This can only account for the thermopower data if the trap-limited regime extends to 50% titanium substitution, where the maximum values of the thermopower are observed. It is unlikely that such a large degree of doping would be required to reach the percolation threshold. Moreover, this does not agree with the results of the last section in which the conductivity increased from $BaV_9TiO_{15}$ to $BaV_7Ti_3O_{15}$. As was the case for other small polaron hopping

models, the percolation based model does not seem to properly account for the magnitude of the thermopower data for $BaV_{10-x}Ti_xO_{15}$.

## Semiconduction in a Localized Band

As described in section 3.9.2, the model of an intrinsic (band) semiconductor can be used to account for the thermopower data of $BaV_{10}O_{15}$. This model can be extended to account for the doping effects of titanium as follows. At 10% titanium doping, the Fermi level decreases towards the valence band. This enhances (on the order of a few $\mu$V/K) the hole contribution to the thermopower. With further doping, up to 50% titanium, the hole contribution continues to increase. At 70% titanium doping, the density of holes is sufficiently high to cause a decrease in the magnitude of the Seebeck coefficient. Furthermore, the approximately $T^{-1}$ temperature dependence observed at higher temperatures in the $BaV_5Ti_3O_{15}$ and $BaV_3Ti_7O_{15}$ materials (analyzed earlier in this section) may be related to the approach of the Fermi level to the mobility edge. As the Fermi level does not crossover the mobility edge, metallic behavior does not occur even in the highly doped $BaV_3Ti_7O_{15}$ compound.

This analysis is very similar to that which has been applied to the series of compounds $VO_x$, where $1< x < 1.32$. This material is exactly compensated at $x \cong 1$, resulting in a thermopower of ~0$\mu$V/K. As $x$ increases, the Fermi level drops into more mobile hole states, which causes the thermopower to increase and remain positive. A further consequence of the increase in $x$ is an increase in the V-V separation, and a corresponding band gap. As the size of the gap increases, so does the activation energy

for conduction.(Banus, Reed et al. 1972; Goodenough 1972) This reveals an important difference between the behavior of $VO_x$ and $BaV_{10-x}Ti_xO_{15}$. While the thermopower is increasing (up to a 50% titanium doping level), the energy gap is *decreasing*. This is confirmed experimentally by the decrease in the activation energy for conduction (table 4.8). The titanium doping is not only shifting the Fermi level, it is causing a broadening of the bands. Eventually, the upper and lower Hubbard sub-bands pictured in figure 3.28(D) overlap. This may account for the peculiar temperature-independent paramagnetic behavior at high temperatures for the highly doped samples. Furthermore, Anderson localization prevents the transition to metallic behavior within the overlap region of the bands.

## Variable Range Hopping at Low Temperatures

Thermopower data can be used, in theory, to differentiate between Mott and ES-VRH forms of variable range hopping. Unfortunately, the measurements do not extend down to low enough temperatures to be useful in that respect. Due to the relatively large resistance of the sample, data at the lowest temperatures were too noisy. One exception is the $BaV_3Ti_7O_{15}$ data, which extends down to 30K. The decrease in thermopower below ~100K is essentially consistent with the $T^{1/2}$ temperature dependence expected for Mott VRH, though a conclusive assignment cannot be made due to the noise level (bottom plot in figure 4.16). The data show that VRH behavior does not occur above ~100K in these materials.

## 4.6 Conclusions

A single crystal X-ray diffraction study of $BaV_9TiO_{15}$ has provided evidence that the structure does not change from $BaV_{10}O_{15}$ with titanium doping. This result has been further confirmed by powder X-ray diffraction over the range of doping, in which a relatively monotonic increase in the cell constants is observed. The somewhat surprising result has been found that this structure may accommodate a doping level of 80% titanium, but the end-member $BaTi_{10}O_{15}$ is not stable.

The series of compounds $BaV_{10-x}Ti_xO_{15}$ exhibits spin glass-like behavior up to a doping level of ~50% titanium, above which there is no apparent collective magnetic transition. This result has been confirmed using an AC susceptibility measurement on $BaV_9TiO_{15}$, which is expected to be consistent with other members of the series. The large Weiss temperatures ($\theta$) determined for $\leq$ 30% titanium doping suggest that the samples are highly frustrated.

Conductivity data indicate that variable range hopping occurs at low temperatures in these materials, and present the possibility of ES-type behavior at liquid helium temperatures up to ~50% titanium doping. At higher temperatures, a combination of conductivity and thermopower data have been used to interpret the conduction mechanism on the basis of two distinct models: small polaron hopping, or a band semiconductor doped away from an intrinsic state. The transport property measurements, in addition, provide evidence that a structural phase transition does not occur in the titanium substituted materials. Further studies will be required to confidently assign the conduction mechanism.

# NOTE TO USERS

Page(s) not included in the original manuscript and are unavailable from the author or university. The manuscript was scanned as received.

232-234

This reproduction is the best copy available.

UMI®

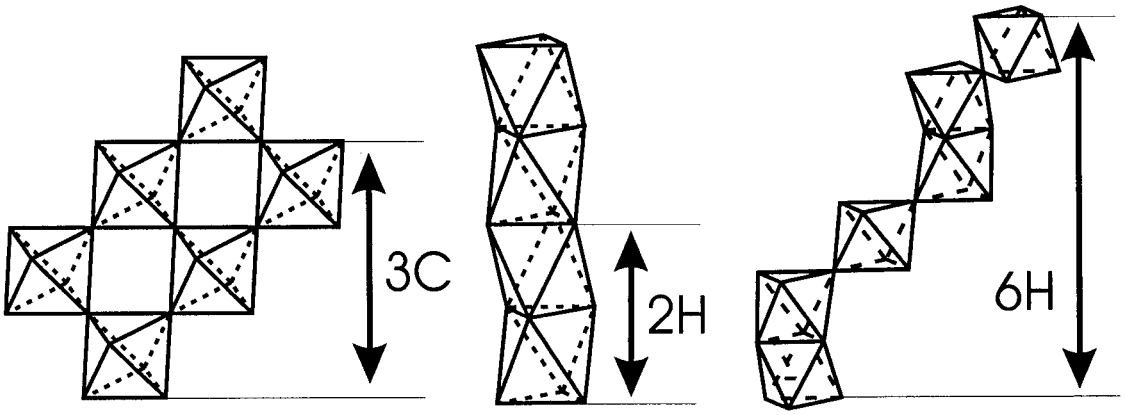


Figure 5.1: Examples of stacking sequences for various perovskite polytypes, including the 3C (cubic), 2H (hexagonal), and 6H (mixture of cubic and hexagonal packing).

The structure of $BaVO_{3.0}$ is shown in figure 5.2(b), and the atomic parameters are given in table 5.1.[1] The model is based upon the 5-layer (5H) structure of $BaCrO_{2.9}$ (space group $P\bar{3}m1$).(Torii 1975) The layers are stacked in a repeating sequence of two hexagonal (h) and three cubic (c) layers, or *ccchh*. The hexagonal layers occur within the cluster of three face-sharing $VO_6$ octahedra. These $V_3O_{12}$ trimers are linked together through corner-sharing octahedra (the cubic layers). Another material which possesses 5H stacking is $Ba_5Ta_4O_{15}$, which differs from $BaVO_3$ only in that the middle octahedron in the trimer is vacant.(Galasso and Katz 1961) Due to the vacant site, the structure may be described as layered. The compounds $Ba_5Nb_4O_{15}$, $Sr_5Ta_4O_{15}$, and the more recently characterized $ALa_4Ti_3RuO_{15}$ (A = Ca, Sr, Ba) series, are all isostructural with $Ba_5Ta_4O_{15}$.(Bontchev, Weill et al. 1992) One polytype of $BaVO_3$ is known. Using high pressure methods a 14H phase has been prepared by Chamberland and Danielson.(Chamberland and Danielson 1971)

[1] Using an oxidation state of $4^+$ for vanadium, a tolerance factor of 1.08 is obtained for $BaVO_{3.0}$. The structure, which is composed of $AO_3$ layers, is consistent with the expectations of a tolerance factor >1.

Reduction of 5H $BaVO_{3.0}$ to $BaVO_{2.9}$ does not alter the structure, but results in vacancies in the middle of the three cubic $BaO_3$ layers. With further reduction a tetrahedral $VO_4$ site is formed (figure 5.2(a)). The compound 5H $BaVO_{2.8}$ is essentially layered, where the *ccchh* blocks are now separated by a cubic $BaO_2$ layer. Atomic parameters are given in table 5.2. This structure type was first suggested for the reduction of $BaCrO_3$.(Schaller and Kemmler-Sack 1984; Schaller and Kemmler-Sack 1984) Possible evidence was later given for a reduced 5H structure containing tetrahedrally coordinated transition metal cations in $BaCo_xMn_{1-x}O_{3-y}$.(Gibb 1992) The existence of the this strucure in $BaCrO_{2.74}$ has been more recently confirmed using high resolution electron microscopy results.(Parras, Varela et al. 1995)

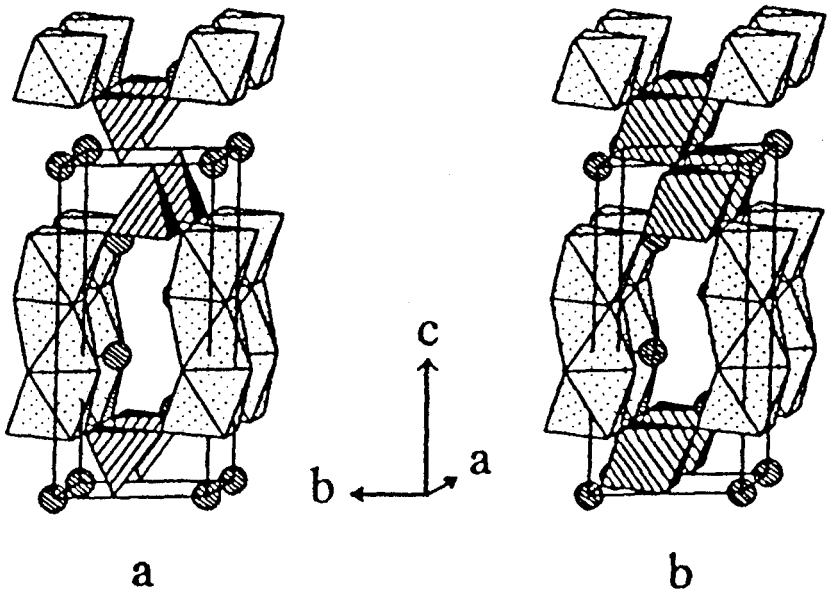


Figure 5.2: Structure of 5H $BaVO_{2.8}$ (a), $BaVO_{2.9}$ (b), and $BaVO_{3.0}$ (b). The shaded circles represent barium. Oxygen removal results in the tetrahedral coordination of one vanadium site in $BaVO_{2.8}$.

It is important to note that until the study of Liu and Greedan, no detailed examination of the physical properties had been performed on a material with the 5H structure. After the recent publication of results on 5H $BaIr_{0.2}Co_{0.8}O_{2.83(1)}$ (Vente and Battle 2000), this represents the third such study.

Table 5.1: Atomic Parameters* in $P\bar{3}m1$ at 300K for $BaVO_{3.0}$

| Atom | *x* | *y* | *z* |
|---|---|---|---|
| Ba1 | 0 | 0 | 0 |
| Ba2 | 0.333333 | 0.666667 | 0.7918 |
| Ba3 | 0.333333 | 0.666667 | 0.4178 |
| V1 | 0 | 0 | 0.7212 |
| V2 | 0.333333 | 0.666667 | 0.1073 |
| V3 | 0 | 0 | 0.5 |
| O1 | 0.5 | 0 | 0 |
| O2 | 0.1704 | -0.1704 | 0.2002 |
| O3 | 0.1534 | -0.1534 | 0.6088 |

Table 5.2: Atomic Parameters* in $P\bar{3}m1$ at 300K for $BaVO_{2.8}$

| Atom | *x* | *y* | *z* |
|---|---|---|---|
| Ba1 | 0 | 0 | 0 |
| Ba2 | 0.333333 | 0.666667 | 0.7624 |
| Ba3 | 0.333333 | 0.666667 | 0.4176 |
| V1 | 0 | 0 | 0.7006 |
| V2 | 0.333333 | 0.666667 | 0.1297 |
| V3 | 0 | 0 | 0.5 |
| O1 | 0.333333 | 0.666667 | -0.0104 |
| O2 | 0.1662 | -0.1662 | 0.1904 |
| O3 | 0.1531 | -0.1531 | 0.6001 |

* atomic parameters were taken from (Liu and Greedan 1994)

## 5.3 Sample Preparation

Polycrystalline samples of the composition $BaVO_{3-x}$ were prepared using a variety of methods. Initial work focused on the direct preparation of $BaVO_3$ using the induction furnace according to the reactions:

$$Ba_3V_2O_8 + \tfrac{3}{5}V + \tfrac{1}{5}V_2O_5 \longrightarrow 3BaVO_3 \qquad (5.3.1)$$

or

$$Ba_3V_2O_8 + VO \longrightarrow 3BaVO_3 . \qquad (5.3.2)$$

Preparation of $Ba_3V_2O_8$ (equation 3.2.3) and VO were described in section 3.2. To obtain the proper oxygen and vanadium stoichiometry, vanadium metal powder (A.D. Mackay 99.5%) and polycrystalline $V_2O_5$ (Aldrich, 99.6%) (or VO) were mixed with $Ba_3V_2O_8$ in stoichiometric quantities. The mixture was pelletized, sealed in a molybdenum crucible under 0.5 atmosphere of argon using a mono-arc welder, and fired at ~1300°C overnight. The resulting product contained $Ba_8V_7O_{22}$ and $Ba_3V_2O_8$; there was no indication from Guinier-Hägg X-ray diffraction analysis for $BaVO_3$. It was clear from this work that the compound $BaVO_3$ could not be directly prepared using high temperature methods. This is in agreement with earlier studies, in which the compound $BaVO_3$ was found to decompose above ~400°C.(Liu and Greedan 1994)

Lack of success in the direct preparation of $BaVO_3$ led to attempts to prepare $BaVO_{2.8}$ using the tube furnace method described by Liu & Greedan ((Liu and Greedan 1994)), as described below. Synthesis of $BaVO_3$ can be achieved through low temperature oxidation of $BaVO_{2.8}$, as will be discussed in section 5.3.4.

### 5.3.1 Tube Furnace

The $BaVO_{2.8}$ preparation of Liu and Greedan involves the reduction of $Ba_2V_2O_7$, which was synthesized according to reaction 5.3.3:

$$2BaCO_3 + V_2O_5 \longrightarrow Ba_2V_2O_7 . \qquad (5.3.3)$$

The $BaCO_3$ (99.7% from Baker Chemical Co.) and $V_2O_5$ were intimately mixed, pelletized, and fired at 1000°C for 24 hours in air. The product, $Ba_2V_2O_7$, was then heated at 1100°C for 24 hours in flowing $H_2$ gas. This produced mainly $Ba_3V_2O_8$, which was then reground, pelletized, and heated at 1350°C in the tube furnace for 24 hours to produce the overall reaction

$$Ba_2V_2O_7 \xrightarrow{H_2} 2BaVO_{2.8} + 1.4H_2O . \qquad (5.3.4)$$

According to previously reported results, the product should be essentially pure, with the exception of some re-oxidation (white material) on the surface of the pellet.(Liu and Greedan 1994) However, the results of this study found the presence of $Ba_4V_2O_9$ and $Ba_8V_7O_{22}$ not only on the surface, but also throughout the pellet. Regrinding and refiring under identical conditions did not modify this result. A variety of pellet sizes were used, but did not produce a pure product.

The entire tube was placed under vacuum to determine if leaks to the laboratory atmosphere were related to the formation of the observed impurities. No leaks were identified, but to ensure that the moisture produced during the reduction did not affect the resulting product, another reaction was performed in the presence of a desiccant. A large quantity of powdered $P_2O_5$ was placed in an alumina boat at the end of the tube (after the

sample), sufficiently far from the furnace that the desiccant would not heat up during the reaction. The above procedure was again repeated. The product from this experimental setup was ~60% $BaVO_{2.8}$, with the remainder mainly $Ba_8V_7O_{22}$ and $Ba_3V_2O_8$. A hard surface layer was present, which was largely composed of $BaSiO_3$ and other barium silicates.

One final attempt was made to form $BaVO_{2.8}$ using the tube furnace. The $P_2O_5$ was replaced with Ce metal in a molybdenum boat. The cerium was placed in the tube such that it would be heated to an intermediate temperature, and would getter any residual oxygen. Using reaction 5.3.4, and the procedure given in the paper by Liu and Greedan, the products were $BaVO_{2.8}$, $Ba_3V_2O_8$, and an unknown phase. Regrinding and refiring did not improve the purity of the product.

### 5.3.2 Sealed Silica Tube

As the tube furnace reactions were unsuccessful in producing pure $BaVO_{2.8}$, the preparation in the paper by Chen et al. was attempted.(Chen, Eichhorn et al. 1993) This procedure involved mixing BaO (Cerac, 99.5%) and $VO_2$ (Cerac, 99.5%) in an argon-filled glove-box at a 1:1 molar ratio. This mixture was placed into a silica ampule, which was then placed into a larger silica ampule containing excess Zr metal. The larger ampule was sealed under vacuum, and the reaction was performed at 1100°C for 24 hrs. Reduction of the initial product by Zr metal was expected to yield a pure product according to

$$BaO + VO_2 \xrightarrow{Zr} BaVO_{2.8} + 0.1ZrO_2. \qquad (5.3.5)$$

The reaction products included $BaVO_{2.8}$, $Ba_3V_2O_8$, and an unknown impurity phase. As $BaVO_{2.8}$ is black, and $Ba_3V_2O_8$ is white, it was visually evident that a great deal of oxidation had occurred where the reagents were in contact with the quartz. The reaction was again performed with the reagents placed in a platinum boat; the Pt boat was left open at one end. The reaction products were now only $BaVO_{2.8}$ and $Ba_3V_2O_8$. A final reaction was attempted with the sample under dynamic vacuum at 1000°C in the presence of Zr getter. In this case a much larger fraction of the sample was $Ba_3V_2O_8$.

It was not possible to form $BaVO_{2.8}$ without also producing $Ba_3V_2O_8$, using the method of Chen et al. It is notable that during the course of this study, neither of the previously published procedures was able to produce pure $BaVO_{2.8}$. In fact, if the published powder X-ray diffraction data is carefully examined, it is clear that very weak peaks (on the order of a few percent of the main peak) are present that do not fit any structural reflections.(Chen, Eichhorn et al. 1993; Liu and Greedan 1994) Moreover, in the paper by Chen et al., regions of the data have been excluded from the refinement which have not been discussed in the paper. This does not invalidate any of the results from these papers, as the impurity levels appear to have been very small. It merely suggests that an alternative preparation route should be explored. Due to the difficulties encountered when utilizing the published synthetic procedures, an induction furnace based preparation method has been developed.

### 5.3.3 Induction furnace

The starting materials $Ba_3V_2O_8$, VO, and V metal were mixed in various ratios to obtain products with the stoichiometry $BaVO_{3-x}$, where x = 0.265 to 0.21. An example in which x = 0.25 is given by

$$Ba_3V_2O_8 + 0.20586VO_{1.118} + 0.79414VO_{0.025} \longrightarrow 3BaVO_{2.75}. \qquad (5.3.6)$$

Thermogravimetric analysis was used to determine the oxygen content of the vanadium metal and VO.[2] These experiments were performed with the intent to synthesize a pure product, and to achieve that by finding the optimum oxygen stoichiometry for the induction furnace method. Reagents were intimately mixed, pelletized, and sealed in molybdenum crucible under 0.5 atmosphere of argon; several flushing operations with argon were performed before the crucible was sealed, to ensure the minimum quantity of residual oxygen. The reactions were fired for periods ranging from 24 hours to 4 days at temperatures of ~1300 to 1400°C.[3] In all cases weak impurity lines were found, though the impurity level was often on the order of a few percent (estimated by the ratio of impurity peak height to maximum peak height of $BaVO_{2.8}$ using Guinier-Hägg X-ray powder diffraction data). Generally, the impurity peaks could not be identified using a search of the powder diffraction files (PDF), or comparison with other known compounds. In the case where x = 0.21, additional weak impurity lines from $Ba_8V_7O_{22}$ were found.

---

[2] While the exact oxygen stoichiometry of V metal and VO has not been given for other equations in this thesis, TGA was used to determine the oxygen content for these reagents in all cases. The exact stoichiometry is shown in equation 5.3.6 for illustrative purposes.

Other reactions were attempted using $V_2O_3$ (prepared as in section 3.2) in place of VO in reaction 5.3.6. In these reactions $Ba_8V_7O_{22}$ and $BaVO_{2.9}$ were found as additional phases. Given that $Ba_8V_7O_{22}$ ($BaV_{0.875}O_{2.75}$) contains a vanadium deficiency relative to $BaVO_{2.8}$, three reactions were carried out with 4%, 8% and 11% molar excess of vanadium. The reagents were weighed out for an oxygen stoichiometry of x = 0.24 (relative to $BaVO_{3-x}$), as shown in equation 5.2.7 for the case of 8% excess vanadium:

$$Ba_3V_2O_8 + 0.084407V_2O_3 + 1.07119VO_{0.025} \longrightarrow 3BaV_{1.08}O_{2.76}. \quad (5.3.7)$$

The preparations in each case contained a mixture of unidentified phases after one firing in the induction furnace for 24 hours at ~1300 to 1400°C.[3] After one refiring in the induction furnace, the 4% excess phase was determined to be pure using data collected on a D8 Advance powder X-ray diffractometer.

The 8% excess vanadium sample contained a mixture of $BaVO_{2.8}$, $BaVO_{2.9}$, $BaVO_{3.0}$, and $Ba_8V_7O_{22}$ after the initial firing. After one refiring step, close inspection of the strongest peaks in the $BaVO_{2.8}$ diffraction pattern revealed a weak high angle tail. This tail is due to a low level of chemical inhomogeneity; this is most likely to occur on the oxygen sublattice, though the excess vanadium may result in inhomogeneity on the cation sublattice as well. The high angle tail does not extent to the region of d-spacings expected for $BaVO_{2.9}$, as illustrated in figure 5.3(a). Further refirings were not attempted,

[3] The temperature was determined using an optical pyrometer to be near 1300°C, though later calibration suggested that the temperature of the sample was ~1400°C for the typical induction furnace setup used in the $BaVO_{3-x}$ project.

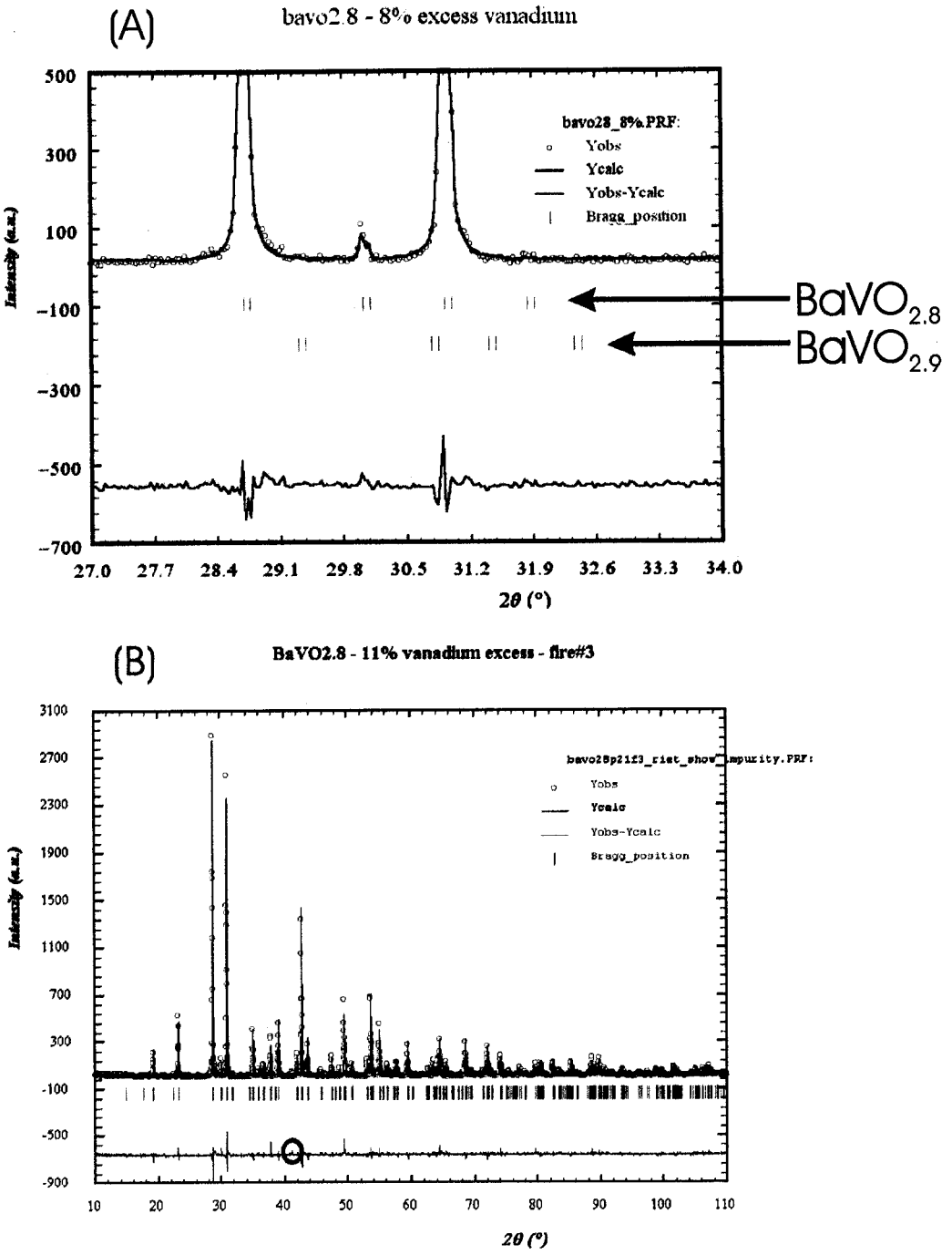


Figure 5.3: Powder X-ray diffraction patterns for the $BaVO_{2.8}$ samples with (a) 8% vanadium excess and (b) 11% vanadium excess. In (a), the $BaVO_{2.9}$ reflection markers have been included to make it clear that this phase is *not present*. The 11% vanadium excess sample contains a small unidentified impurity. The lone impurity peak is circled in the difference pattern at the bottom of this plot.

as this could potentially have introduced more oxygen into the system, and thereby have resulted in the formation of $BaVO_{2.9}$.

The 11% excess vanadium sample contained a mixture of $BaVO_{2.8}$, $BaVO_{2.9}$, $BaVO_{3.0}$, and $Ba_8V_7O_{22}$ from the first firing. Refiring the sample once increased the proportion of $BaVO_{2.8}$, but did not remove the impurity lines. A second refiring produced $BaVO_{2.8}$, and one weak (~1-2%) unidentified impurity line. The magnitude of this peak is compared with the full pattern in figure 5.3(b).

These results indicate that even a slight vanadium deficiency can result in the formation of $Ba_8V_7O_{22}$. This can be avoided by using an excess of vanadium in the initial mixture. It is interesting to note that increasing the quantity of this vanadium excess necessitates a greater number of refirings to obtain a pure product. Each of these refirings would introduce additional oxygen into the system, as well as improving the homogeneity of the products. The composition will be discussed further in section 5.4 using data from inductively coupled plasma mass spectrometry (ICPMS) and powder X-ray diffraction data.

### 5.3.4 Preparation of $BaVO_{3.0}$

As discussed at the beginning of this section, the compound $BaVO_{3.0}$ cannot be prepared directly, as it is not stable at high temperatures.[4] When samples which did not

[4] Results of this work, and those of Liu and Greedan (Liu and Greedan 1994), suggest that $BaVO_{3.0}$ decomposes above ~400°C. Attempts were made to oxidize $BaVO_{2.8}$ using $CO_2$ gas. As this gas is a weaker oxidizing agent, temperatures above 180°C were required before oxidation occurred. The oxidation

contain a vanadium excess were oxidized in air at temperatures from ~150 to 250°C, there were in all cases additional phases present in the product. The additional phases included $Ba_2VO_4$, $Ba_4V_2O_9$, and other unidentified impurities. Oxidation of the 4% excess vanadium sample at 175°C in air for 48 hours produced significant quantities of $Ba_8V_7O_{22}$. This was surprising, considering that the sample before oxidation was determined to be pure by powder X-ray diffraction. The 8% vanadium excess sample contained a few percent of $Ba_8V_7O_{22}$ in the fully oxidized product, as did oxidation of the 11% vanadium excess sample. The $BaVO_{3.0}$ samples with the minimum level of impurity were the 8% and 11% vanadium excess preparations. As a result, these samples were used for the measurements in later sections.[5]

It is relatively difficult to oxidize sintered pellets of $BaVO_{2.8}$. Liu and Greedan reported that is should be possible to synthesize $BaVO_{3.0}$ by heating $BaVO_{2.8}$ pellets in air at 200°C for 24 hours. For the pellets sintered in the induction furnace during this study, a minimum of 4 days, even for very thin pellets, was required to fully oxidize the sample (as determined by the absence of $BaVO_{2.8}$ or $BaVO_{2.9}$ in the powder X-ray diffraction pattern). This is likely related to the fact that the sintered pellets from the induction furnace are extremely dense. Qualitative observations, based upon cutting and grinding operations on these pellets, suggest that the unoccupied volume between crystallites is very low. This hinders the diffusion of oxygen into the pellets, and essentially restricts

---

products using $CO_2$, for the temperature range ~180-400°C, were identical to those obtained from the lower temperature oxidation in air. In addition, oxidation under flowing $O_2$ (g) at lower temperatures did not improve the purity of the product.

[5] These impurity levels are valid for oxidation of very small pellets (~1-2mm thick, less than ~5mm along either side). Larger (and especially thicker) pellets contained higher levels of $Ba_8V_7O_{22}$, or in some cases

the possibilities for oxidation at the center of the pellet; the remaining mechanism involves hopping of oxygen anions between unoccupied sites on the lattice. The fact that $BaVO_{2.8}$ will oxidize slowly even at room temperature indicates that a significant level of ionic diffusion is possible. However, at the low temperatures required to prevent decomposition, this is still an extremely slow process. The impact of this difficulty upon the property measurements will be elaborated upon below.[6]

## 5.4 Chemical and Structural Analysis of $BaVO_{3-x}$

The phase purity and cell parameters have been examined for this series of compounds using a Guinier-Hägg camera with $CuK_{\alpha 1}$ radiation, and a Bruker D8 Advance Bragg-Brentano diffractometer with a $CuK_{\alpha}$ source. Though the purity of these samples has been discussed in the previous section, it is useful to restate this concisely here. The samples lacking in excess vanadium contained weak impurity peaks that could not be identified. The samples with excess vanadium were essentially pure, though a small high angle tail was detected on the strong peaks and attributed to a small degree of chemical inhomogeneity. A weak impurity peak was also detected in the 11% excess vanadium sample. In summary, the level of impurity or inhomogeneity in these samples is present on the order of a few percent or less, according to their powder diffraction patterns.

---

$Ba_3V_2O_8$, even for the samples with vanadium excess. The decomposition product, $Ba_3V_2O_8$, was usually found when higher temperatures were used for the oxidation of large pellets.

[6] Future experiments may show that a low temperature, rapid sintering procedure may result in a poorly sintered pellet, which would likely be more readily oxidized due to the increase in porosity.

The unit cell parameters for a number of preparations used in this study are presented in table 5.3. All of these preparations were carried out in the induction furnace. The data are in good agreement with the results of Liu and Greedan (Liu and Greedan 1994), and differ substantially from the values reported by Chen et al. (Chen, Eichhorn et al. 1993) The slightly smaller cell of Chen et al. implies that their sample may have been slightly oxidized relative to the compounds that have been investigated here.

Table 5.3: Summary of cell information for various preparations of $BaVO_{3-x}$

| Sample | Ba:V ratio (ICPMS) | a (Å) | c (Å) | Volume (Å) |
|---|---|---|---|---|
| $BaVO_{2.8}$ – no V excess - A | 1:1.026(27) | 5.7783(2) | 11.8951(5) | 343.95(2) |
| $BaVO_{2.8}$ – no V excess - B | 1:1.022(11) | 5.7786(4) | 11.898(1) | 344.08(4) |
| $BaVO_{2.8}$ – 4% V excess | 1:1.065(4) | 5.7793(2) | 11.8973(8) | 344.13(2) |
| $BaVO_{2.8}$ – 8% V excess | 1:1.091(7) | 5.7795(1) * | 11.8966(3) * | 344.14(1) * |
| $BaVO_{2.8}$ – 11% V excess | 1:1.357(10) | 5.7794(1) * | 11.8975(2) * | 344.15(1) * |
| $BaVO_{3.0}$ – 8% V excess | 1:1.091(7) | 5.6650(4) | 11.457(2) | 318.42(5) |
| $BaVO_{3.0}$ – 11% V excess | 1:1.357(10) | 5.6671(4) | 11.464(1) | 318.86(4) |
| Previous work | | | | |
| $BaVO_{2.8}$ – Liu et al. | - | 5.7774(5) | 11.893(1) | 343.77(5) |
| $BaVO_{2.8}$ – Chen et al. | - | 5.7685(2) | 11.876(1) | 342.22(4) |
| $BaVO_{3.0}$ – Liu et al. | - | 5.6673(8) | 11.466(2) | 318.91(7) |

* Obtained from Rietveld refinement of D8 Advance powder X-ray diffraction data; all other information was refined from Guinier-Hägg data.

It is surprising to note that a nominal vanadium molar excess up to 11% has essentially no effect on the cell parameters. This suggests that not all of the excess vanadium has been incorporated into the lattice. The ICP-MS results are shown in table 5.3. The Ba:V ratios are close to the expected values, with the exception of the 11% sample. In accordance with the diffraction results, it is likely that at least a fraction of the

excess vanadium is present as a small amount of impurity. This impurity could have been small enough to remain undetected in the powder diffraction data. The small impurity level should not impact significantly upon the property measurements.

## 5.5 Magnetic Susceptibility

### 5.5.1 Bulk DC Susceptibility of $BaVO_{3.0-x}$

A Quantum Design Squid Magnetometer was used to collect DC magnetic susceptibility data over a temperature range from 5 to 350K. Applied fields ranging from 100Oe to 1000Oe were used for these measurements. The Curie-Weiss law (equation 1.2.9) was used to fit data in the upper temperature range. A transition representing collective magnetic behavior is indicated by a divergence between the field cooled (FC) and zero-field cooled (ZFC) data. The temperature at which a ZFC/FC divergence occurs ($T_D$), along with results from the Curie-Weiss law fits, are presented in table 5.4. Plots of the susceptibility data are shown in figures 5.4 to 5.6.

The samples have been distinguished in the previous section based upon whether or not excess vanadium was added to the reaction mixture. There were essentially no significant differences noted between the cell constants of various $BaVO_{2.8}$ samples prepared using the induction furnace method. Similarly, there is no obvious variation in the Curie constant ($C_{exper}$) or Curie-Weiss constant ($\theta$) with excess vanadium. The values obtained for $BaVO_{2.8}$ are similar to those of Liu and Greedan, but never approach the results reported by Chen et al. Therefore, the DC susceptibility results appear to support the analysis of Liu and Greedan, over that of Chen et al. In the model of Liu and

Greedan, the $V_3O_{12}$ trimer of face-sharing octahedra should be composed of a $V^{3+}$-$V^{4+}$-$V^{3+}$ unit. Strong antiferromagnetic coupling of the spins in the trimer results in a net spin of 3/2. When the trimer spin is combined with the remaining noninteracting $S$ = ½ cations (tetrahedrally coordinated by oxygen), and averaged over all five ions, the experimentally observed $S$ = ½ *per vanadium atom* result is obtained.

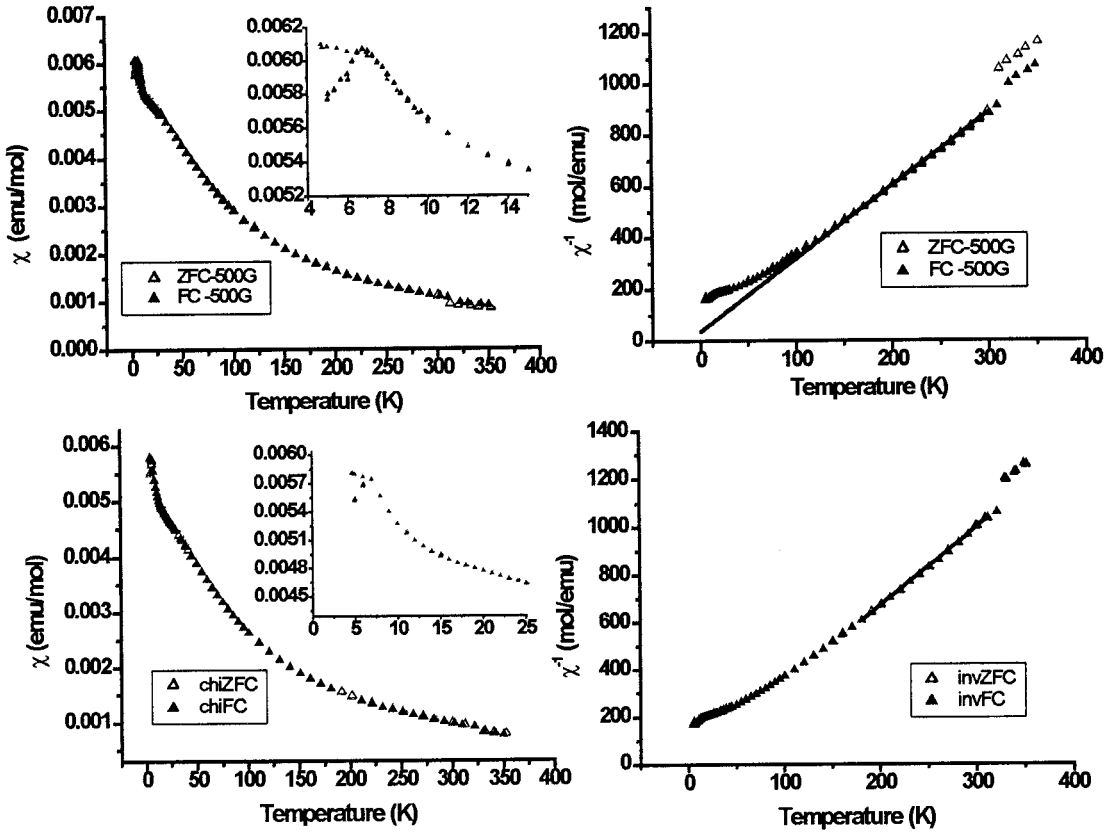


Figure 5.4: DC magnetic susceptibility data for two $BaVO_{2.8}$ samples prepared in the induction furnace with no vanadium excess. Top: Sample A. Bottom: Sample B. Data were collected at 500Oe in each case.

A divergence between the FC and ZFC susceptibility data has been reported by Chen et al. to occur at low temperatures in $BaVO_{2.8}$; this was ascribed to low level ferromagnetic impurities. A divergence of this type was not reported by Liu and

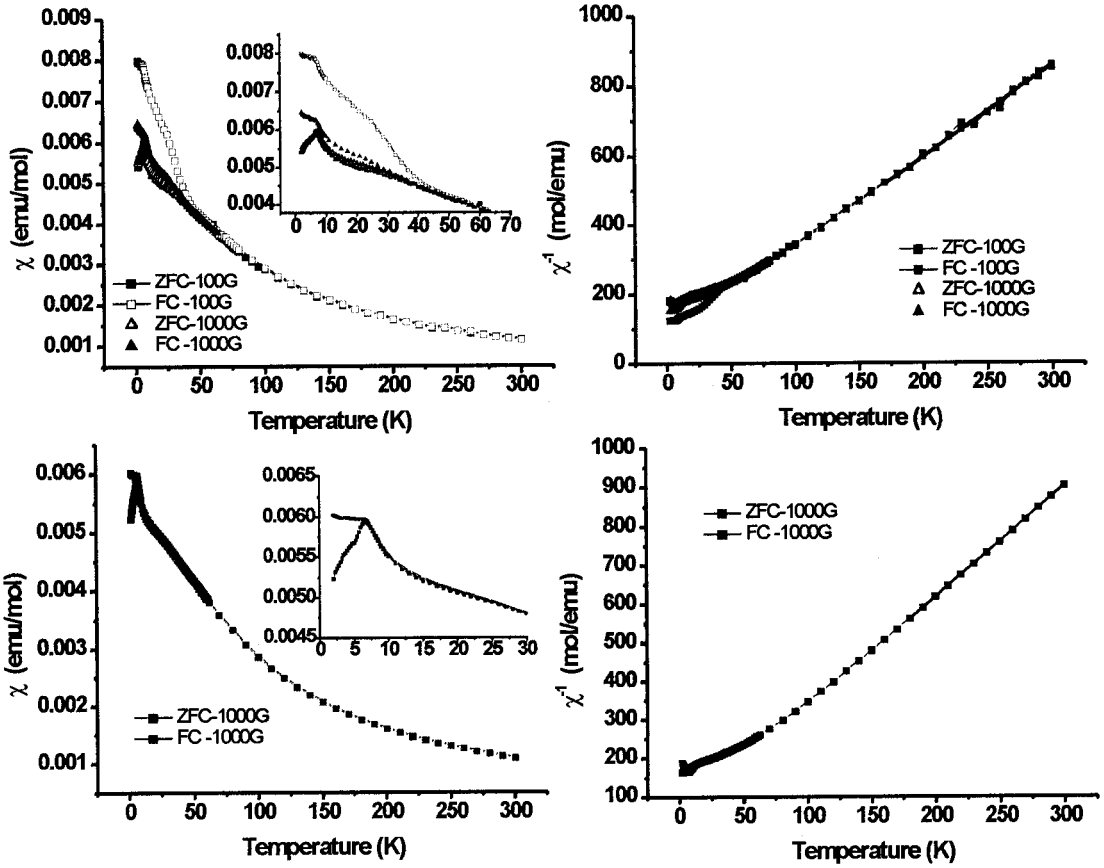


Figure 5.5: DC magnetic susceptibility data for two $BaVO_{2.8}$ samples prepared in the induction furnace with vanadium excess. Top: 8% vanadium excess. Bottom: 11% vanadium excess. Data were collected at 1000Oe in each case, and additionally at 100Oe for the 8% excess sample.

Greedan, which may be due to the fact that the FC susceptibility was not measured (at least this was not reported in the paper). Rather, Liu and Greedan found a broad susceptibility maximum near 20K – a feature typically found in conjunction with short-range magnetic correlations. For all samples in this study, a divergence has been observed near 7K, as presented in table 5.4. The FC/ZFC divergence can be observed in a variety of systems, including spin glasses, superparamagnets, and canted

antiferromagnets. Lack of further data in previous studies meant that these possibilities could not be distinguished.

An additional divergence is observed at higher temperatures for the 8% vanadium excess sample. The high temperature divergence is field dependent, occuring near 50K for a 100Oe field, and ~35K at 1000Oe. Both the divergence and field dependence are expected for a spin glass or cluster glass material.

Table 5.4: DC susceptibility data results for the series $BaVO_{3-x}$

| Sample | $C_{exper}$ (emuK/mol) | θ (K) | TIP (emu/mol) | $T_D$ (K) |
|---|---|---|---|---|
| $BaVO_{2.8}$ – no V excess - A | 0.354(3) | -13(2) | -[a] | 6.75 |
| $BaVO_{2.8}$ – no V excess - B | 0.305(3) | -4(3) | - | 7 |
| $BaVO_{2.8}$ – 8% V excess | 0.380(8) | -27(5) | - | 6.75 |
| $BaVO_{2.8}$ – 11% V excess | 0.351(1) | -18(1) | - | 6.75 |
| $BaVO_{3.0}$ – 8% V excess | - | - | - | - |
| $BaVO_{3.0}$ – 11% V excess | 0.00193(5) | -1.0(2) | $1.80(1)\times10^{-4}$ | - |
| Previous work | | | | |
| $BaVO_{2.8}$ – Liu et al. | 0.385(2) | -28.5(7) | $1.0(7)\times10^{-5}$ | -[b] |
| $BaVO_{2.8}$ – Chen et al. | 0.48 | -53 | negligible | -[c] |
| $BaVO_{3.0}$ – Liu et al. | 0.0116(7) | -6.9(9) | $4.96(7)\times10^{-4}$ | - |

$C_{exper}$ is the experimentally derived Curie constant; θ = Curie-Weiss constant; $T_D$ = divergence temperature; TIP = temperature independent term

[a] The high temperature region was determined to be linear for $BaVO_{2.8}$ in this study. As a result, the temperature independent term was not applied.

[b] Field cooled data was not reported.

[c] Divergence was reported, but an exact temperature was not given.

AC magnetic susceptibility, heat capacity, and powder neutron diffraction data will be examined in the following sections to provide a more thorough understanding of the low temperature magnetic behavior in this material.

# NOTE TO USERS

Page(s) not included in the original manuscript and are unavailable from the author or university. The manuscript was scanned as received.

253

This reproduction is the best copy available.

UMI®

those of Liu and Greedan. In particular, the smaller Curie constant may be an indication that the level of paramagnetic impurity in the 11% vanadium excess sample is lower than in the previous study. Guinier-Hägg powder X-ray diffraction analysis of this sample show that the sample is essentially pure; this result, combined with the DC magnetic susceptibility data, led to the use of this pellet for resistivity measurements described in section 5.11.

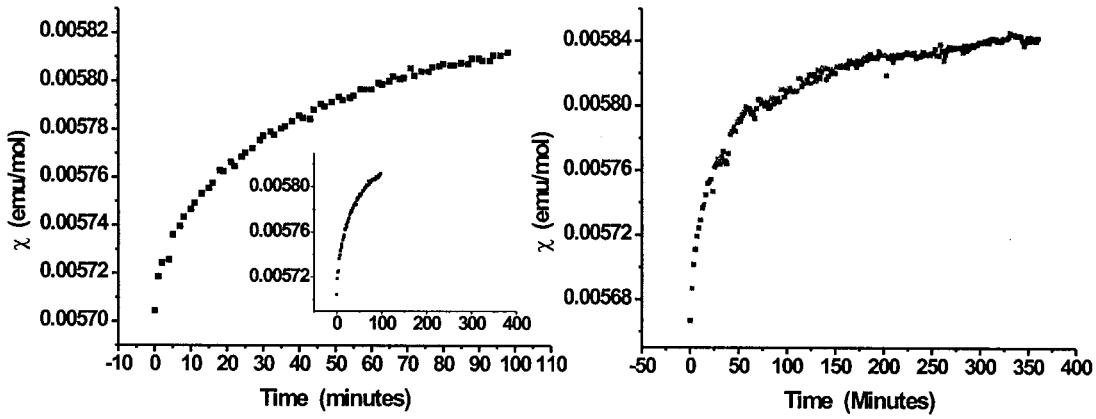


Figure 5.7: Relaxation measurements performed at 5K using a Quantum Design SQUID magnetometer for two $BaVO_{2.8}$ samples prepared in the induction furnace. Left: Sample A - no vanadium excess. Data were collected at 500Oe. Right: 11% vanadium excess. Data were collected at 1000Oe. The inset in the left plot has been scaled to illustrate the near equivalence of the two data sets.

### 5.5.2 Relaxation Measurements on $BaVO_{2.8}$

Isothermal magnetic measurements versus time were performed on a Quantum Design SQUID magnetometer for a sample with no vanadium excess (sample A in tables 5.1 and 5.2), and the sample with 11% vanadium excess. These data are plotted in figure 5.7. The samples were first cooled to 5K in the absence of a field. A delay of approximately 30 minutes was allowed before turning on the field, at which point the

susceptibility was immediately measured. These plots demonstrate the near equivalence of the relaxation behavior in these two samples below the divergence temperature (~7K). This relaxation is consistent with spin glassy behavior.

### 5.5.3 Bulk AC Susceptibility Results for $BaVO_{2.8}$

A sintered pellet of 8% vanadium excess $BaVO_{2.8}$ was measured in a Quantum Design Physical Property Measurement System (PPMS); the results are presented in figure 5.8. The parameters for the measurements include: a 10 Oe driving field; 50 Oe static field; frequencies of 500Hz, 1000Hz, 5000Hz, and 10000Hz; a temperature range of 2 to 70K. Data for all four frequencies were collected simultaneously, rather than measuring over the entire temperature range at a given frequency. As encountered with AC susceptibility measurements of $BaV_{10}O_{15}$, the out-of-phase component ($\chi''$) is negative over a range of temperatures; the reason for this is likely a calibration error of the coil at that frequency. As the feature in $\chi''$ is so weak, only a small error in the calibration would be required to produce this effect.

When compared with the DC susceptibility data, we see that a cusp in the in-phase component, $\chi'$, occurs at nearly the same temperature as $T_D$. There is a frequency dependence in the magnitude of both $\chi'$ and $\chi''$, as is expected for spin glassy materials. However, a shift in $T_D$ with frequency, as is also typically observed in glassy systems, cannot be discerned from the available data. A simple calculation involving the empirical

# NOTE TO USERS

## 5.6 Powder Neutron Diffraction Results for $BaVO_{2.8}$

A sample of $BaVO_{2.8}$ with no excess vanadium (sample A) was examined on the C2 powder neutron diffractometer in Chalk River. Data sets were collected both above (30K) and below (1.5K) the divergence temperature observed in the bulk magnetic susceptibility measurements. The results demonstrate the absence of long range magnetic ordering in this sample. This is most clearly evident from the difference plot, created by subtracting the 30K data from the 1.5K data, shown on the bottom of figure 5.9; the plot is devoid of any peaks that could indicate magnetic ordering. Note that there are indications from the plot, in particular from peaks near 40 and 52 degrees two theta, that a small, unidentified impurity is present. This will not affect the conclusion that no magnetic long range ordering occurs in this material. It is justified to believe that none of the other $BaVO_{2.8}$ samples exhibit long-range magnetic ordering, on the basis that the DC magnetic susceptibility data are quite similar for all of the samples.

## 5.7 Heat Capacity of $BaVO_{2.8}$

Specific heat measurements based upon the relaxation method were carried out on an Oxford Instruments MagLab property measurement system. The sample was affixed onto the measurement chip using Wakefield grease, which also provided a medium for proper thermal contact. The data were collected over a temperature range of 3.4K to 70K (figure 5.10). A fit was performed over a relatively narrow temperature range, from 4.0 to 5.3K, using equation 3.6.2. The slope and intercept correspond to the coefficients $\beta$ and $\gamma$, respectively. The values of these coefficients are 0.00132(3) J/molK$^4$ for $\beta$, and

0.0323(5) J/molK$^2$ for $\gamma$. The large ground state degeneracy for a spin glass material is expected to enhance $\gamma$, producing a significant intercept in a plot of C/T vs $T^2$. A linear term may also be produced by the electronic component of the heat capacity in a metal. As this material is semiconducting, the carriers are not expected to contribute to a linear term at low temperatures.

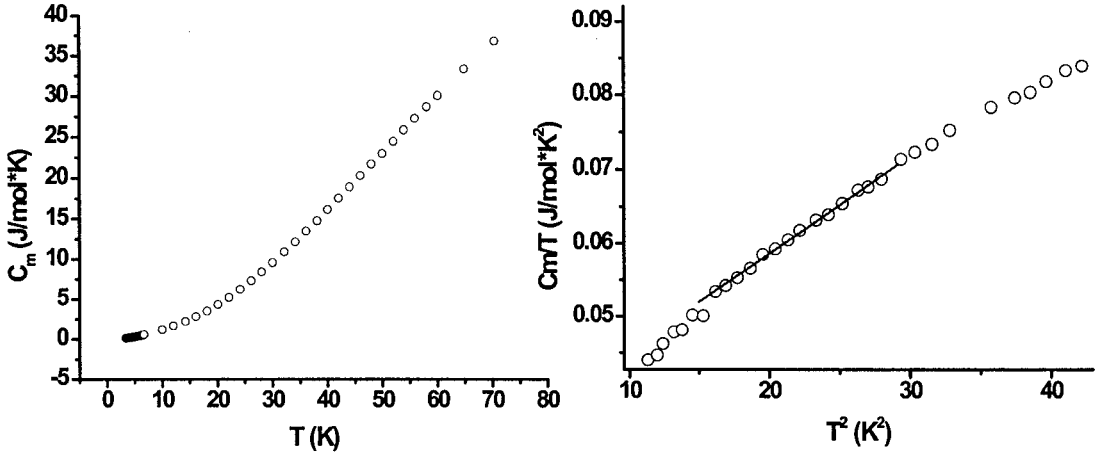


Figure 5.10: Heat capacity data collected using the relaxation method for a sample of $BaVO_{2.8}$ with no molar excess of vanadium (sample A). The fitted line in the right plot is for the Debye model ($\beta T^3$) plus a linear electronic term ($\gamma T$).

As a good lattice standard is not available for $BaVO_{2.8}$, no attempt has been made to extract the magnetic entropy in this case. It is useful to note that no anomaly is present over the measured temperature range. The absence of a peak is relatively clear near 50K, where the higher temperature divergence was observed in the DC susceptibility of this sample. However, it proved difficult to measure the heat capacity over the temperature range from 6.7K to 10K. This difficulty occurs suspiciously close to the cusp in the bulk magnetic susceptibility data. If the time constant changes rapidly near a transition, due to

an extremely sharp peak, the relaxation method can prove unreliable; when an improper time constant is chosen the measured relaxation curves are useless.

## 5.8 Summary of Magnetic Properties for $BaVO_{2.8}$

A cusp has been observed in the low temperature DC and AC bulk magnetic susceptibility that is indicative of cooperative magnetism. Liu and Greedan, and Chen et al., have previously reported this feature from DC magnetic susceptibility data alone. The magnitude of the Curie constant for various samples is consistent with the results of Liu and Greedan. Therefore, the antiferromagnetic coupling model of Liu and Greedan is favored over the V-V bonding model of Chen et al. The current study has shown conclusively using neutron powder diffraction data, that long-range ordering does not occur down to 1.5K in $BaVO_{2.8}$. Results from heat capacity and AC susceptibility measurements do not clearly distinguish between the possibilities of superparamagnetism or spin-glassy behavior as the origin of the divergence in the DC susceptibility.

## 5.9 Transport properties of $BaVO_{2.8}$

### 5.9.1 DC resistivity measurements

While unusual problems with contact resistance precluded any resistivity measurements on the 11% vanadium excess sample, difficulties were not encountered in collecting data on the 8% vanadium excess sample. Silver wire was affixed to the sample using silver epoxy, and allowed to dry overnight to ensure that the epoxy had fully set.

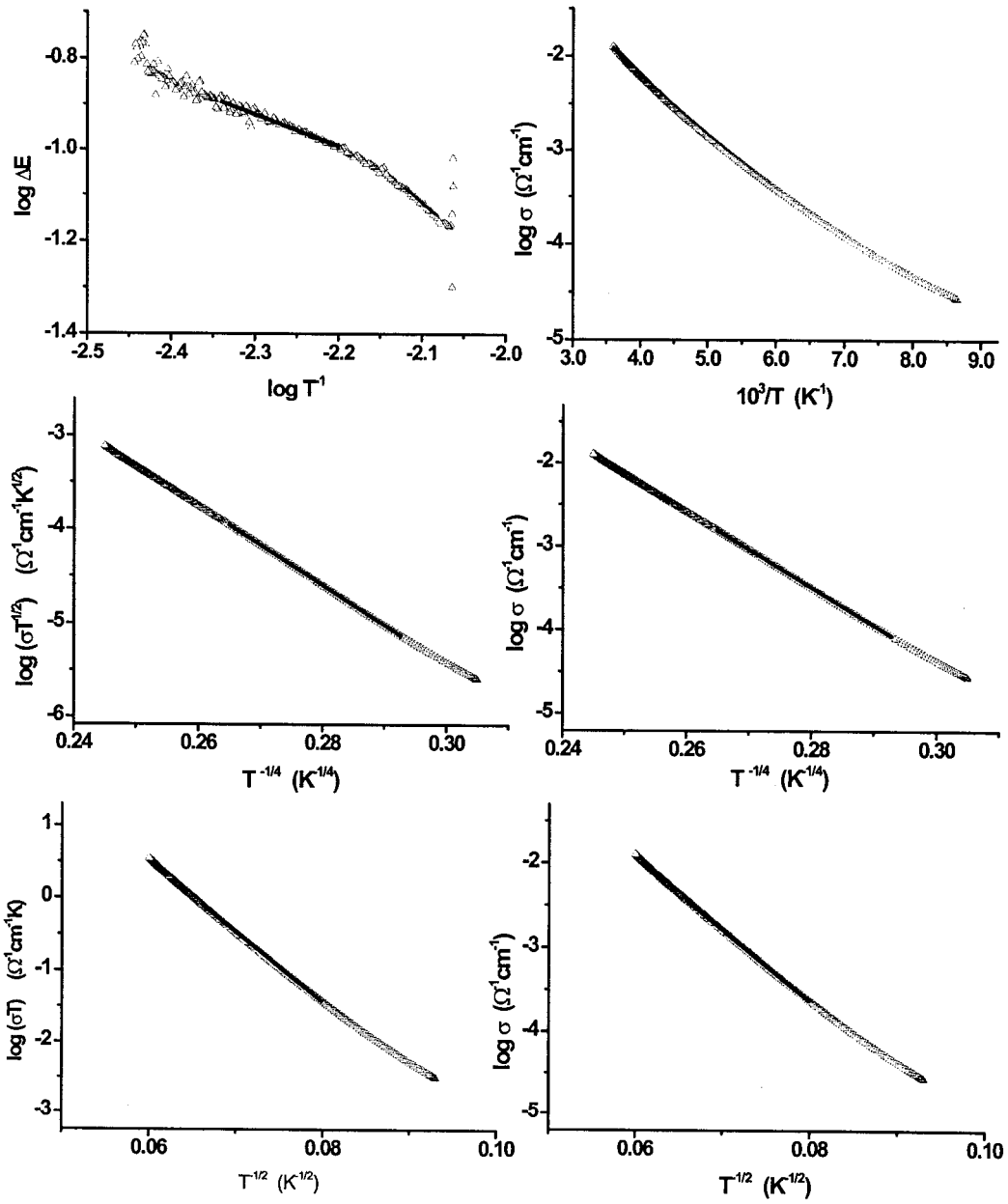


Figure 5.11: DC resistivity measurements collected on a Oxford Instruments MagLab device for the 8% molar excess vanadium $BaVO_{2.8}$ sample. Plots related to various conductivity models have been included. Top Left: Plot of the reduced activation energy for analysis of the conduction exponent. Top Right: Arrhenius plot. Middle: Plotted according to Mott 3D variable range hopping with and without a temperature dependent prefactor. Bottom: Plotted according to Efros-Shklovskii variable range hopping with and without a temperature dependent prefactor. It is difficult to distinguish visually between the two different VRH models from these plots.

DC resistance data were collected on an Oxford Instruments MagLab measurement system, over a temperature range from 278K to 115K, using a four-probe geometry.

An estimate of the activation energy for conduction at high temperatures was obtained from a fit to the Arrhenius equation, over the range 258K to 278K. The intercept of the fit is given in appendix C. Careful examination of the data reveals that a mild curvature persists in the slope for this region. As a result, the derived value, 0.156(1)eV, represents a lower limit of the true high temperature activation energy. This is a much lower energy than the value of 0.52eV reported previously by Liu and Greedan. This could be an indication that the 8% vanadium excess sample is somewhat oxidized. However, the Curie constant obtained from the DC magnetic susceptibility data, in addition to the large volume of the unit cell determined by powder X-ray diffraction analysis, do not suggest that oxidation of the sample has occurred. It is therefore possible that grain boundary effects contributed to the estimate obtained by Liu and Greedan. It is rather common to find such differences for measurements on polycrystalline pellets. The high density of the pellets obtained from the induction furnace method could have minimized the grain boundary effects for the 8% vanadium excess sample of $BaVO_{2.8}$.

In the low temperature region (defined here as less than 250K), the analysis of Hill (described in section 3.9.1) was used to determine the exponent ($\gamma$) of the conductivity. The results are given in figures 5.11 and 5.12, and table 5.5. The data were fitted over a temperature range from 158K to 225K, and over the lower temperature

region of 121K to 131K. The resulting exponents are 0.31(2) and –0.65(4).[9] The negative exponent is not a physical result in the context of standard small polaron or variable range hopping models. The slope of the Arrhenius plot is curved in this temperature range, which indicates that the activation energy for conduction is changing. This is expected for variable range hopping, in which the exponent is given by:

$$\gamma = 1/(d+1), \quad (5.9.1)$$

where $d$ is the dimensionality for Mott's variable range hopping. Note that as the dimensionality cannot be negative, a negative $\gamma$ is not physical. However, the positive exponent is within error of the value expected for Mott VRH in two dimensions, a model which is often applied to measurements on thin films.[Overhof, 1998 #114] This is not unrealistic for $BaVO_{2.8}$, given that the structure is quasi-two-dimensional.

Table 5.5: Application of various models of conduction to the low temperature behavior of $BaVO_{2.8}$

| | Mott 2D-VRH | Mott 3D-VRH | | ES VRH | | $\gamma$ |
|---|---|---|---|---|---|---|
| x (%) | $T_{Mott\text{-}2D}$ (K) | $T_{Mott\text{-}3D}$-pre (K) | $T_{Mott\text{-}3D}$ (K) | $T_{ES}$-pre (K) | $T_{ES}$ (K) | |
| 8 | 1.795 (2)×$10^6$ | 9.06 (1)×$10^7$ | 1.203 (3)×$10^8$ | 4.92 (1)×$10^4$ | 3.77 (1)×$10^4$ | 0.31(2) |

x = percent of excess vanadium used in preparation; $T_{Mott}/T_{ES}$ = characteristic temperature for the Mott/Efros-Shklovskii (ES) models of variable range hopping (VRH) - the suffix 'pre' indicates that a temperature-dependent pre-exponential factor was used in the fit; $\gamma$ = low temperature hopping exponent derived from the data.

[9] Remember that the exponent is calculated from (1+$m$), where $m$ is the slope extracted from the Hill analysis (section 3.9.1).

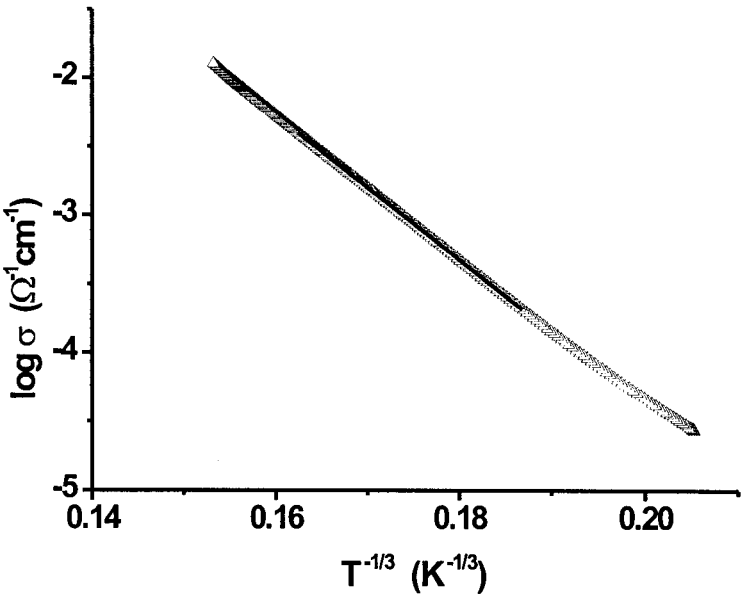


Figure 5.12: DC resistivity measurements collected on a Oxford Instruments MagLab device for the 8% molar excess vanadium $BaVO_{2.8}$ sample. Data has been plotted according to Mott 2D variable range hopping.

### 5.9.2 Thermoelectric measurements

The DC resistivity measurements have been analyzed on the basis of a constant activation energy at high temperature, and Mott 2D variable range hopping at low temperature. A minimum of one other experiment, such as Hall effect, thermopower, or AC conductivity measurements, should be performed to validate these results. Thermoelectric measurements have been performed on the 8% and 11% vanadium excess samples. These data are presented in figure 5.13. The important qualitative results from these measurements include:

(1) The thermopower is positive over all temperatures, indicating that conduction occurs primarily through holes.

(2) A maximum is observed near ~250-260K in both samples, which indicates a crossover in the conduction mechanism. Activation energies extracted from the DC resistivity data in the previous section were fitted at temperatures above 250K due to the results of the thermopower data (table 5.6).

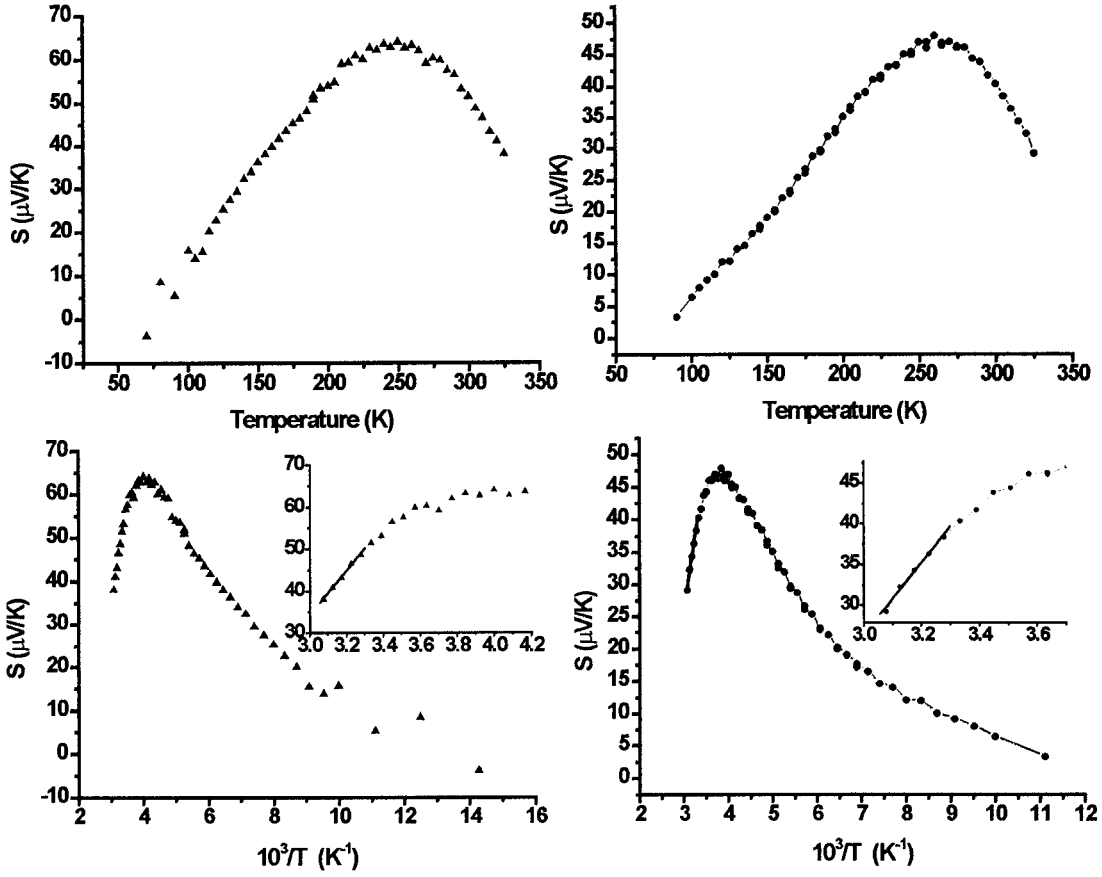


Figure 5.13: Thermoelectric measurements for the 8% (left plots) and 11% (right plots) molar excess vanadium $BaVO_{2.8}$ samples. Bottom: Plotted according to a model of band semiconduction. The insets show the fitted region more clearly.

In order to distinguish between band and polaronic conduction at high temperature, the activation energies for carrier creation ($E_a$) have been extracted from the thermopower data according to equation 1.4.21. The difference between $E_\sigma$ and $E_a$ is

expected to give $E_\mu$. As shown in table 5.6, a significant hopping activation energy ($E_\mu$) is present. This result suggests that the main mode of conduction is by small polaron hopping above the maximum in the thermopower. However, to be confident of these values it will be necessary to collect resistivity and thermopower data to higher temperatures.

The thermopower decreases below the maximum in a manner consistent with variable range hopping, as seen in figure 5.14. The thermopower data were fit to the VRH model over approximately the same range as were the resistivity data. The data are unfortunately not of a high enough quality to distinguish between the 3D and 2D Mott VRH models. To illustrate this point, fits to both the 3D and 2D VRH models are shown in figure 5.14.

A change in slope is observed for the thermopower data of the 11% vanadium excess sample near ~165K. However, a similar change in slope is not obvious for the thermopower data of the 8% vanadium excess sample. While it is not obvious in both sets of data, the change in slope may reflect a change in the conduction mechanism. Note that it corresponds approximately with the deviation from linearity observed below ~158K in the Hill analysis of the DC resistivity data, for the 8% vanadium excess sample. The mechanism of conduction below this temperature (~155-165K) is likely some form of variable range hopping, but is not clear from the current combination of resistivity and themopower data.

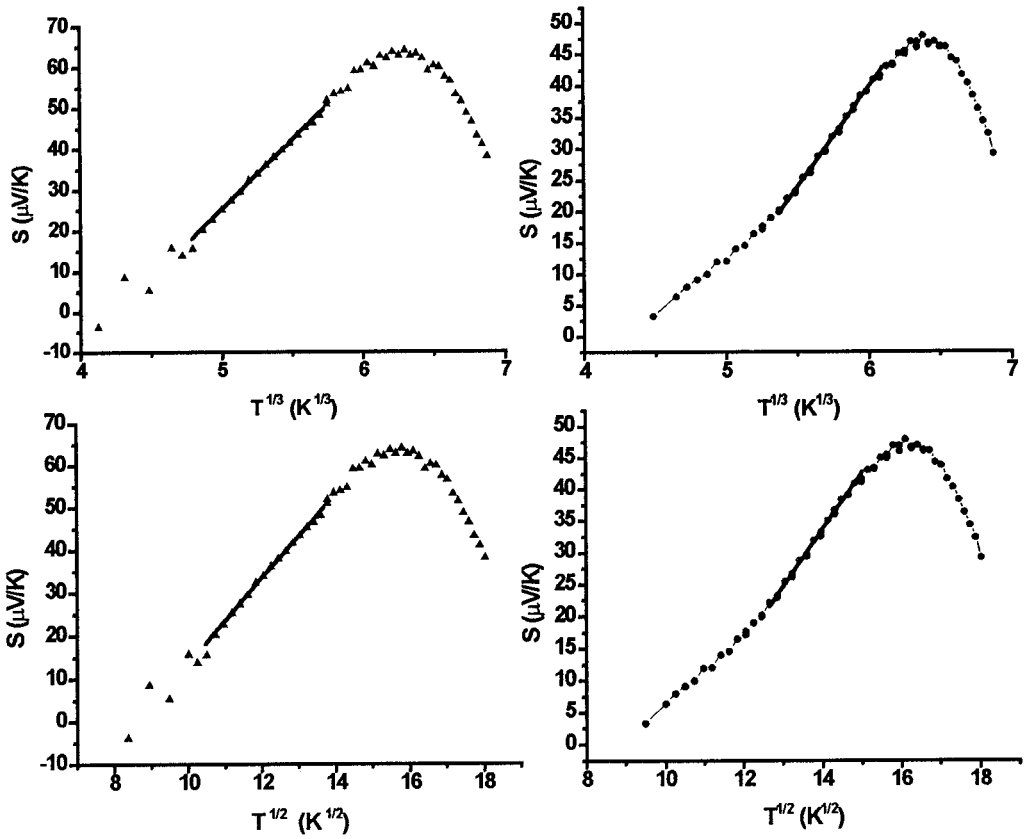


Figure 5.14: Thermoelectric measurements for the 8% (left plots) and 11% (right plots) molar excess vanadium $BaVO_{2.8}$ samples. The plots are related to VRH models. Top: Plotted according to Mott 2D variable range hopping (versus $T^{1/3}$). Bottom: Plotted according to Mott 3D variable range hopping (versus $T^{1/2}$). This figure illustrates how difficult it is to distinguish between the 2D and 3D models based upon these plots.

Table 5.6: Analysis of the high temperature thermopower data for $BaVO_{2.8}$

| Sample | $E_\sigma$ | $E_a$ | $E_\mu$ |
|---|---|---|---|
| $BaVO_{2.8}$ – 8% V excess | 0.156(1) | 0.053(2) | 0.103(2) |
| $BaVO_{2.8}$ – 11% V excess | - | 0.044(3) | - |

$E_\sigma$ = activation energy of conduction from DC resistivity measurements; $E_a$ = activation energy for carrier creation determined from the thermopower data; $E_\mu$ = energy for hopping; all energy values are in units of eV

## 5.11 Transport properties of $BaVO_{3.0}$

### 5.11.1 AC resistivity measurements

A small pellet of 11% vanadium excess $BaVO_{2.8}$, which has been oxidized for four days in air at 260°C, was chosen for resistivity measurements. This is the same pellet that was discussed in section 5.5; powder X-ray diffraction and DC magnetic susceptibility measurement have indicated that this pellet was fully oxidized to $BaVO_{3.0}$. It is therefore surprising that metallic behavior was not observed from 5 to 270K, as had been observed by Liu and Greedan. The data are presented as the left plot in figure 5.15. Moreover, the resistivity is nearly two orders of magnitude higher than reported by Liu and Greedan. An increase in the resistivity could be created by the presence of an impurity phase in the sample, but there was no significant level of impurity detected by the X-ray diffraction analysis. A further oxidation of four days slightly increased the resistivity, as shown on the right side of figure 5.15; this was later shown by X-ray diffraction analysis to be due to the formation of $Ba_3V_2O_8$ impurities.

The resistivity in this material is expected to be highly anisotropic, which may aid in explaining why metallic behavior was not observed. This is reflected in the apparent 2D VRH conductivity seen in the $BaVO_{2.8}$ sample. It is possible that if the grains in the pellet of $BaVO_{3.0}$ are highly oriented, and the resistivity highly anisotropic, that the current could be travelling along a more resistive path in the crystal. Unfortunately, the pellet was destroyed before this possibility could be tested. Another possibility is that defect states in the 11% vanadium excess sample have interrupted the transition to

metallic behavior, due to Anderson-type localization at the band edge. More work is required to discern why the metallic phase was not obtained in this (or any other) sample.

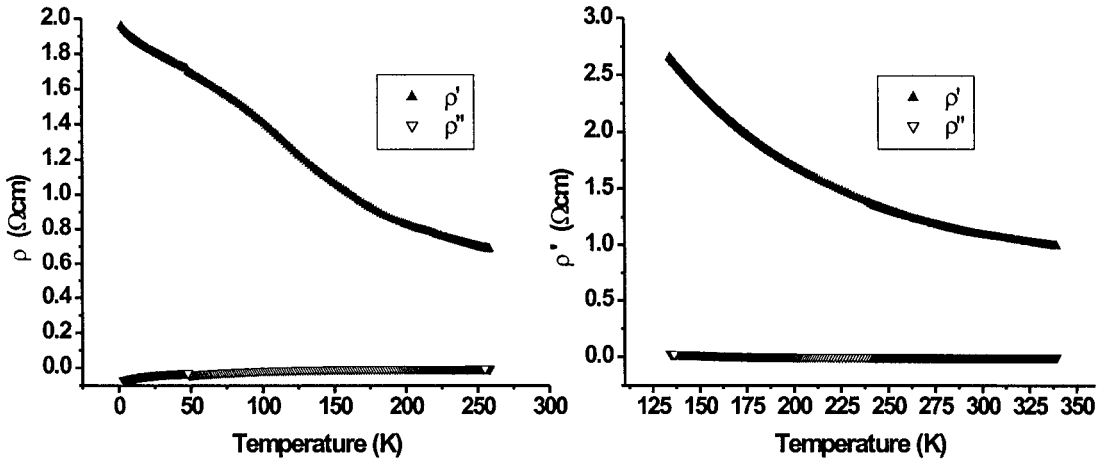


Figure 5.15: AC resistance measurements collected on a Oxford Instruments MagLab device for the 11% molar excess vanadium $BaVO_{2.8}$ sample which has been oxidized in air at 260°C. This is a relatively pure sample of $BaVO_{3.0}$. Left: Plot of the resistivity after four days of oxidation. Right: Plot of the resistivity after a total oxidation time of 8 days for the same pellet. The resistivity is higher after 8 days of oxidation.

### 5.11.2 Thermoelectric measurements

Unfortunately, it proved impossible during this study to produce a sintered pellet of $BaVO_{3.0}$, of an adequate size for thermoelectric measurements on our apparatus, which did not contain significant impurity levels. As has been noted, larger pellets are difficult to oxidize in pure form. Data has been collected on a sample of the 11% vanadium excess preparation that has been oxidized at 375°C under oxygen. The higher temperatures required to oxidize the relatively large pellet have resulted in an impurity level of $Ba_3V_2O_8$ on the order of ~15%. A Rietveld refinement of this sample has been performed, and a plot of the fit is given in figure 5.17.

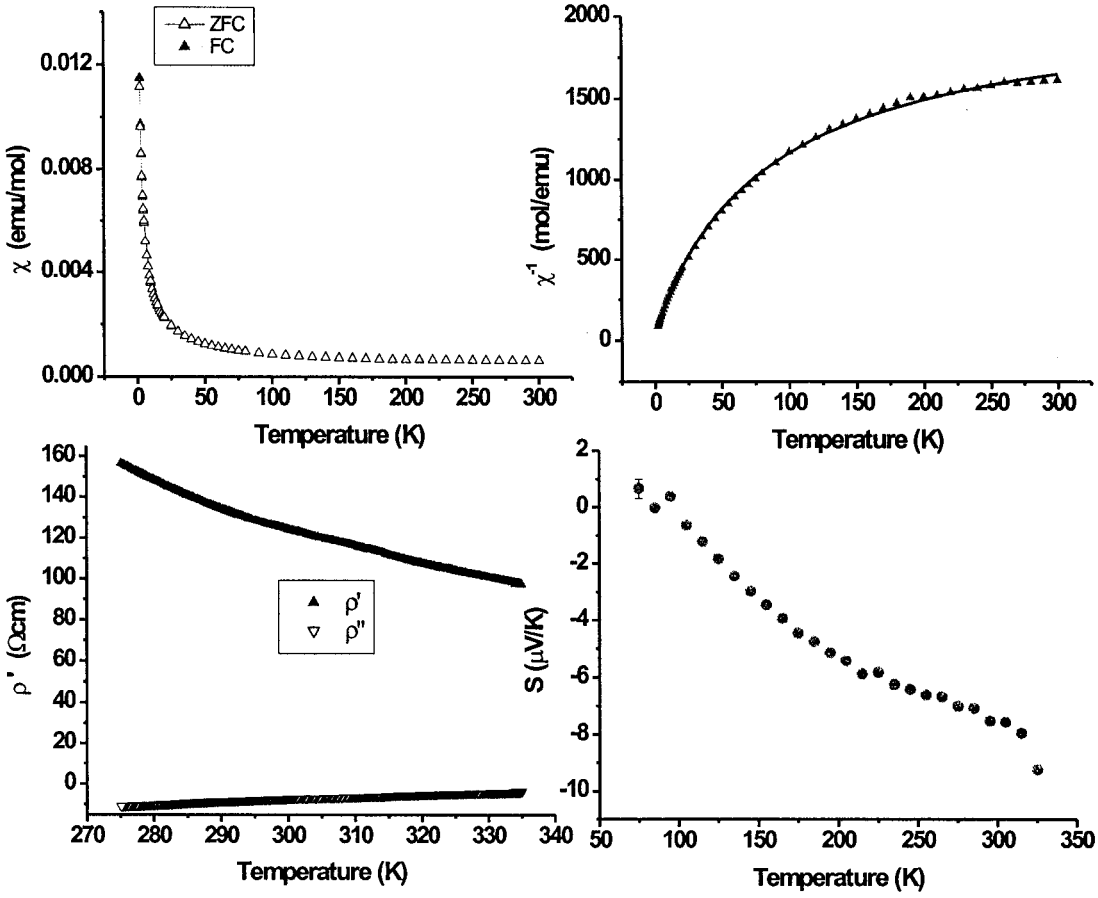


Figure 5.16: DC susceptibility, resistivity and thermopower data for the 11% molar excess vanadium $BaVO_{2.8}$ sample which has been oxidized in under oxygen at 375°C for four days. Top: DC magnetic susceptibility data collected on a Quantum Design SQUID magnetometer. Bottom Left: Plot of the AC resistivity. Bottom Right: Plot of the thermoelectric response.

Resistivity measurements on this sample are presented beside the thermoelectric data. The data, plotted as the resistivity in figure 5.16, show the same qualitative trend as the smaller pellets (which were oxidized at a lower temperature). The main difference is that the curve is displaced towards more insulating values, presumably due to the significant level of $Ba_3V_2O_8$. Due to the high level of impurity it is difficult to draw

quantitative conclusions about the data. It was not possible to measure down to the lowest attainable temperatures due to large potential fluctuations caused by the presence of a resistive impurity. Despite this difficulty, it is clear that oxidation of the $BaVO_{2.8}$ to $BaVO_{3.0}$ has favored *electron* conduction over hole conduction. An increasingly dominant hole contribution results in a Seebeck response near zero with decreasing temperature. In addition, the magnitude of the Seebeck coefficient is in the range expected for metallic conduction.

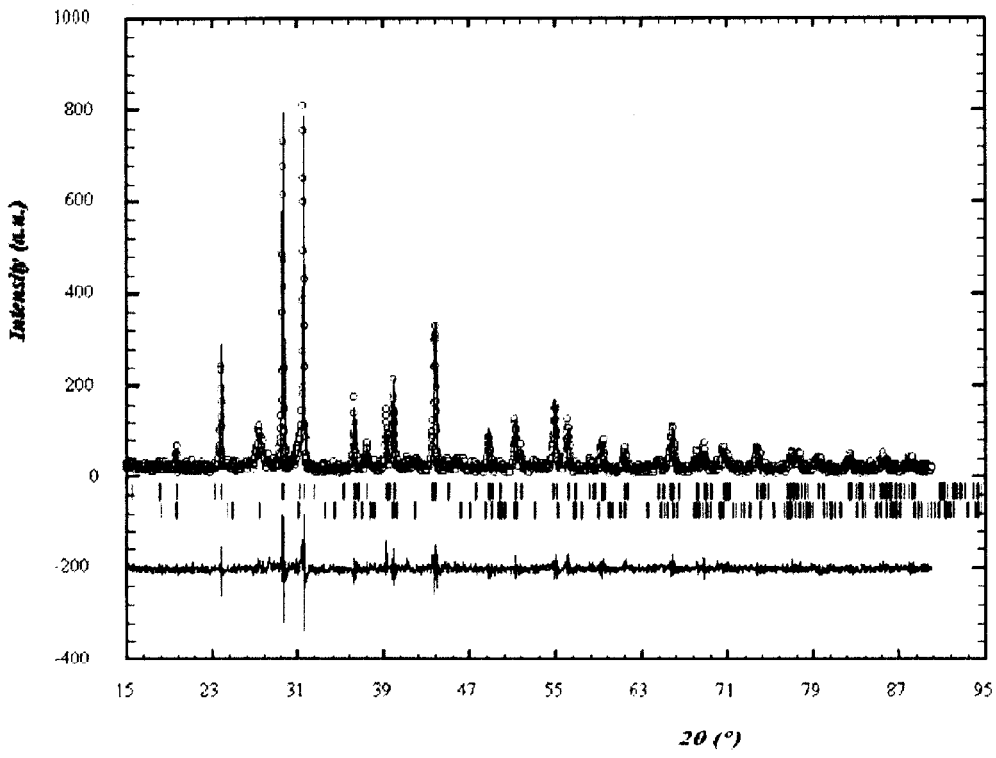


Figure 5.17: Powder X-ray diffraction data for the 11% molar excess vanadium $BaVO_{2.8}$ sample which has been oxidized in under oxygen at 375°C for four days. The upper vertical bars represent reflection markers for the $BaVO_{3.0}$ phase. The lower reflection markers are for the $Ba_3V_2O_8$ impurity phase.

## 5.12 Summary of Transport Property Measurements

A combination of thermopower and resistivity measurements have provided evidence that conduction occurs by small polaronic hopping of holes, with a significant carrier activation energy, in the semiconducting material $BaVO_{2.8}$. Below ~255K, a transition to two-dimensional variable range hopping behavior is proposed.

Metallic behavior was not obtained in an apparently pure sample of $BaVO_{3.0}$. A thermoelectric measurement on a larger, somewhat impure pellet indicates that a crossover to electron conduction occurs due to the oxidation of $BaVO_{2.8}$ to $BaVO_{3.0}$.

## 5.13 Conclusions

Results from heat capacity and AC susceptibility measurements were not able to clearly distinguish between superparamagnetism or spin-glassy behavior as low temperature magnetic ground state. DC susceptibility data favor the antiferromagnetically coupled trimer model of Liu and Greedan. It is somewhat surprising in the light of the strong coupling proposed by this model, that no short-range magnetic order is evident in the neutron diffraction data.

A combination of thermopower and resistivity measurements have provided evidence that a crossover occurs from small polaronic hopping of holes at high temperature, to two-dimensional variable range hopping behavior at low temperature in $BaVO_{2.8}$. Metallic behavior was not obtained in an apparently pure sample of $BaVO_{3.0}$, though thermopower measurements indicate that the dominant carrier has changed from

holes to electrons with increased oxygen content. While it may seem inconsistent to discover that oxidation of a sample would result in a transition to *n*-type conduction, the doping of oxygen into $BaVO_{2.8}$ must produce significant changes in the band structure - changes that may place the Fermi level in the lower part of the conduction band.

# Chapter 6

# Conclusions and Future Work

The compound $BaV_{10}O_{15}$ has been characterized as a highly frustrated material, with temperature dependent transitions visible in the magnetic and transport properties. These transitions have been correlated to a sample dependent, first-order structural phase transition. A decrease in the structural transition temperature correlates well with an increase in the *b* axis length. In addition, the lowest transition temperature (~100K) occurs in the most oxidized sample. Single crystal work has shown a decrease in certain V-V distances, which has been attributed to metal-metal bond formation in the low temperature phase. Furthermore, the atomic displacement factors decrease dramatically upon passing from the high temperature (Cmca) phase into the low temperature (Pbca) phase.

An important extension to this work would be to map out the changes in V-V bond-distance and atomic displacement factors near the structural phase transition at a synchrotron source. These data would lead to a more complete understanding of the structural changes involved in the transition.

As chromium doping should be accessible, it would be interesting to substitute the vanadium in $BaV_{10}O_{15}$ with an equal quantity of titanium and chromium. It would therefore be possible to increase the level of disorder on the transition metal site while

maintaining the same number of *d* electrons. If the titanium and chromium were to compensate one another, the effects of disorder could effectively be studied.

The magnetic properties of $BaV_{10}O_{15}$ are characterized by high levels of frustration. Experimental evidence for this includes a frustration index ($\theta/T_D$) of ~24. The frustrated spins are disturbed at the phase transition, resulting in a jump in the susceptibility with decreasing temperature. A cooperative magnetic transition occurs well below the structural phase transition that contains features of both spin glass behavior and long range magnetic order. The intensity of magnetic neutron diffraction peaks (assigned to long range order) is significantly decreased in the sample that has a low structural transition temperature (105K).

Muon spin relaxation measurements have been carried out only on the $T_S$ = 105K sample. It would be beneficial to compare these data with measurements on samples with a higher structural transition temperature. As a result of long-range magnetic order, an oscillation in the polarization function is expected to occur in these materials.

Materials of the general formula $BaV_{10-x}Ti_xO_{15}$ have been prepared up to a titanium doping level of 80%. Beyond this doping level a mixture of phases is obtained. With 10% titanium doping the structural phase transition is inhibited. Even at a more moderate doping level of 5%, there is no evidence for a structural transition. Lower doping levels remain to be examined, to determine the minimum doping level at which the transition disappears. As studies on pure $BaV_{10}O_{15}$ have shown, careful control of the

stoichiometry is required to ensure that the disappearance of the transition is due to doping alone. It would be interesting to compare the effects of low doping levels with the current data on the sample dependence of pure $BaV_{10}O_{15}$.

The transport properties of the pure and titanium-doped samples are not fully understood. Various models of small polaron hopping have been examined to account for the data. With the small polaron hopping models, the magnitude of the thermopower is particularly difficult to explain. Therefore, an additional model based upon doping of an intrinsic band semiconductor has been proposed. Further work, in the form of Hall effect measurements, would be useful to distinguish between these models.

A new preparation route has been developed for the 5H compound $BaVO_{2.8}$ using the induction furnace. It was determined that up to 8% molar excess of vanadium in the reaction did not produce any impurity peaks in a powder diffractometer pattern. However, the excess vanadium did not significantly affect the lattice parameters. At 11% excess a small impurity peak was detected, which suggests that a further excess of vanadium would not be incorporated into the lattice. High-resolution transmission electron microscopy (HRTEM) would be useful for examining the effect of excess vanadium on the microstructure.

In a study of $BaVO_{2.8}$ using powder neutron diffraction, peaks due to long-range magnetic order were not detected. The possibilities of either a spin-glass or superparamagnetic ground state remain. AC susceptibility measurements employing a

small step size near the divergence temperature (between the field cooled and zero-field cooled data) could indicate the proper ground state.

Transport property measurements on $BaVO_{2.8}$ suggest that two-dimensional variable range hopping is occurring at low temperatures. With oxidation to $BaVO_{3.0}$, the dominant carrier type changed from holes to electrons. While thermopower data suggested metallic behavior for $BaVO_{3.0}$, the resistivity remained semiconducting. Further investigations are necessary to understand the conduction mechanism of $BaVO_3$.

# Appendix A

# Additional Crystallographic Data

### Additional Crystallographic Data for $BaV_{10}O_{15}$

Table A.1: Results for Refinement of Anisotropic Displacement Parameters in Cmca at 130K($Å^2$) ($\times 10^2$)

| | $U^{11}$ | $U^{22}$ | $U^{33}$ | $U^{12}$ | $U^{13}$ | $U^{23}$ |
|---|---|---|---|---|---|---|
| Ba1 | 0.0046(1) | 0.00366(9) | 0.00574(9) | 0.00031(6) | 0 | 0 |
| V1 | 0.0032(2) | 0.0031(2) | 0.0033(2) | 0.0003(1) | 0 | 0 |
| V2 | 0.0073(2) | 0.0060(1) | 0.0067(1) | 0.00273(9) | 0.00363(9) | 0.0036(1) |
| V3 | 0.0048(1) | 0.0049(1) | 0.0042(1) | 0.00059(9) | 0.00138(9) | 0.00182(9) |
| O1 | 0.0120(9) | 0.0039(7) | 0.0038(7) | -0.0001(5) | 0 | 0 |
| O2 | 0.0074(6) | 0.0067(6) | 0.0049(5) | 0.0018(4) | -0.0015(4) | -0.0032(4) |
| O3 | 0.0051(8) | 0.0046(7) | 0.0041(6) | 0 | 0.0009(6) | 0 |
| O4 | 0.0046(6) | 0.0038(5) | 0.0039(4) | 0.0004(4) | 0.0001(4) | 0.0004(4) |
| O5 | 0.0049(8) | 0.0039(7) | 0.0047(6) | 0.0002(5) | 0 | 0 |
| O6 | 0.006(1) | 0.005(1) | 0.005(1) | 0.0004(8) | 0 | 0 |

Table A.2: Results for Refinement of Anisotropic Displacement Parameters in Pbca at 100K($Å^2$) ($\times 10^2$)

| | $U^{11}$ | $U^{22}$ | $U^{33}$ | $U^{12}$ | $U^{13}$ | $U^{23}$ |
|---|---|---|---|---|---|---|
| Ba | 0.00391(8) | 0.00230(8) | 0.00347(8) | 0.00026(5) | 0.00023(4) | 0.00007(5) |
| V1 | 0.0023(2) | 0.0019(1) | 0.0018(1) | 0.00022(9) | 0.00007(9) | 0.0002(1) |
| V2 | 0.0029(1) | 0.0023(1) | 0.0022(1) | 0.0002(1) | 0.0005(1) | 0.0006(1) |
| V3 | 0.0025(1) | 0.0023(1) | 0.0020(1) | -0.00005(9) | 0.0002(1) | 0.0005(1) |
| V2B | 0.0032(2) | 0.0027(1) | 0.0023(1) | -0.0007(1) | -0.0005(1) | 0.0010(1) |
| V3B | 0.0026(1) | 0.0020(1) | 0.0020(1) | 0.00014(9) | -0.0004(1) | 0.0003(1) |
| O1 | 0.0060(7) | 0.0024(6) | 0.0029(6) | 0.0000(4) | -0.0009(4) | -0.0005(5) |
| O2 | 0.0042(6) | 0.0031(6) | 0.0034(5) | 0.0007(4) | 0.0000(4) | 0.0000(5) |
| O2B | 0.0042(6) | 0.0029(6) | 0.0027(5) | -0.0001(4) | -0.0001(4) | -0.0003(5) |
| O3 | 0.0039(6) | 0.0028(6) | 0.0031(5) | -0.0002(4) | 0.0013(5) | 0.0000(5) |
| O4 | 0.0032(6) | 0.0032(6) | 0.0031(5) | 0.0004(4) | 0.0002(4) | 0.0002(5) |
| O4B | 0.0040(6) | 0.0035(6) | 0.0018(5) | -0.0003(4) | 0.0005(4) | -0.0003(5) |
| O5 | 0.0045(6) | 0.0022(6) | 0.0031(5) | 0.0004(4) | -0.0005(4) | 0.0005(5) |
| O6 | 0.0041(9) | 0.0036(9) | 0.0037(8) | 0.0000(6) | 0.0001(6) | -0.0004(7) |

Table A.3: $BaV_{10}O_{15}$ cell data for various preparations

| $T_S$ | Preparation | a (Å) | b (Å) | c (Å) | V ($Å^3$) |
|---|---|---|---|---|---|
| 135 | 23 | 11.5944(1) | 9.9488(1) | 9.3980(2) | 1084.06(2) |
| 135 | 22 | 11.5949(1) | 9.9488(1) | 9.3985(1) | 1084.17(2) |
| 125 | 11 | 11.5968(2) | 9.9504(2) | 9.3992(1) | 1084.59(2) |
| 125 | 5* | 11.597(1) | 9.950(1) | 9.398(1) | 1084.3(2) |
| 116 | 20 | 11.5888(1) | 9.9511(1) | 9.3946(1) | 1083.39(2) |
| 100 | 21 | 11.5873(1) | 9.9546(1) | 9.3944(1) | 1083.61(2) |
| - | 19 | 11.5823(2) | 9.9644(1) | 9.3939(1) | 1084.15(2) |

*from guinier camera, data for the other preparations from Bruker D8 Advance diffractometer

## Additional Crystallographic Data for $BaV_{10-x}Ti_xO_{15}$

Table A.4: Results for Refinement of Anisotropic Displacement Parameters in Cmca at 300K for $BaV_9TiO_{15}$($Å^2$) ($\times 10^2$)

| Site | $U^{11}$ | $U^{22}$ | $U^{33}$ | $U^{12}$ | $U^{13}$ | $U^{23}$ |
|---|---|---|---|---|---|---|
| Ba1 | 0.01182(10) | 0.01017(9) | 0.01033(9) | 0.00102(6) | 0 | 0 |
| V1 | 0.00650(16) | 0.00813(15) | 0.00566(15) | 0.00092(11) | 0 | 0 |
| V2 | 0.00863(13) | 0.00925(12) | 0.00761(12) | 0.00128(8) | 0.00198(8) | 0.00202(9) |
| V3 | 0.00675(12) | 0.00927(12) | 0.00622(11) | -0.00020(8) | 0.00101(9) | 0.00111(8) |
| Ti1 | 0.00650(16) | 0.00813(15) | 0.00566(15) | 0.00092(11) | 0 | 0 |
| Ti2 | 0.00863(13) | 0.00925(12) | 0.00761(12) | 0.00128(8) | 0.00198(8) | 0.00202(9) |
| Ti3 | 0.00675(12) | 0.00927(12) | 0.00622(11) | -0.00020(8) | 0.00101(9) | 0.00111(8) |
| O1 | 0.0122(8) | 0.0086(7) | 0.0062(6) | 0.0002(5) | 0 | 0 |
| O2 | 0.0089(5) | 0.0105(5) | 0.0070(5) | 0.0014(4) | -0.0004(4) | -0.0017(4) |
| O3 | 0.0082(7) | 0.0082(6) | 0.0062(6) | 0 | 0.0015(6) | 0 |
| O4 | 0.0072(5) | 0.0085(5) | 0.0063(5) | 0.0002(4) | -0.0003(4) | 0.0000(4) |
| O5 | 0.0073(7) | 0.0089(6) | 0.0075(7) | 0.0008(5) | 0 | 0 |
| O6 | 0.0072(10) | 0.0090(9) | 0.0058(9) | 0.0008(7) | 0 | 0 |

# Appendix B

# Total Number of Symmetry Allowed Magnetic Structures for $BaV_{10}O_{15}$

### Allowed Basis Vector Combinations for 2-6 Basis Vectors Per Vanadium Site

The allowed combinations of the 12 basis vectors in one irreducible representation can be calculated using the rules listed in section 3.8.3. The example for 2 basis vectors has been worked out in table B.1, and effectively corresponds to six single choices from group A, combined with six single choices from group B (6×6=36 combinations).

Table B.2: Possible combinations of basis vectors for the irreducible representations of the space group Pbca with **k** = (1/2, 0, 0) in which 1 basis vectors from group A, and 2 basis vectors from group B per ion are chosen

| | | | | |
|---|---|---|---|---|
| (A), 4, 5 | (A), 5, 6 | (A), 6, 7 | (A), 7, 8 | (A), 8, 9 |
| (A), 4, 6 | (A), 5, 8 | (A), 6, 8 | (A), 7, 9 | |
| (A), 4, 8 | (A), 5, 9 | | | |
| (A), 4, 9 | | | | |

(A) represents any basis vector from group A (basis vectors 1,2,3,10,11,12)

We can see from the first example that when 1 basis vector is chosen from a group, there are six possible choices. When 2 basis vectors are chosen from a group, table B.2 shows that there are twelve possible choices. Similar arguments will find that for 3 basis vectors from one group, there are eight possible choices. From this information, all possible combinations of group A and B can be calculated, and are as follows:

A) 2 basis vectors: (one from group A, one from group B) = (1A, 1B) = (6 × 6) = 36

B) 3 basis vectors: (1A, 2B)+(2A, 1B) = (6 × 12) + (12 × 6) = 144

C) 4 basis vectors: (1A, 3B)+(3A, 1B)+(2A, 2B) = (6 × 8) + (8 × 6) + (12 × 12) = 240

D) 5 basis vectors: (2A, 3B)+(3A, 2B) = (12 × 8) + (8 × 12) = 192

E) 6 basis vectors: (3A, 3B) = (8 × 8) = 64

**Irreducible Representations for $BaV_{10}O_{15}$**

Table B.3 lists the complete set of basis vectors for the compound $BaV_{10}O_{15}$ in space group Pbca with **k** = (1/2, 0, 0). As all of the vanadium atoms in the asymmetric unit have the same site symmetry, table B.3 is the same for all five atoms.

Table B.1: Possible combinations of basis vectors for the irreducible representations of the space group Pbca with **k** = (1/2, 0, 0) in which **2 basis vectors per ion** are chosen

| | Group A | | | Group B | | | | | | Group A | | |
|---|---|---|---|---|---|---|---|---|---|---|---|---|
| BV | 1 | 2 | 3 | 4 | 5 | 6 | 7 | 8 | 9 | 10 | 11 | 12 |
| 1 | × | × | × | 1,4 | 1,5 | 1,6 | 1,7 | 1,8 | 1,9 | × | × | × |
| 2 | × | × | × | 2,4 | 2,5 | 2,6 | 2,7 | 2,8 | 2,9 | × | × | × |
| 3 | × | × | × | 3,4 | 3,5 | 3,6 | 3,7 | 3,8 | 3,9 | × | × | × |
| 4 | | | | × | × | × | × | × | × | 4,10 | 4,11 | 4,12 |
| 5 | | | | × | × | × | × | × | × | 5,10 | 5,11 | 5,12 |
| 6 | | | | × | × | × | × | × | × | 6,10 | 6,11 | 6,12 |
| 7 | | | | × | × | × | × | × | × | 7,10 | 7,11 | 7,12 |
| 8 | | | | × | × | × | × | × | × | 8,10 | 8,11 | 8,12 |
| 9 | | | | × | × | × | × | × | × | 9,10 | 9,11 | 9,12 |
| 10 | × | × | × | | | | | | | × | × | × |
| 11 | × | × | × | | | | | | | × | × | × |
| 12 | × | × | × | | | | | | | × | × | × |

BV = basis vector; one vanadium site corresponds to eight ion positions - group A basis vectors define moment orientations for four of eight ions, and group B basis vectors for the remaining four ions

Table B.3: The basis functions of the irreducible representations for the space group Pbca with **k** = (1/2, 0, 0)

| BV | Atom 1 | | | Atom 2 | | | Atom 3 | | | Atom 4 | | | Atom 5 | | | Atom 6 | | | Atom 7 | | | Atom 8 | | |
|---|---|---|---|---|---|---|---|---|---|---|---|---|---|---|---|---|---|---|---|---|---|---|---|---|
| | $m_x$ | $m_y$ | $m_z$ | $m_x$ | $m_y$ | $m_z$ | $m_x$ | $m_y$ | $m_z$ | $m_x$ | $m_y$ | $m_z$ | $m_x$ | $m_y$ | $m_z$ | $m_x$ | $m_y$ | $m_z$ | $m_x$ | $m_y$ | $m_z$ | $m_x$ | $m_y$ | $m_z$ |
| $\psi_1$ | 1 | 0 | 0 | 0 | 0 | 0 | 1 | 0 | 0 | 0 | 0 | 0 | -1 | 0 | 0 | 0 | 0 | 0 | -1 | 0 | 0 | 0 | 0 | 0 |
| $\psi_2$ | 0 | 1 | 0 | 0 | 0 | 0 | 0 | -1 | 0 | 0 | 0 | 0 | 0 | -1 | 0 | 0 | 0 | 0 | 0 | 1 | 0 | 0 | 0 | 0 |
| $\psi_3$ | 0 | 0 | 1 | 0 | 0 | 0 | 0 | 0 | 1 | 0 | 0 | 0 | 0 | 0 | -1 | 0 | 0 | 0 | 0 | 0 | -1 | 0 | 0 | 0 |
| $\psi_4$ | 0 | 0 | 0 | 1 | 0 | 0 | 0 | 0 | 0 | 1 | 0 | 0 | 0 | 0 | 0 | -1 | 0 | 0 | 0 | 0 | 0 | -1 | 0 | 0 |
| $\psi_5$ | 0 | 0 | 0 | 0 | 1 | 0 | 0 | 0 | 0 | 0 | -1 | 0 | 0 | 0 | 0 | 0 | -1 | 0 | 0 | 0 | 0 | 0 | 1 | 0 |
| $\psi_6$ | 0 | 0 | 0 | 0 | 0 | -1 | 0 | 0 | 0 | 0 | 0 | -1 | 0 | 0 | 0 | 0 | 0 | 1 | 0 | 0 | 0 | 0 | 0 | 1 |
| $\psi_7$ | 0 | 0 | 0 | 1 | 0 | 0 | 0 | 0 | 0 | -1 | 0 | 0 | 0 | 0 | 0 | 1 | 0 | 0 | 0 | 0 | 0 | -1 | 0 | 0 |
| $\psi_8$ | 0 | 0 | 0 | 0 | 1 | 0 | 0 | 0 | 0 | 0 | 1 | 0 | 0 | 0 | 0 | 0 | 1 | 0 | 0 | 0 | 0 | 0 | 1 | 0 |
| $\psi_9$ | 0 | 0 | 0 | 0 | 0 | -1 | 0 | 0 | 0 | 0 | 0 | 1 | 0 | 0 | 0 | 0 | 0 | -1 | 0 | 0 | 0 | 0 | 0 | 1 |
| $\psi_{10}$ | 1 | 0 | 0 | 0 | 0 | 0 | -1 | 0 | 0 | 0 | 0 | 0 | 1 | 0 | 0 | 0 | 0 | 0 | -1 | 0 | 0 | 0 | 0 | 0 |
| $\psi_{11}$ | 0 | 1 | 0 | 0 | 0 | 0 | 0 | 1 | 0 | 0 | 0 | 0 | 0 | 1 | 0 | 0 | 0 | 0 | 0 | 1 | 0 | 0 | 0 | 0 |
| $\psi_{12}$ | 0 | 0 | 1 | 0 | 0 | 0 | 0 | 0 | -1 | 0 | 0 | 0 | 0 | 0 | 1 | 0 | 0 | 0 | 0 | 0 | -1 | 0 | 0 | 0 |
| $\psi_{13}$ | 1 | 0 | 0 | 0 | 0 | 0 | 1 | 0 | 0 | 0 | 0 | 0 | 1 | 0 | 0 | 0 | 0 | 0 | 1 | 0 | 0 | 0 | 0 | 0 |
| $\psi_{14}$ | 0 | 1 | 0 | 0 | 0 | 0 | 0 | -1 | 0 | 0 | 0 | 0 | 0 | 1 | 0 | 0 | 0 | 0 | 0 | -1 | 0 | 0 | 0 | 0 |
| $\psi_{15}$ | 0 | 0 | 1 | 0 | 0 | 0 | 0 | 0 | 1 | 0 | 0 | 0 | 0 | 0 | 1 | 0 | 0 | 0 | 0 | 0 | 1 | 0 | 0 | 0 |
| $\psi_{16}$ | 0 | 0 | 0 | 1 | 0 | 0 | 0 | 0 | 0 | 1 | 0 | 0 | 0 | 0 | 0 | 1 | 0 | 0 | 0 | 0 | 0 | 1 | 0 | 0 |
| $\psi_{17}$ | 0 | 0 | 0 | 0 | 1 | 0 | 0 | 0 | 0 | 0 | -1 | 0 | 0 | 0 | 0 | 0 | 1 | 0 | 0 | 0 | 0 | 0 | -1 | 0 |
| $\psi_{18}$ | 0 | 0 | 0 | 0 | 0 | -1 | 0 | 0 | 0 | 0 | 0 | -1 | 0 | 0 | 0 | 0 | 0 | -1 | 0 | 0 | 0 | 0 | 0 | -1 |
| $\psi_{19}$ | 0 | 0 | 0 | 1 | 0 | 0 | 0 | 0 | 0 | -1 | 0 | 0 | 0 | 0 | 0 | -1 | 0 | 0 | 0 | 0 | 0 | 1 | 0 | 0 |
| $\psi_{20}$ | 0 | 0 | 0 | 0 | 1 | 0 | 0 | 0 | 0 | 0 | 1 | 0 | 0 | 0 | 0 | 0 | -1 | 0 | 0 | 0 | 0 | 0 | -1 | 0 |
| $\psi_{21}$ | 0 | 0 | 0 | 0 | 0 | -1 | 0 | 0 | 0 | 0 | 0 | 1 | 0 | 0 | 0 | 0 | 0 | 1 | 0 | 0 | 0 | 0 | 0 | -1 |
| $\psi_{22}$ | 1 | 0 | 0 | 0 | 0 | 0 | -1 | 0 | 0 | 0 | 0 | 0 | -1 | 0 | 0 | 0 | 0 | 0 | 1 | 0 | 0 | 0 | 0 | 0 |
| $\psi_{23}$ | 0 | 1 | 0 | 0 | 0 | 0 | 0 | 1 | 0 | 0 | 0 | 0 | 0 | -1 | 0 | 0 | 0 | 0 | 0 | -1 | 0 | 0 | 0 | 0 |
| $\psi_{24}$ | 0 | 0 | 1 | 0 | 0 | 0 | 0 | 0 | -1 | 0 | 0 | 0 | 0 | 0 | -1 | 0 | 0 | 0 | 0 | 0 | 1 | 0 | 0 | 0 |

BV = basis vector; $m_x$, $m_y$, $m_z$ = projections of the moment along each axis; $\psi_{1\text{-}12} = \Gamma_1^2$; $\psi_{13\text{-}24} = \Gamma_2^2$

# Appendix C

# Additional Resistivity Data

### Prefactor from Fitting to Various Hopping Models in $BaV_{10}O_{15}$

Conductivity data have been fit by a wide range of models in the high and low temperature ranges. A general formula for the conductivity is given by equation C.1.

$$\sigma = \sigma_o T^m (-\frac{B}{T})^n \qquad \text{(C.1)}$$

Here $\sigma_o$ is the constant part of the prefactor, and $T^m$, where $m \neq 0$, is the temperature dependent part. The constant B is discussed in section 3.9.1, and listed in table 3.15. The exponential constants *m* and *n* are model dependent, and are described in section 1.4 of the introduction. Conductivity data was plotted as $\ln(\sigma T^m)$ versus $T^{-n}$, and fitted over the linear portion of the plot. Values of the prefactor ($\ln(\sigma_o)$) are given in table C.1. Low temperature fits were performed over the range 35K to 46K for the Arrhenius and Mott polaronic models, and 35K to 60K for the variable range hopping (VRH) models. High temperature fits were over the temperature range 180K to 290K for the $T_S$ = 105K sample, and 250-320K for the $T_S$ = 135K sample.

Table C.1: Prefactor ($\ln(\sigma_o)$) for several different models of charge transport for the $T_S$ = 105K sample of $BaV_{10}O_{15}$

| T | Arrhenius | Mott Polaron | Mott VRH | | Efros-Shklovskii VRH | |
|---|---|---|---|---|---|---|
| | $\Omega^{-1}cm^{-1}$ | $\Omega^{-1}cm^{-1}K$ | $\Omega^{-1}cm^{-1}K^{1/2}$ | $\Omega^{-1}cm^{-1}$ | $\Omega^{-1}cm^{-1}K$ | $\Omega^{-1}cm^{-1}$ |
| | | | $T^{-1/2}$ | $T^0$ | $T^{-1}$ | $T^0$ |
| High | 6.700 (9) | 13.142 (7) | - | - | - | - |
| Low | -1.48 (4) | 3.20 (5) | 25.42 (4) | 21.51 (5) | 5.41 (2) | 6.63 (3) |

T = temperature range; units are presented in the second row, and the temperature dependent part of the prefactor ($T^m$) is indicated in the third row.

Table C.2: Prefactor ($\ln(\sigma_o)$) for different models of charge transport for the $T_S$ = 135K sample of $BaV_{10}O_{15}$

| T | Arrhen | Mott Polaron |
|---|---|---|
| K | $\Omega^{-1}cm^{-1}$ | $\Omega^{-1}cm^{-1}K$ |
| 250-320 | 3.67 (2) | 10.32 (1) |

T = temperature range; units are presented in the second row

## Prefactor from Fitting to Various Small Polaron Hopping Models in $BaV_{10-x}Ti_xO_{15}$

Table C.3: Prefactor ($\ln(\sigma_o)$) for several different models of charge transport in $BaV_{10-x}Ti_xO_{15}$

| x (%) | Arrhen | Mott Polaron | Holstein Polaron | | Mott VRH | | Efros-Shklov VRH | |
|---|---|---|---|---|---|---|---|---|
| | $T^0$ | $T^1$ | $T^1$ | $T^{3/2}$ | $T^{-1/2}$ | $T^0$ | $T^{-1}$ | $T^0$ |
| 10 | 4.25 (4) | 10.85 (4) | 10.85 (4) | 14.15 (4) | 13.08 (2) | 17.12 (2) | 12.04 (3) | 5.97 (2) |
| 30 | 4.63 (1) | 11.23 (2) | 11.23 (2) | 14.53 (2) | 12.4 (1) | 16.0 (1) | 10.67 (6) | 5.77 (4) |
| 50 | 4.343 (2) | 10.954 (2) | 10.954 (2) | 14.26 (3) | 8.79 (3) | 12.75 (3) | 7.61 (6) | 3.22 (4) |
| 70 | 5.139 (1) | 11.64 (2) | 11.64 (2) | 14.896 (2) | 8.33 (1) | 12.57 (2) | 14.52 (2) | 7.2 (1) |

x = percent titanium substitution; the exponent for the temperature dependent part of the prefactor ($T^m$) is indicated in the second row.

## Prefactor from Fitting to Various Hopping Models in $BaVO_{2.8}$

Table C.4: Prefactor ($\ln(\sigma_o)$) for several different models of charge transport in $BaVO_{2.8}$

| x (%) | Arrhen | Mott 2D VRH | Mott 3D VRH | | Efros-Shklov VRH | |
|---|---|---|---|---|---|---|
| | $T^0$ | $T^0$ | $T^{-1/2}$ | $T^0$ | $T^{-1}$ | $T^0$ |
| 8 | 2.14 (5) | 14.214 (5) | 16.72 (1) | 21.28 (2) | 14.42 (2) | 7.17 (1) |

x = percent of excess vanadium used in preparation; the exponent for the temperature dependent part of the prefactor ($T^m$) is indicated in the second row.

# Appendix D

# Hill Analysis of Variable Range Hopping Exponent

### Method to Determine the Exponent of the Conductivity

A method to determine the exponent (n) of conductivity (see equation C.1) is given below. First defining the activation energy as in equation 3.9.1

$$\Delta E = -k\frac{d(\ln\sigma)}{d(1/T)}$$

Substituting in the natural logarithm of equation C.1

$$-k\frac{d(\ln\sigma)}{d(1/T)} = -k\left[\frac{d}{d(1/T)}(m\ln T) + \frac{d}{d(1/T)}(-B(T)^{-n})\right] \qquad \text{(D.1)}$$

Differentiating, we get

$$\Delta E = -k\left[(-mT) + (-BnT^{(1-n)})\right] \qquad \text{(D.2)}$$

A double logarithmic plot of log(ΔE) versus log(T) should give a slope of (1-n), as long as the analysis is performed at sufficiently low temperatures. The temperature should be low enough that the temperature dependence of the prefactor will not have a significant effect on the fit. More specifically, at $T<<(Bn/m)^{1/n}$.(Hill 1976)

# Bibliography


N. V. Agrinskaya and V. I. Kozub. *Solid State Comm.*, 91(11): 853-857, **1994**.

J. Akimoto, Y. Gotoh, M. Sohma, K. Kawaguchi and Y. Oosawa. *J. Solid State Chem.*, 113: 384-392, **1994**.

A. A. Al-Shahrani, S. Abboudy and A. W. Brinkman. *J. Phys. D: Appl. Phys.*, 29: 2165-2169, **1995**.

T. L. Aselage, D. Emin, S. S. McCready and R. V. Duncan. *Phys. Rev. Lett.*, 81(11): 2316-2319, **1998**.

P. W. Atkins. *Physical Chemistry*. W.H. Freeman and Company, New York,**1990**.

I. G. Austin and N. F. Mott. *Adv. Phys.*, 18: 41-97, **1969**.

M. C. Baird. *Metal-Metal Bonds in Transition Metal Compounds*. Progress in Inorganic Chemistry. F. A. Cotton. John Wiley & Sons, Inc., New York. 9**:** 1-151, **1968**.

M. D. Banus, T. B. Reed and A. J. Strauss. *Phys. Rev. B*, 5(8): 2775-2784, **1972**.

W. Bao, C. Broholm, G. Aeppli, S. A. Carter, P. Dai, C. D. Frost, J. M. Honig and P. Metcalf. *J. Mag. Mag. Mat.*, 177-181: 283-286, **1998**.

W. A. Bassett and G. E. Brown. *Annu. Rev. Earth Planet Sci.*, 18: 387-447, **1990**.

D. C. d. Beaulieu and H. K. Müller-Buschbaum. *Z. Naturforsh.*, 35b: 669-671, **1980**.

E. F. Bertaut. *Acta Cryst.*, A24: 217-231, **1968**.

E. F. Bertaut. *J. Magn. Magn. Mat.*, 24: 267-278, **1981**.

K. Binder and A. P. Young. *Rev. Mod. Phys.*, 58(4): 801-976, **1986**.

D. L. Bish and J. E. Post, Eds. *Modern Powder Diffraction*. Reviews in Mineralogy. Mineralogical Society of America, Washington, D.C., **1989**.

F. J. Blatt, P. A. Schroeder, C. L. Foiles and D. Greig. *Thermoelectric Power of Metals*. Plenum Press, New York,**1976**.

R. Bontchev, F. Weill and J. Darriet. *Mat. Res. Bull.*, 27: 931-938, **1992**.

H. Bottger and V. V. Bryksin. *Phys. Stat. Sol. B*, 78: 9, **1976**.

S. T. Bramwell and M. J. P. Gingras. *Science*, 294: 1495-1501, **2001**.

M. J. Burns and P. M. Chaikin. *J. Phys. C: Solid State Phys.*, 18: L743-L749, **1985**.

E. Canadell. *Chem. Mater.*, 10: 2770-2786, **1998**.

P. A. Cox. *The Electronic Structure and Chemistry of Solids*. Oxford University Press, New York,**1987**.

B. Capoen, G. Biskupski and A. Briggs. *Solid State Commun.*, 113: 135-139, **2000**.

F. Cardarelli. *Materials Handbook: A Concise Desktop Reference*. Springer -Verlag London Ltd., London,**2000**.

R. L. Carlin and A. J. v. Duyneveldt. *Magnetic Properties of Transition Metal Compounds*. Springer-Verlag, New York,**1977**.

P. M. Chaikin. *An Introduction to Thermopower for Those Who Might Want to Use It to Study Organic Conductors and Superconductors*. Organic Superconductivity. V. Z. Kresin and W. A. Little. Plenum Press, New York. , **1990**.

P. M. Chaikin and G. Beni. *Phys. Rev. B*, 13(2): 647-651, **1976**.

R. Chakravarthy, L. M. Rao, S. K. Paranjpe, S. K. Kulshreshtha and S. B. Roy. *Phys. Rev. B*, 43(7): 6031-6036, **1991**.
B. L. Chamberland and P. S. Danielson. *J. Solid State Chem.*, 3: 243-247, **1971**.
G. V. Chandrashekhar, H. L. C. Barros and J. M. Honig. *Mat. Res. Bull*, 8: 369-374, **1973**.
B.-H. Chen, B. W. Eichhorn, H. L. Ju and R. L. Greene. *Inorg. Chem.*, 32: 5715-5719, **1993**.
J. Clarke. *Scientific American*, August: 46-53, **1994**.
A. I. Coldea, L. E. Spring, S. J. Blundell, J. Singleton and W. Hayes. *J. Phys.: Condens. Matter*, 11: 9053-9072, **1999**.
M. F. Collins. *Magnetic Critical Scattering*. Oxford University Press, Oxford,**1989**.
P. A. Cox. *Transition Metal Oxides: An Introduction to their Electronic Structure and Properties*. Oxford University Press, New York,**1992**.
Quantum Design. *Magnetic Property Measurement System (MPMS) Reciprocating Sample Option User's Manual*, **1999**.
Quantum Design. *Physical Property Measurement System (PPMS) Application Note on Magnetometry*, **1999**.
Quantum Design. *Physical Property Measurement System (PPMS) Resistivity Option User's Manual*,**1999**.
Quantum Design. *Introduction to: AC Susceptibility*,**2002**.
J. Dumas and C. Schlenker. *J. Phys. C: Solid State Phys.*, 12: 2381-2399, **1979**.
A. L. Efros and B. I. Shklovskii. *J. Phys. C: Solid State Phys.*, 8: L49-L51, **1975**.
S. R. Elliot. *Physics of amorphous materials*. Longman Scientific & Technical, New York,**1990**.
D. Emin. *Phys. Rev. Lett.*, 32(6): 303-307, **1974**.
D. Emin. *J. Solid State Chem.*, 12: 246-252, **1975**.
D. Emin. *Hopping and related phenomena 5 : proceedings of the 5th International Conference on Hopping and Related Phenomena*. International Conference on Hopping and Related Phenomena, Glasgow, Scotland, UK. World Scientific, (**1993**).
D. Emin. *Phys. Rev. B*, 48(18): 13691-13702, **1993**.
D. Emin. *Phys. Rev. B*, 59(9): 6205-6210, **1999**.
A. Feltz and S. Schmalfuss. *Kristall u. Technik*, 6(3): 367-376, **1971**.
A. Feltz and S. Schmalfuss. *Z. Anorg. Allg. Chem.*, 417: 130-136, **1975**.
M. Fisher. *Phil. Mag.*, 17: 1731-1743, **1962**.
F. Galasso and L. Katz. *Acta Crystallogr.*, 14: 647-650, **1961**.
A. Ghosh. *J. Chem. Phys.*, 102(3): 1385-1389, **1994**.
A. Ghosh. *Philos. Mag. B*, 63(2): 477-484, **1991**.
D. M. Giaquinta and H.-C. z. Loye. *J. Am. Chem. Soc.*, 114: 10952-10953, **1992**.
T. C. Gibb. *J. Mater. Chem.*, 2(4): 387-393, **1992**.
M. J. P. Gingras and B. C. d. Hertog. *Can. J. Phys.*, 79: 1339-1351, **2001**.
M. J. P. Gingras, B. C. d. Hertog, M. Faucher, J. S. Gardner, S. R. Dunsiger, L. J. Chang, B. D. Gaulin, N. P. Raju and J. E. Greedan. *Phys. Rev. B*, 62(10): 6496-6511, **2000**.
E. Gmelin. *Thermochim. Acta*, 29: 1-39, **1979**.
E. Gmelin. *Thermal Analysis Highlights*. Elsevier Science Publisher, Bratislava,**1987**.

J. B. Goodenough. *Chem. Mater.*, 10: 2980-2993, **1998**.
J. B. Goodenough. *J. Solid State Chem.*, 1: 349-358, **1970**.
J. B. Goodenough. *J. Solid State Chem.*, 3: 490-500, **1971**.
J. B. Goodenough. *Magnetism and the Chemical Bond*. Interscience, New York,**1963**.
J. B. Goodenough. *Mat. Res. Bull*, 2: 37-48, **1967**.
J. B. Goodenough. *Mat. Res. Bull.*, 2: 165-184, **1967**.
J. B. Goodenough. *Mat. Res. Bull.*, 5: 621-630, **1970**.
J. B. Goodenough. *Metallic Oxides*. Progress in Solid State Chemistry. Pergamon, New York. 5: 145-399, **1971**.
J. B. Goodenough. *Nature*, 404: 821-822, **2000**.
J. B. Goodenough. *Phys. Rev. B*, 5(8): 2764-2774, **1972**.
E. S. R. Gopal. *Specific Heats at Low Temperatures*. Plenum Press, New York,**1966**.
E. Gratz. *J. Magn. Magn. Mat.*, 24: 1-6, **1981**.
J. E. Greedan. *Magnetic Oxides*. Wiley, New York,**1994**.
J. E. Greedan. *J. Mater. Chem.*, 11: 37-53, **2001**.
F. Gronvold. *Pure & Appl. Chem.*, 47: 251-266, **1976**.
R. M. Hill. *Phys. Stat. Sol. A*, 35: K29-K34, **1976**.
R. R. Heikes and J. R. W. Ure. *Thermoelectricity: Science and Engineering*. Interscience Publishers, Inc., New York,**1961**.
R. M. Hill. *Phys. Stat. Sol. A*, 35: K29-K34, **1976**.
B.-S. Hong, S. J. Ford and T. O. Mason. *Key Engineering Materials*, 125-126: 163-186, **1997**.
J. Hubsch and G. Gavoille. *Phys. Rev. B*, 26(7): 3815-3823, **1982**.
M. Imada, A. Fujimori and Y. Tokura. *Rev. Mod. Phys.*, 70(4): 1039-1263, **1998**.
Oxford Instruments. *Heat Capacity (Relaxation) Probe Technical Reference*,**2000**.
Oxford Instruments. *Magnetic Properties Probe for MagLabEXA Technical Reference*,**2000**.
T.A. Instruments. *DSC 2910 Differential Scanning Calorimeter Operator's Manual*,**1993**.
M. Jaime, M. B. Salamon, M. Rubinstein, R. E. Treece, J. S. Horwitz and D. B. Chrisey. *Phys. Rev. B*, 54(17): 11914-11917, **1996**.
Y. Jin and B. Wunderlich. *Thermochim. Acta*, 226: 155-161, **1993**.
Y. Kanke, F. Izumi, E. Takayama-Muromachi, K. Kato, T. Kamiyama and H. Asano. *J. Solid State Chem*, 92: 261-272, **1991**.
S. I. Khondaker, I. S. Shlimak, J. T. Nicholls, M. Pepper and D. A. Ritchie. *Solid State Commun.*, 109: 751-756, **1999**.
A. Kimura, D. X. Li and Y. Shiokawa. *Solid State Commun.*, 113: 131-134, **2000**.
C. R. Kmety, Q. Huang, J. W. Lynn, R. W. Erwin, J. L. Manson, S. McCall, J. E. Crow, K. L. Stevenson, J. S. Miller and A. J. Epstein. *Phys. Rev. B*, 62(9): 5576-5588, **2000**.
H. Kuwamoto, J. M. Honig and J. Appel. *Phys. Rev. B*, 22(6): 2626-2636, **1980**.
J. I. Langford and D. Louer. *Rep. Prog. Phys.*, 59: 131-234, **1996**.
M. H. R. Lankhorst and J. E. t. Elshof. *J. Solid State Chem.*, 130: 302-310, **1997**.
A. C. Larson and R. B. v. Dreele (1994). *GSAS General Structure Analysis System*. Los Alamos National Laboratory, Los Alamos, LANSCE.

S. L. Lee, S. H. Kilcoyne and R. Cywinski, Eds.. *Muon Science: Muons in Physics, Chemistry and Materials*. Scottish Universities Summer School in Physics. Scottish Universities Summer School in Physics & Institute of Physics Publishing, Philadelphia, **1999**.
N. V. Lien and R. Rosenbaum. *J. Phys.: Condens. Matter*, 10: 6083-6090, **1998**.
K. G. Lisunov, E. Arushanov, G. A. Thomas, E. Bucher and J. H. Schon. *J. Appl. Phys.*, 88(7): 4128-4134, **2000**.
G. Liu and J. E. Greedan. *J. Solid State Chem.*, 110: 274-289, **1994**.
G. Liu and J. E. Greedan. *J. Solid State Chem.*, 122: 416-427, **1996**.
F. E. Mabbs and D. J. Machin. *Magnetism and Transition Metal Complexes*. Chapman and Hall, London,**1973**.
A. Maignan, A. Sundaresan, U. V. Varadaraju and B. Raveau. *J. Magn. Magn. Mater.*, 184: 83-88, **1998**.
G. Malmros and P. E. Werner. *Acta Chem. Scand.*, 27: 493, **1973**.
R. Mansfield, S. Abboudy and P. Fozooni. *Phil. Mag. B*, 57(6): 777-790, **1988**.
D. B. Marsh and P. E. Parris. *Phys. Rev. B*, 54(23): 16602-16607, **1996**.
D. B. Marsh and P. E. Parris. *Phys. Rev. B*, 54(11): 7720-7728, **1996**.
K. Matsuhira, Y. Hinatsu and T. Sakakibara. *J. Phys: Condens. Matter*, 13: L737-L746, **2001**.
N. Mott. *Philos. Mag. B*, 65(4): 767-773, **1992**.
N. F. Mott. *Festkor. A. S.*, 19: 331-361, **1979**.
N. F. Mott. *Conduction in Non-Crystalline Materials*. Oxford University Press, New York,**1987**.
J. A. Mydosh. *Spin Glasses, An Experimental Introduction*. Taylor & Francis, London,**1993**.
P. Nagels. *Polaronic Conduction in Oxide Glasses Containing V2O5*. Hopping and Related Phenomena. H. Fritzsche and M. Pollak. World Scientific Publishing Company, River Edge. **:** 385-392, **1990**.
T. K. Nath, N. Sudhakar, E. J. McNiff and A. K. Majurndar. *Phys. Rev. B*, 55(18): 12389-12401, **1997**.
D. R. Noakes and G. M. Kalvius. *Phys. Rev. B*, 56(5): 2352-2355, **1997**.
C. J. O'Connor. *Prog. Inorg. Chem.*, 29: 203-283, **1982**.
M. Pai and J. M. Honig. *Phys. Stat. Sol. B*, 108: K79-K83, **1981**.
T. Palanisamy, J. Gopalakrishnan and M. V. C. Sastri. *Z. Anorg. Allg. Chem.*, 415: 275-284, **1975**.
M. Parras, A. Varela, H. Seehofer and J. M. Gonzalez-Calber. *J. Solid State Chem.*, 120: 327-331, **1995**.
M. Pollak. *Philos. Mag. B*, 42(6): 781-798, **1980**.
M. Pollak. *Philos. Mag. B*, 65(4): 657-667, **1992**.
R. Raffaelle, H. U. Anderson, D. M. Sparlin and P. E. Parris. *Phys. Rev. B*, 43(10): 7991-7999, **1991**.
T. V. Ramakrishnan. *J. Solid State Chem.*, 111: 4-10, **1994**.
A. P. Ramirez. *Ann. Rev. Mater. Sci.*, 24: 453, **1994**.
L. S. Ramsdell. *Am. Mineral.*, 32: 64-82, **1947**.

T. B. Reed and E. R. Pollard. *J. Cryst. Growth*, 2: 243-247, **1968**.
J.A. Reedijk, H. C. F. Martens and H. B. Brom. *Phys. Rev. Lett.*: 9398, **1999**.
H. M. Rietveld. *Acta Crystallogr.*, 22: 151-152, **1967**.
H. M. Rietveld. *J. Appl. Crystallogr.*, 2: 65-71, **1969**.
D. B. Rogers, R. D. Shannon, A. W. Sleight and J. L. Gillson. *Inorg. Chem.*, 8: 841, **1969**.
R. Rosenbaum. *Phys. Rev. B*, 44(8): 3599-3603, **1991**.
T. F. Rosenbaum and S. A. Carter. *J. Solid State Chem.*, 88: 94-103, **1990**.
J. Rossat-Mignod. *Magnetic Structures*. Neutron Scattering : Part C. K. Skold and D. L. Price. Academic Press, Inc., Toronto. 23: 69-157, **1987**.
H.-U. Schaller and S. Kemmler-Sack. *J. Less-Common Met.*, 97: 299-315, **1984**.
H.-U. Schaller and S. Kemmler-Sack. *J. Less-Common Met.*, 96: 11-22, **1984**.
M. Schindler, F. C. Hawthorne and W. H. Baur. *Chem. Mater.*, 12: 1248-1259, **2000**.
E. Schmidbauer. *J. Phys.: Condens. Matter*, 10: 8279-8292, **1998**.
R. D. Shannon. *Acta. Cryst.*, A32: 751, **1976**.
G. M. Sheldrick (1997). *SHELXL97*: Program for the Refinement of Crystal Structures. Germany, University of Gottingen.
I. Shlimak. *Philos. Mag. B*, 81(9): 1093-1103, **2001**.
J. Spalek. *J. Solid State Chem.*, 88: 70-93, **1990**.
J. Spalek and J. M. Honig. *Chem. Mater.*, 10: 2910-2929, **1998**.
G. L. Squires. *Introduction to the theory of thermal neutron scattering*. Dover, Cambridge University Press, New York,**1996**.
S. Srinath and S. N. Kaul. *Europhys. Lett.*, 51(4): 441-446, **2000**.
G. H. Stout and L. H. Jensen. *X-ray Structure Determination: A Practical Guide*. John Wiley & Sons, Toronto,**1989**.
Y. Torii. *Chem. Lett.*, 6: 557-562, **1975**.
J. B. Torrance, P. Lacorre, C. Asavaroengchai and R. M. Metzger. *Physica C*, 182: 351-364, **1991**.
Y. Ueda, K. Kosuge and S. Kachi. *J. Solid State Chem.*, 31: 171-188, **1980**.
B. K. Vainshtein, V. M. Fridkin and V. L. Indenbom. *Structure of Crystals*. Springer-Verlag, Germany,**1994**.
J. F. Vente and P. D. Battle. *J. Solid State Chem.*, 152: 361-373, **2000**.
J. Villain. *Z. Physik B*, 33: 31-42, **1979**.
M. Viret, L. Ranno and J. M. D. Coey. *Phys. Rev. B*, 55(13): 8067-8070, **1997**.
M. B. Weissman. *Rev. Mod. Phys.*, 65(3): 829-839, **1993**.
M. T. Weller and C. S. Knee. *J. Mater. Chem.*, 11: 701-712, **2001**.
R. M. Wentzcovitch, W. W. Schulz and P. B. Allen. *Phys. Rev. Lett.*, 72(21): 3389-3392, **1994**.
M. A. White. *Thermochim. Acta*, 74: 55-62, **1984**.
H. W. Williams and B. L. Chamberland. *Anal. Chem.*, 41(14): 2084-2086, **1969**.
A. S. Wills. *Physica B*, 680: 276-278, **2000**.
A. S. Wills. *Phys. Rev. B*, 63: 64430-64443, **2001**.
A. S. Wills and I. D. Brown (1999). *VaList*. CEA, France.

A. Wold and K. Dwight. *Preparation and Characterization of Conducting Transition Metal Oxides*. Advances in the Synthesis and Reactivity of Solids. JAI Press Ltd., **1991**.
P.-z. Wong, S. v. Molnar, T. T. M. Palstra, J. A. Mydosh, H. Yoshizawa, S. M. Shapiro and A. Ito. *Phys. Rev. Lett.*, 55(19): 2043-2046, **1985**.
A. I. Yakimov, A. V. Dvurechenskii, N. P. Stepina, L. A. Scherbakova, C. J. Adkins, V. Z. Chorniy, V. A. Dravin and R. Groetzschel. *J.Phys: Condens. Matter*, 9: 889-899, **1997**.
K. Yamaura, D. P. Young and R. J. Cava. *Phys. Rev. B*, 63: 64401-64405, **2001**.
M. Yethiraj. *J. Solid State Chem.*, 88: 53-69, **1990**.
K. Yoshii and H. Abe. *J. Solid State Chem.*, 156: 452-457, **2001**.
R. A. Young, Ed. *The Rietveld Method*. IUCr Monographs on Crystallography. Oxford University Press, New York, **1993**.
J. Zaanen, G. A. Sawatzky and J. W. Allen. *Phys. Rev. Lett.*, 55(4): 418-421, **1985**.
A. G. Zabrodskii. *Sov. Phys.-Semicond.*, 11(3): 345-347, **1977**.
A. G. Zabrodskii. *Philos. Mag. B*, 81(9): 1131-1151, **2001**.
P. Y. Zavalij and M. S. Whittingham. *Acta Cryst.*, B55: 627-663, **1999**.
Y. Zhang, P. Dai, M. Levy and M. P. Sarachik. *Observation of a Crossover from Mott to Efros-Shklovskii Variable Range Hopping in n-CdSe*. Hopping and Related Phenomena. H. Fritzsche and M. Pollak. World Scientific Publishing Company, River Edge. : 85-92, **1990**.
J.-S. Zhou, J. Chan and J. B. Goodenough. *Phys. Rev. B*, 47(9): 5477-5480, **1993**.
I. P. Zvyagin. *The Hopping Thermopower*. Hopping Transport in Solids. M. Pollak and B. Shklovskii. Elsevier Science Publishers, New York. , **1991**.